Radiation Pattern Shaping by Applying Machine Learning Method

By

Jiashu Yang

A dissertation submitted in partial fulfillment of the
requirements for the degree of

Doctor of Philosophy
of
University College London.

March 24, 2022

Declaration of Authorship

I, Jiashu Yang, confirm that the work presented in this thesis is my own. Where information has been derived from other sources, I confirm that this has been indicated in the work.

Signature:

Date:

Acknowledgements

First and foremost, I would like to express my deepest gratitude to my supervisor Prof. Kin-Fai (Kenneth) Tong, who gave me consistent support and valuable guidance during my Ph.D. research. I still remember how excited I was when I received the offer from you. I learned a lot from your broad knowledge, inspiring ideas and enthusiasm in scientific research. Also, thank you so much for offering me the opportunity to work with Rothamsted Research, which was a tremendous help to my life and study.

I am deeply grateful to Dr. Ka-Sing (Jason) Lim. It was a great experience and a fruitful collaboration with your group. Thank you for your patience and guidance during the project.

Also, I take this opportunity to thank China Scholarship Council (CSC) and University College London (UCL). Thanks for the joint scholarship for my Ph.D. study.

I also would like to thank my friends who gave me their kind help whenever I need. I would like to express my gratitude to Bingyang Wen, thanks for your help and guidance during my study.

Finally, I would like to give my gratitude to my family. Thanks for your support to my study and life for so many years. You always gave me encouragement when I was confused and down. I would not be where I am today without your strong support.

Abstract

In this study, a new design method for designing surface wave antennas was proposed. The proposed antennas will support the vertical-looking radar (VLR) systems for better pest monitoring. The distribution of the metallic cells on the low-profile surface wave antenna is designed by using the Wasserstein generative adversarial network (WGAN) and bidirectional gated recurrent unit (Bi-GRU) neural network prediction method with the desired cosecant-squared radiation pattern serving as input. The proposed neural network prediction method consists of two parts, which are i) from the far-field radiation pattern to the near-zone *E*-field and ii) from the near-zone *E*-field to the on-surface metallic cell pattern. In the first prediction part, the average prediction error among E_x, E_y and E_z components on the surface wave antenna of 50 test cases is 4.3%. And the average prediction accuracy achieves 99.54% in the prediction of the metallic cell pattern from the near-zone *E*-field. A dual-sided 30° cosecant-squared radiation pattern serves as the input for the neural network prediction model in the surface wave antenna design. The predicted antenna geometry shows less than 1 dBi variation in radiation pattern when compared to the input dual-sided 30° cosecant-squared radiation pattern. The fabricated surface wave antenna works in the frequency band 33.77 – 35.05 GHz, which covers the frequency band of the mmWave FMCW VLR system. With the help of the turntable of the mmWave VLR system, such antenna provides a circular observation area with a diameter of 9.8 m.

Impact Statement

Up to 40% of global crop production is lost to plant pests and diseases, says the U.N. Food and Agriculture Organization 2021 [1]. Plant diseases cost the global economy more than $220 billion and invasive insects cost at least $60 billion all over the world each year [1]. Effective and professional pest control action must be taken. Pests monitoring is vital since it provides ecologists and entomologists with migration information, which can be used to pest control strategies and reduce the use of pesticide. Many insect species fly within a few hundred meters of height and rely on wind-borne migration. This aerial bio-flow has important implications for ecological, physiological and genetic studies of insects, with applications in pest management, conservation and environmental change programs. Millimetre-wave (mmWave) frequency modulated continuous wave (FMCW) vertical-looking radar (VLR) systems are one of the feasible ways to monitor high-flying insects.

In this thesis, a dual-sided cosecant-squared radiation pattern surface wave antenna has been proposed to be used in a mmWave FMCW VLR system and it is designed by applying neural network prediction models. The antenna geometry has great advantages of simple geometry, low-profile and large observation area. The proposed neural network prediction model consists of two parts, which are i) from the desired far-field radiation pattern to the near-zone E-field prediction and ii) from the near-zone E-field to the on-surface metallic cell pattern prediction. Conventionally, the relationship from the near-field to far-field (NF2FF) can be defined by the Fourier transform. However, it leads to a challenging inverse problem due to the fact that the far-field E-pattern is a summation of E_ϕ and E_θ. Therefore, either E_θ or E_ϕ cannot be obtained by giving $E(r,\theta,\phi)$ unless E_θ or E_ϕ is zero. However, E_θ and E_ϕ are not equal to zero since the cross polarisation cannot be exactly zero in real antennas. The combination of Wasserstein generative adversarial network (WGAN) and bidirectional gated recurrent unit (Bi-GRU) neural networks, which is the first prediction part, are proposed to tackle the inverse problem of NF2FF. And the second prediction part, another Bi-GRU prediction model, describes the relationship between the near-zone E-field and the metallic cell pattern. The proposed antenna designed by the neural network model is fabricated for verifying the large observation area achieved and can provide more useful migration information to ecologists and entomologists.

On the other hand, this research demonstrates the feasibility of utilising a neural network prediction method to design surface wave antennas according to the desired radiation pattern. It shows the combination of the surface wave antenna and neural network prediction method can effectively control the radiation pattern or scatter the surface wave to free space on a specific angle. This novel method can be extended to general antenna design, such as metasurface, which will benefit the wireless communications industry a lot.

Contents

1 INTRODUCTION 24

1.1 FMCW VLR SYSTEM 25

1.2 AIM 27

1.3 RESEARCH CONTRIBUTION 29

1.3.1 Publications 30

1.4 THESIS OVERVIEW 30

2 BACKGROUND THEORY AND LITERATURE REVIEW 32

2.1 SURFACE WAVE AND SURFACE WAVE LAUNCHER 32

2.1.1 Surface wave 33

2.1.2 Surface wave launcher 34

2.2 LEAKY-WAVE ANTENNAS AND HOLOGRAPHIC ANTENNAS 39

2.2.1 Leaky-wave antennas 40

2.2.2 Holographic antennas 49

2.3 COSECANT-SQUARED RADIATION PATTERN 51

2.3.1 Cosecant-squared radiation pattern formation 53

2.4 NEURAL NETWORK 58

2.4.1 Biological neuron and artificial neuron 59

2.4.2 Neural network structure 60

2.4.3 Neural network training 61

2.4.4 Types of neural networks 73

2.4.5 Applications in antenna design 76

2.5 SUMMARY 82

3 THE PROPOSED NEURAL NETWORK METHOD 83

3.1 PROPOSED ANTENNA STRUCTURE 85

3.2 METHODOLOGY OF THE NEAR-ZONE *E*-FIELD PREDICTION FROM THE FAR-FIELD RADIATION PATTERN 88

3.2.1 Near-field to far-field transformation 90

3.2.2 Neural network model structure of the near-zone *E*-field prediction 92

3.2.3 Neural network model training of the near-zone *E*-field prediction 98
3.2.4 Training data preparation of the near-zone *E*-field prediction 101
3.2.5 Evaluation methods 106
3.3 METHODOLOGY OF THE METALLIC CELL PATTERN PREDICTION FROM NEAR-ZONE *E*-FIELD 109
3.3.1 Mathematical prediction model and multi-layer perceptron classifier 110
3.3.2 Neural network model structure of the metallic cell pattern prediction 119
3.3.3 Neural network model training of the metallic cell pattern prediction 120
3.3.4 Data preparation of the metallic cell pattern prediction 121
3.4 SUMMARY 122
4 SIMULATION RESULTS AND DISCUSSION 123
4.1 COPLANAR SURFACE WAVE LAUNCHER 123
4.1.1 S_{11} and efficiency of coplanar surface wave launcher 123
4.1.2 Impedance matching of the surface wave launcher 126
4.1.3 EM simulation results of the proposed antenna 129
4.1.4 Frequency and time domain solver 134
4.2 PREDICTION RESULTS FROM FAR-FIELD RADIATION PATTERN TO NEAR-ZONE *E*-FIELD 136
4.2.1 Prediction results of the near-zone *E*-field 137
4.2.2 Discussion 142
4.3 PREDICTION RESULTS FROM NEAR-ZONE *E*-FIELD TO METALLIC CELL PATTERN 159
4.3.1 Simulation results 159
4.3.2 Discussion 161
4.4 SUMMARY 169
5 COSECANT-SQUARED RADIATION PATTERN SURFACE WAVE ANTENNA 171

5.1 COSECANT-SQUARED RADIATION PATTERN ANTENNA 172
5.1.1 Results of the neural network prediction models 174
5.1.2 EM simulation results 177
5.1.3 Experimental results.. 185
5.2 THE ANGULAR COVERAGE RANGE OF THE DUAL-SIDED COSECANT-SQUARED RADIATION PATTERN 193
5.3 LIMITATIONS AND DISCUSSION... 200
5.3.1 Limitations 200
5.3.2 Discussion 205
5.4 SUMMARY 215
6 CONCLUSIONS AND FUTURE WORK 216
6.1 CONCLUSIONS 216
6.1.1 Proposed neural network prediction models 216
6.1.2 Proposed surface wave antenna 216
6.2 FUTURE WORK 217
6.2.1 Future work in antenna.. 217
6.2.2 Future work in neural network prediction models 218
7 REFERENCE 220
A. APPENDIX: NEAR-FIELD TO FAR-FIELD TRANSFORMATION.. 234
B. APPENDIX: MATHEMATICAL PREDICTION MODEL........ 239
1) MATHEMATICAL PREDICTION MODEL – E-FIELD MAGNITUDE.... 241
2) MATHEMATICAL PREDICTION MODEL – E-FIELD PHASE 248

List of Figures

Figure 1.1. FMCW vertical-looking radar system [6]................................26

Figure 1.2. Simplified block diagram of the FMCW VLR.........................26

Figure 1.3. Schematic of the vertical-looking beam...................................27

Figure 2.1. The *E*-field distribution of the TSW propagation [18].............33

Figure 2.2. Planar LWA with a directive SWL embedded in the ground plane [27]...36

Figure 2.3. The SWL feed system [26]..37

Figure 2.4. Full-wave simulated *E*-field (top view) [26]...........................37

Figure 2.5. 3D model showing the switched beam SIW horn array along with the top view of an element [32]...39

Figure 2.6. Transition from a closed waveguide to a leaky mode supporting structure [36]...40

Figure 2.7. The geometry of the slotted SIW LWA [39]............................42

Figure 2.8. LWA in hybrid NRD-strip technology [41]............................43

Figure 2.9. Schematic of the planar superstrate-based LWA [36]..............44

Figure 2.10. LWA with a truncated dielectric superstrate [43]...................45

Figure 2.11. Leaky waveguide with PRS [36]...46

Figure 2.12. The (a) side view, (b) top view of the planar 2D LWA [45]...46

Figure 2.13. The holographic metasurface antenna [50]............................50

Figure 2.14. The holographic antenna excited by a microstrip patch [51]. .51

Figure 2.15. Diagram of cosecant-squared radiation pattern......................52

Figure 2.16. Geometry of the shaped reflector in the vertical plane [53]....54

Figure 2.17. Radiation pattern in elevation plane [53]...............................54

Figure 2.18. Cosecant-squared radiation pattern achieved by stacked beam [9]. 56

Figure 2.19. N-element linear array to form cosecant-squared radiation pattern [54]. 56

Figure 2.20. The optimized radiation pattern obtained using DE and the ideal cosecant-squared radiation pattern [54]. 57

Figure 2.21. Biological neuron in the human nerve system [60]. 59

Figure 2.22. Mathematical model of neuron [61]. 59

Figure 2.23. The structure of the feedforward neural network architecture. 60

Figure 2.24. Flow chart of neural network training processes. 61

Figure 2.25. The logistic (sigmoid) function and its derivative. 64

Figure 2.26. The hyperbolic tangent (tanh) function and its derivative. 65

Figure 2.27. The rectified linear unit (ReLU) function and its derivative. 66

Figure 2.28. Gradient descent algorithm. 68

Figure 2.29. The hyperbolic tangent function and its saturated area. 70

Figure 2.30. Neural network structure with random nodes dropped out. 72

Figure 2.31. The structure of the recurrent neural network. 74

Figure 2.32. The structure of convolution neural network [98]. 75

Figure 2.33. Geometry of PIFA on MDNC substrate: (a) top view, (b) side view [106]. 77

Figure 2.34. Neural network outputs versus the second database (target). Data for radiation efficiency, gain, resonant frequency and bandwidth [106]. 78

Figure 2.35. Geometry layout of antennas: (a) top view of single patch antenna, (b) side view of the lower patch antenna, (c) 3D view of the stacked patch antenna [107]. 79

Figure 2.36. Flowchart of the optimiser [107]. 79

Figure 2.37. Regression plot [107]. 80

Figure 2.38. Error performance plot [107]. 80

Figure 2.39. Geometry of the slotted waveguide array antenna: (a) top view, (b) side view, (c) bottom view, (d) radiating waveguide [108]. 81

Figure 3.1. Flowchart of the proposed method. 84

Figure 3.2. The proposed surface wave antenna with coplanar surface wave launcher. 85

Figure 3.3. The top view of the proposed surface wave antenna with the zoomed-in coplanar SWL (without K-connector)....................................... 86

Figure 3.4. Radiation pattern comparison of CST simulation and NF2FF transformation at 34.5 GHz. 91

Figure 3.5. The diagram of WGAN [120]... 93

Figure 3.6. Gated recurrent unit cell [93]. 94

Figure 3.7. The structure of a Bi-GRU layer [110]. 96

Figure 3.8. The diagram of the proposed Bi-GRU model for radiation prediction... 97

Figure 3.9. Diagram of far-field radiation pattern data extraction (antenna side view).. 102

Figure 3.10. Diagram of field monitors in near-zone *E*-field data extraction (view from the negative *y*-direction of the antenna). 103

Figure 3.11. E_x, E_y and E_z components on the metallic cells. 104

Figure 3.12. E_x, E_y and E_z components on the line at $(0, y, 0.12\lambda_0)$........... 104

Figure 3.13. E_x, E_y and E_z components on the line at $(0.12\lambda_0, y, 0.5\lambda_0)$. ... 105

Figure 3.14. Magnitude comparison between prediction and CST simulation at 34.5 GHz. 112

Figure 3.15. Phase comparison between prediction and CST simulation at 34.5 GHz. 112

Figure 3.16. Prediction error of the Mathematical prediction model......... 113

Figure 3.17. The *E*-field magnitude and phase of the antenna with $0.069\lambda_0$ spacing between two metallic cells. 114

Figure 3.18. The diagram of the MLP classifier. 115

Figure 3.19. MLP classifier metallic cell pattern prediction result. 117

Figure 3.20. Diagram of metallic cell pattern prediction of the MLP classifier. 118

Figure 3.21. Diagram of metallic cell pattern prediction of the Bi-GRU neural network model. 119

Figure 3.22. The diagram of the proposed Bi-GRU model for metallic cell pattern prediction. 120

Figure 3.23. Diagram of the array of field monitors in near-zone *E*-field data extraction (antenna top view). 121

Figure 4.1. The proposed SWL (top view). 124

Figure 4.2. The S_{11} of the coplanar SWL. 125

Figure 4.3. The radiation and total efficiency of the SWL. 125

Figure 4.4. The Z_{11} magnitude of the coplanar SWL under different ratios *k*. 127

Figure 4.5. The real and imaginary part of Z_{11} of the coplanar SWL under different ratios *k*. 128

Figure 4.6. The S_{11} of the coplanar SWL under different ratios *k*. 128

Figure 4.7. Diagram of the angular range (not in scale). 130

Figure 4.8. The on-surface *E*-field distribution of the coplanar SWL. 130

Figure 4.9. On-surface *E*-field along the line OA and OB. 131

Figure 4.10. The surface wave antenna structure of (a) single row, and (b) multi rows. 132

Figure 4.11. The on-surface *E*-field of one metallic cell row surface wave antenna. 132

Figure 4.12. The on-surface *E*-field of five metallic cell rows surface wave antenna. 133

Figure 4.13. The radiation pattern of the surface wave antenna with the different number of rows of the metallic cells. 133

Figure 4.14. S_{11} comparison of frequency and time domain solver. 135

Figure 4.15. Radiation pattern comparison of frequency and time domain solver. 136

Figure 4.16. E_x comparison on the line at $(0, y, 0.12\lambda_0)$. 138

Figure 4.17. E_y comparison on the line at $(0, y, 0.12\lambda_0)$. 138

Figure 4.18. E_z comparison on the line at $(0, y, 0.12\lambda_0)$. 139

Figure 4.19. E_x comparison on the line at $(0.12\lambda_0, y, 0.5\lambda_0)$. 139

Figure 4.20. E_y comparison on the line at $(0.12\lambda_0, y, 0.5\lambda_0)$. 140

Figure 4.21. E_z comparison on the line at $(0.12\lambda_0, y, 0.5\lambda_0)$. 140

Figure 4.22. Far-field radiation pattern prediction results (predicted pattern 1). 143

Figure 4.23. Far-field radiation pattern prediction results (predicted pattern 2). 145

Figure 4.24. Far-field radiation pattern prediction results (predicted pattern 3). 145

Figure 4.25. Diagram of the array of field monitors in near-zone *E*-field data extraction (Arrays 1 to 4). 148

Figure 4.26. Diagram of the array of field monitors in near-zone *E*-field data extraction (Arrays 5 and 6). 148

Figure 4.27. Prediction performance of Bi-GRU models trained by the different number of arrays of *E*-field monitors. 150

Figure 4.28. Prediction performance of Bi-GRU models trained by the different number of training datasets. 151

Figure 4.29. The relationship between MSE and the number of training datasets. 153

Figure 4.30 The percentage value of MSE improvement. 153

Figure 4.31. The relationship between CF and the number of training datasets. 154

Figure 4.32. The percentage value of CF improvement. 155

Figure 4.33. The relationship between R^2 and the number of training datasets. 156

Figure 4.34. The percentage value of R^2 improvement. 156

Figure 4.35. The relationship between fidelity and the number of training datasets. 157

Figure 4.36. The percentage value of fidelity improvement. 158

Figure 4.37. Metallic cell pattern prediction result of the surface wave antenna with constant period length λ_0 MSR = 1:4. 160

Figure 4.38. Metallic cell pattern prediction results (gradually increasing period length). 162

Figure 4.39. Metallic cell pattern prediction results (gradually decreasing period length). 162

Figure 4.40. Metallic cell pattern prediction results (random period length). 163

Figure 4.41. Metallic cell pattern prediction results of different MSR with constant period length case. 165

Figure 4.42. Metallic cell pattern prediction results of different MSR with gradually increasing period length. 165

Figure 4.43. Metallic cell pattern prediction results of different MSR with gradually decreasing period length. 166

Figure 4.44. Metallic cell pattern prediction results of different MSR with random period length. 166

Figure 4.45. The relationship between prediction accuracy and the number of training datasets. 168

Figure 4.46. The percentage value of prediction accuracy improvement. . 169

Figure 5.1. The beam diagram of (a) existing antenna in the mmWave VLR and (b) proposed surface wave antenna. 172

Figure 5.2. Diagram of surface wave antenna design and verification. 173

Figure 5.3. The input dual-sided 30° cosecant-squared radiation pattern. . 174

Figure 5.4. The predicted near-zone *E*-field on the line at (0, *y*, 0.12λ_0)... 175

Figure 5.5. The predicted near-zone *E*-field on the line at (0.12λ_0, *y*, 0.5λ_0). 176

Figure 5.6. The predicted metallic cell pattern of the central radial row... 177

Figure 5.7. The 30° dual-sided cosecant-squared radiation pattern surface wave antenna. 178

Figure 5.8. Simulated S_{11} of the surface wave antenna........ 178

Figure 5.9. The radiation and total efficiency of the surface wave antenna. 179

Figure 5.10. E_x comparison on the line at (0, *y*, 0.12λ_0). 180

Figure 5.11. E_y comparison on the line at (0, *y*, 0.12λ_0). 181

Figure 5.12. E_z comparison on the line at (0, *y*, 0.12λ_0). 181

Figure 5.13. E_x comparison on the line at (0.12λ_0, *y*, 0.5λ_0)........ 182

Figure 5.14. E_y comparison on the line at (0.12λ_0, *y*, 0.5λ_0)........ 182

Figure 5.15. E_z comparison on the line at (0.12λ_0, *y*, 0.5λ_0)........ 183

Figure 5.16. The 3D far-field radiation pattern of the surface wave antenna at 34.5 GHz. 183

Figure 5.17. The far-field radiation pattern (*yz*-plane) of the surface wave antenna at 34.5 GHz. 184

Figure 5.18. Dimensions of the fabricated prototype of the surface wave antenna. 186

Figure 5.19. Dimensions of the surface wave launcher. 187

Figure 5.20. Experiment setup in the anechoic chamber. 187

Figure 5.21. Simulated and measured S_{11} of the surface wave antenna. ... 188

Figure 5.22. Simulated and measured gain at (ϕ, θ) = (90°, 30°) of the surface wave antenna. 189

Figure 5.23. Simulated and measured *E*-plane at 34 GHz. 190

Figure 5.24. Simulated and measured *H*-plane at 34 GHz. 190

Figure 5.25. Simulated and measured *E*-plane at 34.5 GHz. 191

Figure 5.26. Simulated and measured *H*-plane at 34.5 GHz. 191

Figure 5.27. Simulated and measured *E*-plane at 35 GHz. 192

Figure 5.28. Simulated and measured *H*-plane at 35 GHz. 192

Figure 5.29. E_x, E_y, and E_z comparison on the line at $(0, y, 0.12\lambda_0)$ of 10º dual-sided case. 194

Figure 5.30. E_x, E_y, and E_z comparison on the line at $(0.12\lambda_0, y, 0.5\lambda_0)$ of 10º dual-sided case. 195

Figure 5.31. E_x, E_y, and E_z comparison on the line at $(0, y, 0.12\lambda_0)$ of 20º dual-sided case. 196

Figure 5.32. E_x, E_y, and E_z comparison on the line at $(0.12\lambda_0, y, 0.5\lambda_0)$ of 20º dual-sided case. 196

Figure 5.33. The predicted metallic cell pattern of the central radial row (10º dual-sided case). 197

Figure 5.34. The predicted metallic cell pattern of the central radial row (20º dual-sided case). 198

Figure 5.35. The far-field radiation pattern (*yz*-plane) of the 10º dual-sided case. 198

Figure 5.36. The far-field radiation pattern (*yz*-plane) of the 20º dual-sided case. 199

Figure 5.37. E_x, E_y, and E_z comparison on the line at $(0, y, 0.12\lambda_0)$ of 40º dual-sided case. 201

Figure 5.38. E_x, E_y, and E_z comparison on the line at $(0.12\lambda_0, y, 0.5\lambda_0)$ of 40º dual-sided case. 202

Figure 5.39. The predicted metallic cell pattern of the central radial row. 202

Figure 5.40. The far-field radiation pattern (*yz*-plane) of the 40º dual-sided case. 203

Figure 5.41. Dual-sided cosecant-squared radiation pattern with outside range suppression. 205

Figure 5.42. Surface wave antenna with (a) rectangular shape and 5º angular separation, (b) trapezium shape and 5º angular separation, (c) rectangular shape and 10º angular separation. 206

Figure 5.43. E_x comparison on the line at (0, y, 0.12λ_0) of three antennas. 207

Figure 5.44. E_y comparison on the line at (0, y, 0.12λ_0) of three antennas. 207

Figure 5.45. E_z comparison on the line at (0, y, 0.12λ_0) of three antennas. 208

Figure 5.46. E_x comparison on the line at (0.12λ_0, y, 0.5λ_0) of three antennas. 208

Figure 5.47. E_y comparison on the line at (0.12λ_0, y, 0.5λ_0) of three antennas. 209

Figure 5.48. E_z comparison on the line at (0.12λ_0, y, 0.5λ_0) of three antennas. 209

Figure 5.49. Radiation pattern comparison of three antennas. 210

Figure 5.50. 30º dual-sided cosecant-squared radiation pattern with outside range linearly suppressed. 212

Figure 5.51. 30º dual-sided cosecant-squared radiation pattern with outside range exponentially suppressed. 212

Figure 5.52. 30º dual-sided cosecant-squared radiation pattern with different suppressed values. 214

Figure A.1. Sampling rectangular plane. 236

Figure A.2. Radiation pattern of NF2FF transformation. 238

Figure B.1. Changing patterns of the on-surface E-field magnitude at 34.5 GHz. 239

Figure B.2. Changing patterns of the on-surface E-field phase at 34.5 GHz. 240

Figure B.3. Normalised magnitude changing pattern of each metallic cell at 34.5 GHz. 241

Figure B.4. The fitting curve of the maxima of each metallic cell at 34.5 GHz. 242

Figure B.5. Magnitude comparison between prediction and CST simulation at 34.5 GHz. 243

Figure B.6. The relationship between parameters and frequency in the enter zone magnitude mathematical model. 245

Figure B.7. The relationship between parameters and frequency in the cell zone magnitude mathematical model. 245

Figure B.8. The relationship between parameters and frequency in the exit zone magnitude mathematical model. 246

Figure B.9. The relationship between parameters and frequency in the SW zone magnitude mathematical model. 246

Figure B.10. The relationship between parameters and frequency in the magnitude maxima prediction mathematical model. 247

Figure B.11. Magnitude prediction error. 247

Figure B.12. Phase changing pattern of each metallic cell at 34.5 GHz. ... 248

Figure B.13. Phase comparison between prediction and CST simulation at 34.5 GHz. 249

Figure B.14. The relationship between parameters and frequency in the enter zone phase mathematical model 250

Figure B.15. The relationship between parameters and frequency in the cell zone magnitude phase model. 251

Figure B.16. The relationship between parameters and frequency in the exit zone magnitude phase model. 251

Figure B.17. The relationship between parameters and frequency in the SW zone magnitude phase model. 252

Figure B.18. Phase prediction error. 252

List of Tables

Table 2.1. Comparison of different activation functions. 66

Table 3.1. The parameters of the coplanar SWL. 87

Table 3.2. Difference between training mode and evaluation mode.......... 101

Table 3.3. The hyperparameters of the MLP classifier. 116

Table 4.1. Near-zone *E*-field prediction error of the test case. 141

Table 4.2. Averaged near-zone *E*-field prediction error of 50 test cases. .. 142

Table 4.3. The numerical results of the Bi-GRU prediction performance. 144

Table 4.4. The numerical results of the Bi-GRU prediction performance of predicted patterns 1, 2 and 3. 146

Table 4.5. The positions of the field monitor arrays. 149

Table 4.6. Prediction performance of Bi-GRU models trained by the different number of *E*-field monitor arrays. 150

Table 4.7. Prediction performance of Bi-GRU models trained by the different number of training datasets. 151

Table 5.1. The discrepancies between the predicted and simulated near-zone *E*-field. 180

Table 5.2. The discrepancies between the predicted and simulated near-zone *E*-field (10º dual-sided case). 195

Table 5.3. The discrepancies between the predicted and simulated near-zone *E*-field (20º dual-sided case). 197

List of Abbreviations

AI	Artificial Intelligence
BN	Batch Normalisation
Bi-GRU	Bi-directional Gated Recurrent Unit
CB-CPW	Conductor Backed Coplanar Waveguide
CNN	Convolutional Neural Network
CF	Correlation Factor
DE	Differential Evolution
EM	Electromagnetic
FDTD	Finite Difference Time Domain
FEM	Finite Element Method
FIT	Finite Integration Technique
FMCW	Frequency-Modulated Continuous Wave
GRU	Gated Recurrent Unit
GAN	Generative Adversarial Network

GO-PO	Geometrical Optic and Physical Optic
GO	Geometrical Optics
GDS	Grounded Dielectric Slab
ILA	Integrated Lens Antennas
IWO	Invasive Weed Optimisation
LWA	Leaky-Wave Antenna
LSTM	Long Short Term Memory
MDNC	Magneto Dielectric Nano-Composite
ML	Machine Learning
MSR	Mark-to-Space Ratio
MSE	Mean Square Error
MLP	Multi-Layer Perceptron
NLP	Natural Language Processing
NF2FF	Near-field to far-field
NRD	Nonradiative Dielectric

PIFA	Planar Inverted-F Antenna
PRS	Partially Reflective Surface
PSO	Particle Swarm Optimisation
ReLU	Rectified Linear Unit
RNN	Recurrent Neural Network
SGD	Stochastic Gradient Descent
SIW	Substrate Integrated Waveguide
SWL	Surface Wave Launcher
TSW	Trapped Surface Wave
VLR	Vertical-Looking Radar
VCO	Voltage Control Oscillator
WGAN	Wasserstein Generative Adversarial Network

1 Introduction

Pests are the most diverse species of animals living on earth. Some pests can constitute a major threat to entire countries or a group of nations [2]. Insects are responsible for two major kinds of damage to people and agricultural products. First is direct injury done to the plant by the insect, which eats the leaves or roots of the growing crops. For example, corn rootworms emerge from the ground in June and July and begin their destruction of corn silk and leaves. The second type is that the insects transmit bacterial, viral or fungal infections to crops or people. One prominent example is the tsetse fly that puts about 100 million people and 60 million head of cattle at risk in sub-Saharan Africa due to the transmission of trypanosomiasis [3].

Agricultural pests can not only ruin gardens, but they can also ruin entire crops meant to feed hundreds of people. Farmers and scientists are striving to combat a variety of pests to ensure the fruits, vegetables and grains grow successfully. Many insect species fly within a few hundred meters of height and rely on wind-borne migration. This aerial bio-flow has important implications for ecological, physiological and genetic studies of insects, with applications in pest management, conservation and environmental change programs [4]. The high-flying migratory insects, together with their relatively small body size and nocturnal characteristic, indicates that it is hard to observe their migration features such as the movement and height of flying. Therefore, the study of insect migration relied on the interpretation of indirect evidence of long-distance flights, such as catches in light traps. However, light-trap catches are strongly influenced by the lunar cycle and weather, and also, there may be a time gap of several days between immigration and the resultant peak in light-trap catches [5]. Therefore, an entomological scanning radar for observing insect migration at high altitudes has developed. However, long-term direct monitoring in the field is difficult for traditional radar since the equipment is complex and data collection requires a simple mobile system. In 1995, a vertically orientated centimetre-wave radar system was developed for monitoring insect migration continuously and autonomously, but with limited target identification capabilities as it does not have beam nutation and cannot derive more information from the returned signals [5]. A millimetre-wave (mmWave) frequency modulated continuous wave (FMCW) vertical-looking radar (VLR) system becomes a feasible way to monitor high-flying insects [6]. However, the observation area is limited by using the exiting antenna in FMCW VLR. In this thesis, the author proposes to use the neural network method to design a surface wave antenna that can generate cosecant-squared radiation pattern. The proposed surface wave antenna can provide a wider observation area and an almost constant receiving power value due to the character of the cosecant-squared radiation pattern.

1.1 FMCW VLR system

FMCW radar constantly sends out linearly modulated signals and determines the targe distance based on the difference in transmitted and received frequency. Compared with pulse radar, FMCW radar can achieve high range resolution at a relatively low cost. Normally, the pulse radar has a strong transmitted signal and thus it masks all target echoes from very close targets. Therefore, the FMCW radar system is suitable for low-flying insects monitoring. The aforementioned portable mmWave FMCW VLR, shown in Figure 1.1 [6], has been co-designed and built with Rothamsted Research to monitor the migration of small crop pests such as aphids and beetles at different heights. The VLR is designed to detect insects flying up to 200 m above the ground. It works 24 hours a day on a 15-minute period basis with 5-minute data capturing and 10-minute data processing. After processing, the results can show the target’s displacement direction, body alignment and speed.

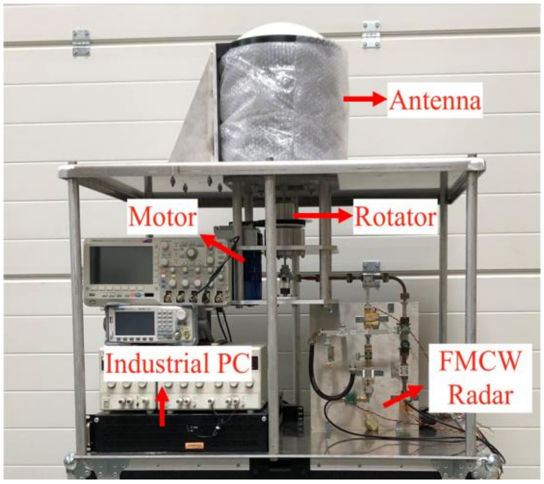

Figure 1.1. FMCW vertical-looking radar system [6].

The block diagram of the mmWave FMCW VLR system prototype is shown in Figure 1.2. In this VLR system, the output frequency of the voltage control oscillator (VCO) is set from 34 GHz to 35 GHz. The bias voltage ±5 V and the output power is 22 dBm. The input signal employed in this system is a 1.5 kHz triangular wave with 0.7 V peak-to-peak value. The isolator and circulator are designed to regulate the signal. One output signal of the directional coupler goes to the audio card (PCIe-9834) directly to check the VCO working status. The other output is mixed with the received signal in the mixer to generate an IF signal to be processed by the audio card in the industrial PC. DC and components above 30 MHz are filtered out by the band-pass filter.

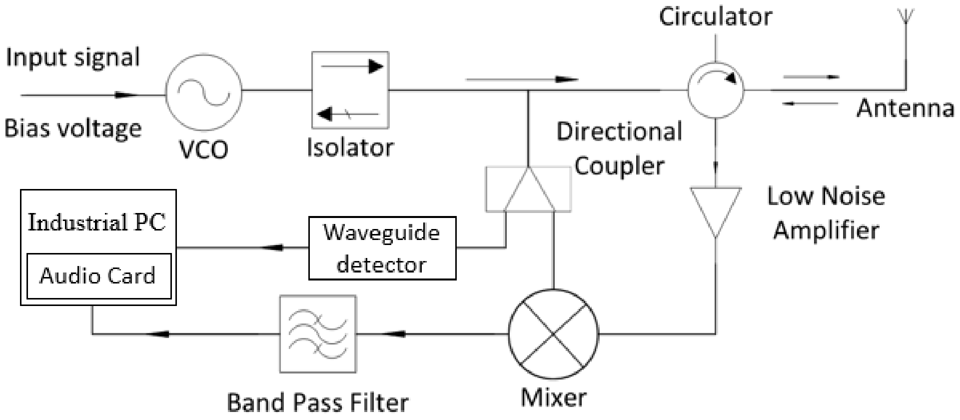

Figure 1.2. Simplified block diagram of the FMCW VLR.

The antenna utilised in the preliminary system is a scalar feed horn antenna with the gain enhancement of a Gaussian lens antenna. The antenna delivers a 38 dBi nominal gain and 1.9° 3-dB beamwidth. The antenna radiates linear polarised waves and offers excellent aperture efficiency, high cross polarisation rejections and low sidelobe levels. The antenna is installed for upward-looking. The main beam is offset by 0.18° from the vertical axis by tilting the upward-pointing waveguide, as shown in Figure 1.3. The turntable, connected to the horn, is driven by a 3-phase motor rotating at an angular speed of 6 turns per second to form a conical-shaped scanning area. Targets flying through the beam are detected and the returned signal is processed to determine the size, shape and speed of the targets.

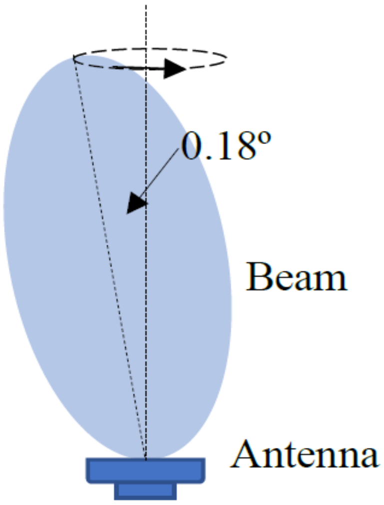

Figure 1.3. Schematic of the vertical-looking beam.

1.2 Aim

In the existing VLR system, the antenna utilised for upward-looking is a scalar feed horn antenna. The beam is pointing upward with an offset of 0.18° for widening the angular coverage. The angle adjustment needs to be very accurate and is complicated to perform. And such antenna only provides a limited circular observation area with a diameter of 1.2 m. Such narrow observation can only detect limited number of insects and this may introduce statistical error when ecologists and entomologists want to estimate the quantity during insects migration. Therefore, a larger observation area is required.

Cosecant-squared radiation pattern antennas could offer considerable improvements to the VLR system design. It is because they will enable an adapted distribution in the radiation pattern, which result in better space scanning. This radiation pattern can provide a more stable signal strength when a target moves with a constant height within the beam. Conventionally, such antennas are utilised in air-surveillance radar systems to detect an approaching target at a constant height with constant power [7], which means the received power is independent of the radar slant range.

In the mmWave FMCW VLR pest monitor system, the antenna could therefore be replaced by a cosecant-squared radiation pattern antenna to make the practical adjustment easier. Due to the cosecant-squared radiation pattern, insects flying in constant height reflect constant power. Once the height changes, the received power changes as well and the computer will record the altitude changing directly.

Conventionally, the cosecant-squared radiation pattern can be achieved by curve shaped reflectors [8], stack horns [9] and phased array antennas [10]. Although the deformation of a reflector could form the cosecant-squared radiation pattern, it is hard to make the curve angle accurately and the large dish is incompatible with the compact VLR system. And the antenna array has the disadvantage of being high cost. The surface wave antenna with a cosecant-squared radiation pattern is beneficial due to its low cost, simple structure and low profile which is compatible with the VLR system.

Therefore, in this thesis, the aim is to design a surface wave antenna with cosecant-squared radiation pattern in the far-field by using a neural network-based method. Such structure is a low profile, low fabrication cost surface wave antenna and compatible with the FMCW system, and offers a large observation area.

1.3 Research contribution

The main contribution of this research is demonstrating how neural network-based methods can be utilised to tailor the radiation pattern of a surface wave antenna. The novel method proposed is to predict the metallic cell pattern on surface wave antennas which provide the desirable far-field cosecant-squared radiation pattern.

The whole method is mainly divided into two prediction parts: i) from the far-field radiation pattern to near-zone *E*-field, and ii) from the near-zone *E*-field to metallic cell pattern on the antenna surface. In the first part, the combination of Wasserstein generative adversarial network (WGAN) and bidirectional gated recurrent unit (Bi-GRU) neural network is proposed to predict the near-zone *E*-field from the required far-field radiation pattern. Conventionally, the near-field to far-field transformation (NF2FF) can be achieved by using Fourier transform. However, it leads to a challenging inverse problem due to the fact that the far-field *E*-pattern ($E(r,\theta,\phi)$) is a summation of E_ϕ and E_θ. Either E_θ or E_ϕ cannot be obtained by giving $E(r,\theta,\phi)$ unless E_θ or E_ϕ is zero. However, E_θ and E_ϕ are not equal to zero since the cross polarisation cannot be exactly zero in real antennas. In the proposed method, the WGAN is utilised to produce the near-zone *E*-field and Bi-GRU is to confirm the relationship between near-zone *E*-field and the far-field radiation pattern. With the help of the combination of WGAN and Bi-GRU, the corresponding near-zone *E*-field that can generate the desirable far-field radiation pattern can be predicted. For the second part of the prediction, another Bi-GRU neural network is introduced to predict the metallic cell pattern on the antenna surface by using the near-zone *E*-field as input. This Bi-GRU neural network model is served as a surrogate model to study the relationship between the near-zone *E*-field and the on-surface metallic cell pattern. High prediction accuracy can be achieved by using the Bi-GRU prediction model.

To the author’s best knowledge, this research is the first attempt that applies neural network-based prediction methods to design surface wave antennas to which the radiation pattern can be tailored. The feasibility of the proposed method shows that the neural network method can be used to effectively control the radiation pattern or scatter the surface wave to free space on a specific angle range.

1.3.1 Publications

In this section, part of this work has been previously published and will be presented here. Another journal paper related to this work is to be submitted.

J. Yang, K. F. Tong, K. S. Lim, A. Reynolds, and C. Rawlings, "Development of Millimeter-wave FMCW Vertical-looking Entomological Radar System," *2019 IEEE Int. Work. Electromagn. Appl. Student Innov. Compet. iWEM 2019*, pp. 1–2, 2019.

J. Yang and K. F. Tong, "Cosecant-Squared Radiation Pattern Surface Wave Antenna For Millimeter-wave FMCW Vertical-Looking Radar System," *IEEE Asia-Pacific Microw. Conf.*, pp. 801–803, 2020.

J. Yang and K. Tong, "Metallic Pattern Prediction For Surface Wave Antennas Using Bidirectional Gated Recurrent Unit Neural Network," *IEEE-APS Top. Conf. Antennas Propag. Wirel. Commun.*, pp. 82–86, 2021.

1.4 Thesis overview

This thesis has six chapters, and the thesis outline is listed as follows:

Chapter 1 presents the background of the study, the aim of this thesis and poses the contributions of this research. Specifically, the reason for further research on the VLR system to track the insects is explained. And the aim has been demonstrated in detail. The research contribution explicitly demonstrates the novelty of the proposed neural network-based method.

Chapter 2 reviews the relevant antennas in this research area, including holographic antennas, leaky-wave antennas (LWA) and surface wave antennas, to consolidate the background theory of the proposed design. The concepts and characteristics of surface wave and surface wave launcher (SWL) will also be studied in Chapter 2 to gain a better understanding of the working principle of surface wave antennas. Different cosecant-squared radiation pattern formation techniques will be reviewed and their drawbacks will be discussed. Furthermore, Chapter 2 also explains the neural network basics, including the structure, the training setting and different models of the neural network.

Chapter 3 focuses on the mechanism and methodology of how to utilise the neural network to design cosecant-squared radiation pattern surface wave antennas. The proposed antenna structure will be delivered first. The neural network prediction method is mainly divided into two prediction parts: i) from the far-field radiation pattern to near-zone E-field and ii) from near-zone E-field to metallic cell pattern on the surface. The methodology of the two parts will be explicitly introduced and explained.

Chapter 4 presents the electromagnetic (EM) simulation results of the surface wave launcher in the proposed antenna structure. Neural network prediction results of the two parts will be presented and the performance of the prediction will be evaluated.

Chapter 5 delivers how to use the proposed neural network-based method to design a cosecant-squared radiation pattern surface wave antenna. The experimental verification of the fabricated antenna prototype will be presented. Different angular ranges of the cosecant-squared radiation patterns will be applied to verify the neural network prediction model. The limitation of the proposed method will also be discussed.

Chapter 6 concludes the proposed method for designing the metallic cell pattern on the surface of the antenna using the neural network prediction models. Corresponding future work will then be presented to develop a systematic way for predicting the metallic cell patterns according to other input radiation patterns.

2 Background theory and literature review

In this thesis, the objective is to design a low profile, high-performance and low-cost antenna that can produce user-defined radiation pattern by applying the neural network method. The proposed antenna takes advantage of different techniques, such as surface wave and surface wave launcher (SWL). Inspired by the concepts of the LWA and holographic antenna, the proposed antenna combines the surface wave and LWA and applies metallic cells on the antenna surface as scatterers to radiate the surface wave to the free space. Different far-field radiation patterns can be achieved by different distributions of metallic cells on the antenna surface. The neural network models are trained to study the relationship between the distribution of metallic cells and the far-field radiation pattern. Once enough training is finished, the neural network models can be used as a predictor to design the antenna (the distribution of metallic cells) according to the user-defined far-field radiation pattern.

In this chapter, the surface wave and SWL will be introduced and explained, and different SWL will be analysed. The essential information of LWA and holographic antenna will be highlighted. Cosecant-squared radiation pattern will be introduced and the techniques that achieve such pattern will be discussed. Finally, the basics of the neural network will be introduced and discussed.

2.1 Surface wave and surface wave launcher

Surface wave is essential to LWA and holographic antennas. Surface wave propagates along the interface between two different media without radiation before being scattered out to free space by scatterers in these antennas. And in these antennas, the surface wave could cover a large area of the surface with a single feeding port. The SWL is a structure that excites surface waves and could be a planar horn [11], a dipole array [12], a waveguide [13] and printed slots [14]. The physical size of the antenna could be reduced with the help of a printed SWL. In the research of this thesis, a low profile SWL is required since the need of the compact VLR system.

2.1.1 Surface wave

Surface wave is a non-radiating wave that propagates along the interface between two different media and decay exponentially as they move away from the interface [15][16]. According to the physical properties, surface wave can be classified into 11 types [17]. When a wave is incident at a boundary from a denser medium and if the incident angle is equal to or larger than the critical angle, the wave will be confined or trapped to the surface. Trapped surface wave (TSW) is a type of surface wave and it travels along the inductive boundaries and keeps being trapped between the two mediums without radiating to 3D space [18].

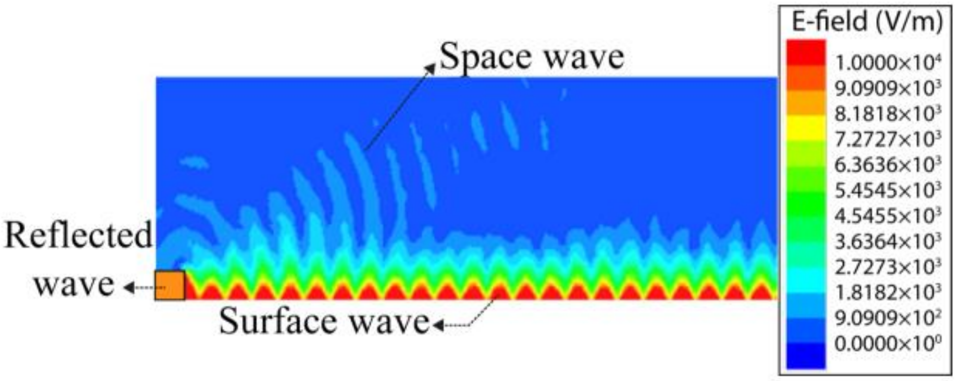

Figure 2.1. The *E*-field distribution of the TSW propagation [18].

The plane TSW can be formed by inductive boundaries, such as dielectric-coated plane conductor and corrugated surface [17]. In [18], a 52 GHz wideband TSW propagation system by using the dielectric coated conductor was implemented. Figure 2.1 shows the *E*-field distribution along the dielectric-coated conductor with surface impedance $j200\Omega$ at 60 GHz. The surface impedance can be evaluated by (2.1 and (2.2 described in [18].

$$X = 2\pi f \mu_0 [\frac{\varepsilon_r - 1}{\varepsilon_r} h + \frac{\Delta}{2}] \tag{2.1}$$

$$\Delta = \sqrt{\frac{1}{\pi f \mu_0 \sigma}} \tag{2.2}$$

Where f is the operating frequency, ε_r is the dielectric constant, h is the thickness of the dielectric substrate and μ_0 is the permeability of free space. Δ denotes the skin depth of a copper sheet, σ is the conductivity.

The surface resistance is associated with energy dissipation, whereas the surface reactance is related to the energy stored at the interface. Specifically, the surface resistance determines the attenuation of the surface wave in the propagation direction, while the surface reactance defines the decay of the wave away from the surface in the propagation direction [19]. Higher surface reactance indicates more energy tends to store to the surface. Conventionally, a plane surface wave structure guides wave propagating along its surface and does not radiate due to constant surface reactance. To induce radiation, the surface impedance must be changed, such as taper, sudden termination of the guiding structure or an abrupt junction with a different material surface. However, introducing abrupt transitions will not only radiate but also introduce reflection. To obtain substantial radiation and minimise reflections, a series of junctions is necessary and the changes in reactance at the junctions have to be kept small [20]. Surface wave antennas are usually used to yield high-gain fan-beam radiation pattern in the far-field. Frequency coverage of surface wave antennas normally extends from very high frequency band to millimetre-wave frequency band, which enables many wireless applications [21].

2.1.2 Surface wave launcher

The manipulation of surface waves has received widespread interest. The surface wave is excited through the SWL and it has peak strength of E-field at the SWL aperture. The surface wave decays rapidly near the SWL aperture and is considered as unstable. With the surface wave propagating, the exponentially decaying becomes gentle and is considered as stable. If a stable surface wave is promised, then the antenna design could focus on how to effectively scatter the surface wave to free space at a specific direction or control the shape of the radiation pattern. A convenient way of launching surface waves is through the use of waveguide horn, however, it cannot achieve the low profile in antenna design. Surface wave launchers such as substrate integrated waveguide (SIW) [22][23], truncated parallel plate waveguide structure [24][25], microstrip and SIW [26] can provide the advantage of being low profile.

2.1.2.1 Printed slots directive SWL

A novel design in [27] proposed a LWA that is excited by a directive SWL embedded in the ground plane, as shown in Figure 2.2. The SWL is described by a main radiating driven slot (length of 1.92 mm) with two secondary folded reflectors (individual length of 2.75 mm) and four tuning slots (individual length of 0.65 mm). The slot configuration acts as magnetic dipole sources for the LWA [28]. The main radiating slot couples energy into the dielectric substrate while the two secondary folded reflector slots increase forward directivity to achieve unidirectional surface wave propagation [29]. The planar SWL is typically fed by a 50Ω coplanar waveguide transmission line. By selecting the appropriate substrate ($\varepsilon_r = 10.2$, $h = 1.27$ mm, $\tan\delta = 0.0023$ at 10 GHz), energy can be efficiently coupled into the dielectric substrate. Although the planar directive SWL is low profile and can be printed on the back conductor, the design of the three slots is complex and the tiny size of the slots is difficult to fabricate. Therefore, in the author’s proposed design, SIW technique with coplanar waveguide feed is applied to offer a similar performance to this SWL.

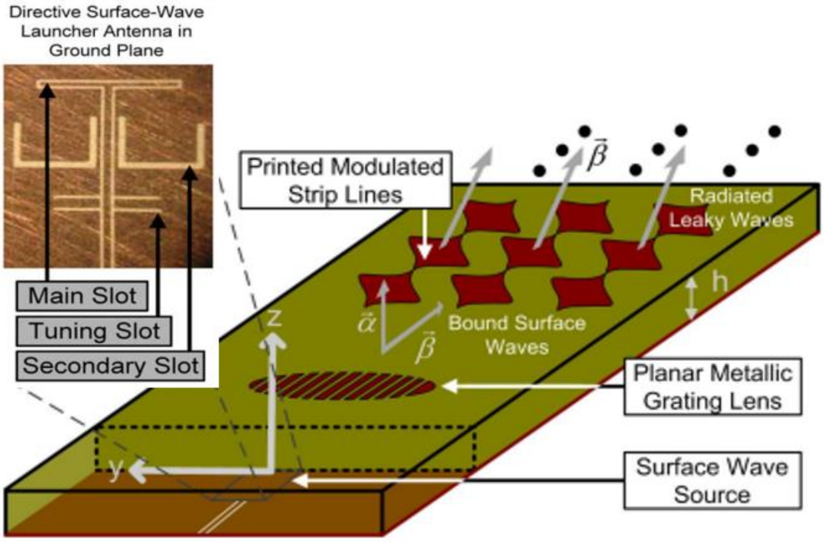

Figure 2.2. Planar LWA with a directive SWL embedded in the ground plane [27].

2.1.2.2 Microstrip SIW SWL

SIW allows the implementation of a rectangular waveguide in planar form and such structures can offer the advantages of being low profile and compact. A SWL designed by microstrip and SIW technology has been shown in Figure 2.3. This system consists of three parts, which are microstrip transition, the leaky SIW T-junction, and the sub-wavelength matching section for surface wave. The dielectric substrate selected in this structure is Rogers RT5880 ($\varepsilon_r = 2.2$, $\tan\delta = 0.009$ at 10 GHz) with a thickness of 1.575 mm. The parameters T-junction width ($W = 7.8$ mm), length ($L = 50$mm), via spacing ($P = 4.5$mm), separation distance ($S = 5$ mm), patches separation ($D = 4.8$ mm) and gap ($G = 0.48$ mm) are optimised for via diameter of 1 mm. This structure operates at 15 GHz and offers a uniform surface wave front, as shown in Figure 2.4. Although this design could provide the desired surface wave, the three parts design are complex and large in size. In the author’s proposed design, the SIW structure is selected and the microstrip to SIW transition is replaced by a coplanar waveguide to SIW transition, which can provide a more compact SWL area.

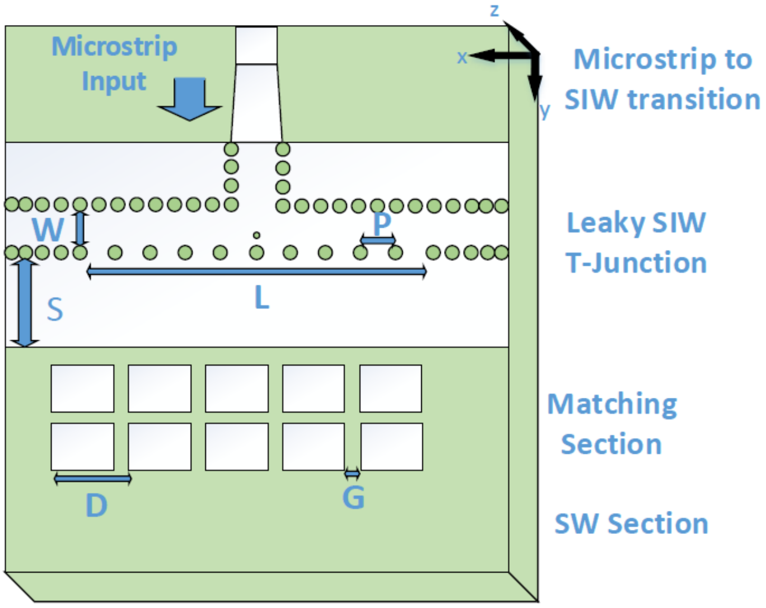

Figure 2.3. The SWL feed system [26].

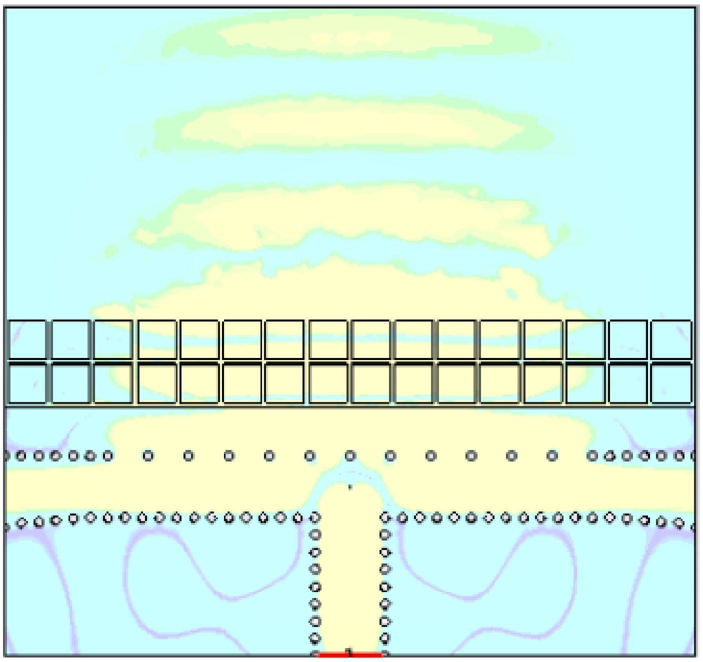

Figure 2.4. Full-wave simulated *E*-field (top view) [26].

2.1.2.3 Planar SIW horn SWL

Another design that uses SIW horn to excite surface wave is shown in Figure 2.5, all dimensions are in mm. The design is an array consisting of eight identical horn elements which oriented 45° relative to one another. Each element can be individually excited to produce endfire beams in the horizontal plane. The SIW horn is fed through the conductor backed coplanar waveguide (CB-CPW)-to-SIW transition [23]. The via walls improve isolation between the elements since the ratio p/d is less than 2, where p and d are the via period length and diameter respectively [30]. It also reduces mutual losses between elements. There are periodic metal strips with gradually increasing gaps and decreasing widths, on the flaring of the horn elements. The substrate used is Rogers RT5880 ($\varepsilon_r = 2.2$, $\tan\delta = 0.009$ at 10 GHz). The nature of the period strips improves both the impedance and gain bandwidth. The flared portion is quadratically tapered over the length and serves to improve matching by reducing the overall aperture reflections. The leaky-wave radiation from the periodic strips improves the endfire gain in the radially outward direction while reducing the side and back lobe levels [31]. This design has a unique SWL that outperforms the previous SWL design. However, the design is optimised for point-to-point communication and is not suitable for adjusting the beam angle. In the author’s proposed design, this structure needs to be modified by removing the period strips due to the requirement of compact size.

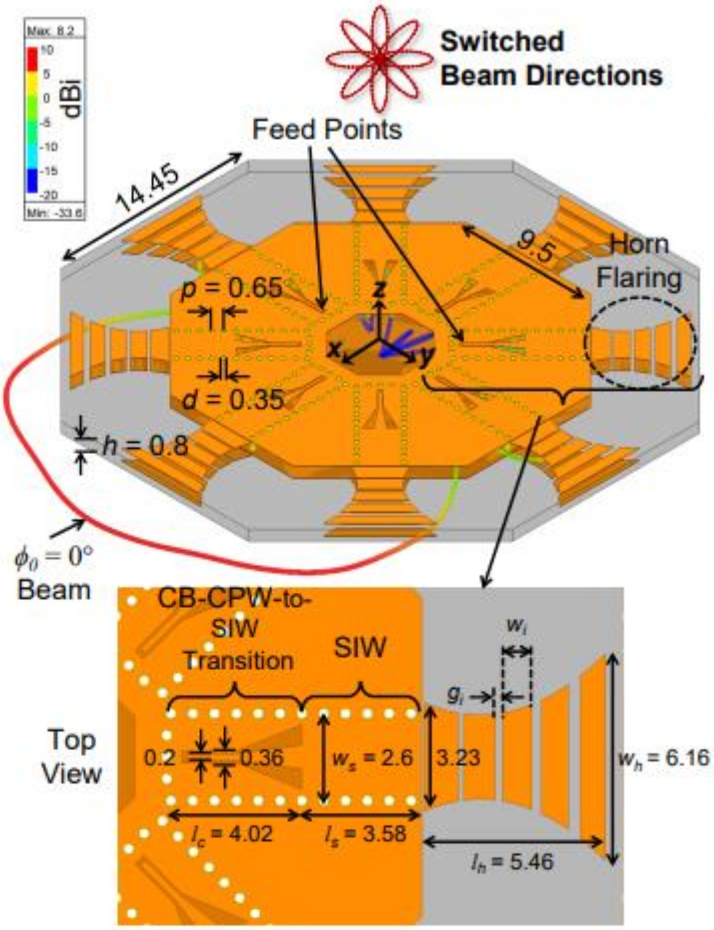

Figure 2.5. 3D model showing the switched beam SIW horn array along with the top view of an element [32].

The next important technique that has been brought into the proposed design is LWAs. LWAs can achieve high directive radiation with a single feed. And they are advantageous as they can help to reduce the cost and losses at high frequency. Therefore, they are suitable for millimetre and submillimeter waves applications.

2.2 Leaky-wave antennas and holographic antennas

LWAs are popular in the microwave and millimetre-wave frequency band since they have high directivity, low profile and wide bandwidth with only a simple structure and without a complicated feed network [33]. Similar to LWA, the holographic surface can provide a given direction of the maximum radiated power density. The holographic antenna is advantageous as it is simple configuration, high gain and beamforming ability [34]. In this section, different LWAs and holographic antennas will be discussed.

2.2.1 Leaky-wave antennas

A leaky wave is considered mathematically as a complex plane wave and the radiation pattern can be expressed in terms of the complex propagation constant [21]. Leaky wave antennas are a subset of travelling wave antennas. Basically, they use a travelling wave on a guiding structure but leaks out of the radiating aperture. Leaky wave antennas are popular in the microwave frequency band since they have a high directivity and wide bandwidth with only a simple structure and without a complicated feed network as used in a phased array [33]. The feeding network of the phased array requires directional couplers and controlled phased shifters, whereas the LWAs use SIW or dipole as feed. LWAs have the capability of frequency scanning of the radiation pattern, which many applications can take advantage of. Leaky-wave radiation can occur from a closed waveguide with some continuous or periodic slit cut. The condition that leaky-wave can radiate is the mode of propagation should be a fast mode ($\beta < k_0$), where β is phase constant and k_0 is the free-space wavenumber [35].

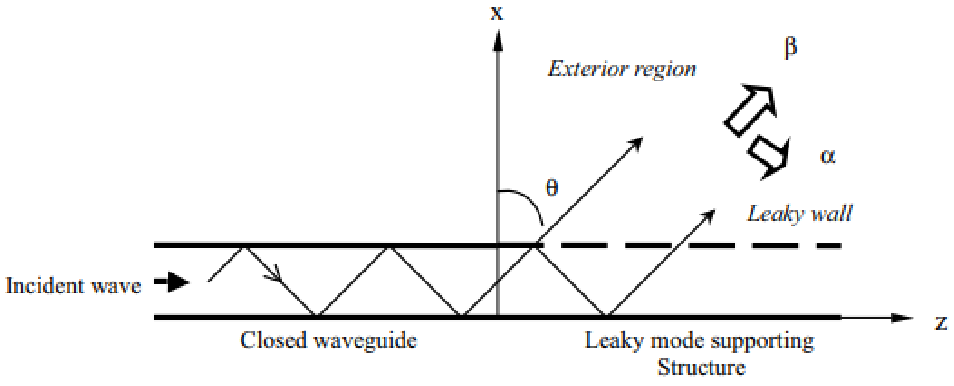

Figure 2.6. Transition from a closed waveguide to a leaky mode supporting structure [36].

A simple LWA structure is depicted in Figure 2.6. The incident wave travels from the closed waveguide to a leaky structure where leaky-wave causes some perturbation to the propagation mode. The longitudinal wave number and the attenuation factor are defined as β_z and α_z respectively. The leaky mode then has a complex wavenumber $k_z = \beta_z - j\alpha_z$, where β_z is less than the free space wavenumber k_0 to ensure the wave is on the fast mode. The main radiation beam is directed along $\theta = \sin^{-1}(\beta_z/k_0)$ where θ is the beam angle measured from the broadside. Since the phase constant β_z is a function of frequency, it follows that the radiation beam can be steered by frequency scanning. The beamwidth depends mainly on the attenuation factor. Reducing α_z will result in higher directivity and narrower beamwidth [36].

Depending on the geometry, principle of operation and nature of structural perturbation, LWA can be divided into four possible categories. Since the leaky-wave structure can be either uniform/quasi-uniform or periodic, and also can be identified as one or two-dimensional [21]. Compared with uniform leaky wave antennas, periodic structures generally have better backward directivity and large scanning range. Periodic LWA enjoy several advantages such as low loss, flexible radiation characteristics, and mechanical simplicity [37]. Uniform LWA provide radiation into the forward quadrant and thus steering the beam from broadside to forward end-fire directions. The scanning range of periodic LWA enables large range that reaches from the backward end-fire through broadside directions to the forward quadrant [37]. The dominant mode of a uniform LWA is fast wave propagation. The dominant mode of a periodic LWA is in fact a slow wave, which does not radiate through the structure. However, the introduction of a periodic pattern produces an infinite set of space harmonics. The leaky mode of a periodic LWA relies on the first space harmonics (β_{-1}).

There are many structures and techniques that can achieve leaky-wave. Examples are shown and reviewed in the following sections.

2.2.1.1 Endfire SIW LWA

The SIW is a class of efficient integrated transmission lines compatible with planar technologies, which offers high power handling capability, high quality factor and electrical and mechanical shielding with self-consistent property [38]. The SIW has been widely developed for integrated microwave and millimetre-wave antennas. Figure 2.7 shows a slotted SIW LWA and it consists of a SIW with a periodic array of transverse slots on the top metal plane. The conductive vias are inserted into the substrate to connect the bottom ground plane and top metal plane. Leakage is obtained by introducing the periodic array of transverse slots on the top metallic plane of the structure, which interrupts the current flow on the surface. This type of SIW LWA has a wide impedance bandwidth and a narrow beam that scans with frequency. This antenna enables the beam scanning in the forward quadrant as frequency changes and the beam radiated would normally be a conical shape. The beam becomes a pencil beam at endfire when infinite ground plane is applied due to the polarisation.

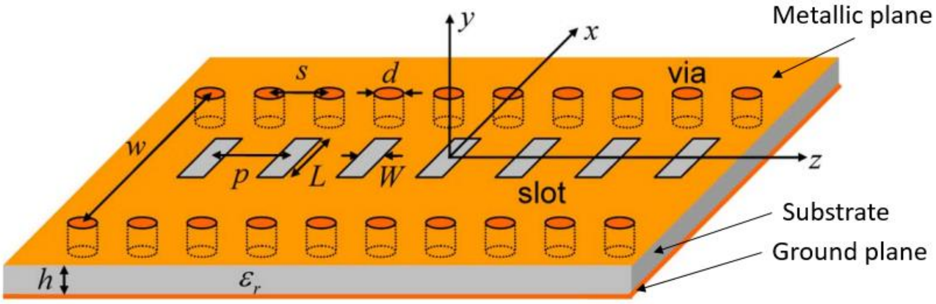

Figure 2.7. The geometry of the slotted SIW LWA [39].

2.2.1.2 Nonradiative dielectric (NRD) LWA

Nonradiative dielectric (NRD) waveguides consist of a dielectric rectangular slab placed between two metallic parallel plates. Due to the dielectric slab, the electromagnetic field is confined in the vicinity of the dielectric region, however, the electromagnetic field decays exponentially. The NRD waveguides are good structure to minimise the losses and the manufacturing difficulties associated with high frequencies components [40].

The original bounded NRD waveguide can be made leaky if a suitable perturbation in the structure is applied [41]. Normally, a symmetric dielectric slab is placed between two metal walls. The shape of the dielectric slab can be changed to have a desired leaky effect and it can be asymmetric or other special shapes. By controlling the asymmetry level of the dielectric slab, the leakage rate of the antenna can be modified and thus affect the angular width of the main beam in the far-field. On the other hand, by adjusting the parallel-plate height *L* properly, the leakage rate of the structure can be controlled as well. Alternatively, as shown in Figure 2.8, a strip-circuit is printed on the dielectric-air interface to induce the asymmetry radiation mechanism and to control the leakage rate [41]. Modulating the strip width and position can design a tapered illumination, while taking advantage of the electrical performances of the NRD transmission medium. This structure allows for an easier, cheaper and more flexible tapering mechanism. Although this kind of NRD is easy to fabricate and low cost, its high profile and large size is not suitable for the compact radar system.

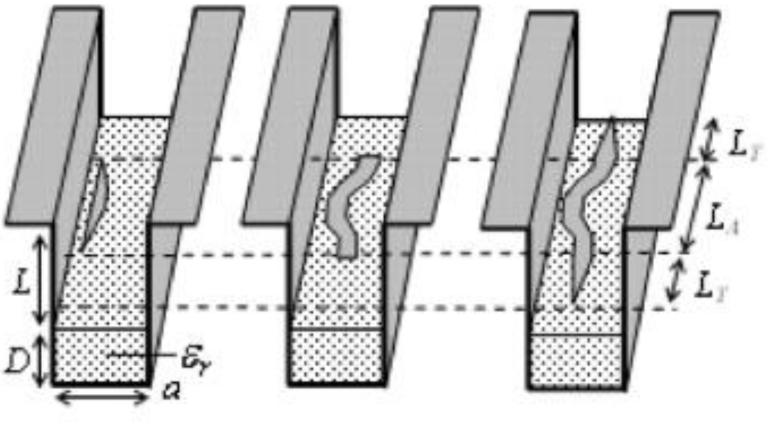

Figure 2.8. LWA in hybrid NRD-strip technology [41].

2.2.1.3 Planar superstrate-based LWA

The planar superstrate-based LWA consists of a metallic ground plane and a partially reflective surface (PRS) made by the dielectric slab. Normally, a simple dipole element or a slot on the ground plane embedded within the structure launches several leaky-wave modes between the ground plane and the PRS [42]. The resulting radiation pattern is due to a leakage of energy from the PRS. Depending on the chosen scan angle, the radiation pattern can be either a broadside pencil beam or a conical beam at a scan angle [42].

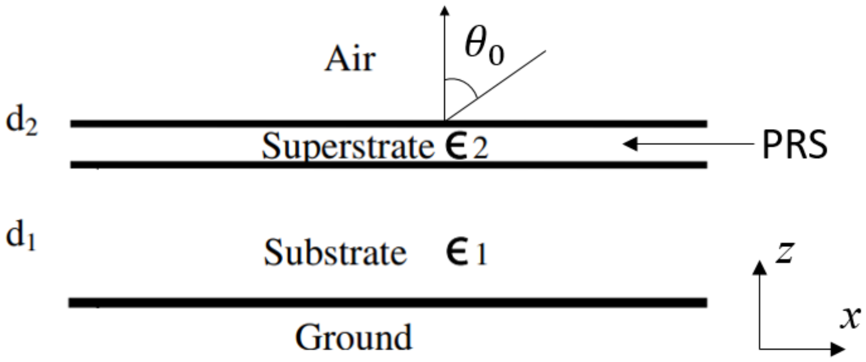

Figure 2.9. Schematic of the planar superstrate-based LWA [36].

As shown in Figure 2.9, the lower substrate with thickness d_1 has a lower dielectric constant ε_1 while the upper superstrate has a high ε_2 with thickness d_2. To achieve maximum directivity, the relation between the dielectric constant of two layers should be $\varepsilon_1 << \varepsilon_2$. To have a radiation beam at angle θ_0 from broadside, the thickness can be chosen based on (2.3 and (2.4.

$$d_1 = \frac{\pi/k_0}{\sqrt{\varepsilon_1 - sin^2(\theta_0\,)}} \tag{2.3}$$

$$d_2 = \frac{\pi/(2k_0)}{\sqrt{\varepsilon_2 - sin^2(\theta_0\,)}} \tag{2.4}$$

where the k_0 is the free space wavenumber, d_1 and d_2 are the thickness of substrate and superstrate respectively, and ε_1 and ε_2 are the dielectric constant of substrate and superstrate respectively.

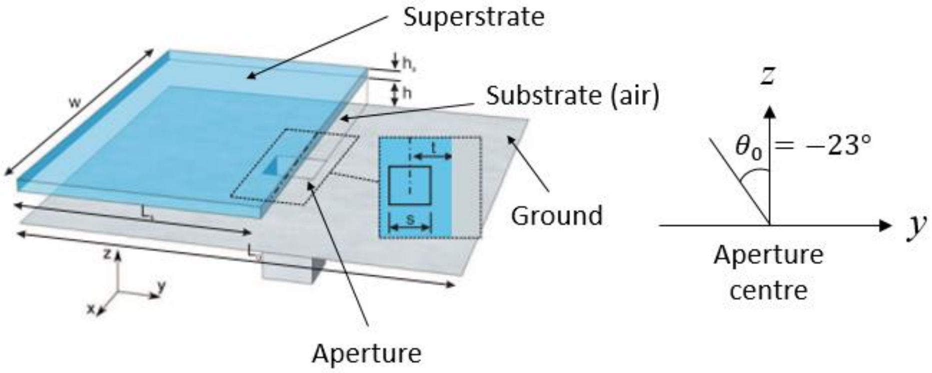

Figure 2.10. LWA with a truncated dielectric superstrate [43].

In [43], the antenna topology utilised a superstrate configuration in the form of a truncated dielectric layer over a ground plane as shown in Figure 2.10. A single aperture on the ground plane is used to feed the LWA. The truncation of the dielectric layer and the size of the feed are designed to excite a one-sided leaky-wave mode travelling along the superstrate. The LWA operates at 10 GHz and presents a radiation pattern with the main beam at θ = -23º.

2.2.1.4 Planar PRS-based LWA

Figure 2.11 shows a two parallel plate guide having a grounded substrate and a PRS on the top. The PRS is characterised by an effective transfer impedance *jX* defined as the ratio of the tangential *E*-field to the discontinuity of the tangential magnetic field across the PRS [36]. The PRS can be realised by the periodic patches or a thin layer of high permittivity superstrate, which acts as a capacitive screen [44]. When impedance *X* is 0, the structure is a closed waveguide with a set of discrete modes. For a finite impedance *X*, there is a leaky mode with complex propagation constant, which can be used to design a leaky-wave antenna with desired beam angle. This kind of antenna is desirable for its compatibility with other planar devices, low profile and directive beam pattern [36].

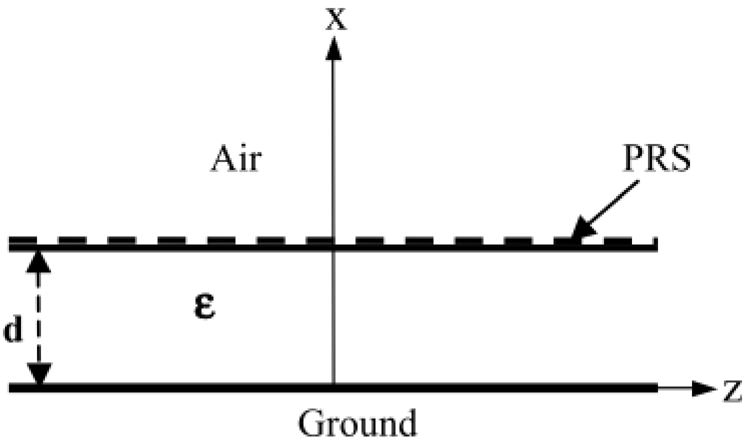

Figure 2.11. Leaky waveguide with PRS [36].

Figure 2.12 shows a planar 2D LWA defined by a grounded dielectric slab (GDS) covered with metallic strips as PRS was proposed in [45]. The leaky-wave section is a grounded dielectric layer covered with a PRS. Printed slots SWL has been utilised as a feeding technique for the high gain planar LWA.

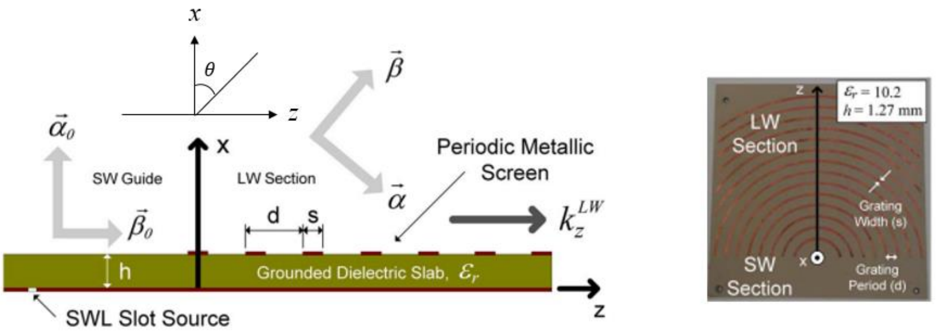

(a)

(b)

Figure 2.12. The (a) side view, (b) top view of the planar 2D LWA [45].

The period (d) and the metal strip width (s) have the relationship $s << d$. The substrate thickness (h) and relative permittivity (ε_r) are chosen as 1.27 mm and 10.2 to support the surface wave mode. The phase constants (β_n) of the spatial harmonics are given by

$$\beta_n = \beta_{SW} + \frac{2n\pi}{d}; \qquad n = \pm 1, \pm 2, \ldots \tag{2.5}$$

Where β_{SW} denotes the longitudinal phase constant of the surface wave mode.

Radiation occurs from a spatial harmonic when β_n is less than k_0. The spatial harmonic β_{-1} is the main radiating spatial harmonic and the direction of the radiation peak is $\theta = \sin^{-1}(\beta_{-1}/k_0)$. The radiation beam direction θ goes from backward enfire to broadside to forward endfire with frequency increasing.

The power leaked as radiation per unit length along z is given by

$$P_{rad} = j\omega\varepsilon_0 {E_{z0}}^2 \frac{s}{d}[(1 - \frac{s}{d})/u_0 - \frac{s}{d}\sum_{n\neq 0} sinc(\frac{\pi ns}{d})/\, u_n] \tag{2.6}$$

Where E_{z0} is the E_z component at the substrate surface, $u_0 = \sqrt{\beta_0^2 - k_0^2}$ and $u_n = \sqrt{\beta_n^2 - k_0^2}$.

The summation is over all positive and negative n. It is worth noting that u_n are real for all positive values of n when $\beta_0 > k_0$, whereas u_n can be imaginary for negative values of n when $- k_0 < \beta_n < k_0$. The terms that are related to this condition would be the real power radiation, which is the real part of $P_{rad.}$ The other terms account for the reactive component of $P_{rad.}$ The change in the propagation constant of the incident surface wave mode can be obtained as

$$\Delta\gamma \equiv \alpha + j\Delta\beta = \frac{P_{rad}}{2P_{SW}} \tag{2.7}$$

Where P_{SW} is the incident surface power which depends on E_{z0}, h and ε_r.

Assuming the n = -1, spatial harmonic is the only radiating mode, the peak radiation occurs at an angle θ_P away from broadside and can be approximated by

$$\theta_P = sin^{-1}(\frac{\beta_0 + \Delta\beta - 2\pi/d}{k_0}) \tag{2.8}$$

The beam directivity (D) is inversely proportional to the attenuation factor and can be expressed as

$$D = \frac{\sqrt{k_0^2 - (\beta_{-1} + \Delta\beta)^2}}{\alpha} \tag{2.9}$$

The power radiation pattern (R) is a function of beam angle and is dependent on k_z^{LW}, which gives the generated far-field radiation pattern for the LWA structures

$$R(\theta) = \frac{cos^2\theta}{|sin\theta - k_z^{LW}/k_0|^2} \tag{2.10}$$

Considering d = 7.49 mm, s = 1.498 mm in the design, the planar LWA gives the gain value greater than 10 dBi and achieves the impedance bandwidth about 20%.

The design proves the combination of surface wave and leaky-wave successfully reduces the antenna profile. Also, the far-field radiation pattern is derived from the perturbed E-field on the surface. And this idea inspires the research in this thesis. However, the mathematical analysis has assumptions which can only apply to periodic metal strips case. More possibilities of the different distributions of the metal strips have been ignored. Therefore, the derived far-field radiation pattern mathematical equations cannot be used to generate the metal strips according to the different user-defined radiation pattern. In this research, a neural network-based method is introduced and implemented to study the relationship between the distribution of the metal strips and the far-field radiation pattern. After training the neural network model, it can be used to predict the metal strips on the surface according to user-defined far-field radiation pattern.

2.2.2 Holographic antennas

One special kind of LWA is the holographic antenna, which has attracted considerable interest as well. Holographic antennas were first proposed in 1968 based on optical holography [46]. The optic concept of holography has been extended to microwave frequencies offering the potential for antenna applications. The holographic surface can provide the maximum radiated power intensity at a given direction, and this can be achieved by the interference of the incident wave from a feed source and a plane wave coming from the direction of maximum radiation [47]. When a hologram designed in accordance with an interference pattern of two wavefronts is illuminated, the other wavefront is readily reconstructed on the surface of the hologram [48]. The holographic antenna represents a class of antennas which the radiation aperture is formed by the diffraction of the incident field by a conductive metallic cell pattern etched on the grounded dielectric slab [49]. The holographic antenna is comprised of two parts which are the reference wave part and the radiation part. Conventionally, the reference wave part is sourced by SWL and the radiation part is formed by conductive metallic strips on the dielectric substrate. The holographic antenna is advantageous as it is low profile, simple configuration and lightweight compared to reflector and lens technologies. It also provides high gain and beamforming ability.

Figure 2.13 shows a low-profile microwave holographic antenna comprised of a dual-metasurface (radiation part) and a 4-element Yagi feed (reference wave part) [50]. This design utilises two metasurfaces with an aperture size of 0.0134 m^2 to generate a single pencil beam. The continuous metallic conducting strips are periodically placed on the upper metasurface of the antenna. The working frequency of the holographic antenna is 20 GHz and the antenna shows an excellent performance in the frequency range from 19.75 GHz to 21.25 GHz. The aperture efficiency and 1 dB gain bandwidth achieved are 28% and 7.5% respectively. Compared with other printed antennas, this antenna has the beamforming ability by adjusting the distribution of the metallic strips.

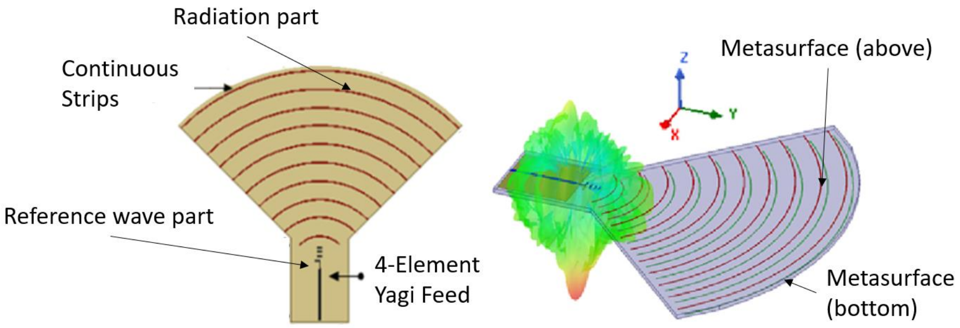

Figure 2.13. The holographic metasurface antenna [50].

Another design in [51] shows a surface wave based hologram fed by a 1D travelling wave microstrip patch array. This holographic antenna can alternatively be described as a periodic surface wave based LWA excited by a fundamental mode periodic microstrip LWA. The metallic cells are printed on a 1.905 mm RT/Duroid6010LM ($\varepsilon_r = 10.2$, $\tan\delta = 0.0023$) GDS. The series-fed patch array is placed across the centre of the antenna. The holograms are symmetrically distributed above and below the array, as shown in Figure 2.14. The beam of the broadside of the *E*-plane is formed by the symmetric holographic surface. In *H*-plane, the radiation beam scans with frequency from backward to forward direction through the broadside. A reflection compensation technique is introduced to facilitate the broadside beam for the series-fed array. The maximum peak radiation at broadside direction achieved is 17.7 dBi antenna gain in both *E* and *H*-plane at 7.7 GHz. At 7.62 GHz, the aperture efficiency is 18.6%, which is an improvement compared with a single patch excitation of the hologram.

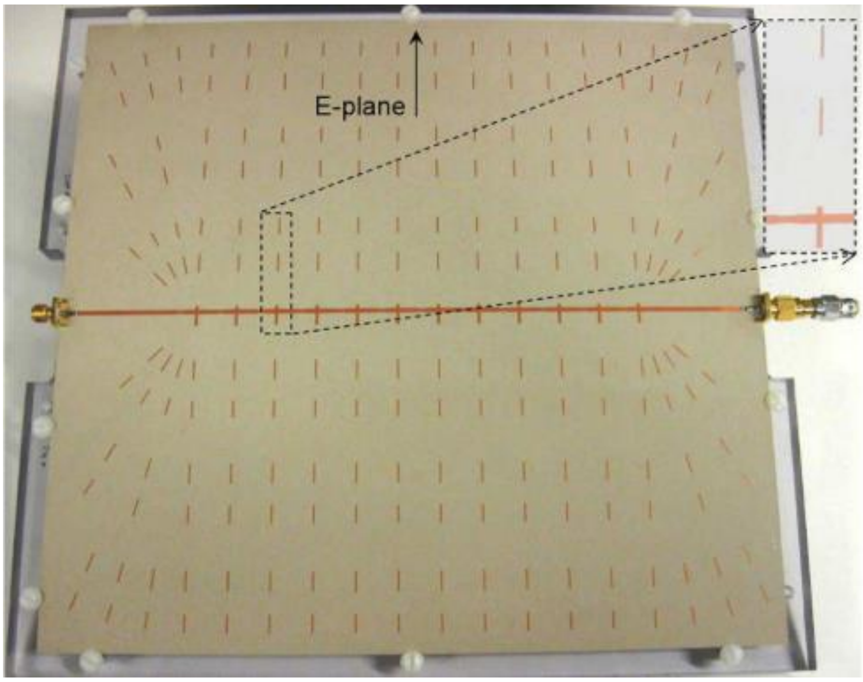

Figure 2.14. The holographic antenna excited by a microstrip patch [51].

Both [50] and [51] shows the surface wave based holographic antenna can achieve different radiation pattern in the far-field by using different hologram interference pattern (metallic strips). However, they focus on the main beam direction instead of the whole shape of the radiation pattern. In this thesis, inspired by the combination of the surface wave and metallic cell patterns on the antenna surface, the surface wave based antenna with metallic strips (cells) printed on the surface is used to generate *E*-field and far-field radiation pattern data to train the neural network model.

2.3 Cosecant-squared radiation pattern

Cosecant-squared radiation pattern antennas are frequently utilised in air-surveillance radar systems to detect an approaching target at a constant height with constant power [7]. These enable an adapted distribution in the radiation pattern, which result in a better space scanning. The gain value decreases with the increasing elevation angle. Therefore, a more stable signal strength can be received when a target moves at a constant height within the beam, which means the received power is less dependent on the radar slant range as described in the Friis equation ((2.11).

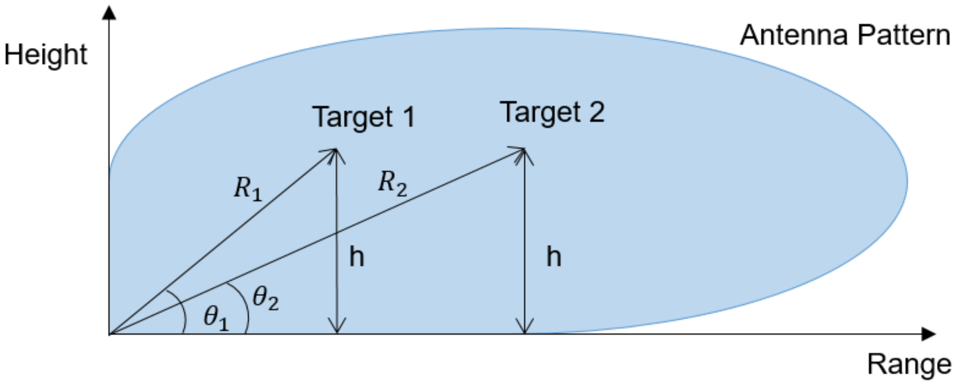

Figure 2.15. Diagram of cosecant-squared radiation pattern.

Considering a cosecant-squared radiation pattern in Figure 2.15, according to Friis equation, the received power is given by

$$P_r = \frac{P_t G^2 \lambda^2 \sigma}{(4\pi)^3 R^4} \tag{2.11}$$

where P_t and P_r are the transmitted and received power of the VLR system respectively. G is the gain of antenna, λ is the wavelength and R is the slant range from the radar (target distance). σ is the radar cross section of the insect and can be calculated using the Rayleigh scattering function as $\sigma = Ck^4V^2$, where k is the wavenumber, V is the volume of the target and C is a constant determined by the aspect ratio (length/width) and complex dielectric constant [52].

The target distance R can be expressed as

$$R = \frac{h}{sin\ \theta} = h \cdot csc\ \theta \tag{2.12}$$

where θ is the elevation angle defined by the height and target distance.

For the same target flying at the same height level within the cosecant-squared radiation pattern region,

$$P_r \propto \frac{G^2}{R^4} \propto \frac{G}{R^2} \tag{2.13}$$

By substituting (2.12 into (2.13, the received power at the antenna end is given by

$$P_r \propto \frac{G}{(csc\ \theta)^2} \tag{2.14}$$

From (2.14, the received power remains constant if the target moves at the same heigh level towards the receiving antenna within the beam area. Therefore, if the antenna has a cosecant-squared radiation pattern, the received power could be independent of the elevation angle θ and becomes constant.

2.3.1 Cosecant-squared radiation pattern formation

There are different methods to achieve a cosecant-squared radiation pattern which include 3D geometry such as curve shaped reflectors [8][53], stacked horns [9], reflect array antennas [54][55], shaped lens antennas [56] as well as 2D planar structure such as printed phased array antennas [10][57].

2.3.1.1 Shaped reflector

[53] suggests using a shaped reflector to form a cosecant-squared radiation pattern. For the curved shaped reflector, a feed antenna is located in the focal point of the reflector and generates a relatively sharp radiation beam since the waves propagate away from the reflector in the ideal case. In order to get the cosecant-squared radiation pattern, part of the radiation beam needs to be curved. The geometry of the reflector surface can be calculated using the geometrical optics (GO) method to achieve the cosecant-squared radiation pattern in the elevation plane [53].

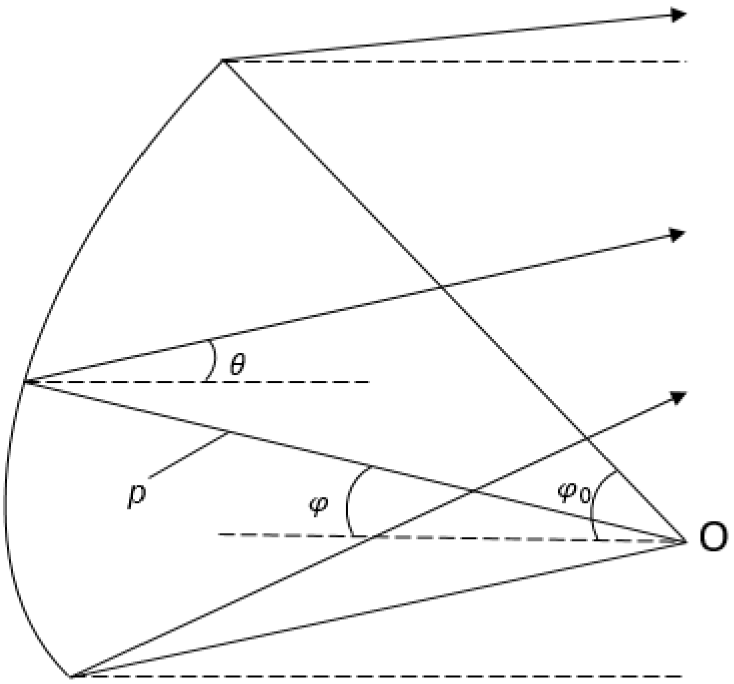

Figure 2.16. Geometry of the shaped reflector in the vertical plane [53].

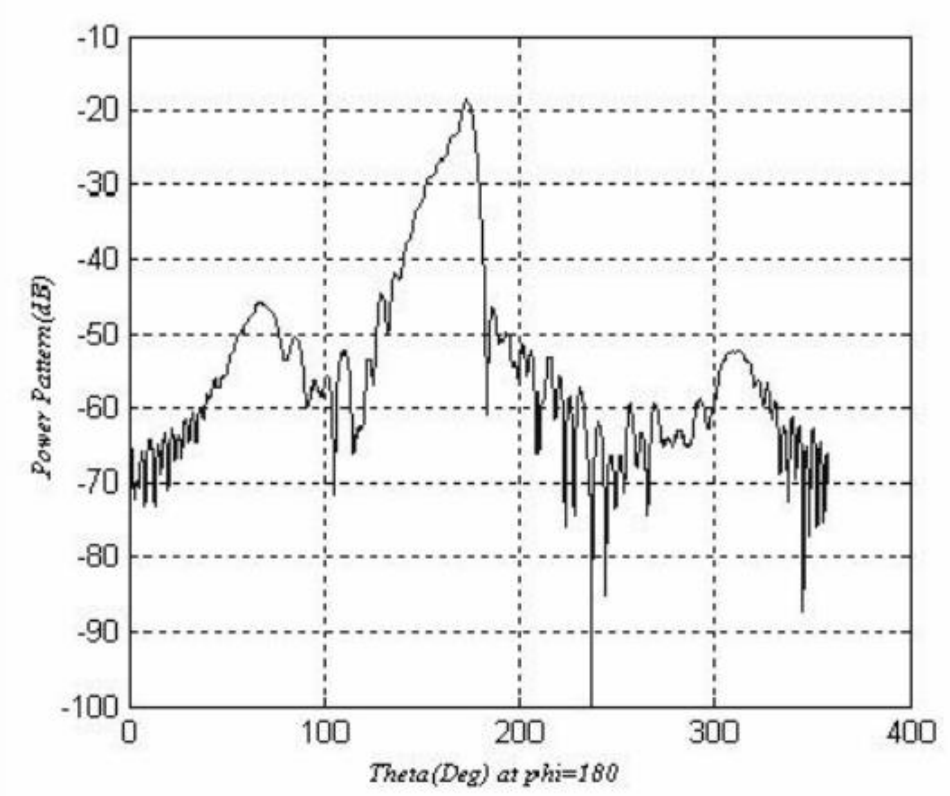

Figure 2.17. Radiation pattern in elevation plane [53].

The configuration in this elevation plane is illustrated in Figure 2.16. Point O is the phase centre of the point feed source and is taken as the origin of the coordinates. φ and θ are the incident and reflection angles respectively. And p is the distance between the origin and the reflector surface. The shaped surface can be achieved in the vertical plane by obtaining $p(\theta)$ through (2.15 by equating powers before and after the reflection within a small angular sector. After determining $p(\theta)$, the reflector surface can be defined by (2.16, where $I(\varphi)$ is the vertical pattern of the feed and $G(\theta)$ is the desired pattern of the reflector antenna. The achieved cosecant-squared radiation pattern is shown in Figure 2.17.

$$ln\frac{p}{p_0} = \int_{\varphi_0}^{\varphi} tan\frac{\varphi + \theta}{2} d\varphi \tag{2.15}$$

$$G(\theta)d\theta = \frac{I(\varphi)}{p} d\varphi \tag{2.16}$$

2.3.1.2 Stacked horn

The cosecant-squared radiation pattern can also be achieved by using multiple feed to a parabolic reflector. Every horn emits a sharp beam in the forward direction. By distributing the transmit power unevenly on the single radiating elements, the cosecant-squared radiation pattern can be achieved, as shown in Figure 2.18.

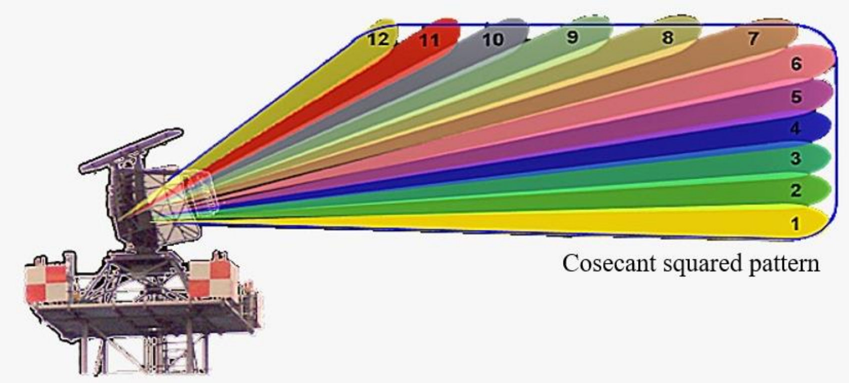

Figure 2.18. Cosecant-squared radiation pattern achieved by stacked beam [9].

2.3.1.3 Antenna array with the optimisation algorithm

Antenna arrays with uniform/non-uniform spacing or different feeding of elements can form the cosecant-squared radiation pattern as well. In [54], a cosecant-squared radiation pattern is synthesised from a uniformly spaced but non-uniformly excited linear antenna array by applying the differential evolution (DE) algorithm. The antenna structure is shown in Figure 2.19. The uniform spacing of the array elements is considered as half of the desired signal wavelength. Excitation coefficients and the static phase shift of the array elements are optimisation parameters of the DE algorithm. The achieved radiation pattern is shown in Figure 2.20.

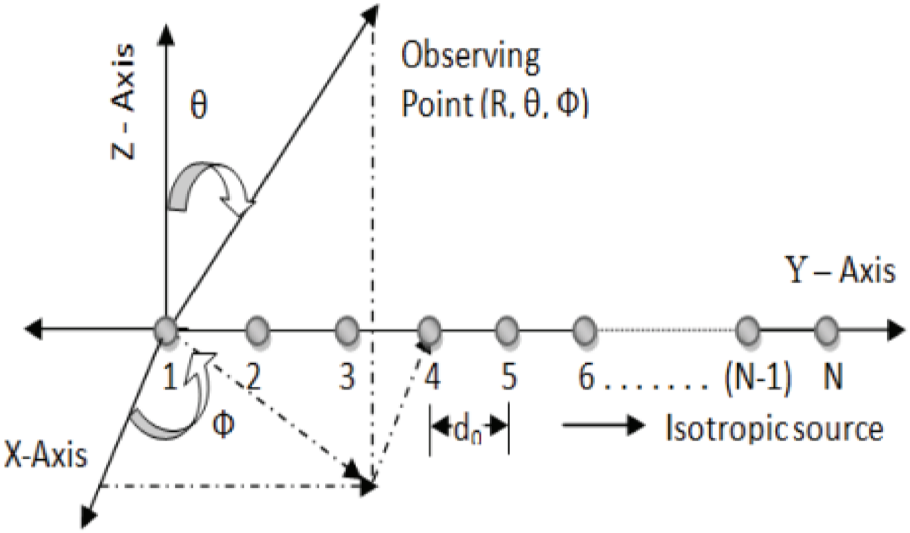

Figure 2.19. N-element linear array to form cosecant-squared radiation pattern [54].

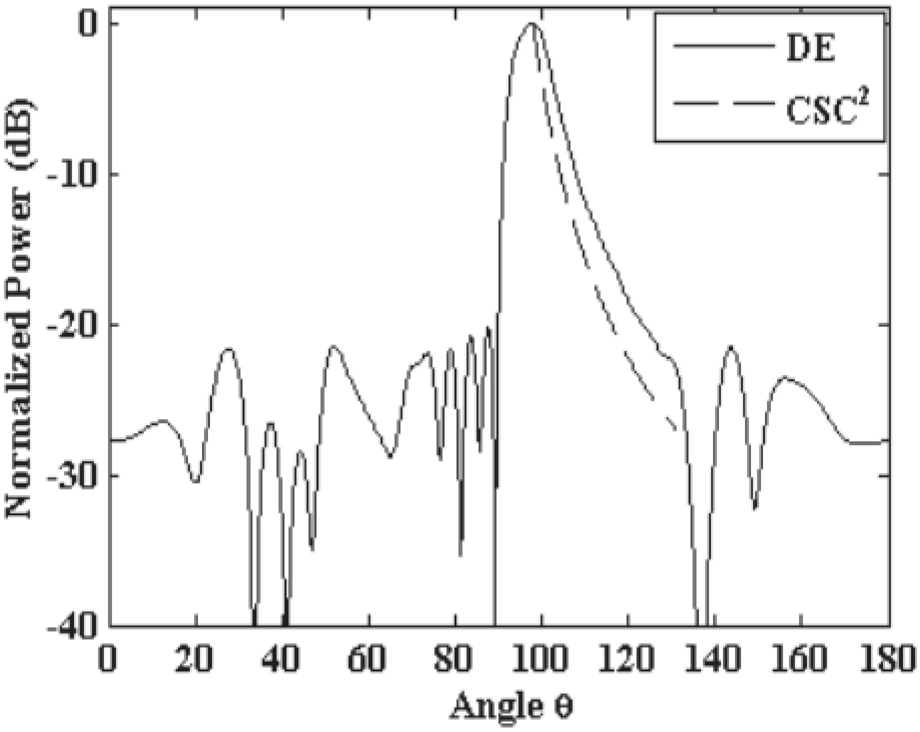

Figure 2.20. The optimized radiation pattern obtained using DE and the ideal cosecant-squared radiation pattern [54].

Different optimisation algorithms are applied to antennas to form the cosecant-squared radiation pattern. In [55], applying invasive weed optimisation (IWO) to the multi-feed offset parabolic reflector and a linear array of horn antennas separated by one wavelength spacing in focal point can provide desired cosecant-squared radiation pattern. In arbitrarily shaped integrated lens antennas (ILA) design [56], the methodology consists of a multidimensional conjugate gradient optimisation method that minimises the distance between a given power and the far-field radiation pattern of the trial lens shapes. And the lens profile initialising the optimisation loop is deduced from various synthesis methods based on GO. The lens performance is analysed by using the hybrid geometrical and physical optic (GO-PO) method.

Although the deformation of a reflector can generate the required cosecant-squared radiation pattern, it is hard to make the curve angle accurately and the large dish is incompatible with the compact radar system. The stack horn technique would increase the size and weight of the antenna system and is costly due to multiple horns applied. In [54], [55] and [56], the feeding horns need to be installed at a distance away from the main reflector for good illumination, which brings in large size, heavy weight, and high fabrication cost.

In this project, the desired design should be low profile and compatible with the FMCW VLR. Therefore, in this thesis, a surface wave antenna is studied to generate the cosecant-squared radiation pattern.

2.4 Neural network

Machine learning (ML) is a subfield of artificial intelligence (AI). ML enables a system to automatically learn and progress from experience without being explicitly programmed. In ML, a set of algorithms parse data and learn from the data and use those learnings to discover patterns of interest. And the neural network is a type of ML algorithm.

The definition of a neural network is a computing system consisting of many simple, highly interconnected processing elements, which process information by their dynamic state response to external inputs [58]. According to Garrett [59], neural network is a computational mechanism that is able to acquire, represent and compute mapping from one multivariate space of information to another. Neural networks are designed to help people solve complex problems in real life as they can study and model the relationships between inputs and outputs that are non-linear and complex. Moreover, neural networks can model highly volatile data and variances needed to predict rare events. Neural networks can improve decision processes in medical and disease diagnosis, financial predictions for stock prices, robotic control systems, chemical compound identification and computer vision.

In this section, the basics of artificial neural networks, including the mechanisms of biological and artificial neurons and how artificial neurons work, will be introduced. The basic structure and training processes of the neural networks will be studied. At the end of this section, three commonly used neural network types will be introduced.

2.4.1 Biological neuron and artificial neuron

The basic computational unit of the human brain is a neuron. In Figure 2.21 [60], the dendrites carry the signal to the soma, where all signals get summed. If the final summation is beyond a certain threshold, the neuron can fire and send a spike along its axon.

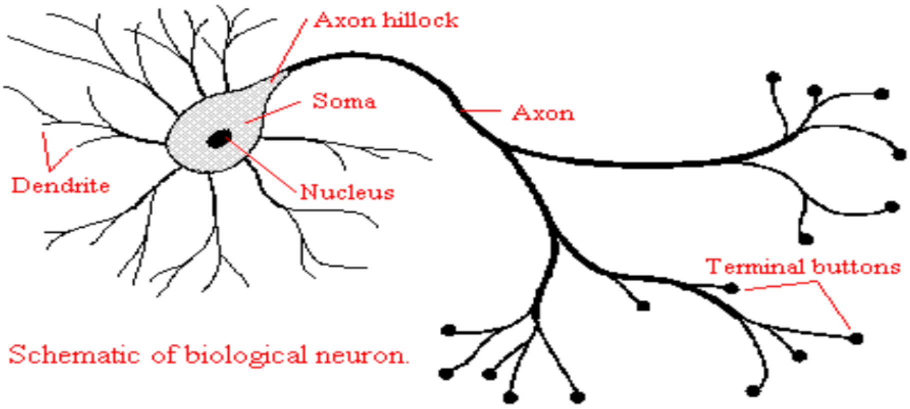

Figure 2.21. Biological neuron in the human nerve system [60].

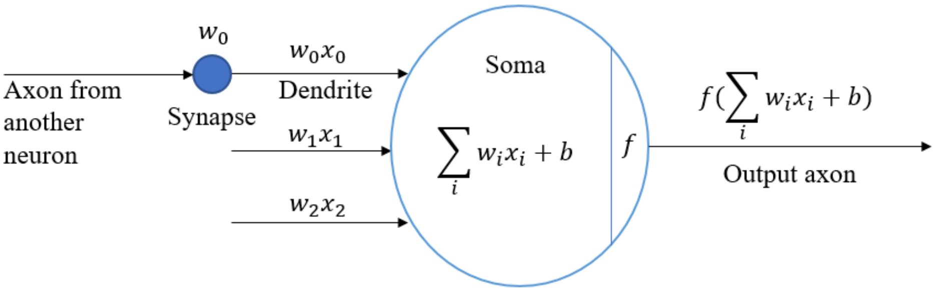

Figure 2.22. Mathematical model of neuron [61].

Neural network is a computational model that is inspired by the way biological neural network in the human brain process information. As shown in Figure 2.22, the basic unit of computations in a neural network is a node or unit, also known as a neuron in computation. In Figure 2.22, it is the mathematical model of a biological neuron, where *w* denotes the weights, *x* indicates information, *b* is called bias and *f* means the activation function. The node (soma) receives inputs from other nodes or external sources and each input has an associated weight (*w*) to express its relative importance to other inputs. The weights, considered as the synaptic (terminal buttons) strengths, control the strength of influence and the direction, either positive (excitatory) or negative (inhibitory) of one neuron on another. The node applies a sum function to all inputs. The activation function is utilised to determine the relationship between the output value and the threshold.

2.4.2 Neural network structure

A neural network typically consists of input, hidden and output layers. In Figure 2.23, it is a simple feedforward structure of the neural network architecture consisting of one input layer, two hidden layers and one output layer. The input layer is a block of the input nodes. The input nodes are described as synapses in the human brain system. And these nodes are designed to pass the information to the next layer without any computation. The hidden layers are the layer behind the input layer where intermediate processing and computations are performed. They perform computations and transfers the weights from the input layer to the next layer. The output layer is the output of the neural network, which is the final layer of the neural network. The activation function is utilised in this layer to map the results from the last layer to the desired output format.

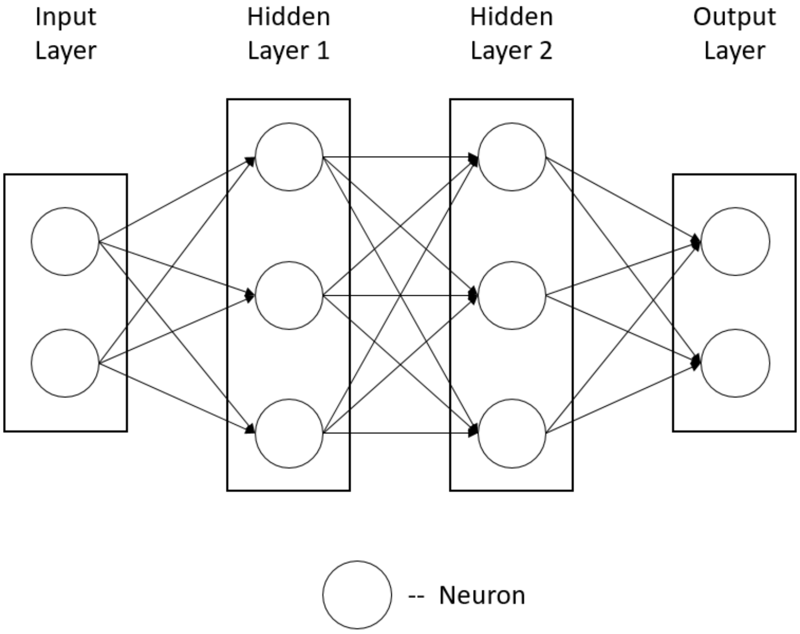

Figure 2.23. The structure of the feedforward neural network architecture.

2.4.3 Neural network training

In this section, the process of neural network training will be explained step by step. The process can be divided into five stages: they are i) definition of the neural network model, ii) preparation of the training datasets, iii) pre-processing of the training datasets, iv) initialisation of weights and biases of the weight function and v) training of the neural network model.

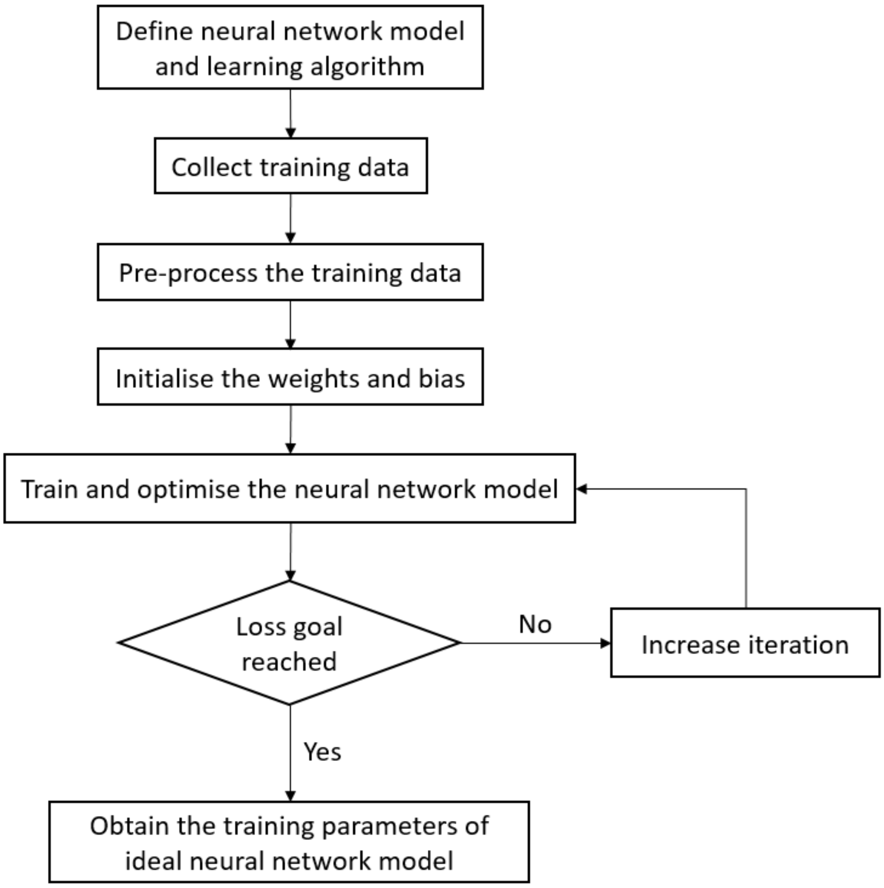

Figure 2.24. Flow chart of neural network training processes.

i. When defining the neural network model, the neural network type and the hyperparameters such as the number of layers and nodes in each layer need to be defined first. There are different types of neural networks such as long short term memory (LSTM) [62], generative adversarial network (GAN) [63] and gated recurrent unit (GRU) [64]. Different types have different characteristics and thus have different applications. Different activation functions for different layers must be designed. The cost function is used to evaluate the loss between prediction and the study label. The training purpose is to minimise the value of the cost function.

ii. Training datasets selection is an essential part of the success of the neural network architecture. Different types of training datasets and research purposes decide which neural network model and learning algorithm should be selected. The training datasets are comprised of training data and study labels, where the training data act as the study material and the study labels are the answers. Training data and study labels are also known as the input and output of the neural network respectively.

iii. The idea of pre-processing the training datasets is to help the training process be efficient and accurate. Different activation function has different output range. Therefore, the study labels must be processed to the corresponding range to have accurate training results.

iv. In the initialising stage, the weights and biases values of the weight function can be selected randomly. The bias is a constant, which gives the neural network an extra parameter to tune to improve the fit.

v. In the training step, a single epoch is that the neural network model computes the input and activation function of each layer in the forward direction and back propagates the loss value to update the weight function. The gradient descent algorithm is often used for minimising the loss. It works by having the model predictions on training data and using the prediction loss to update the model to reduce the loss [65]. The final goal of the training step is to achieve the minimum loss after several training epochs.

2.4.3.1 Learning algorithm

The learning algorithm is the rule that modifies the parameters in the neural network for producing the desired output based on the given input [66]. This learning process typically amounts to modifying the weights. The weights are essential to the recognising abilities of the neural network. Information from inputs is fed forward through the network to modify the weights between nodes. The weights modification can be optimised through backward propagating the loss generated during the training process. The neural network processes the input and output values in the training datasets and modifies the value of the weights to reduce the difference between predicted and target values. This value difference is called loss. The loss is minimised across many epochs (training iterations) until a specific level of accuracy is achieved [67].

2.4.3.2 Activation function

The activation function is defined as the output derived from a set of input values fed to a node or a layer. In most cases, the purpose of an activation function is to add non-linearity to the neural network. In this section, four basic activation functions, which are identity, logistic (Sigmoid), hyperbolic tangent (Tanh) and rectified linear unit (ReLU), will be introduced, and their advantages and disadvantages will be discussed.

The activation function can be basically divided into two types, linear and non-linear. The linear activation function is known as the identity function, where the activation is proportional to the input. The linear activation function cannot help with the complexity and various parameters of usual data that is fed to the neural networks. It cannot be used in the backpropagation learning mechanism as the backpropagation requires the non-constant derivative to update the weights.

The non-linear activation functions are the most popular activation functions. There are some commonly used non-linear activation functions such as logistic (sigmoid), hyperbolic tangent and rectified linear unit (ReLU). Figure 2.25 shows the logistic function and its derivative. The logistic activation function is used in the models, which predict the probability as an output. This is due to the range of the logistic activation function being from 0 to 1, which is the same as the probability. The function is differentiable, which means it can be used in the backpropagation neural network. As shown in the plot of the derivative of the logistic function, the gradient values (derivative) are only significant for range from -6 to 6. And the graph gets much flatter in the rest of the range. As the gradient values approach zero, the neural network may suffer from the vanishing gradient problem in the models with a large number of layers. This is the limitation of the logistic function.

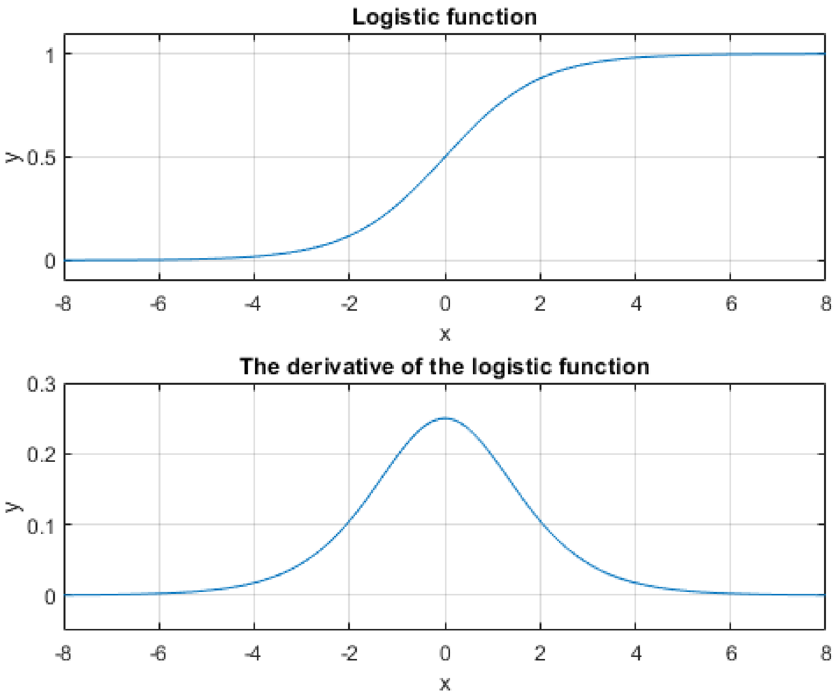

Figure 2.25. The logistic (sigmoid) function and its derivative.

The hyperbolic tangent (tanh) function is similar to the logistic activation function but with a different output range, which is from -1 to 1. In the hyperbolic tangent function, the larger the input, the closer the output will be to 1. Whereas the smaller the input, the closer the output will be to -1. The output of the hyperbolic tangent function is zero centred. Thus, the output values can be easily marked as strongly negative, neutral or strongly positive. The hyperbolic tangent function is usually used in hidden layers of a neural network as its value range between -1 to 1, therefore, the mean value for the hidden layer is or close to zero. It helps in centering the data and makes the learning process for the next layer easier. However, it also faces the similar problem of vanishing gradient in the neural network models with a large number of layers, as can be seen in the derivative in Figure 2.26.

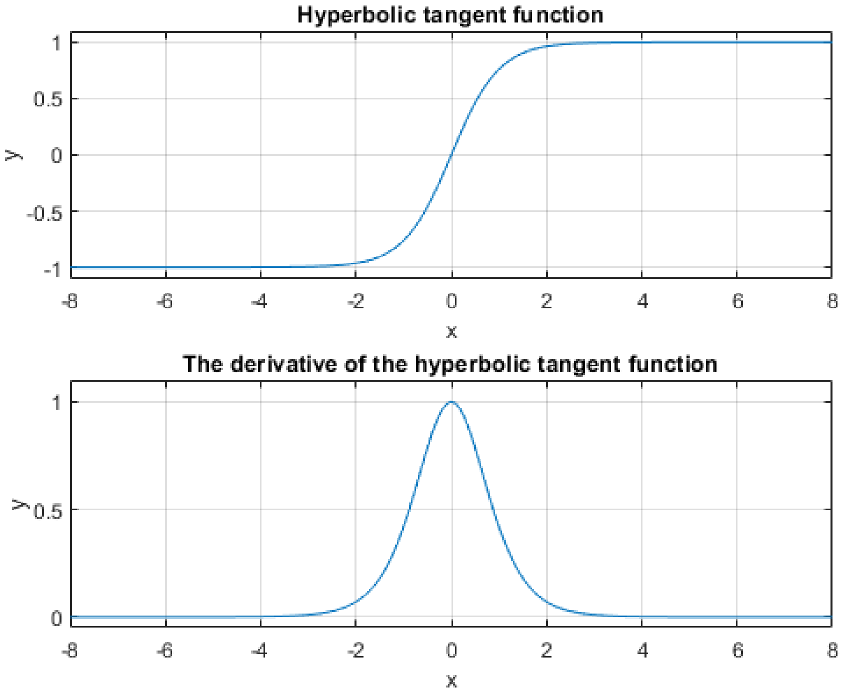

Figure 2.26. The hyperbolic tangent (tanh) function and its derivative.

The rectified linear unit (ReLU) function is half rectified, as can be seen in Figure 2.27. The function is linear for values greater than zero, whereas the negative values are zero. An important benefit of the ReLU is its capability of outputting a true zero value. This means that negative inputs can output zero values allowing the activation of hidden layers in neural networks to contain true zero values. This is called a sparse representation and it can accelerate learning and simplify the model [68]. Since the neurons will be deactivated if the output is less than zero, the ReLU function is more computationally efficient when compared to the logistic function and hyperbolic tangent function. The derivative of the ReLU is easy to calculate, therefore, it can be used in the backpropagation algorithms. The limitation of ReLU is its gradient of the negative part is zero whenever the neuron is not activated. This means that a neuron with this problem will output an activation value of 0. This is referred to as dying ReLU [69].

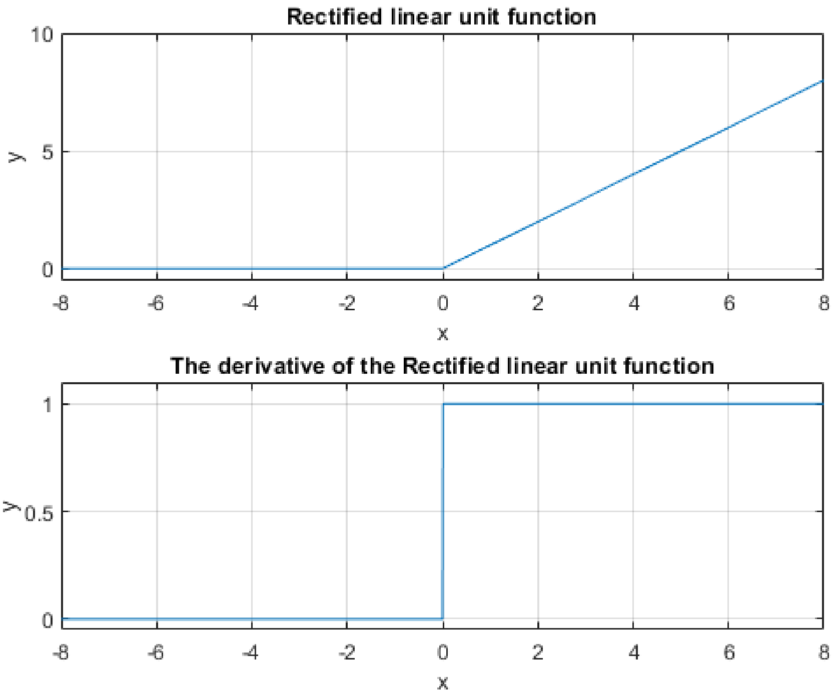

Figure 2.27. The rectified linear unit (ReLU) function and its derivative.

The comparison of the four activation functions has been shown in Table 2.1 in terms of the expression and range of the function and corresponding derivatives.

Table 2.1. Comparison of different activation functions.

Name	Function	Derivative	Range
Identity	$f(x) = x$	$f'(x) = 1$	$(-\infty, \infty)$
Logistic (Sigmoid)	$f(x) = \dfrac{1}{1 + e^{-x}}$	$f'(x) = f(x)(1 - f(x))$	(0,1)
Hyperbolic tangent (Tanh)	$f(x) = \dfrac{e^x - e^{-x}}{e^x + e^{-x}}$	$f'(x) = 1 - f(x)^2$	(0,1)
Rectified Linear Unit (ReLU)	$f(x) =$ max$\{0, x\}$, Where $\begin{cases} 0, if\ x \leq 0 \\ x, if\ x\ > 0 \end{cases}$	$f'(x) = \begin{cases} 0, if\ x \leq 0 \\ 1, if\ x\ > 0 \end{cases}$	$[0, \infty)$

2.4.3.3 Hyperparameters in neural network model

Hyperparameters are the variables that determine the network structure and how the network is trained. The hyperparameters are divided into two categories, which are network structure related and training algorithm related respectively [70]. In terms of the network structure related hyperparameters, there are five hyperparameters such as the numbers of the hidden layers and nodes, dropout, network weight initialisation and activation function. As for the hyperparameters of the training algorithm, the learning rate, momentum, number of epochs, batch size and batch normalisation are widely used hyperparameters [71][72]. The hidden layers and nodes, network weight initialisation and activation function have been introduced in the previous section. The rest of the hyperparameters, including batch size, learning rate, momentum, batch normalisation and dropout, will be explained in this section.

2.4.3.3.1 Batch size, learning rate and momentum

Gradient descent is an optimisation algorithm for finding the minimum of a function [73]. The optimisation is divided into two steps. Firstly, it computes the gradient that is the first-order derivative of the function at the current point. Then it moves in the opposite direction of the gradient increase from the current point by the computed step [74]. Figure 2.28 shows how the gradient descent algorithm work. The incremental step, also known as the learning rate, defines how quickly a network updates its parameters. The small value of the learning rate sacrifices the learning process time but converges smoothly. On the contrary, a larger learning rate speeds up the learning process but may not converge. Momentum is a term used in gradient descent algorithms and it is designed to accelerate the optimisation process and improve the capability of the optimisation algorithm [75]. The momentum algorithm accumulates an exponentially decaying moving average of past gradients and continues to move in their direction [76]. The value of momentum is defined in the range 0 to 1 and often has a value close to 1. A momentum value of 0 indicates the gradient descent without momentum.

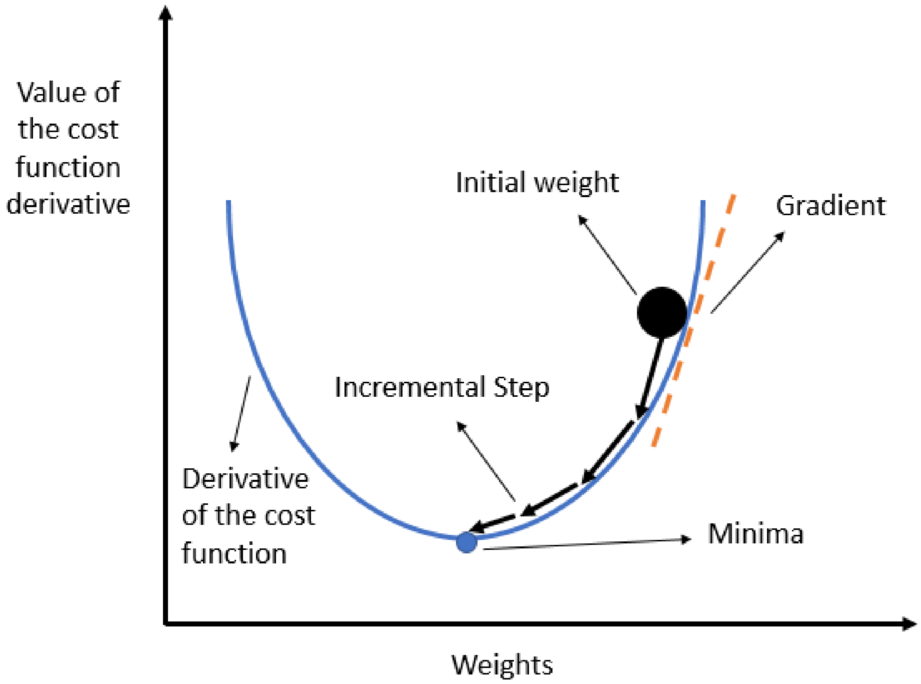

Figure 2.28. Gradient descent algorithm.

Gradient descent can vary in terms of the number in training datasets used to calculate the loss. Different gradient descent configurations give different computational efficiency and the fidelity of the gradient. There are three main gradient descents, including stochastic, batch and mini-batch gradient descent.

Stochastic gradient descent (SGD) is a variation of the gradient descent algorithm that calculates the loss and updates the model for each example in the training data [77]. One training example is passed through the neural network at a time. The weights of all the layers of the network are updated after every training sample. Therefore, it is often called an online learning algorithm. It is easier to fit into memory due to a single training sample being processed by the network [78]. However, frequent updates are computationally expensive due to using all resources for processing one training sample at a time [79]. Batch gradient descent describes calculating the loss in the training data and updating the neural network model after all training samples have been studied [80]. One cycle through the entire training dataset is called a training epoch. Therefore, the batch gradient descent updates the model at the end of each training epoch. The low update frequency of batch gradient descent results in a more stable error gradient. However, in terms of training speed, the batch gradient descent becomes very slow for large datasets. Mini-batch gradient descent is a mixture of both stochastic and batch gradient descent. It splits the training dataset into small batches that are used to calculate an approximation of the true gradient [80]. The training dataset is divided into multiple groups called batches and each batch has a number of training samples. A single batch is passed through the network, which computes the loss of every sample in the batch and uses their average to update the parameters of the neural network. Mini-batch gradient descent allows for a robust convergence and avoids local minima. Mini-batch sizes are often tuned to an aspect of the computational architecture on which the implementation is being executed. One crucial optimisation in building a neural network is selecting an appropriate batch size. Such value is normally a power of two that fits the memory requirement of the GPU or CPU hardware, like 32, 64, 128 [81]. Small values give a learning process that converges quickly at the cost of inaccurate gradient and noise in the training process. In contrast, large values can have accurate gradient estimation but slow convergence speed.

2.4.3.3.2 Batch normalisation

Training neural networks with tens of layers is challenging as the neural network model is updated layer by layer backward from the output to the input using an estimated loss under the assumption that the weights in the layers prior to the current layer do not change [82]. In practice, all layers are changed during an update simultaneously. When the parameters of a layer change, the distribution of inputs to subsequent layers will change as well. These kinds of changes of input distributions, called internal covariate shift, can be problematic for neural networks, especially some deep neural networks with massive layers in the model [82]. In neural networks, the parameters need to go to the activation function to make the output meaningful. In Figure 2.29, a hyperbolic tangent function is acted as an activation function and is used to explain the internal covariate shift. In general, the input data of the activation layer is supposed to be distributed as a standard normal distribution across the *x*-axis. However, in some deep neural network models, those input data shift to the saturated area, shown as the area outside the yellow area in Figure 2.29, while training would make the parameters forward and backward propagation inefficient or even cause the neural network to fail to predict.

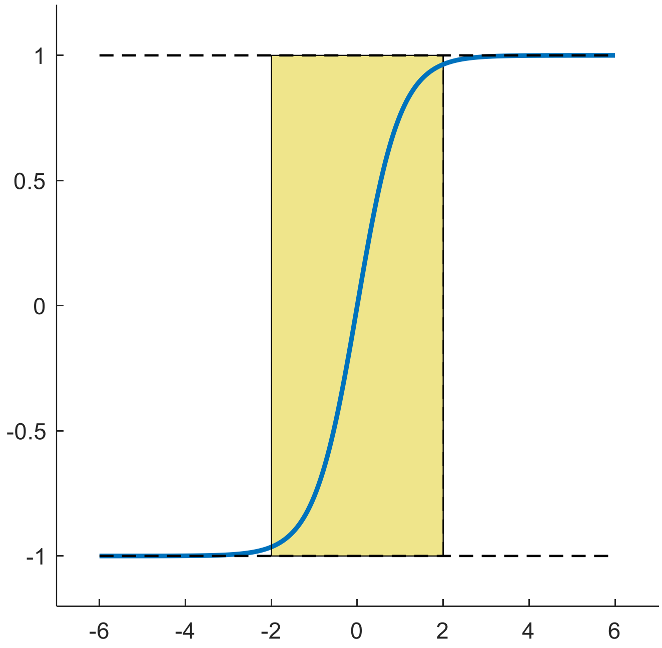

Figure 2.29. The hyperbolic tangent function and its saturated area.

Batch normalisation (BN) is a method intended to mitigate internal covariate shift and enable the neural network to be faster and more stable through normalisation of each layer of the neural network model by rescaling [82]. BN has the effect of stabilising the learning process and dramatically reducing the number of training epochs required to train deep networks [83]. BN scales the output of the layer by standardising each input variable of the previous layer. This standardisation refers to rescaling data to have a mean of zero and a standard deviation of one, also known as standard Gaussian distribution. BN can be implemented during training by calculating the mean and standard deviation of each input variable to a layer per mini-batch and using these statistics to perform the standardisation [84]. It is impractical to use the entire training datasets to train and normalise a SGD method based neural network model at each training step. This is the reason that the mini-batch is used to calculate the mean and variance. Basically, the BN can be expressed as

$$y_i = BN_{r,b}(x_i) \tag{2.17}$$

Where x_i denotes the input and y_i is the output. Parameters r and b are scaling and shifting factors respectively.

Considering a mini-batch B of size m, the BN algorithm can be expressed as following equations.

$$u_B = \frac{1}{m}\sum_{i=1}^{m} x_i \tag{2.18}$$

$$t_B^2 = \frac{1}{m}\sum_{i=1}^{m} (x_i - u_B)^2 \tag{2.19}$$

$$\hat{x}_i = \frac{x_i - u_B}{\sqrt{t_B^2 + e}} \tag{2.20}$$

$$y_i = r\hat{x}_i + b \tag{2.21}$$

Where u_B and t_B^2 is the mean and variance of the mini-batch respectively. $\hat{x}_i$ denotes the normalised value of the mini-batch. e is a constant added to the mini-batch variance for numerical stability.

However, simply normalising each input layer may change what the layer can represent. For example, directly normalising the inputs of a hyperbolic tangent function would constrain them to the linear regime of the non-linearity [82], which means most of the data would be restricted to the coloured area in Figure 2.29. Thus, the transformation inserted in the neural network needs to be represented by the identity transform to overcome this issue. In (2.21, a pair of parameters r and b, which scale and shift the normalised values, are learned along with the original model parameters. By using these two parameters, the original input data would be recovered.

2.4.3.3.3 Dropout

Neural networks with multiple non-linear hidden layers are very expressive models that can learn very complicated relationships between their inputs and outputs [85]. However, overfitting is a serious problem in such networks. Overfitting refers to a model that studies the training datasets too well [86]. It happens when a neural network model learns the detail and noise in the training datasets to the extent that it negatively impacts the performance of the model on new data [87]. In this case, the model learns the noise and random fluctuations in the training data. And the noise does not apply to the new data and negatively impacts the ability of the models to generalise.

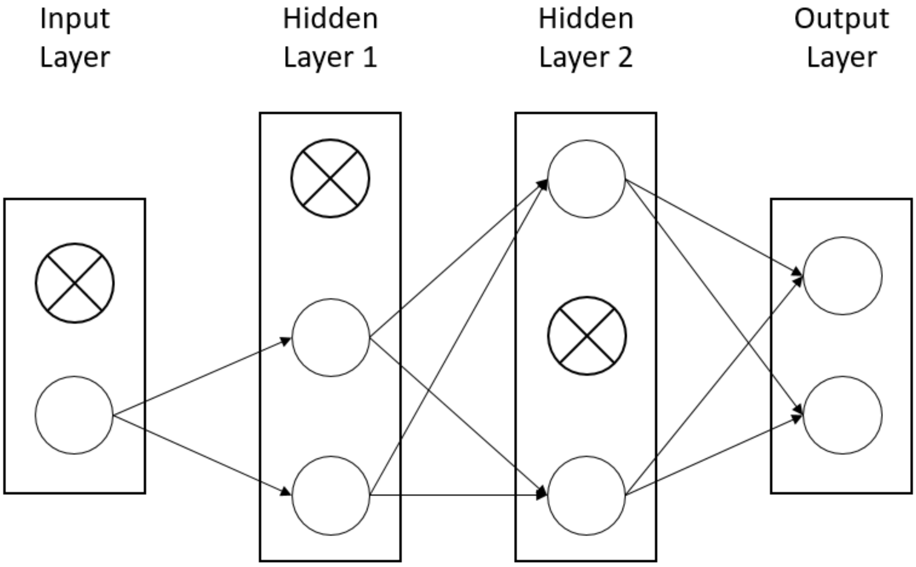

Figure 2.30. Neural network structure with random nodes dropped out.

Dropout is a regularisation technique to prevent overfitting [85]. It takes effect at the training stage which relies on stochastically dropping out nodes in each layer during training [88]. As shown in Figure 2.30, dropping a node out means temporarily removing it from the network, along with all its forward and backward connections. The choice of which units to drop is random. The default interpretation of the dropout is the probability of training a given node in a layer and the range is defined in 0 to 1, where 1 means no dropout and 0 means no output as all nodes have been removed.

2.4.4 Types of neural networks

Different types of neural networks use different principles in determining their rules and algorithms. There are many types of artificial neural networks, each with its unique strengths. In this section, three popular types of neural networks, Multi-Layer Perceptron (MLP), Recurrent Neural Network (RNN) and Convolutional Neural Networks (CNN) will be introduced.

2.4.4.1 Multi-Layer Perceptron

Multi-layer perceptron (MLP) is the neural network that incorporates three or more layers, including an input and an output and one or more hidden layers. It is a class of a feedforward neural network. The flow of information occurs in the forward direction, from the input layer to output. The information from the input layer is utilised to calculate the intermediate function in the hidden layers, which is then applied to the output layer to calculate the final results. MLP model is the most basic deep neural network consisting of a series of fully connected layers, which means each node in one layer connects with a certain weight to every node in the following layer. An MLP usually uses a non-linear activation function, such as logistic function and hyperbolic tangent function, to classify data that cannot be separated linearly [89]. The advantages of MLP are its capability to learn non-linear models and learn models in real-time. However, MLP is sensitive to feature scaling and requires tuning a number of hyperparameters such as the number of hidden neurons, layers and iterations. MLP with hidden layers has a non-convex loss function where there exists more than one local minimum. Therefore, different random weight initialisations can lead to different validation accuracy. This type of neural network is applied extensively in tabular datasets classification, regression prediction problems and data compression [90].

2.4.4.2 Recurrent Neural Networks

A recurrent neural network (RNN) is a type of neural network in which the output of a particular layer is saved and fed back to the input, as shown in Figure 2.31. The recurrent network can have signals travelling in both directions by introducing recurrent structures in the network. The input layer is formed in the same way as in the MLP. However, in subsequent layers, the recurrent neural network process begins. From each time step to the next, each neuron will remember information from the previous time step, which means each neuron acts as a memory cell while computing and carrying out operations [91]. In RNN, each subsequent layer is a collection of non-linear functions of weighted sums of outputs and the previous state. The basic unit of RNN is called cell, and each cell consists of layers and a series of cells that enables the sequential processing of RNN models. RNN models are widely used in natural language processing (NLP) is very effective in the text to speech conversion and context recognition technology as the decisions from the past iterations can influence current ones [76].

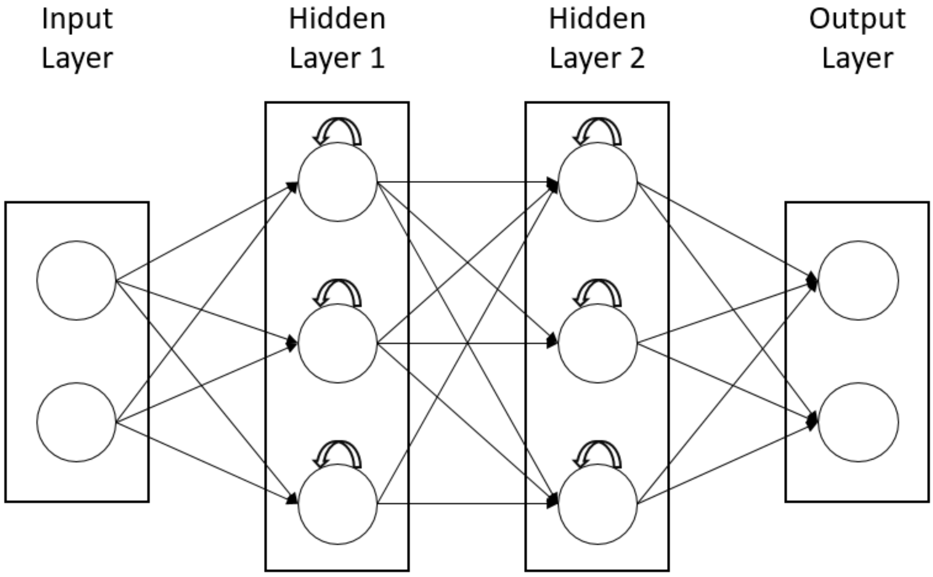

Figure 2.31. The structure of the recurrent neural network.

Gated recurrent unit (GRU) is a gating mechanism in recurrent neural networks [92]. GRU is a sequence processing model and suitable for designing the effective sequence learning system to address sequence-in-sequence-out due to its slow memory decay characteristic, where the memory is defined as a function that maps previous elements in a sequence to the current output [93]. Compared with other sequence processing models, such as LSTM model, GRU has fewer parameters and is simpler as it only has input and update gates [94]. GRU has shown its strength in speech signal modelling and natural language processing due to the gating network signalling that controls how the previous memory and present input are used to update the current activation and then produce the current state, which makes the predicted state more reliable [64]. However, the traditional GRU model could only process data from the forward sequence without considering the reverse sequence. Bidirectional-GRU (Bi-GRU) model combines two GRU together, one taking the input in a forward direction while the other in a backward direction. Bi-GRU uses two independent hidden layers to process data from forward and reverse at the same time. Such structure enables the neural network model to learn more context information and improve the classification accuracy [95].

2.4.4.3 Convolutional Neural Networks

Convolutional neural network (CNN) is a type of feedforward neural network employed in computer vision and NLP [96]. The neural network system automatically extracts features of the inputs, such as images and videos from the real world, to complete a specific task, including image classification, face authentication and image semantic segmentation [97].

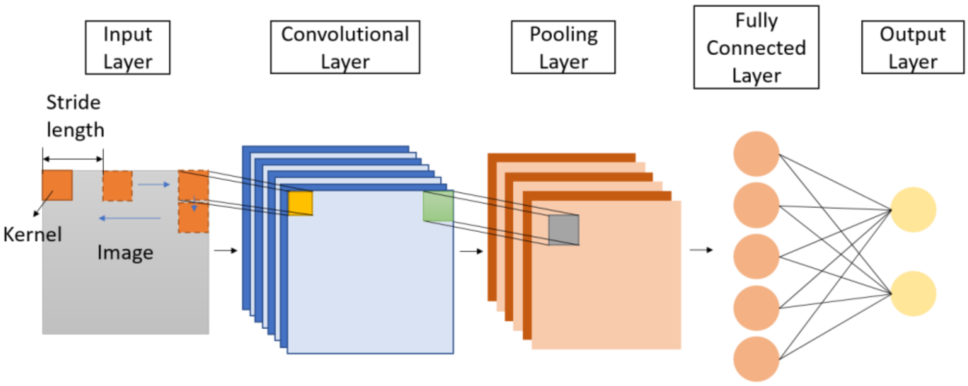

Figure 2.32. The structure of convolution neural network [98].

As shown in Figure 2.32, the CNN contains multiple convolution layers, which are responsible for the extraction of essential features from the image [98]. The earlier layers are responsible for simple details and the later layers are responsible for complicated features [99]. Before passing the results to the next layer, the convolutional layer uses a convolutional operation on the input. The network can be much deeper with fewer parameters due to convolutional layers. The element involved in carrying out the convolution operation in the first part of a convolutional layer is called the kernel, also known as the filter [100]. The kernels are used to convolute over the input image and produce maps. The kernel moves to the right through the convolutional layer with a certain stride value (fixed step length) till it parses the complete width and hops down to move to the left with the same stride value and repeats the process until the entire image is traversed [100]. These kernels are initialised randomly and are updated via backpropagation. After the convolution layer, there is a pooling layer which is responsible for the aggregation of the maps produced from the convolutional layer [101]. There are two types of pooling, max pooling and average pooling. For regularisation, CNN also introduces an option for adding dropout layers, which drop certain neurons to reduce overfitting. The CNN adds a fully connected layer to the pooling layer to flatten the image into a column vector. And the flattened output is fed to a feedforward neural network to train.

2.4.5 Applications in antenna design

The neural networks can be trained to learn any arbitrary nonlinear input-output relationships from corresponding datasets, and they have been applied to RF and microwave computer-aided design [102]. Neural networks are trained to model the electrical behaviour of passive and active circuits. These trained neural networks can then be used in simulation and design. Neural networks are efficient alternatives to conventional methods, such as numerical modelling methods, which could be computationally expensive [102]. Neural networks have been used for a wide variety of microwave applications, such as transmission-line components [103], impedance matching [104] and amplifiers [105]. In this section, examples of antenna design using neural networks will be discussed.

Figure 2.33 shows the design of a planar inverted-F antenna (PIFA) with magneto dielectric nano-composite (MDNC) by using the MLP neural network model [106]. Starting with the volume fraction and particle radius of the nano-magnetic material, the different antenna parameters, such as radiation efficiency, gain, resonant frequency and bandwidth, can be predicted by the MLP neural network model. In this design, two databases are created. The first one is the material properties, which are volume fraction and particle radius. The second database contains the electrical properties of the material, such as electric and magnetic loss tangent, permittivity and permeability. The MLP neural network model, trained by the two databases, is used to create the relation between the performance of the antenna and its properties. A total error of 7% is achieved between the MLP prediction and the second database. Figure 2.34 shows a comparison of the MLP prediction and the second database (target) regression curve.

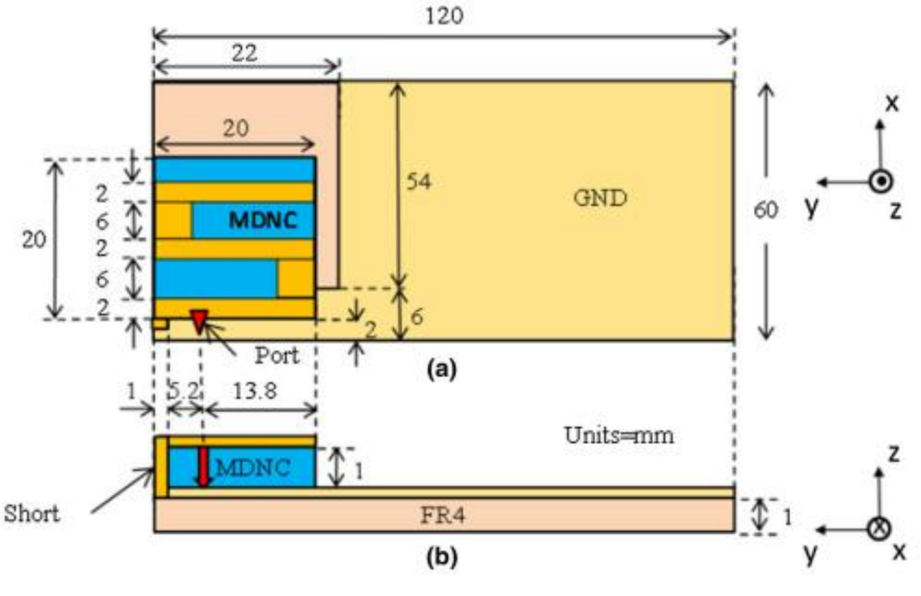

Figure 2.33. Geometry of PIFA on MDNC substrate: (a) top view, (b) side view [106].

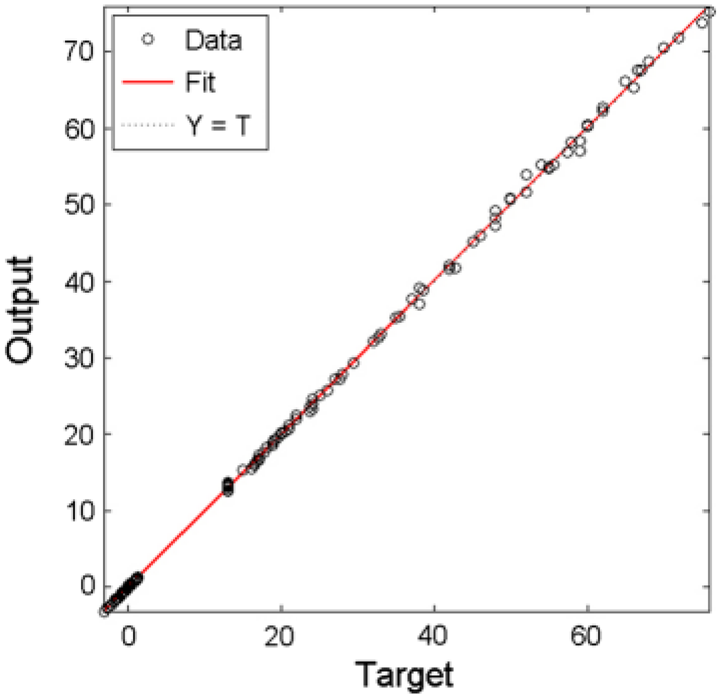

Figure 2.34. Neural network outputs versus the second database (target). Data for radiation efficiency, gain, resonant frequency and bandwidth [106].

In [107], a multi-band patch antenna is designed by a trained neural network and embedded in a particle swarm optimization (PSO) algorithm. The structure of the basic microstrip antenna and the stacked patch antenna, along with its design parameters, are shown in Figure 2.35. As shown in Figure 2.35 (a) and (b), the basic microstrip antenna consists of a rectangular patch on the top surface of a grounded dielectric substrate. Figure 2.35 (c) shows the two-layer stacked patch antenna, where another patch has been placed above the lower patch separated by an air gap. The dimensions of the lower and upper patch are (L_1, W_1) and (L_2, W_2) respectively. The feed point of the lower patch is (x_f, y_f). As shown in Figure 2.36, after the geometrical parameters of the antenna are decided by the PSO, a mapping function is built by the neural network model. The frequencies and bandwidths can then be related to the antenna geometrical parameters. The performance of the neural network can be observed by the regression plot and the mean squared error, as shown in Figure 2.37 and Figure 2.38 respectively. The designed antenna has been fabricated and tested. The comparison between measured and simulated results shows good agreement.

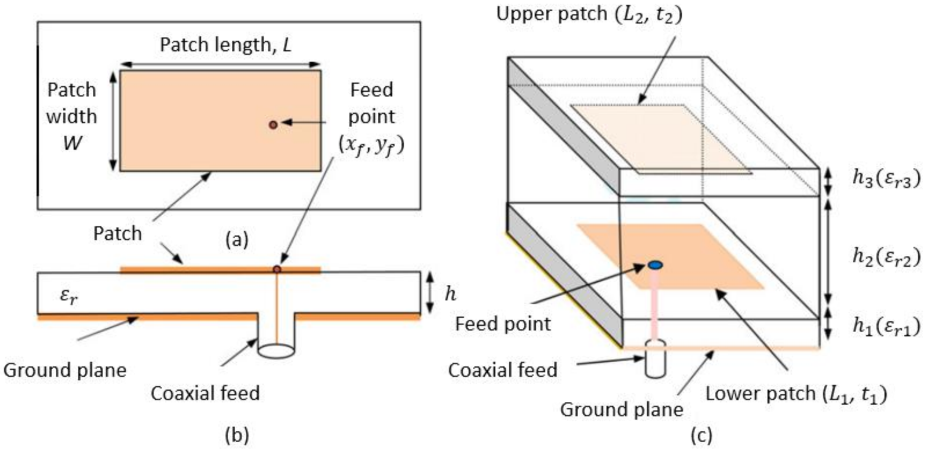

Figure 2.35. Geometry layout of antennas: (a) top view of single patch antenna, (b) side view of the lower patch antenna, (c) 3D view of the stacked patch antenna [107].

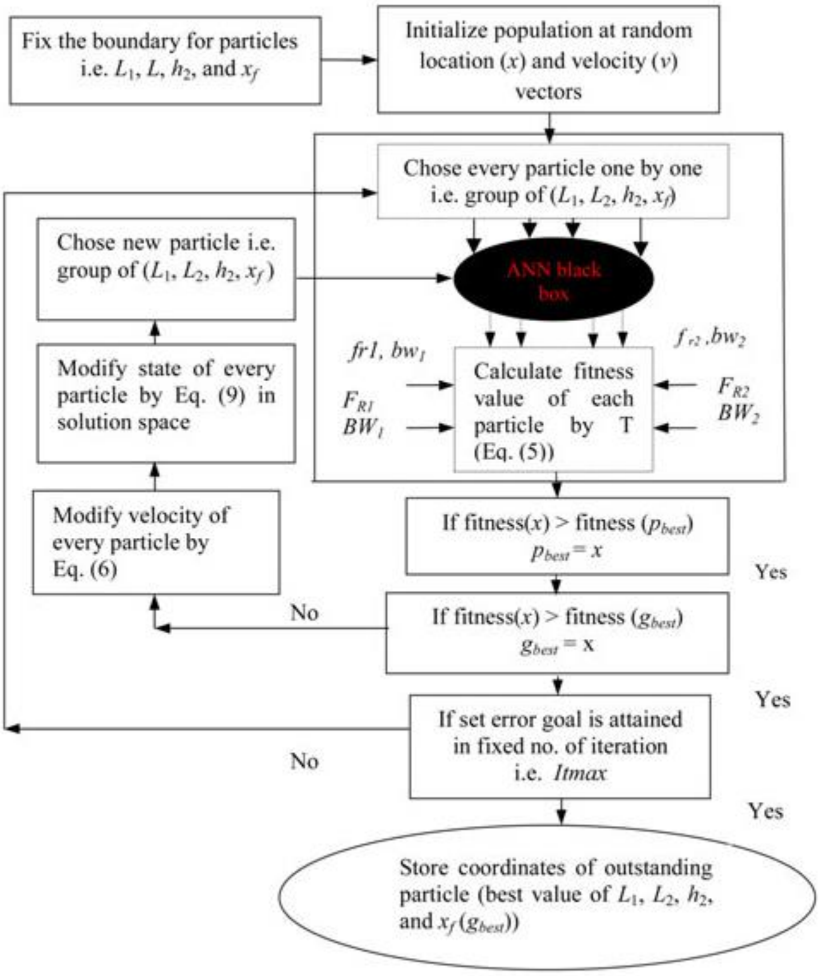

Figure 2.36. Flowchart of the optimiser [107].

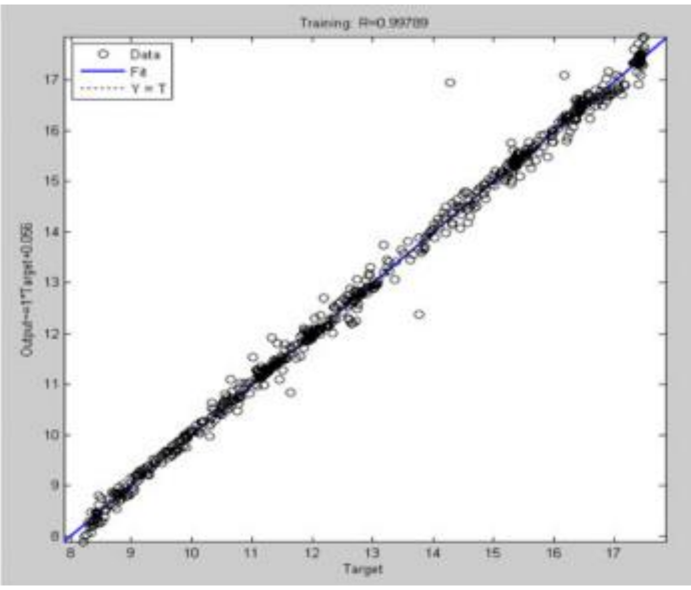

Figure 2.37. Regression plot [107].

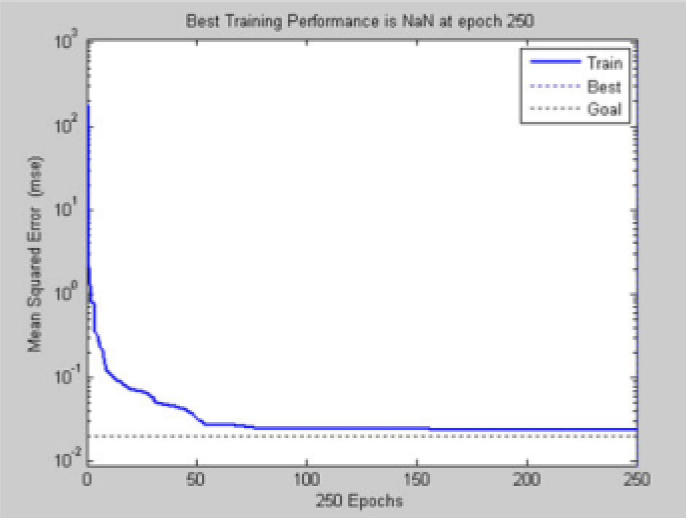

Figure 2.38. Error performance plot [107].

In [108], the design of a W-band slotted waveguide antenna array by using the MLP neural network model has been presented. The MLP neural network model consists of three layers, which are one input layer, one hidden layer and one output layer. The input layer consists of seven design parameters that include the length and orientation angle of the coupling slots (l_c, θ_1, θ_2, θ_3, θ_4 and θ_5) and the length of the radiating slots (l_R). The hidden layer consists of 10 hidden nodes, and the output layer consists of a single node that is defined as the sum of the S_{11}, sidelobe level, and backlobe level at 78 GHz. In the numerical experiment, 189 sample data are collected by varying the value of these seven design parameters, and the corresponding changes in performance parameters are recorded by simulating the antenna structure in HFSS. The dataset is used for training, cross-validation and testing of the MLP neural network model. The antenna is fabricated using 3D printing techniques after obtaining the optimised values of the design parameters. The measurement and simulation results in terms of S_{11} and the gain of the antenna have been compared and a good agreement with acceptable errors has been shown.

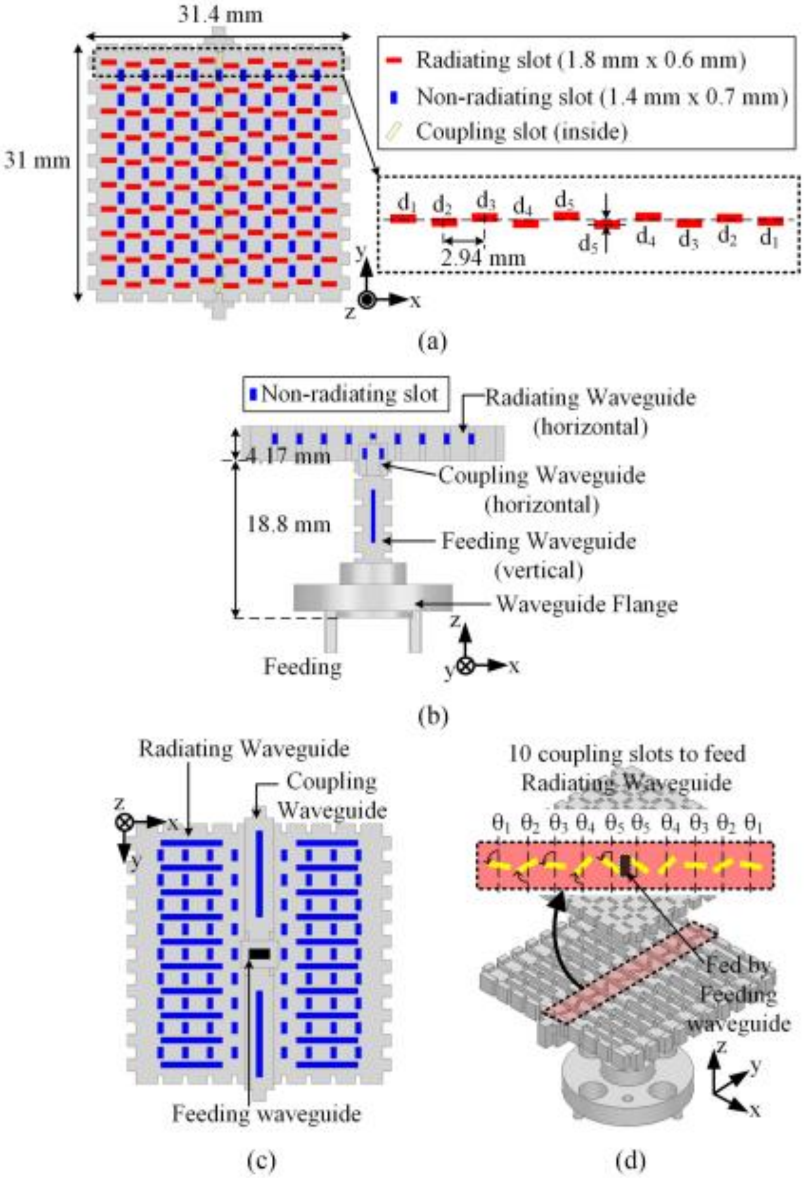

Figure 2.39. Geometry of the slotted waveguide array antenna: (a) top view, (b) side view, (c) bottom view, (d) radiating waveguide [108].

2.5 Summary

In this chapter, antenna design techniques such as surface wave antennas, SWL, LWAs and holographic antennas have been reviewed. In this thesis, the objective is to design a low profile, high-performance and low-cost surface antenna according to the user-defined radiation pattern by applying the neural network method. With the support of the aforementioned antenna design techniques, the proposed antenna is a surface wave antenna with metallic cells on the surface. In the next chapter, the proposed antenna will be discussed. The methodology of the proposed neural network-based method for designing the antenna will be introduced in detail.

3 The proposed neural network method

This chapter focuses on the mechanism and methodology for utilising the Wasserstein generative adversarial network (WGAN) [109] and bi-directional gated recurrent unit (Bi-GRU) [110] neural network to design the cosecant-squared radiation pattern surface wave antennas. This method is proposed to predict the metallic cell pattern on the surface wave antennas with the desired far-field radiation pattern, which is served as the input to the neural network prediction models. The method is mainly divided into two prediction parts: i) from the far-field radiation pattern to near-zone *E*-field and ii) from near-zone *E*-field to metallic cell pattern on the surface. In the near-zone *E*-field prediction, the prediction model consists of the WGAN and the Bi-GRU neural network model. The WGAN model is used to generate a near-zone *E*-field. The relationship between far-field radiation pattern and near-zone *E*-field is studied by the Bi-GRU neural network model 1. And then based on the prediction of Bi-GRU model 1, the generated near-zone *E*-field from WGAN can be transformed to a desired far-field radiation pattern. In the second part of the proposed method, the Bi-GRU neural network model 2 is utilised to predict the metallic cell pattern. In this part, the near-zone *E*-field is the input to the Bi-GRU neural network model 2 and the metallic cell pattern is the output. The detailed flowchart of the proposed method is shown in Figure 3.1.

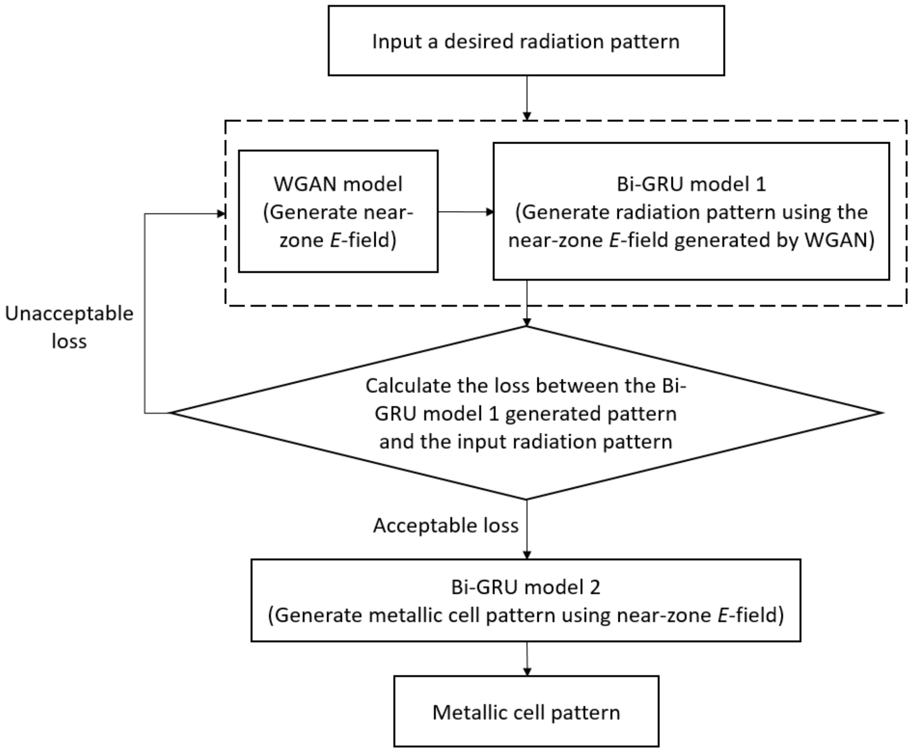

Figure 3.1. Flowchart of the proposed method.

From Figure 3.1, a user-defined cosecant-squared radiation pattern is input to the algorithm first. The WGAN model will generate a random near-zone *E*-field and the Bi-GRU model 1 will produce a corresponding far-field radiation pattern based on the WGAN generated near-zone *E*-field. The produced radiation pattern will be compared with the input radiation pattern to compute the loss (difference). If the loss is unacceptable, this procedure will be iterated until the loss is acceptable. Once the loss is acceptable, it means the WGAN generated *E*-field can be used to feed the Bi-GRU neural network model 2 to generate the metallic cell pattern.

3.1 Proposed antenna structure

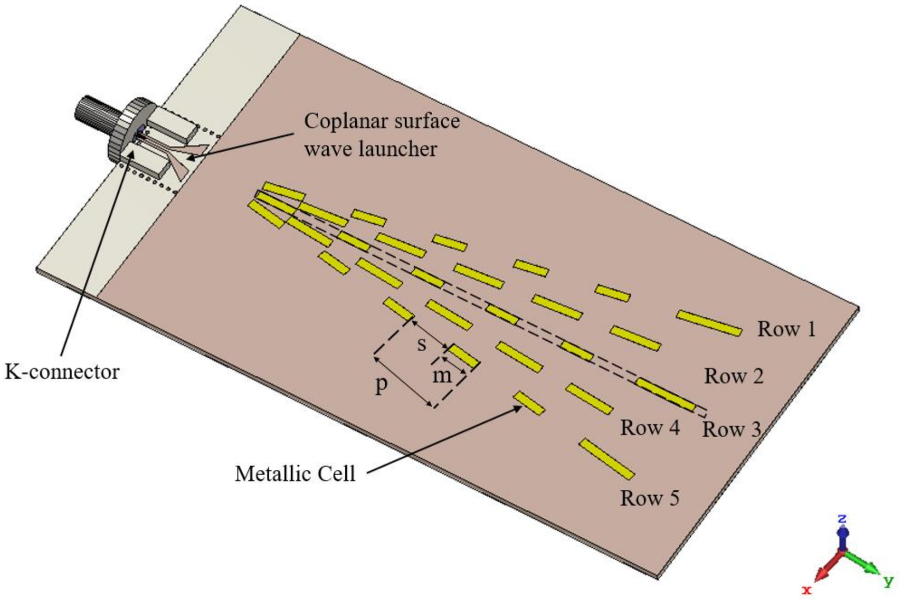

Figure 3.2. The proposed surface wave antenna with coplanar surface wave launcher.

In this neural network-based method, a planar millimetre-wave (mmWave) surface wave antenna is proposed to provide the training data to the neural networks. Figure 3.2 shows the geometry of the proposed antenna operating at 34.5 GHz. The antenna comprises a coplanar surface wave launcher (SWL), five radial rows of metallic rectangular shape cells and a piece of conductor-backed microwave dielectric substrate.

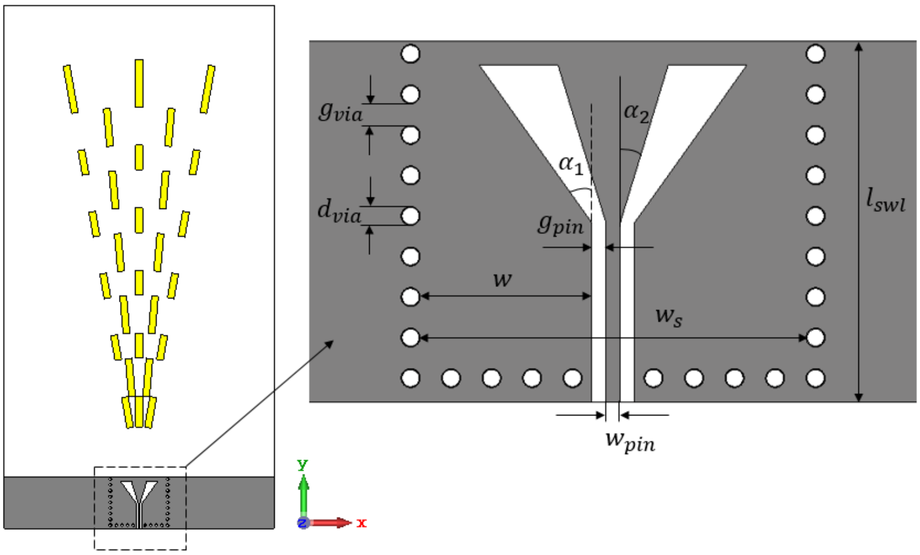

Figure 3.3. The top view of the proposed surface wave antenna with the zoomed-in coplanar SWL (without K-connector).

The geometry of the proposed coplanar SWL is shown in Figure 3.3. This design is inspired by [32] and the grounded coplanar waveguide (GCPW) to substrate integrated waveguide (SIW) transition structure. Such structure provides a linear polarisation in *yz*-plane. The top and bottom metal conductor plates on the substrate are copper and side walls are realised by periodic rows of copper-plated via holes. The d_{via} and g_{via} of the via holes are chosen to minimise the radiation leakages from the side walls. The two ground planes of GCPW generates parallel-plate modes, thus the side walls consisting of periodic rows of via holes are used to connect the top copper plate of the CPW to the lower ground plane to suppress the parallel-plate modes outside the walls [111]. The spacing (w_s) between the side walls should be large enough to avoid interference with GCPW field components. The maximum value of w_s is decided by the propagation of higher order leaky-wave SIW modes in the GCPW [112]. The maximum value of w_s is decided by the equation in [113][114], as

$$w_{eff} = w_s - 1.08\frac{d_{via}^2}{d_{via} + g_{via}} + 0.1\frac{d_{via}^2}{w_s} \qquad (3.1)$$

Where $w_{eff} = \frac{c}{2f_c\sqrt{\varepsilon_r}}$, c is the speed of light in the free space, f_c is the cut-off frequency.

The g_{pin} and w_{pin} have to meet the condition in (3.2 in [22] to avoid the propagation of microstrip line modes in the GCPW area.

$$0.2 \leq \frac{g_{pin}}{g_{pin} + w_{pin}} \leq 0.8 \tag{3.2}$$

The w_{pin} is decided by the K-connector in this design, which is 0.3 mm. The optimised value of $g_{pin} = 0.2$ mm is determined through matching the impedance of the GCPW structure to the K-connector, and the results will be presented in the next chapter.

At the end of the coplanar waveguide, there is a GCPW-SIW transition interface where the centre strip is tapered. The parameters of the coplanar SWL are listed in Table 3.1.

Table 3.1. The parameters of the coplanar SWL.

Parameter	Value	Parameter	Value
w_{pin}	0.3 mm	g_{pin}	0.2 mm
d_{via}	0.4 mm	g_{via}	0.45 mm
$\tan(\alpha_1)$	0.85	$\tan(\alpha_2)$	0.35
l_{swl}	7.56 mm	w	3.7 mm

The surface is excited through the SWL and propagates radially along the surface. When the surface wave hits the metallic cells, the surface wave will be scattered. The metallic cells on the surface act as the scatterers to have the surface wave radiated into free space, and the waves are summed to form the far-field radiation pattern. The five radial rows of metallic cells are separated by 5° in ϕ direction. The Rows 1, 3 and 5 are the same and consist of six metallic cells, while the Rows 2 and 4 are the same and have five metallic cells. The position of the metallic cells in Row 2 is determined by the position of gaps in Row 3, such that metallic cells in Row 2 fit precisely where the gaps are in Row 3. A parameter mark-to-space ratio (MSR) is introduced to describe the length ratio of the metallic cells and the space between the cells within a period where mark (*m*) is the metallic cell and space (*s*) indicates the gap. The parameter period (*p*) indicates the period length, consisting of a mark and a space.

In the electromagnetic (EM) simulations, a K-connector (Amphenol SV Microwave 1621-60050) is implemented as the feed of this surface wave antenna instead of a waveguide. The geometry of the K-connector affects the radiation pattern at high frequency. Therefore, the K-connector needs to be designed and simulated along with the surface wave antenna in CST. The operating frequency of the K-connector is up to 50 GHz. In this research, a cosecant-squared radiation pattern in the *yz*-plane is to be determined. Therefore, the metallic cells in the antenna described in Figure 3.2 are located symmetrically along the *y*-axis. The thickness of the metallic cells is 0.0175 mm. The metallic cells are printed on a piece of 0.787 mm thick microwave substrate Rogers RT5880 (ε_r = 2.2, tanδ = 0.009 at 10 GHz), which will provide the surface impedance $j117\Omega$ with the appropriate excitation efficiency of 94.2% of the SWL. The substrate is 77.56 mm in length and 40 mm in width.

3.2 Methodology of the near-zone *E*-field prediction from the far-field radiation pattern

In the near-zone *E*-field prediction, the proposed method uses two neural network models, which are the WGAN and the Bi-GRU models. The WGAN model is used to generate the near-zone *E*-field and the Bi-GRU model is applied to predict the far-field radiation pattern based on the WGAN generated near-zone *E*-field. This proposed method does not predict the near-zone *E*-field from the far-field radiation pattern directly, as using low dimensional data to predict high dimensional data is difficult and unreliable. As mentioned before, the radiation pattern prediction focuses on the *yz*-plane (ϕ = 90°). In the matrix point of view, the size of the radiation pattern matrix (vector) would be 1×700 (low dimensional data). When processing the data of the near-zone *E*-field, the near-zone *E*-field is a matrix with the size of 6×700 (high dimensional data). Compared with the near-zone *E*-field data, the far-field radiation pattern is the lower dimensional data and it is difficult to predict the higher dimensional data. The data matrix will be discussed later in this section. Therefore, the combination of WGAN and Bi-GRU is proposed to predict the near-zone *E*-field based on the user-defined far-field radiation pattern. In this combination of neural network models, the Bi-GRU model is critical to this method. Since the WGAN can only generate near-zone *E*-field and cannot recognise if the generated near-zone *E*-field is corresponding to the user-defined far-field radiation pattern. The Bi-GRU model is used to build the relationship from the near-zone *E*-field to the far-field radiation pattern and can transfer the WGAN generated near-zone *E*-field to the far-field radiation pattern. And the transferred radiation pattern can be used to compare with the user-defined radiation pattern to evaluate the loss (difference). If the loss is acceptable, it means that the WGAN generated near-zone *E*-field corresponds to the user-defined radiation pattern.

In this section, the conventional method of the near-field to far-field transformation (NF2FF) will be presented and the reason why NF2FF is not feasible to predict the near-zone *E*-field will be discussed. Due to the limitation of the NF2FF, the neural network-based method is attempted to predict the near-zone *E*-field from the far-field radiation pattern. The structure and the training process of the neural network model will be delivered. Data preparation is essential to neural network training, and this will be presented in this section. Once the neural network model is trained, it can be used to predict the near-zone *E*-field based on the input radiation pattern and the accuracy of the predicted results will be assessed. The evaluation of the prediction accuracy would be the vital part after training. Different evaluation methods to assess the prediction accuracy of the neural network model will be introduced at the end of this section and the assessment will be presented in the next chapter.

3.2.1 Near-field to far-field transformation

The Fourier transform-based near-field to far-field transformation (NF2FF) has been investigated before using the neural network method to build the relationship between far-field radiation pattern and near-zone *E*-field. In this section, the algorithm of the near-field to far-field will be introduced. The computation will be explained and the results compared with the CST simulation will be presented.

The NF2FF uses analytical methods to transform the near-field data to compute the far-field radiation characteristics [115][116]. The near-field amplitude and phase distributions can be obtained by simulation over a preselected surface which may be a plane, a cylinder or a sphere. The complexity of the transformation increases from the planar to the cylindrical, and to the spherical surfaces. The planar transformation is computational cheap as it is suitable for applying the fast Fourier transform algorithm [117]. In contrast, the spherical system requires the most expensive computation.

In this simulation, the planar system is selected to implement the NF2FF computation. The relationship between the near-field and the far-fields for planar systems follows the transform techniques of [118], can be expressed as

$$E(x,y,z) = \frac{1}{4\pi^2} \iint_{-\infty}^{\infty} f(k_x,k_y) e^{-jkr} dk_x dk_y \tag{3.3}$$

Where $f(k_x,k_y)$ is the plane wave spectrum of the field, r is the direction of propagation of the plane wave and k denotes the wavenumber. The detailed calculation will be presented in Appendix A. The far-field radiation pattern of the antenna in spherical coordinate can be calculated as

$$E_\theta(r,\theta,\phi) \approx j \frac{ke^{-jkr}}{2\pi r} (f_x cos\phi + f_y sin\phi)$$

(3.4)

$$E_{\phi}(r,\theta,\phi) \approx j\frac{ke^{-jkr}}{2\pi r}cos\theta(-f_x sin\phi + f_y cos\phi)$$

(3.5)

$$E(r,\theta,\phi) = E_{\theta}(r,\theta,\phi) + E_{\phi}(r,\theta,\phi) \approx j\frac{ke^{-jkr}}{2\pi r}[cos\theta\, f\left(k_x, k_y\right)]$$

(3.6)

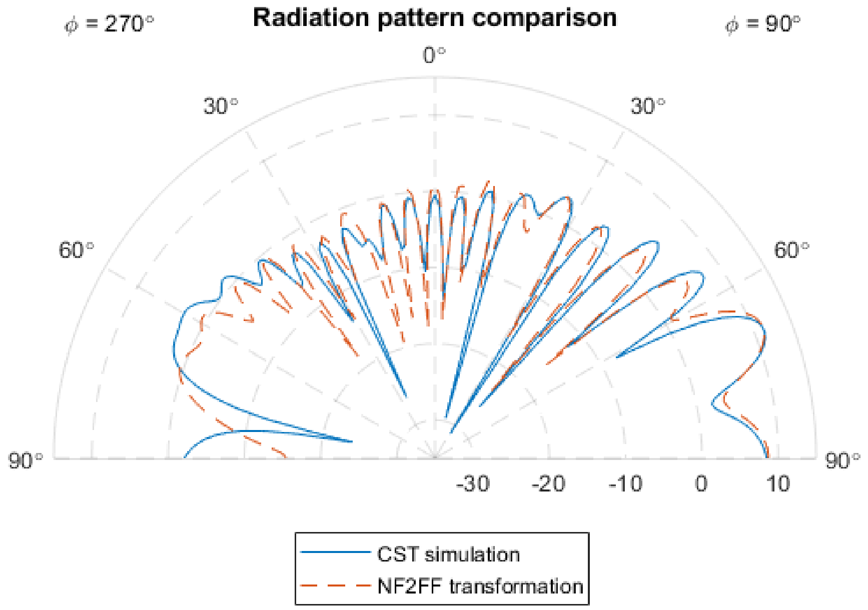

Figure 3.4. Radiation pattern comparison of CST simulation and NF2FF transformation at 34.5 GHz.

The far-field radiation pattern at 34.5 GHz calculated by the NF2FF transformation is shown in Figure 3.4. The MSE value between the simulated and transformed pattern is 27.65. The discrepancy is mainly from the nulls value. For example, the transformed radiation pattern has -11.83 dBi at (ϕ, θ)

= (90°, 15°) while the CST simulation shows -29.61 dBi. The reason is that the rectangular grids are 3600 in the NF2FF transformation, while the CST simulation has one million mesh grids. Therefore, the computation accuracy of the NF2FF transformation is not enough compared with the CST simulation. Although there are some discrepancies, the envelope of the NF2FF transformed radiation pattern is similar to the CST simulation.

Although the NF2FF shows a similar radiation pattern with the CST simulated radiation pattern, it is challenging to predict the near-field from the far-field radiation pattern. In the NF2FF algorithm, the far-field ($E(r,\theta,\phi)$) is calculated by adding E_θ and E_ϕ together, as indicated in (3.6. It is challenging to do the inverse from the far-field to calculate the near-field. Since either E_θ or E_ϕ cannot be obtained by giving $E(r,\theta,\phi)$ unless E_θ or E_ϕ is zero. However, E_θ and E_ϕ are not equal to zero since the cross polarisation cannot be exactly zero in real antennas. Therefore, the neural network-based method is considered to tackle the inverse problem. In this section, the combination of WGAN and Bi-GRU neural network prediction model is chosen as an appropriate method to predict the near-zone *E*-field from the far-field radiation pattern.

3.2.2 Neural network model structure of the near-zone *E*-field prediction

As the NF2FF cannot predict the near-zone *E*-field due to the challenging inverse problem, the combination of WGAN and Bi-GRU neural network prediction model is attempted to tackle the problem. In this section, the neural network model structures and their working mechanism will be introduced. The training setting of two neural network models will be summarised. In terms of data preparation, different arrays of field monitors are applied to extract the near-zone *E*-field from a commercial electromagnetic simulation software CST Microwave Studio. The far-field radiation pattern data is extracted through the 34.5 GHz far-field monitor. The magnitude of the extracted data will be scaled from 0 to 1 to fit into the neural network model.

3.2.2.1 WGAN model structure

GAN is an approach for generative modelling using the deep learning method. Generative modelling automatically discovers and learns the patterns and features in the input datasets in such a way that the model can be used to generate new examples that plausibly could have been drawn from the original datasets. In this research, the convolutional neural network is used in GAN. WGAN is the type of GANs that uses Wasserstein distance as the loss function. Wasserstein Distance is a measure of the distance between two probability distributions [119]. Each GAN has two essential elements, including a generator and a discriminator. Figure 3.5 shows the diagram of WGAN. The generator takes a fixed-length random vector from the problem domain as input and produces the plausible *E*-field samples with the expectation that it looks real to the discriminator. The vector is drawn randomly from a Gaussian distribution. After training, points in this multidimensional vector space will correspond to points in the problem domain. The discriminator takes input from both the training datasets *E*-field samples and the generated *E*-field samples of the generator and tries to classify the generated *E*-field as real or fake. The discriminator acts as a classification model. The decision (real or fake), also known as the loss value, is used to update the generator and discriminator.

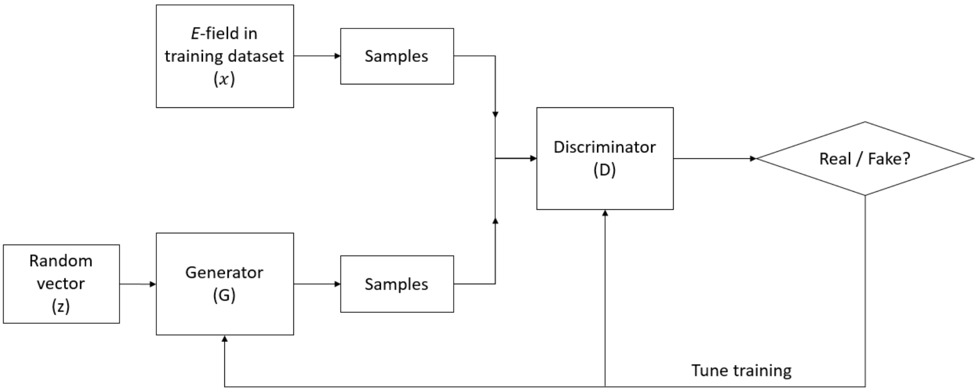

Figure 3.5. The diagram of WGAN [120].

3.2.2.2 Bi-GRU model structure

The Bi-GRU model is the bidirectional GRU and GRU cell is the basic unit. GRU neural network is a variant of recurrent neural networks. GRU has two gated units, which are reset gate (r_t) and update gate (z_t), as shown in the GRU cell diagram in Figure 3.6, where Concat is the vector concatenation operation.

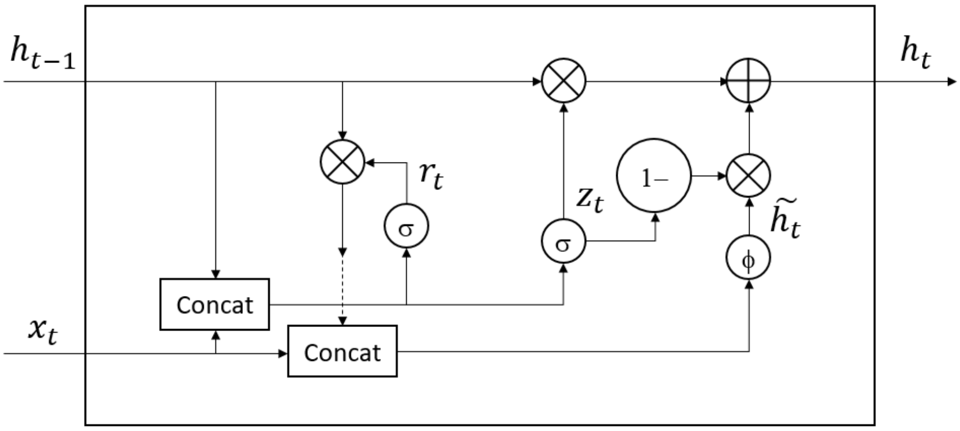

Figure 3.6. Gated recurrent unit cell [93].

GRU works in the following sequence. Firstly, it calculates the state of the reset gate r_t and the update gate z_t through the last transmitted hidden state h_{t-1} and the input x_t of the current state.

$$r_t = \sigma(w_r \cdot [h_{t-1}, x_t]) \tag{3.7}$$

$$z_t = \sigma(w_z \cdot [h_{t-1}, x_t]) \tag{3.8}$$

Where r_t and z_t are the gated control of reset and update gate respectively. σ denotes the logistic (sigmoid) activation function, w_r and w_z are the weight of the reset gate and update gate respectively. For the logistic function, the data range is mapped to the range [0, 1], which would act as the gated signal. Secondly, the reset gate is used to calculate the reset data h'_{t-1}, and h'_{t-1} and input x_t can then be spliced together by vector concatenation operation. The candidate state $\widetilde{h_t}$ is processed to the scale [-1, 1] by applying hyperbolic tangent (tanh) activation function, denoted by ϕ.

$$h'_{t-1} = h_{t-1} \cdot r_t \tag{3.9}$$

$$\widetilde{h_t} = \phi(w_{\widetilde{h}} \cdot [h'_{t-1}, x_t]) \tag{3.10}$$

The final step is the memory updating stage, which is the most critical part. In this stage, the current state vector h_t is a linear interpolation between the previous activation h_{t-1} and the current candidate state $\widetilde{h_t}$. The weighting factors are set by the update gate z_t, and they decide how much the units will update their activations. If z_t is close to zero, the current state depends more on the current input, which means it deletes the past memory and forgets the previously calculated states. However, if z_t is close to one, the previous state remains unchanged and implies more data are remembered. The gate used in this state enables forgetting and selecting memories at the same time. The first term $z_t \cdot h_{t-1}$ can be considered as a selective forgetting model, while the second term means the update gate selectively memorises the current state.

$$h_t = z_t \cdot h_{t-1} + (1 - z_t) \cdot \widetilde{h_t} \tag{3.11}$$

Traditional GRU model focuses on forward direction to process the data. In real antenna design, the surface wave propagates towards the positive *y*-direction and has wave reflection backward. This implies that the bi-directional effect needs to be considered when using neural network model to predict the near-zone *E*-field and the metallic cell pattern. Thus, Bi-GRU would be an appropriate solution as it combines forward GRU with reverse GRU.

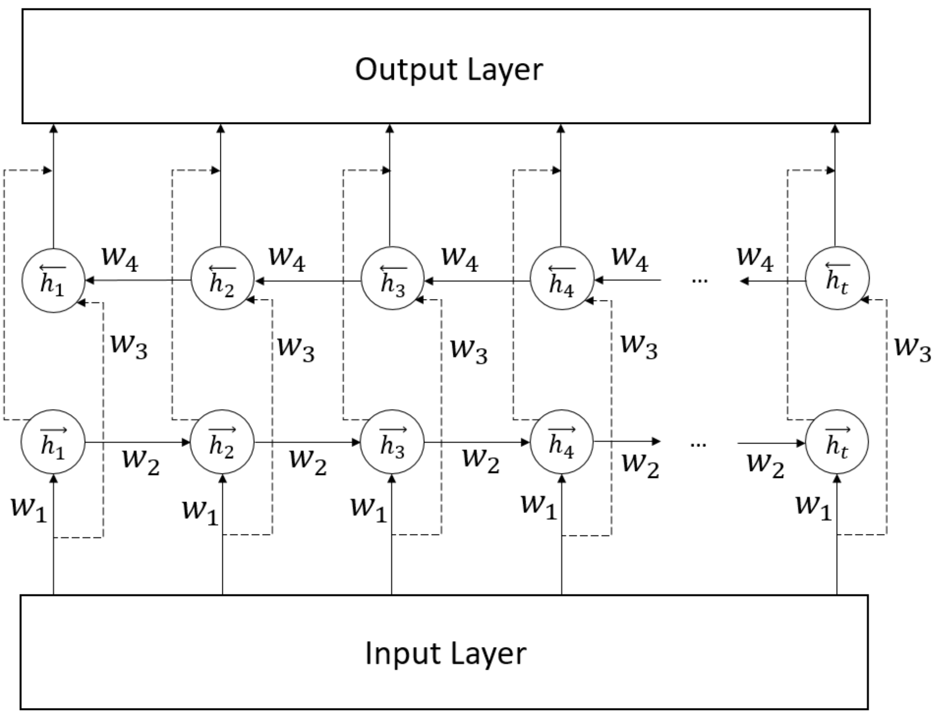

Figure 3.7. The structure of a Bi-GRU layer [110].

Figure 3.7 shows the structure of the Bi-GRU layer, which is the combination of the two different directional GRU cells, including the forward and backward GRU cells. In this structure, the GRU cell with $\overrightarrow{h_t}$ is forward and and $\overleftarrow{h_t}$ is backward. The two directional GRU cells are provided with the same input, and the output to the next layer is determined by both forward and backward GRU cells. The hidden states of the two directional GRU cells are $\overrightarrow{h_t}$ and $\overleftarrow{h_t}$ respectively. The hidden state can be calculated by (3.11 in this structure, it can also be expressed as

$$\overrightarrow{h_t} = f(w_1 x + w_2 \overrightarrow{h_{t-1}} + \vec{b}) \tag{3.12}$$

$$\overleftarrow{h_t} = f(w_3 x + w_4 \overleftarrow{h_{t-1}} + \overleftarrow{b}) \tag{3.13}$$

Where f is the computation function, x denotes input and b is bias. w_1, w_2, w_3 and w_4 are the weight factors.

And the output of this Bi-GRU layer is

$$output = \sigma(W \cdot [\overrightarrow{h_t}, \overleftarrow{h_t}] + B) \quad (3.14)$$

Where σ denotes the logistic activation function, W and B are the weights and biases. Square bracket means to concatenate the forward and backward outputs.

The training structure of the Bi-GRU model is shown in Figure 3.8. It consists of one input layer, two Bi-GRU layers and one output layer. The input layer has six input neurons which are the near-zone E-field components. These six neurons are fully connected to the Bi-GRU layer to compute the weights and bias. In the Bi-GRU layers, both Bi-GRU layer 1 and 2 contains 256 GRU cells (neurons). And the output layer has one neuron, which outputs the predicted far-field radiation pattern.

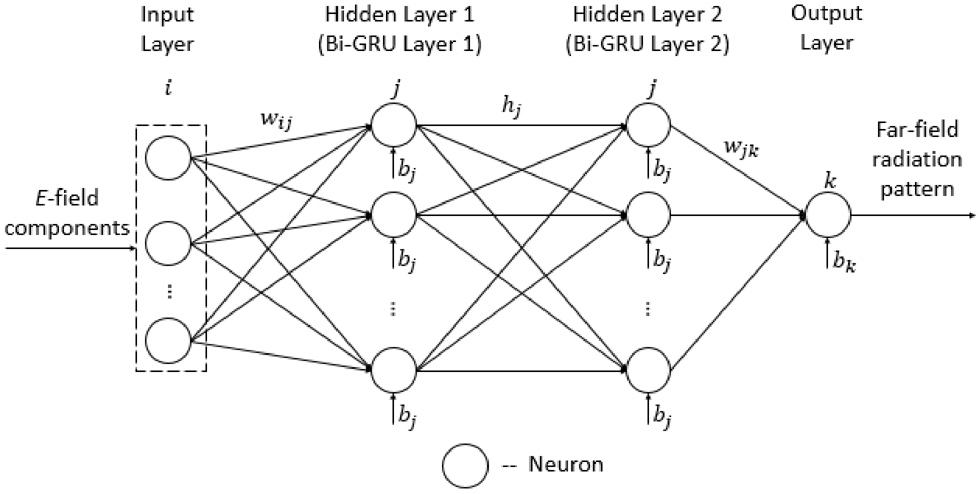

Figure 3.8. The diagram of the proposed Bi-GRU model for radiation prediction.

3.2.3 Neural network model training of the near-zone *E*-field prediction

3.2.3.1 Training of WGAN

During building the WGAN model, the generator consists of four transposed convolutional (inverse convolution) layers. The ReLU activation function is applied to each layer except the last layer. The activation of the last layer is the logistic function. In the discriminator, five convolutional layers are used and the activation function implemented is LeakyReLU [121].

Considering *z* is the input to the generator, *G(z)* is the output of the generator. *x* is the training data. The output of the discriminator is between 0 and 1. Training the discriminator involves presenting it with samples from the training datasets until it achieves acceptable accuracy. The discriminator training aims to minimise the loss function in (3.15. The training objective of the generator is to fool the discriminator by producing examples that the discriminator thinks are real. Mathematically, the aim is to minimise the value of (3.16.

$$D\_Loss = \nabla \frac{1}{m} \sum_{i=1}^{m} [f(x^{(i)}) - f(G(z^{(i)}))] \tag{3.15}$$

$$G\_Loss = \nabla \frac{1}{m} \sum_{i=1}^{m} [f(G(z^{(i)}))] \tag{3.16}$$

Where ∇ is Hamiltonian and f is a 1-Lipschitz function following the constraint $|f(x_1) - f(x_2)| \leq |x_1 - x_2|$.

With the operation in (3.15 and (3.16, the discriminator can have better performance in distinguishing the real and generated near-zone *E*-field, while the generator can fool the discriminator the most and produce a more plausible near-zone *E*-field.

3.2.3.2 Training of Bi-GRU

The *E*-field from the output of WGAN is supposed to be the input of the far-field radiation pattern prediction Bi-GRU model. In Figure 3.8 , two Bi-GRU layers are used, and each layer contains 256 GRU cells. There is a hyperparameter called bidirectional in Bi-GRU neural network model. Since the surface wave propagates towards the forward direction and has wave reflection backwards, this hyperparameter is set as 'True' in the simulation.

In Figure 3.8, the neurons are interconnected for the basic neuron computation. The multiplication of the neuron input and the connection weight coefficient between the input layer and hidden layer can be calculated by the interconnection. The bias value is also added to the neuron to give an extra parameter to tune. The expression of this computation is expressed as

$$z_{hidden} = \sum_{i=1}^{I} w_{ij} x_i + b_j \tag{3.17}$$

Where I is the number of elements in the input, x_i is the value of the input applied to the neurons, and b_j is the bias on the hidden nodes. w_{ij} denotes the synaptic weight coefficient between the input neurons and hidden neurons and z_{hidden} means the weight function of the hidden layer.

$$h_j = f(\sum_{i=1}^{I} w_{ij} x_i + b_j) \tag{3.18}$$

And the results of (3.17 are subjected to an active function, which is the logistic function in this simulation. The activation function generates neuron output via f calculation in (3.18, where h_j is the output of the hidden layer. Similar computations can be applied to the output layer, which are shown in (3.19 and (3.20.

$$z_{output} = \sum_{j=1}^{J} w_{jk} h_j + b_k \tag{3.19}$$

$$y_k = f(\sum_{j=1}^{J} w_{jk} h_j + b_k) \tag{3.20}$$

Where z_{output} is the weight function of the output layer. J is the number of elements in the hidden layer, h_j is the value of the output for the hidden layer, b_k is the bias on the output neuron and w_{jk} is the synaptic weight coefficient between the hidden and output neurons. f denotes the logistic activation function and y_k is the value of the output.

The loss (ε), defined as the mean squared difference between prediction results and study labels, is computed as

$$\varepsilon = \frac{1}{N} \sum_{i=1}^{N} (y_i - \hat{y}_i)^2 \tag{3.21}$$

Where N is the total number of samples in the training datasets, y_i denotes the study labels and $\hat{y}_i$ implies the prediction results.

With the loss updates, the weight functions have been updated by using (3.22 and (3.23. These computations are repeated and iterated for 300 epochs or until the acceptable loss is achieved. In this prediction, the acceptable loss is defined as the loss difference of two consecutive epochs being less than 5% for ten epochs.

$$w_{ij}(n+1) = w_{ij}(n) + \Delta w_{ij}(n) \tag{3.22}$$

$$w_{jk}(n+1) = w_{jk}(n) + \Delta w_{jk}(n) \tag{3.23}$$

3.2.3.3 Training and evaluation mode of the neural network model

There are two operation modes, training mode and evaluation (inference) mode when implementing the neural network model. The training mode needs to be triggered in the training stage, while the evaluation mode has to be turned on in the inference stage. When the training mode of the neural network model is triggered, it indicates that the neural network model is currently in the training phase. The neural network model keeps some layers, such as dropout and batch-normalisation, which depend on the current phase. The normalisation relies on the mini-batch of training datasets. All the datasets will be considered as training datasets under the current phase. The dropout layers are activated in the training mode. However, in the evaluation mode, the dropout layers are deactivated and the normalisation is based on the test datasets. When the evaluation mode is on, it sets the dropout and batch normalisation layers to inference mode before running the evaluation. Failing to do so will yield inconsistent evaluation results. Therefore, the evaluation mode has to be triggered before inference so that the neural network model can accurately predict the results. If resuming training is required, call the training mode function to set these layers back to the training mode.

Table 3.2. Difference between training mode and evaluation mode.

	Training mode	Evaluation mode
Operation mechanism	• Normalisation layers use training datasets. • Dropout layers are activated.	• Normalisation layers use test datasets only. • Dropout layers are deactivated.

3.2.4 Training data preparation of the near-zone *E*-field prediction

The training datasets are essential to neural network training. In this research, the total number of the training datasets is 5000, which means 5000 surface wave antennas have been simulated in CST to provide the near-zone *E*-field, far-field radiation pattern and metallic cell pattern data. In these 5000 surface wave antennas, the distribution of the metallic cell at the central radial row is defined by the period length of the metallic cell and the MSR of each period. The period length and MSR are randomly chosen among these 5000 surface wave antennas. The metallic cell length can be calculated by using the period length and MSR. The metallic cell lengths are random as well due to the randomly chosen period length and MSR. In this section, the near-zone *E*-field and far-field radiation pattern data are extracted from the CST simulated results of these 5000 antenna models.

In the data preparation of the near-zone *E*-field prediction, the training datasets consist of the near-zone *E*-field and the far-field radiation pattern data. The far-field radiation pattern data acts as the training label. In preparing the training label, the upper half of the far-field radiation pattern, which is from $(\phi, \theta) = (270°, 90°)$ to $(90°, 90°)$, has been taken. The far-field radiation pattern is extracted through the far-field monitor from CST. The step size of the radiation pattern data extracted from CST is 1^{o}, which is a 1×181 matrix. Then this radiation pattern is processed by interpolation algorithm and becomes a 1×700 matrix in order to be consistent with the near-zone *E*-field data.

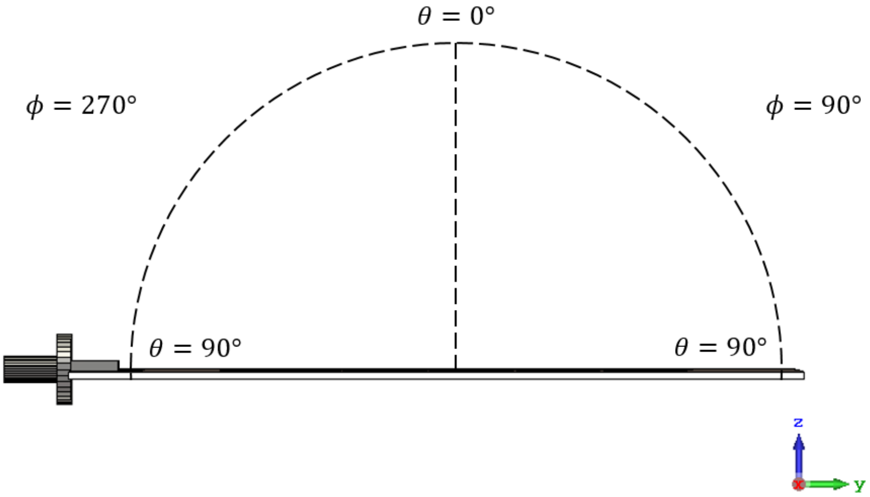

Figure 3.9. Diagram of far-field radiation pattern data extraction (antenna side view).

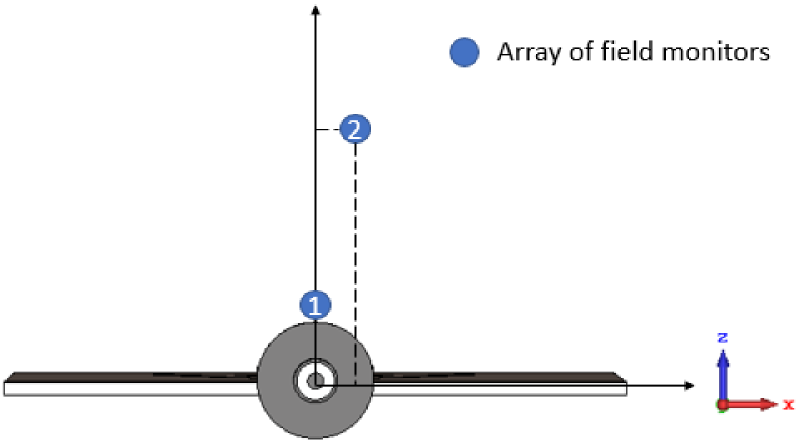

Figure 3.10. Diagram of field monitors in near-zone *E*-field data extraction (view from the negative *y*-direction of the antenna).

The near-zone in this research is defined as the area from $0.12\lambda_0$ above the metallic cell surface to λ_0 from the metallic cell surface. The reason is that the *E*-field right on the metallic cell shows spikes and very large values, as shown in Figure 3.11. It can be seen that the *E*-field values are zero where the metallic cells are located. Those *E*-field values have a very strong pattern as zeros indicate the position of the metallic cells. Such a strong pattern will be studied by the neural network model, and this will reduce the learning effectiveness and cause error prediction. In the case of noise existing in the prediction, the predicted *E*-field may not be exact zeros at the positions of metallic cells. The neural network will not consider them as metallic cells. Therefore, the on-surface *E*-field is avoided when preparing the near-zone *E*-field data. The $0.12\lambda_0$ above the metallic cell surface is considered as an appropriate level to extract the *E*-field data, as shown in Figure 3.12. In Figure 3.12, the near-zone *E*-field does not show a strong pattern with the position of metallic cells. And the value range is more reasonable than the on-surface case. On the other hand, the near-zone is limited by the height level of λ_0 from the surface as it is the transition zone between near-field and far-field.

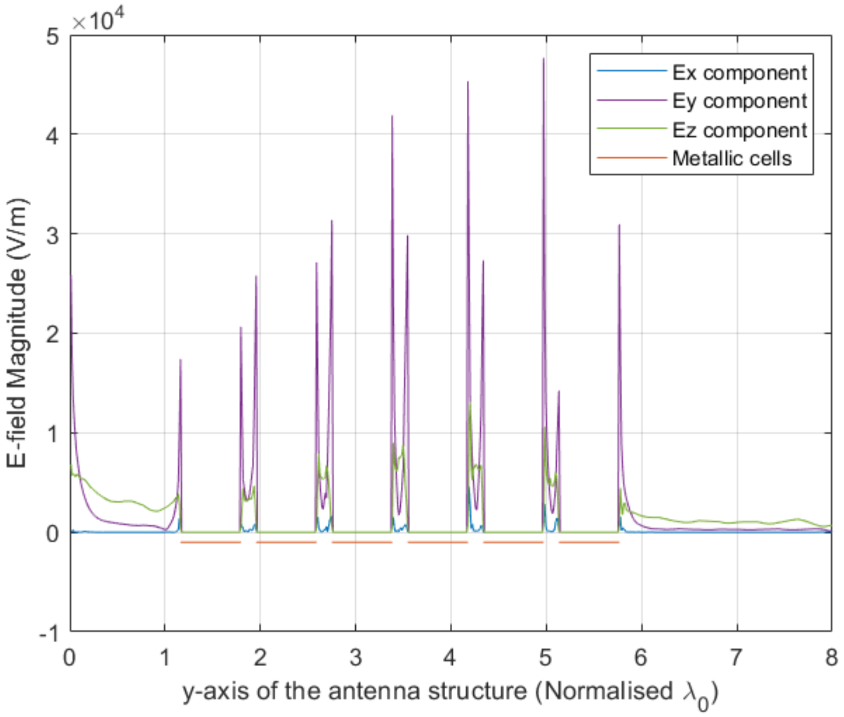

Figure 3.11. E_x, E_y and E_z components on the metallic cells.

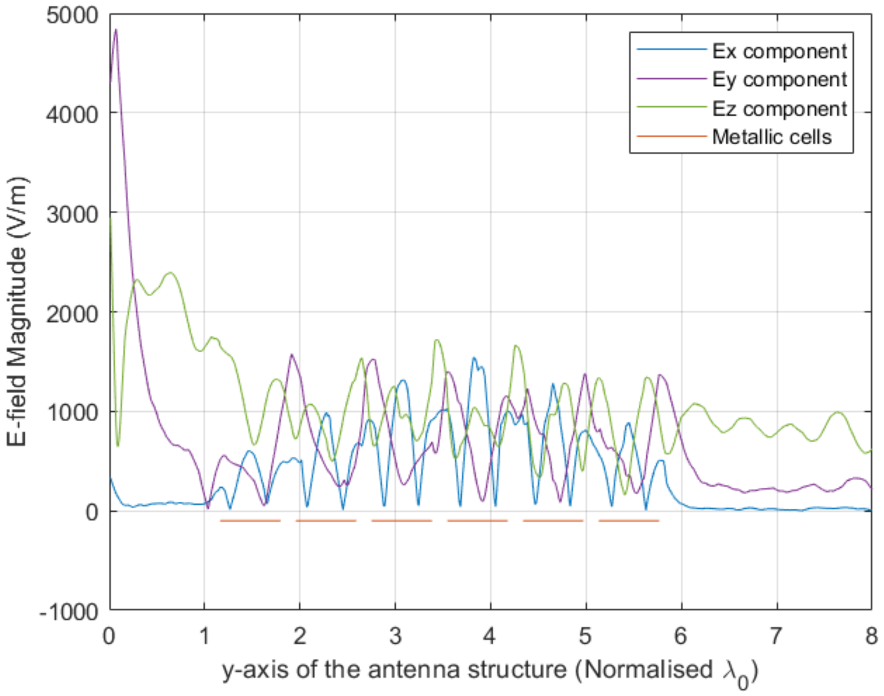

Figure 3.12. E_x, E_y and E_z components on the line at (0, y, $0.12\lambda_0$).

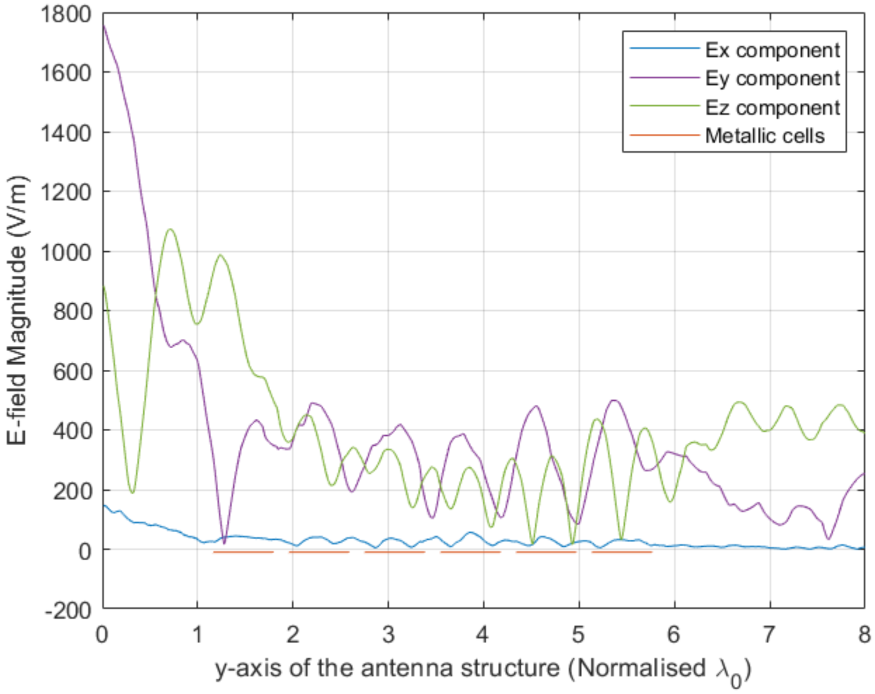

Figure 3.13. E_x, E_y and E_z components on the line at ($0.12\lambda_0$, y, $0.5\lambda_0$).

Figure 3.13 shows the three components of the near-zone *E*-field on the line at ($0.12\lambda_0$, y,$0.5\lambda_0$). There is no such strong pattern regarding the metallic cell distributions. The value of E_x is relatively small compared with E_y and E_z components. However, the variation at metallic cells positions can be observed, which implies the relationship between the metallic cell and the near-zone *E*-field. Therefore, when preparing the near-zone *E*-field data, two arrays of field monitors are placed at positions 1 and 2 along the *y*-axis direction of the surface wave antenna. Position 1 is located on the line at (0, y, $0.12\lambda_0$) and position 2 is located on the line at ($0.12\lambda_0$, y, $0.5\lambda_0$). Each array extracts the magnitude of the E_x, E_y and E_z components of the near-zone *E*-field with the step size of 0.1 mm. The correlation factors of E_x, E_y and E_z components of positions 1 and 2 are 0.0352, 0.1923 and 0.5497, which means the *E*-field of the two positions does not have a strong correlation. Training data with strong correlation is considered as the same data to the neural network model. The training will become inefficient when strong correlation data are used. Therefore, positions 1 and 2 can be regarded as appropriate positions to extract the data. More positions of the arrays will be applied to investigate the effect on prediction performance in the next chapter.

In terms of the size of the near-zone E-field data, each array of the near-zone E-field data is a 3×700 matrix. Combining the arrays of two positions, the training data of the near-zone E-field becomes the 6×700 matrix. Before feeding the E-field and far-field radiation pattern data into the neural network model, all of the input data are normalised between 0 and 1 by using MinMaxScaler to accelerate the training speed. The equation of the MinMaxScaler can be expressed as

$$x_n = \frac{x - X_{min}}{X_{max} - X_{min}} \tag{3.24}$$

Where the x is the original input data and x_n denotes the scaled input data. X_{max} and X_{min} are the maximum and minimum values of the input data.

After the training, the first two rows of the 6×700 matrix of the near-zone E-field data is fed to the metallic cell pattern Bi-GRU model to predict the metallic cell pattern on the upper surface of the antenna.

3.2.5 Evaluation methods

The evaluation of the prediction accuracy is important to neural network prediction. It is a measure to evaluate the performance of the neural network model. In this section, different evaluation methods will be introduced. It is worth mentioning that the test labels are the observed standard values. In this research, the test labels are generated by CST simulation software. In evaluation, the assessment is performed by calculating and evaluating the difference between the predicted results and the test labels.

In the prediction of the near-zone E-field, the prediction accuracy is described by the percentage error, which is given by

$$percentage\ error = \frac{1}{n}\sum_{i=1}^{n}\frac{|y_i - \hat{y}_i|}{y_i} \tag{3.25}$$

Where y_i are the observed standard values (test labels), $\hat{y}_i$ are the predicted values and n is the total number of data points.

The Bi-GRU model utilised in defining the relationship between far-field radiation pattern and near-zone E-field can be considered as a regression problem. Therefore, the evaluation is more complex than the classification problem. In order to perform a comprehensive assessment, four different evaluation methods are initially introduced to assess the performance of the Bi-GRU neural network model. The four evaluation methods are mean squared error (MSE), correlation factor (CF), R-squared (R^2) and fidelity (cross-correlation, CR). In (3.26 to (3.29, the far-field radiation pattern observed standard values are known as test labels. The predicted values are the far-field radiation pattern data transformed from the near-zone E-field predicted by the Bi-GRU neural network model.

MSE measures the average of the squared error in statistics, which are the average squared difference between the estimated values (predicted) and the observed standard values (test labels).

$$MSE = \frac{1}{n}\sum_{i=1}^{n}(y_i - \hat{y}_i)^2 \tag{3.26}$$

Where y_i are the observed standard values (test labels), $\hat{y}_i$ are the predicted values and n is the total number of data points.

In statistics, the CF is a measure of linear correlation between two sets of data as it reflects the strength and direction of the linear relationship. It is the ratio between the covariance of the two variables and the product of their standard deviations. The range of correlation factor is between -1 and 1, where 1 and -1 mean the strong linear relationship and 0 means no linear relationship.

$$CF = \frac{\sum(x_i - \bar{x})(y_i - \bar{y})}{\sigma(x)\sigma(y)} \tag{3.27}$$

Where y_i and x_i are the values of observed standard values and predicted values respectively. $\bar{y}$ and $\bar{x}$ are the mean values of observed standard values and predicted values respectively. σ denotes the standard deviation calculation.

The R^2, also known as the coefficient of determination, is a statistical measure of fit that indicates how much variation of a dependent variable is explained by the independent variable in a regression model. In this prediction case, it is the proportion of the variation in the standard dataset that is predicted from the neural network model. The range of the R^2 value is $(-\infty,1]$. When R^2 is 1, it means the prediction is 100% correct. Most of the prediction model has R^2 in the range [0,1]. The negative R^2 indicates the model is valueless and the prediction result is not acceptable.

$$R^2 = 1 - \frac{\sum_{i=1}^{n}(\hat{y}_i - y_i)^2}{\sum_{i=1}^{n}(\bar{y}_i - y_i)^2} \tag{3.28}$$

Where y_i are the observed standard values, $\hat{y}_i$ are the predicted values, $\bar{y}$ are the mean values of the observed standard values and n is the total number of data points.

The fidelity, also known as cross-correlation, refers to the similarity of two series as a function of the displacement of one relative to the other. The fidelity is similar in nature to the convolution of two functions. The normalisation is applied to have the value scaled.

$$CR = \sum_{k=-\infty}^{\infty} x(k)y(n+k) \tag{3.29}$$

Where $x(k)$ denotes predicted values of the radiation pattern and $y(k)$ is the observed standard values of the far-field radiation pattern. And n is displacement, also known as lag.

3.3 Methodology of the metallic cell pattern prediction from near-zone *E*-field

The mathematical prediction models, consisting of Fourier, Gaussian and exponential equations, have been investigated to predict the metallic cell pattern before applying the neural network-based method. The mathematical prediction method is based on the curve fitting technique. The mathematical prediction model takes significant time to prepare the curve fitting data and it cannot be used to predict the case that contains two metallic cells spaced less than $0.069\lambda_0$ (0.6 mm). This will be discussed later in this section. Therefore, a neural network-based method is expected to tackle the prediction limitation problem of the mathematical prediction model. Prior to using Bi-GRU neural network model to predict the metallic cell pattern, the multi-layer perceptron (MLP) classifier neural network model is tried. However, the MLP classifier cannot give an accurate prediction since it cannot consider the surface wave propagation and reflection effect. Therefore, the Bi-GRU is chosen as an appropriate neural network prediction model to undertake the prediction of metallic cell pattern from the near-zone *E*-field.

In this section, the mathematical prediction models and the MLP classifier will be discussed to explain why they cannot be used in the prediction of the metallic cell pattern. Then the methodology of the implementation of the Bi-GRU neural network model to predict the metallic cell pattern from the near-zone *E*-field will be introduced. This Bi-GRU model structure is the same as the one used in the near-zone *E*-field prediction but the input layer. The neural network model structure, training setting and data preparation are similar to the Bi-GRU model used in near-zone *E*-field prediction and will be covered in this section.

3.3.1 Mathematical prediction model and multi-layer perceptron classifier

In this section, the implementation and the results of the mathematical prediction models and MLP classifier will be briefly introduced and presented. The detailed methodology and results of the mathematical prediction models will be presented in Appendix B. The reason why the mathematical prediction model and MLP classifier are not suitable for predicting the metallic cell pattern will be analysed.

3.3.1.1 Mathematical prediction models

Building the relationship between metallic cell pattern along the *y*-axis of the antenna and on-surface *E*-field by using mathematical models was the initial idea before applying the neural network model to predict the metallic cell pattern of the antenna. The main idea is to apply the curve fitting tools to the on-surface *E*-field by using Fourier, Gaussian and exponential equations. The mathematical prediction models can describe the on-surface *E*-field under different antenna designs and frequencies given the metallic cell position as input. The mathematical prediction models focus on 1) the relationship between the on-surface *E*-field magnitude and the metallic cells position and 2) the relationship between the on-surface *E*-field phase and the metallic cells position. Once the mathematical prediction models are derived, the magnitude and phase of the on-surface *E*-field can be predicted using the position of the metallic cells. The other way round, the position of the metallic cells can also be obtained by the mathematical prediction models using the magnitude and phase of the on-surface *E*-field.

In the mathematical prediction models, the proposed surface wave antenna is utilised to provide the simulation results of the on-surface *E*-field data. By setting an array of field monitors at the height of $0.012\lambda_0$ (0.1 mm) above the cells along the *y*-axis, the magnitude and phase of the on-surface *E*-field of the surface wave antenna are extracted from CST. When the wave propagates through the surface, the magnitude and phase of the *E*-field have different changing patterns at different positions relative to the cell. This variation pattern through each cell can be divided into four zones, which are enter zone, cell zone, exit zone and surface wave (SW) zone. The magnitude and phase of the *E*-field show the regular and periodic changing patterns when the wave propagates through the metallic cell. The *E*-field variation in the four zones is studied by using different orders of Fourier, Gaussian and exponential mathematical prediction models. (3.30, (3.31 and (3.32 show the first order of the Fourier, Gaussian and exponential mathematical prediction model.

$$f(x) = a_1 + a_2\cos(wx) + a_3\sin(wx) \tag{3.30}$$

$$g(x) = b_1 e^{-(\frac{x-b_2}{b_3})^2} \tag{3.31}$$

$$h(x) = c_1 e^{c_2 x} \tag{3.32}$$

Where a_1, a_2, a_3, w, b_1, b_2, b_3, c_1 and c_2 are the mathematical prediction model parameters.

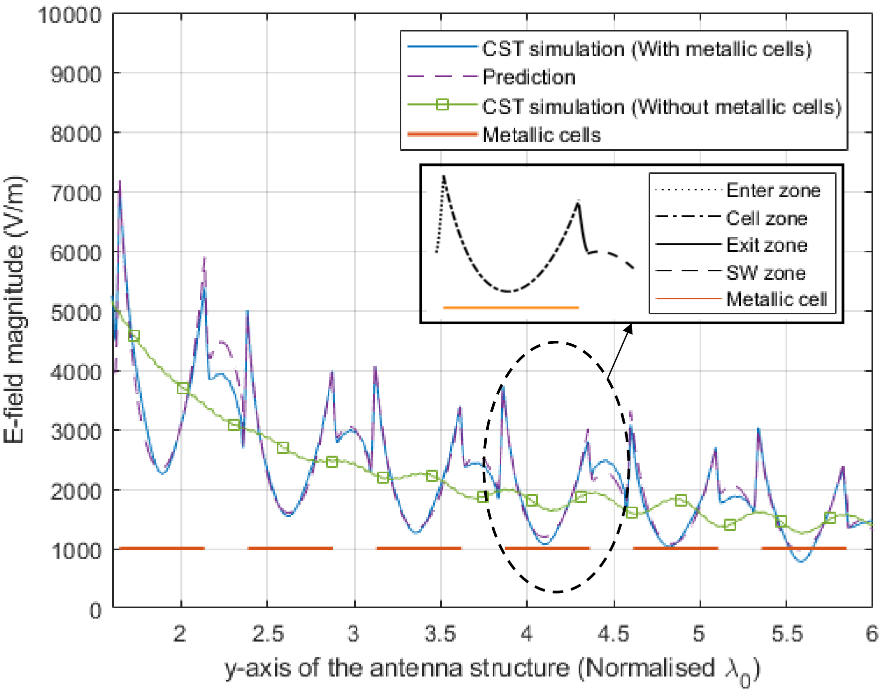

Figure 3.14. Magnitude comparison between prediction and CST simulation at 34.5 GHz.

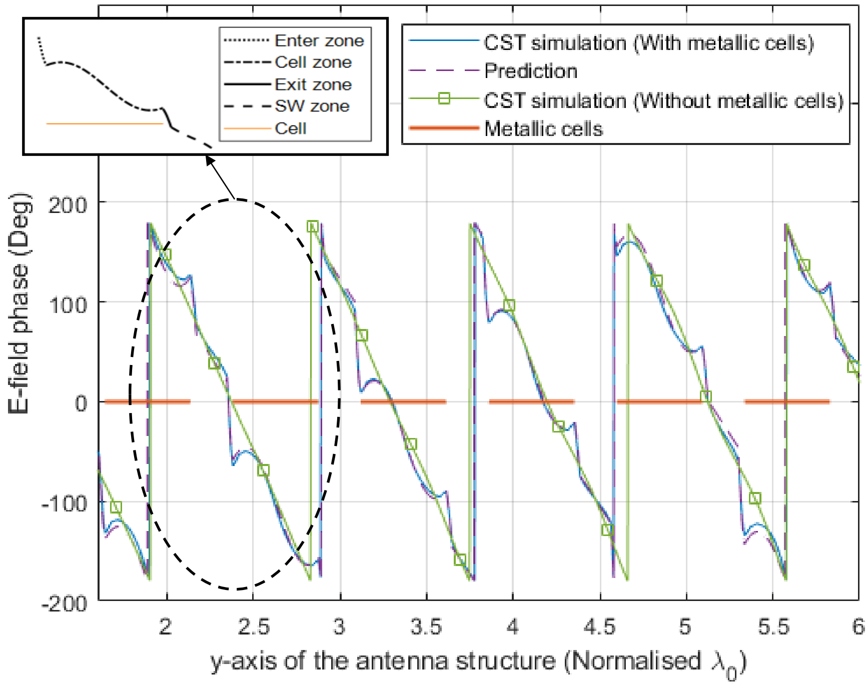

Figure 3.15. Phase comparison between prediction and CST simulation at 34.5 GHz.

The comparisons of magnitude and phase of the *E*-field at 34.5GHz are shown in Figure 3.14 and Figure 3.15 respectively. The magnitude and phase of the surface wave without the cells are also presented in the figures for comparison; the variation of magnitude and phase in the four zones can then be easily observed. In Figure 3.14, the magnitude has a sudden rise in the enter zone and has a drop in the exit zone. In the surface wave zone, the magnitude tends to follow the changing trend of the magnitude of the surface wave launcher structure. In Figure 3.15, the phase increases in the enter and exit zone. While in the surface wave zone, the phase velocity is getting close to the phase change of standard surface wave. In this prediction, a span of 1 GHz bandwidth, which is similar to the operating frequency band of the mmWave VLR, is chosen to evaluate the prediction performance. The averaged error of magnitude and phase prediction from 0 to 6λ_0 along *y*-axis are shown in

Figure 3.16. The prediction error of magnitude is 4.62%, while the phase prediction error is 4.6º at 34.5GHz.

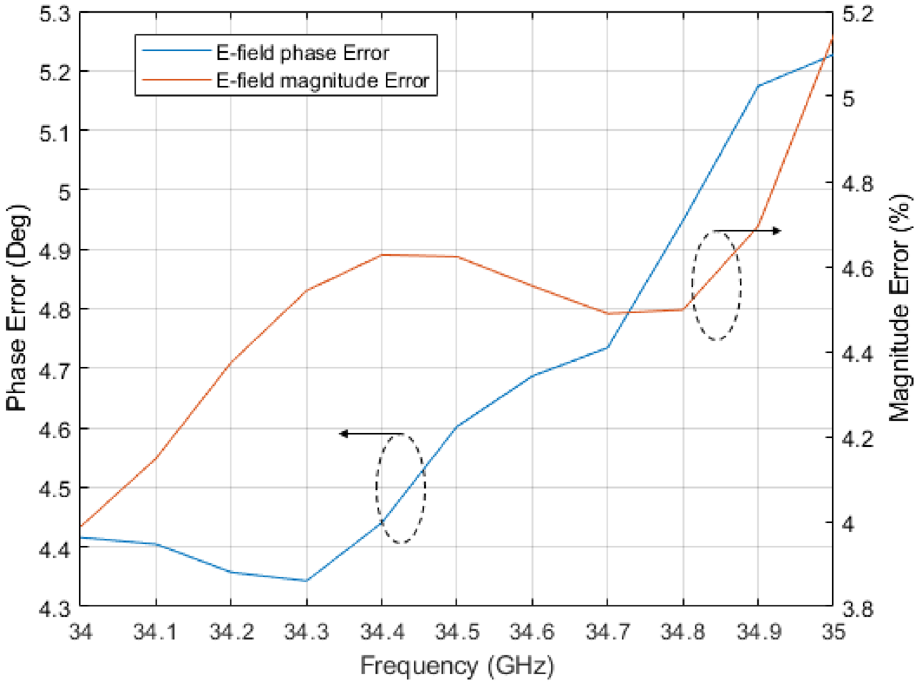

Figure 3.16. Prediction error of the Mathematical prediction model.

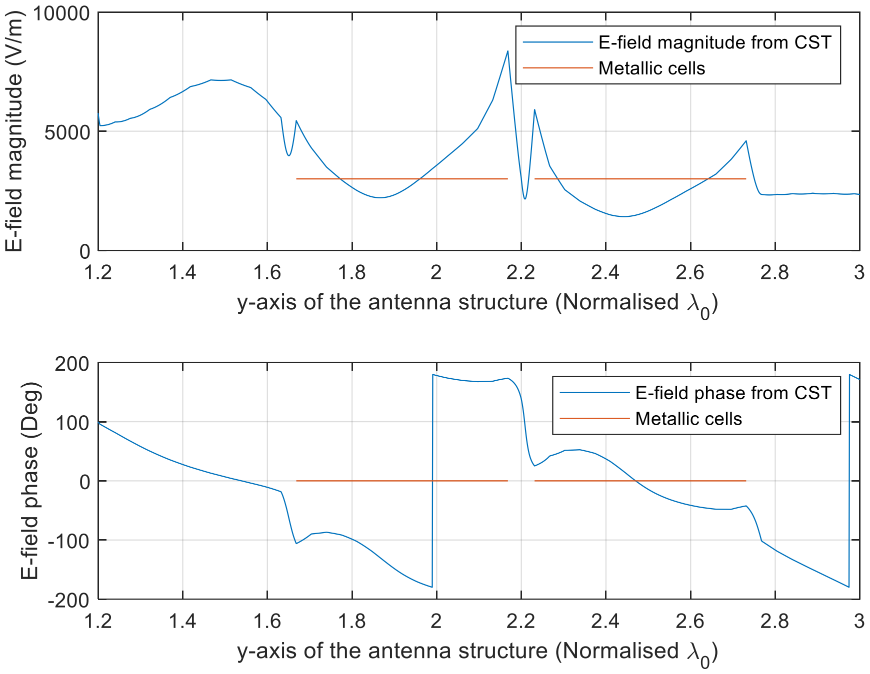

Figure 3.17. The *E*-field magnitude and phase of the antenna with 0.069λ_0 spacing between two metallic cells.

The prediction results of the magnitude and phase approve the effectiveness of the mathematical prediction models working on the *E*-field prediction of the antenna structure with constant periodic metallic cells distribution. However, the limitation of the mathematical prediction models is that the spacing between two adjacent metallic cells should be larger than 0.6mm (0.069λ_0). Otherwise, the exit and SW zone of the former metallic cell and the enter zone of the latter metallic cell will be overlapped. Once overlapped, the derived equations of the changing pattern do not exist anymore. As shown in the magnitude case in Figure 3.17, the changing pattern between the first and the second metallic cell does not follow the derived changing pattern and this change becomes unpredictable. On the other hand, the *E*-field prediction should not be limited to the cases with the constant period distribution of the metallic cells. More possibilities such as gradual increasing, gradual decreasing and random distribution of the metallic cells need to be predicted. A neural network-based prediction method can extract and study the features of the data with irregular metallic cell patterns and give an accurate prediction. Therefore, the neural network prediction model becomes a possibility to predict the *E*-field. The first attempted neural network model is the MLP classifier due to its simple structure.

3.3.1.2 Multi-layer perceptron classifier

The MLP classifier is utilised before using the Bi-GRU prediction model to predict the metallic cell pattern. Compared to the Bi-GRU neural network model, all the hyperparameters of the MLP classifier are defined by the sklearn library in python [122] and are easy to tune by changing the value directly.

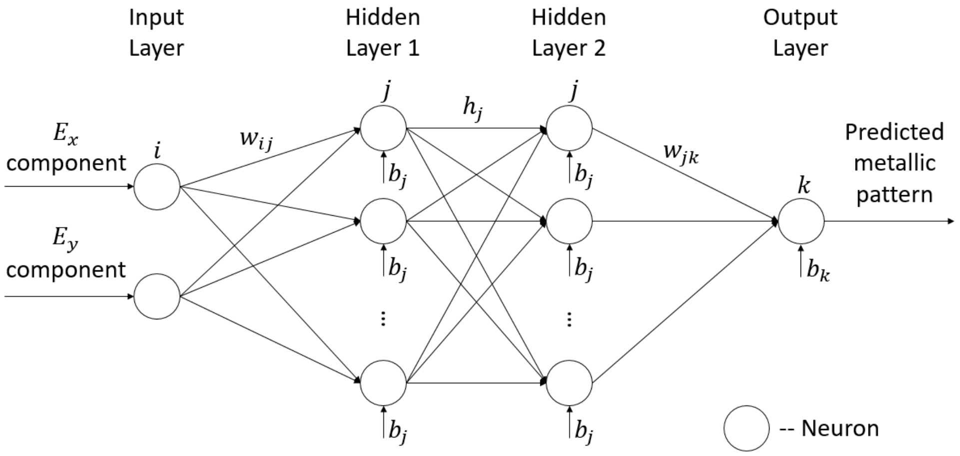

Figure 3.18. The diagram of the MLP classifier.

As shown in Figure 3.18, the number of hidden layers of MLP is two and each layer contains 256 hidden neurons. The near-zone *E*-field is served as the input to the MLP classifier. In the MLP classifier, the near-zone *E*-field data is extracted for an array of field monitors placed on the line at (0, *y*, 0.12λ_0). Each array extracts the magnitude of the E_x and E_y components of the near-zone *E*-field with the step size of 0.1 mm. And the data size of the near-zone *E*-field is 2×700. The metallic cell patterns data of the antenna model is converted to binary numbers as the training label to the MLP classifier, where 1 is metal and 0 denotes no metal. And the data size of the metallic cell pattern training label is 1×700. The activation function for the hidden layer is the logistic function. The solver is set as lbfgs, which is an optimiser in the family of quasi-Newton methods. This optimiser approximates the inverse of the Hessian matrix to perform parameter updates. It can converge faster and perform better for small datasets (thousands of training samples). MLP classifier uses hyperparameter alpha for regularisation, which helps in avoiding overfitting by penalising weights with large magnitudes. In this simulation, the alpha is set as 0.0001. The initial learning rate is 0.005 and the learning rate mode is set as adaptive, which means the learning rate keeps the initial learning rate as long as the training loss keeps decreasing. Each time two consecutive epochs fail to decrease training loss by the optimisation tolerance value (0.0001), the current learning rate is divided by 5. The maximum number of iterations is 300. The solver iterates 300 times or until convergence, which is defined as the loss is not improving by the optimisation tolerance. The random state is set as 1 to determine random number generation for weights and biases initialisation. The hyperparameters of this MLP classifier are listed in Table 3.3.

Table 3.3. The hyperparameters of the MLP classifier.

Hyperparameter	**Value**	**Hyperparameter**	**Value**
Hidden Layer	2	Hidden Neuron	256
Solver	lbfgs	alpha	0.001
Initial learning rate	0.0005	Learning rate mode	Adaptive
Optimisation tolerance (tol)	0.0001	Maximum number of iterations	300
Random state	1	Activation	logistic

During the training stage, the weights and biases are updated. In terms of the loss, MLP uses cross-entropy for classification problems, as shown in

$$\varepsilon = -yln\hat{y} - (1-y)\ln(1-\hat{y}) + \alpha\left|\left|W\right|\right|_2^2 \tag{3.33}$$

Where the $\alpha\left|\left|W\right|\right|_2^2$ is the regularisation term. y are the observed standard values and $\hat{y}$ are the predicted values.

Starting from initial random weights and biases, the MLP classifier minimises the loss function by repeatedly updating weights. After computing the loss, a backward pass propagates it from the output layer to the previous layers, providing each weight parameter with an update value to decrease the loss. For binary classification, the logistic activation function passes through weights and biases to obtain output values between zero and one. A threshold of 0.5 is assigned samples of outputs larger or equal 0.5 to the positive class, and the rest to the negative class. The training stops when it reaches the maximum number of iterations or when the improvement in loss is below the optimisation tolerance.

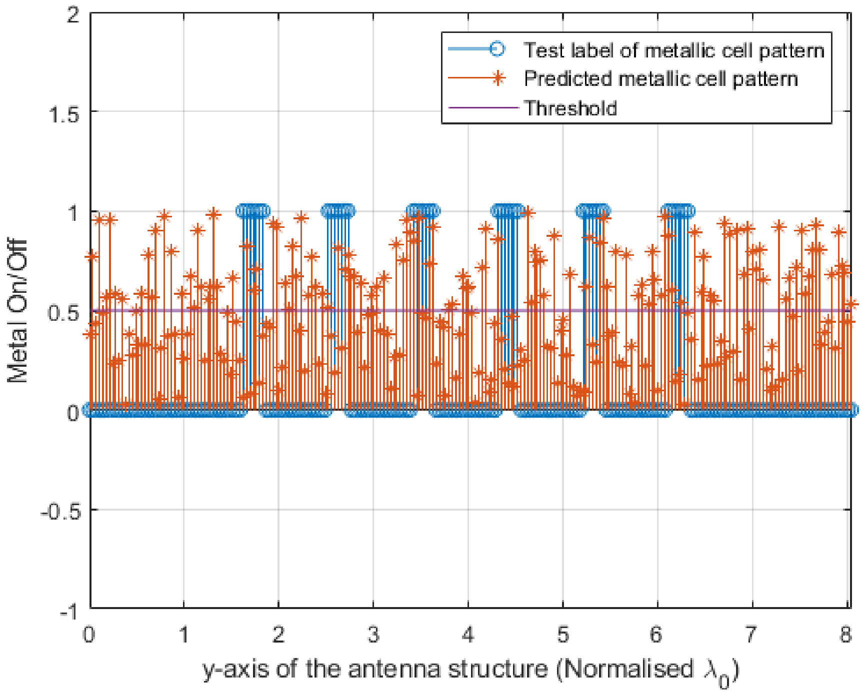

Figure 3.19. MLP classifier metallic cell pattern prediction result.

In Figure 3.19, the predicted metallic cell pattern is labelled in orange asterisks. The blue circle markers are the test labels, which are the standard metallic cell pattern of this antenna extracted from CST simulation software. The *y*-axis metal on/off is the binary number of the metallic cell pattern where on (1) indicates metal and off (0) is no metal. The predicted values are not overlapped with the test label of the metallic cell pattern. It is obvious that the MLP classifier fails to predict the metallic cell pattern as most of the data points are wrongly predicted.

In MLP classifier prediction, the input consists of E_x and E_y components of the near-zone E-field. The MLP only consider the magnitude of E_x and E_y as the factors when predicting the metallic cell pattern. Figure 3.20 shows the metallic cell pattern along the *y*-axis of the antenna and the corresponding E-field components. The position index stands for the distance from the surface wave launcher in the antenna design, where the unit is mm. The MLP classifier independently predicts the metal on and off of every single grid without considering the effect of the adjacent grids. For example, if the *E*-field value at the first grid is the same as the one at the last grid, the MLP classifier would output the same metallic cell pattern prediction result. However, the metallic status (on or off) at the different positions can be different even with the same E_x and E_y value.

In reality, the propagation and reflection effect of the surface wave needs to be considered since the adjacent grids will affect the *E*-field of each other. The metallic cell pattern may not be the same even with the same *E*-field value as the position of the metallic cell pattern is another essential factor to the prediction. In this case, the *E*-field components have to be considered as a sequential input. Therefore, the MLP classifier is not feasible for this prediction problem. The Bi-GRU neural network model has memory units, which are used to keep the previous state of the neuron. And its bidirectional characteristic considers the propagation and reflection of the surface wave above the substrate. The Bi-GRU neural network model considers the metal status of every grid due to its sequential characteristic when prediction, as shown in Figure 3.21. Therefore, the Bi-GRU neural network model is suitable for tackling this problem.

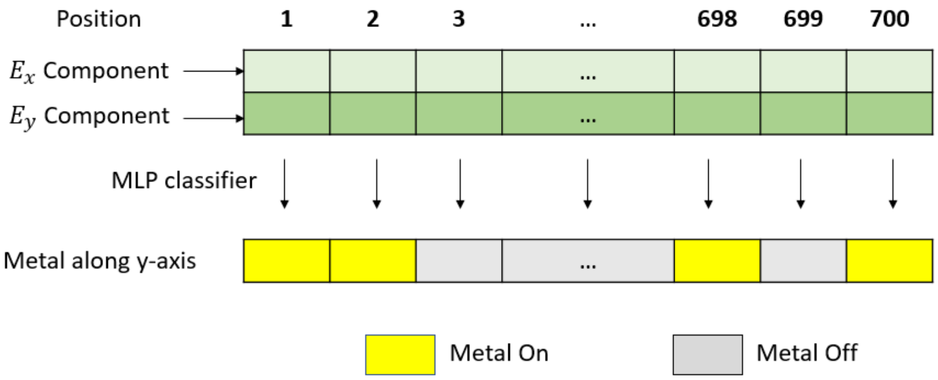

Figure 3.20. Diagram of metallic cell pattern prediction of the MLP classifier.

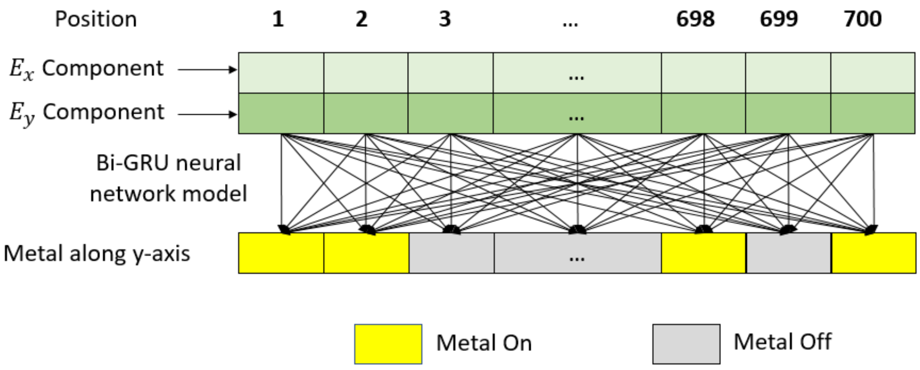

Figure 3.21. Diagram of metallic cell pattern prediction of the Bi-GRU neural network model.

3.3.2 Neural network model structure of the metallic cell pattern prediction

The mathematical prediction model and the MLP classifier are proved to be not suitable for the metallic cell pattern prediction. Therefore, the Bi-GRU is chosen to predict the metallic cell pattern since it considers the wave propagation and reflection effect. The training structure of the metallic cell pattern prediction Bi-GRU model is shown in Figure 3.22. It consists of one input layer, two Bi-GRU layers and one output layer. There are two input neurons in the input layer, which are the E_x and E_y components. And these two neurons are fully connected to the first Bi-GRU layer to compute the state of the neurons. There are 256 GRU cells in each Bi-GRU layer and one output neuron in the output layer. The output neuron will output binary value 0 or 1 to indicate the metallic cell pattern on the antenna surface.

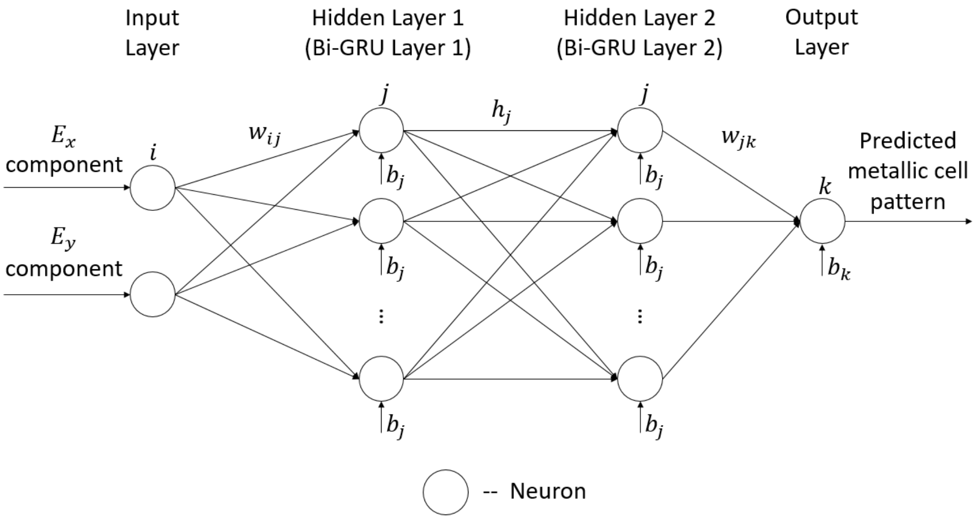

Figure 3.22. The diagram of the proposed Bi-GRU model for metallic cell pattern prediction.

3.3.3 Neural network model training of the metallic cell pattern prediction

This Bi-GRU neural network model training setting is similar to the Bi-GRU model used in near-zone *E*-field prediction. In the metallic cell pattern prediction model, as shown in Figure 3.22, the hyperparameter bidirectional in the algorithm is set as ‘True’ in this model. The training process follows the procedures from (3.17 and (3.23. These computations are repeated and iterated for 300 epochs or until the acceptable loss is achieved. In the metallic cell pattern prediction, the acceptable loss is defined as the loss difference of two consecutive epochs being less than 5% for ten epochs. The output of (3.20 is in the range 0 to 1, which can be rounded up and down to describe whether there is a metallic cell or not.

3.3.4 Data preparation of the metallic cell pattern prediction

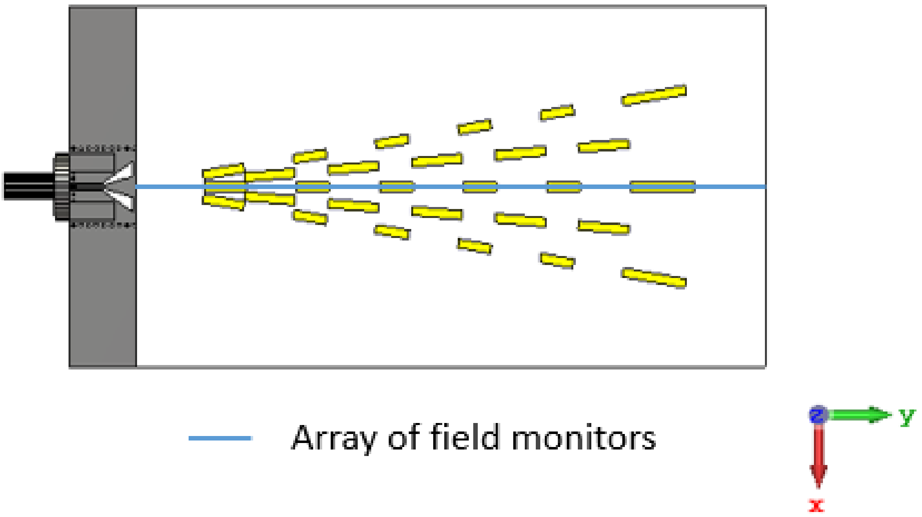

Figure 3.23. Diagram of the array of field monitors in near-zone *E*-field data extraction (antenna top view).

Since Rows 1, 3 and 5 are the same and the position relationship between Row 3 and Row 2 is known, the distribution of the metallic cells on the surface can be confirmed by the distribution of the central row of cells. Therefore, the prediction of the metallic cell pattern focuses on the line along the *y*-direction. The line, 70 mm in length, starts from the aperture of the SWL and ends at the far end of the substrate, as indicated in the blue line in Figure 3.23.

In the data preparation of the metallic cell pattern prediction, the training datasets consist of the near-zone *E*-field and the metallic cell pattern data. The metallic cell pattern acts as the training label. The number of the training datasets are 5000. An array of field monitors is placed on the line at (0, *y*, $0.12\lambda_0$). This field monitor array is the same as the array set in position 1 in Figure 3.10. However, only the magnitudes of the E_x and E_y components of the surface wave antenna are used. The data extraction step size is 0.1 mm. Before feeding the *E*-field data into the neural network model, the MinMaxScaler in (3.24 pre-processes the data extracted from CST to accelerate the training. The size of the input training data is a 2×700 matrix.

In terms of the metallic cell patterns of the antenna model, they are converted to binary numbers as the training label where 1 is metal and 0 denotes no metal. And the data size of the training label is 1×700. The difference in matrix size implies the Bi-GRU neural network model builds a mapping relationship from near-zone *E*-field to the metallic cell pattern, considering the effect of the propagation and reflection of the surface wave.

3.4 Summary

In this chapter, the details of the proposed novel method of using the neural network method to design cosecant-squared radiation pattern surface wave antenna have been introduced. The method is mainly divided into two prediction parts, which are from the far-field radiation pattern to near-zone *E*-field and from near-zone *E*-field to metallic cell pattern on the surface. The flowchart of the proposed method has been shown. The methodology of how to implement the neural network models has been introduced in detail, including the prediction model structure, training setting and data preparation. In the next chapter, the prediction results of both parts will be presented. The factors that affect the performance of the prediction of both parts will be discussed in detail. In Chapter 5, according to the requirement of the mmWave VLR, a cosecant-squared radiation pattern will be the input to the neural network models to predict the metallic cell pattern of the antenna. The predicted metallic cell pattern will be 3D-modelled into the surface antenna structure in CST. The EM simulation results regarding the S_{11}, efficiency and far-field radiation pattern will be presented. The fabricated antenna prototype will be validated in the anechoic chamber.

4 Simulation results and discussion

In this chapter, the electromagnetic (EM) simulation results of the coplanar surface wave launcher (SWL) will be presented. And the prediction results of near-zone *E*-field and on-surface metallic cell patterns predicted by the proposed neural network-based method will be presented. The results and discussion in this chapter are divided into three sub-sections, and in each sub-section, the results will be shown first and the discussion regarding the results will be covered.

4.1 Coplanar surface wave launcher

The coplanar SWL plays a vital role in the proposed surface wave antenna. In this section, the simulated S_{11} and efficiency of the SWL will be presented. The angular range on the azimuth plane of the launcher is essential for deciding the angle separation between the radial metallic cell rows. Therefore, the angular range investigation of the surface wave will be discussed through the analysis of the on-surface *E*-field. In the proposed surface wave antenna, five radial rows of metallic cells are designed to lower the fluctuation level and reduce the nulls in the radiation pattern. This will be proved and explained by comparing the S_{11}, on-surface *E*-field and far-field radiation pattern of a single metallic cell row and five metallic cell rows antenna respectively. In the EM simulation, the frequency domain solver is used to save the simulation time as producing the training datasets of the neural network takes a significant amount of time when using the time domain solver. The performance of different solvers will be presented and discussed through the comparisons of the same antenna.

4.1.1 S_{11} and efficiency of coplanar surface wave launcher

Inspired by [32] and the concept of the ground coplanar waveguide (GCPW) to substrate integrated waveguide (SIW) transition, the proposed SWL is designed to excite the surface wave, as shown in Figure 4.1. The SWL is printed on a piece of 0.787 mm thick microwave substrate Rogers RT5880 (ε_r = 2.2, tanδ = 0.009 at 10 GHz). The dimensions of the via hole diameter (d_{via}) and separation spacing (g_{via}) are 0.4 mm nad 0.45 mm respectively. The w_{pin} is decided by the K-connector in this design, which is 0.3 mm. The gap width of g_{pin} is 0.2 mm. The α_1 and α_2 are 40.4° and 19.3° respectively.

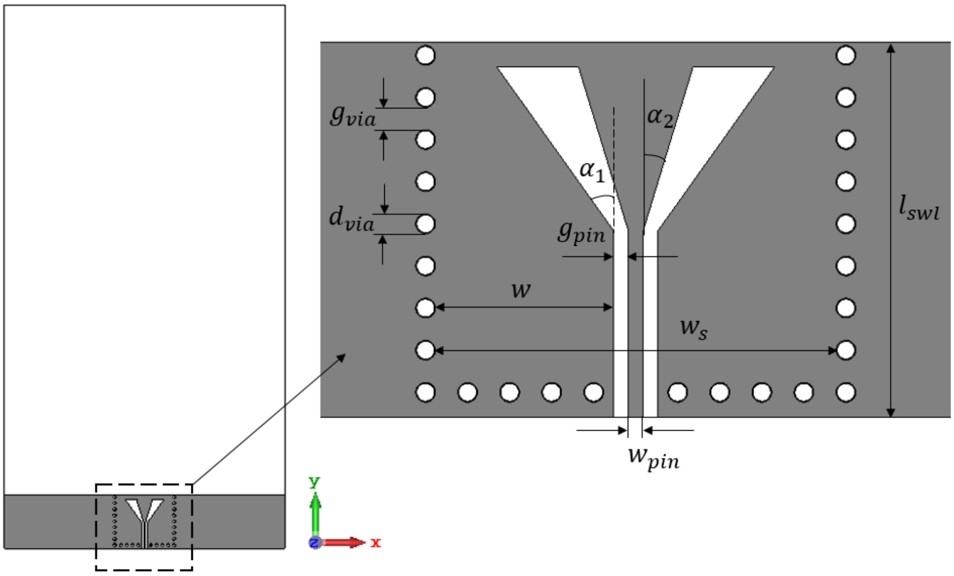

Figure 4.1. The proposed SWL (top view).

The EM simulation results of the S_{11} and the efficiency are shown in Figure 4.2 and Figure 4.3 respectively. The S_{11} shows the operating frequency of the coplanar SWL is 34.5 GHz with a bandwidth of 2.9%. The total efficiency and the radiation efficiency at the centre frequency are 94.2% and 94.4% respectively. Within the frequency band from 34 to 35 GHz, the total efficiency of the coplanar SWL is over 80.74%.

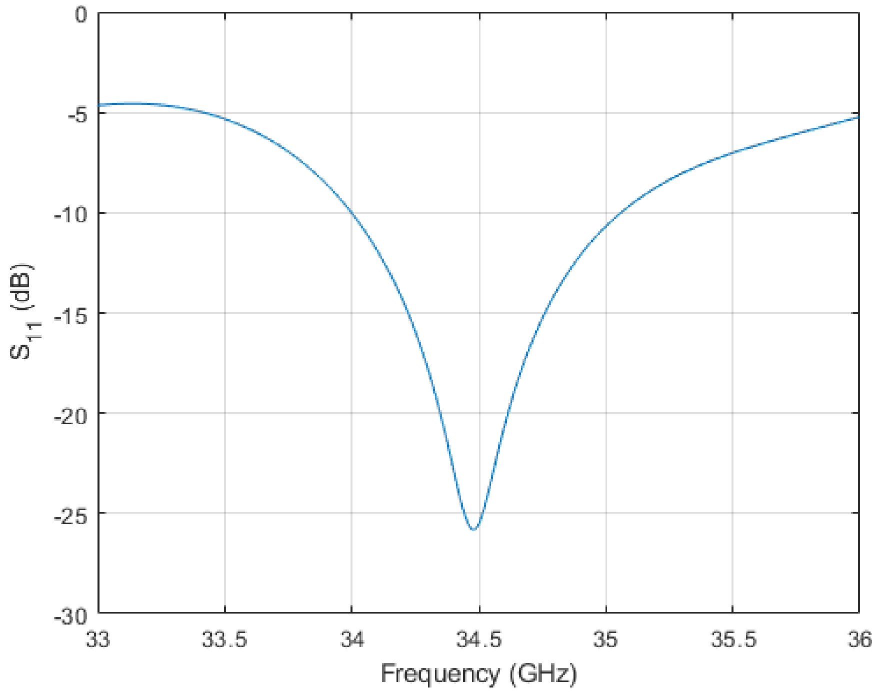

Figure 4.2. The S_{11} of the coplanar SWL.

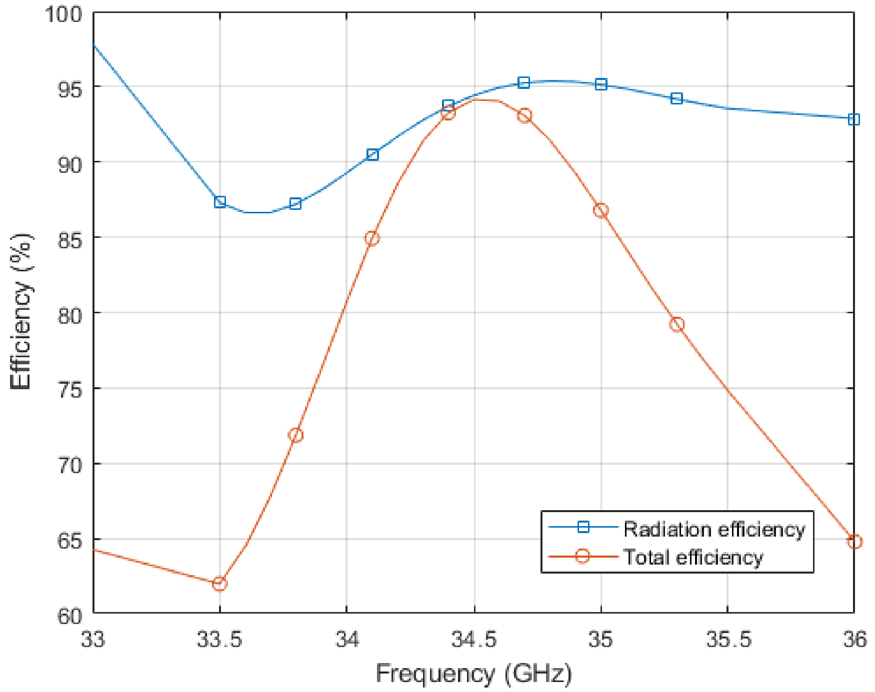

Figure 4.3. The radiation and total efficiency of the SWL.

4.1.2 Impedance matching of the surface wave launcher

As shown in Figure 4.1, a GCPW line is utilised in the proposed SWL. In the GCPW structure, the impedance is controlled by the thickness (h), effective dielectric constant (ε_{eff}) of the substrate and the ratio (k) of the width of metallic trace (w_{pin}) to the width of the track width plus the gaps (g_{pin}) either side [123] and is given by

$$Z_0 = \frac{60\pi}{\sqrt{\varepsilon_{eff}}} \frac{1}{\frac{K(k)}{K(\sqrt{1-k^2})} + \frac{K(k_1)}{K(k_1')}} \tag{4.1}$$

$$k = \frac{w_{pin}}{w_{pin} + 2g_{pin}} \tag{4.2}$$

$$k_1 = \frac{\tanh(\frac{\pi w_{pin}}{4h})}{\tanh(\frac{\pi(w_{pin} + 2g_{pin})}{4h})} \tag{4.3}$$

$$k_1' = \sqrt{1 - k_1^2} \tag{4.4}$$

Where h is the thickness of the substrate, ε_{eff} denotes the effective dielectric constant and K is the complete elliptic integral of the first kind.

The ratio k is the essential factor in determining the impedance of the GCPW transmission line. The K-connector used in the proposed surface wave antenna is air-dielectric and the impedance is 50Ω. Therefore, the impedance of the GCPW line should be evaluated to match the 50Ω of the K-connector. As the w_{pin} is decided by the connector, which is 0.3 mm. And the thickness and dielectric constant of the substrate are fixed. Therefore, the g_{pin} is the only adjustable factor in controlling the ratio k, which can be used to tune the impedance. The minimum value of g_{pin} is 0.1 mm due to the fabrication limitations. Figure 4.4 and Figure 4.5 show the magnitude and the real and imaginary part of the Z_{11} of the coplanar SWL under different ratios. Figure 4.6 shows the S_{11} of the coplanar SWL under different ratios. The case of k = 0.43 gives the Z_{11} of 49.4Ω and shows -25.83 dB S_{11} at 34.5 GHz. The ratio k = 0.43 suggests the optimal gap width g_{pin} with the value of 0.2 mm. Therefore, the gap width uses 0.2 mm in the proposed SWL.

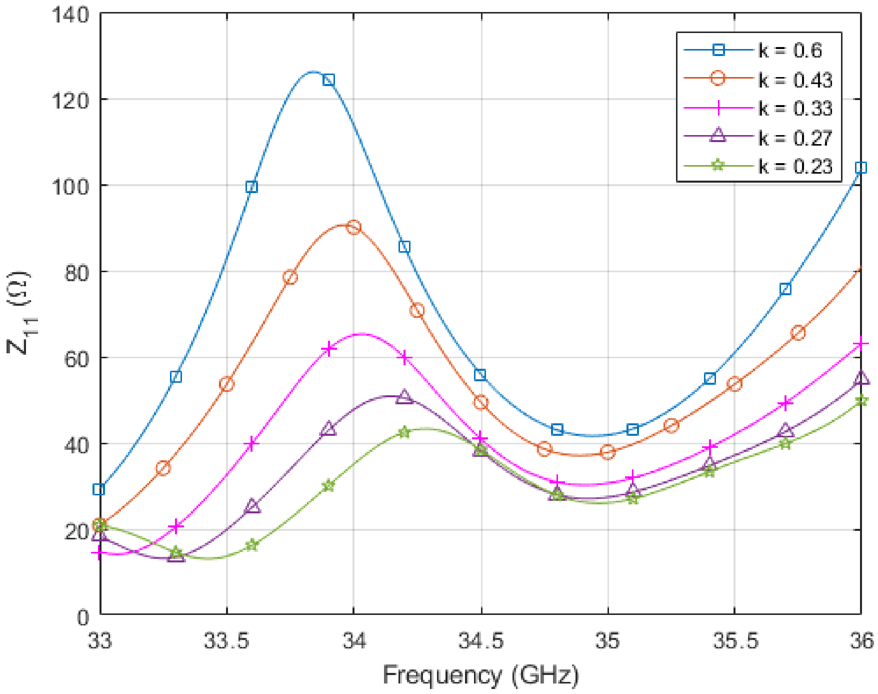

Figure 4.4. The Z_{11} magnitude of the coplanar SWL under different ratios k.

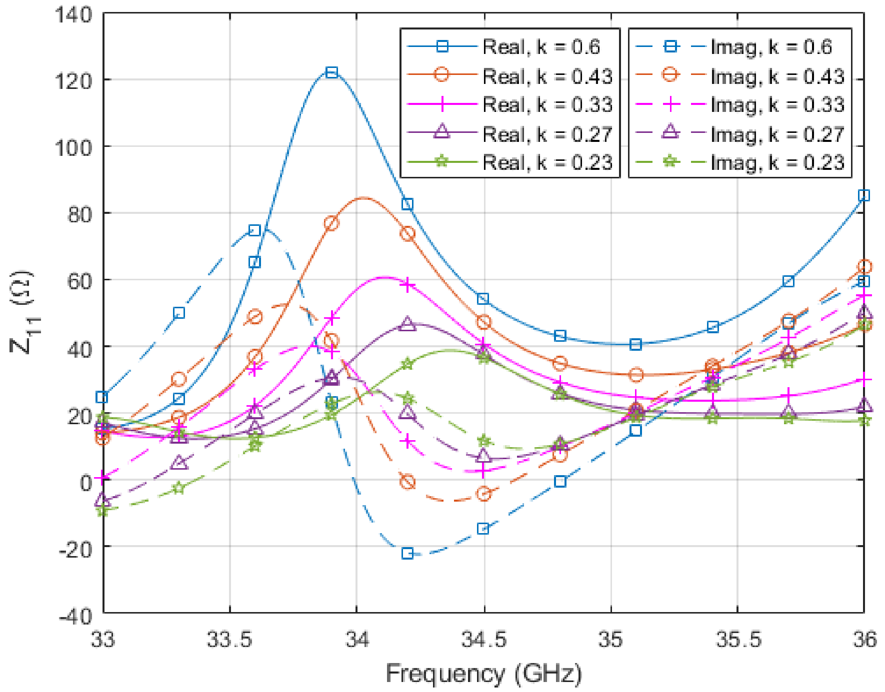

Figure 4.5. The real and imaginary part of Z_{11} of the coplanar SWL under different ratios *k*.

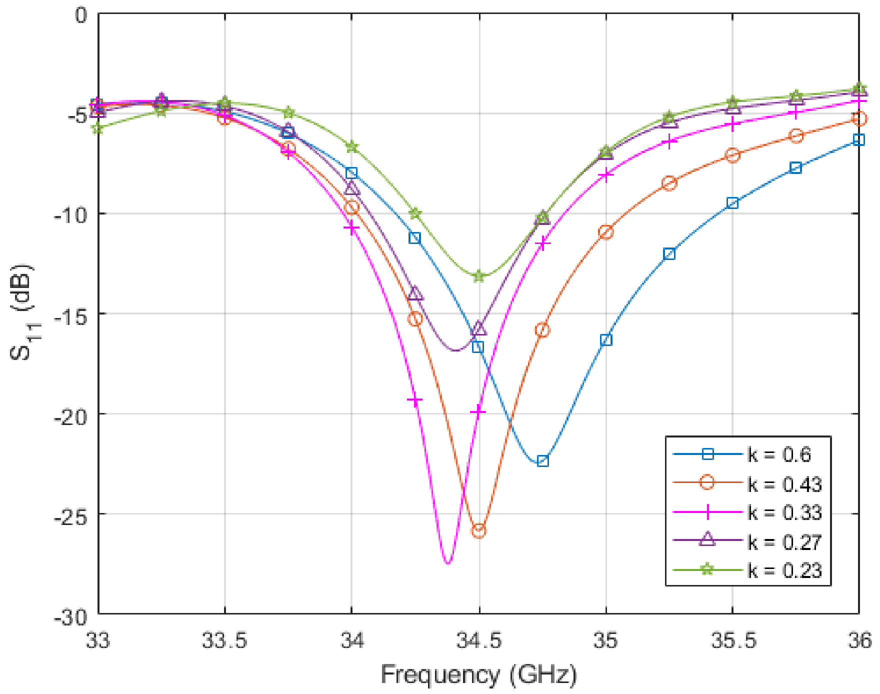

Figure 4.6. The S_{11} of the coplanar SWL under different ratios *k*.

4.1.3 EM simulation results of the proposed antenna

In this section, the on-surface *E*-field (0.1 mm above the top of the substrate surface) propagated from the coplanar SWL will be investigated. The main purpose of this investigation is to define the angular distribution of the metallic cells rows on the surface. The angular range is introduced and defined as the angular width between the points in which the maximum on-surface *E*-field level drops 10 dB. Therefore, the metallic cells located within the angular coverage of the coplanar wave launcher can scatter the surface wave to the free space effectively. The fast changing of the on-surface *E*-field causes significant fluctuation in the far-field radiation pattern. Surface wave antenna with five rows of metallic cells is investigated to demonstrate that the multi rows structure can provide a more gentle *E*-field change in the near-zone than the single row structure and will result in more stable cosecant-squared radiation pattern, which has less than 1 dBi variation, in the far-field. The on-surface *E*-field and far-field radiation pattern comparison of single row and multi rows structure will be provided.

4.1.3.1 The angular range of the coplanar SWL

Figure 4.7 shows the diagram of the angular range of the SWL. Figure 4.8 shows the corresponding on-surface *E*-field at 34.5 GHz of Figure 4.7. As mentioned, the on-surface *E*-field is defined as 0.1 mm above the substrate surface. The angle $\angle \mathrm{DOE}$ denotes the angular range of the proposed SWL. Due to the symmetric geometry of the surface wave antenna, the *E*-field magnitude of points D and E is the same. According to the angular range definition, i.e. the angular width in which the maximum on-surface *E*-field drops 10 dB from the point D', the angular range of the coplanar SWL ($\angle \mathrm{DOE}$) is found to be 51°. The *E*-field at point D is 10 dB less than the point D' on the line OB, where the OD' is the same as OD in length. Regarding the metallic cells design, all of the radial rows are located within the area of AOC to ensure that most of the surface wave can be scattered to the free space. Figure 4.9 shows the *E*-field on the line OA and OB. It can be observed that the *E*-field value of line OA is close to the value of line OB, and the mean difference is 0.52 dB. This indicated the 32º angular area of AOC can be used to accommodate the metallic cells. Therefore, the angular separation is chosen as 5º to make sure all the radial rows are located within the 32º angular coverage.

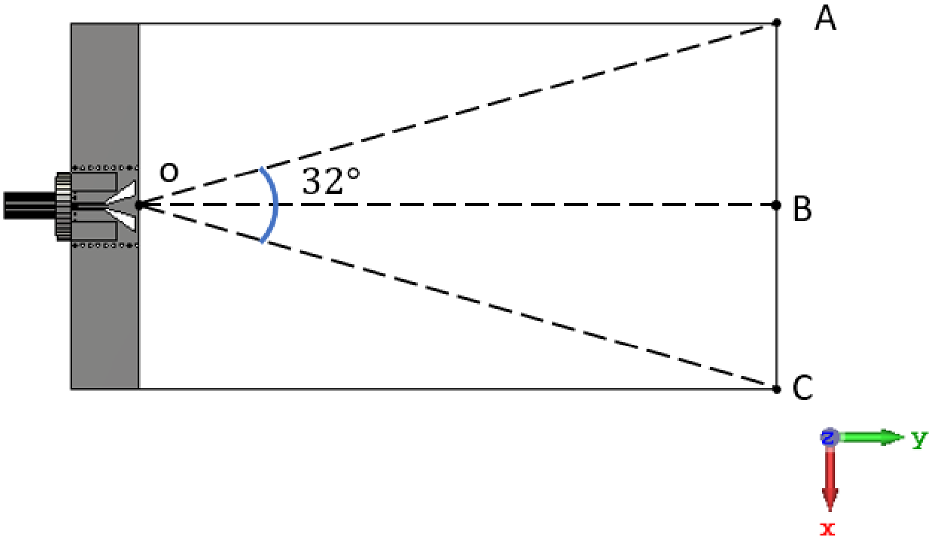

Figure 4.7. Diagram of the angular range (not in scale).

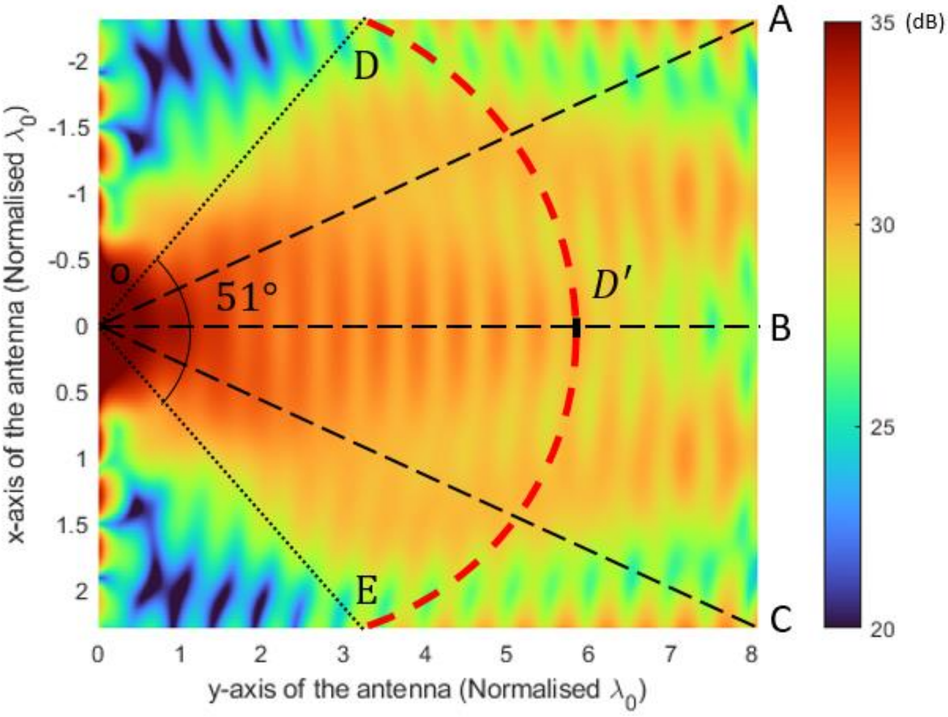

Figure 4.8. The on-surface *E*-field distribution of the coplanar SWL.

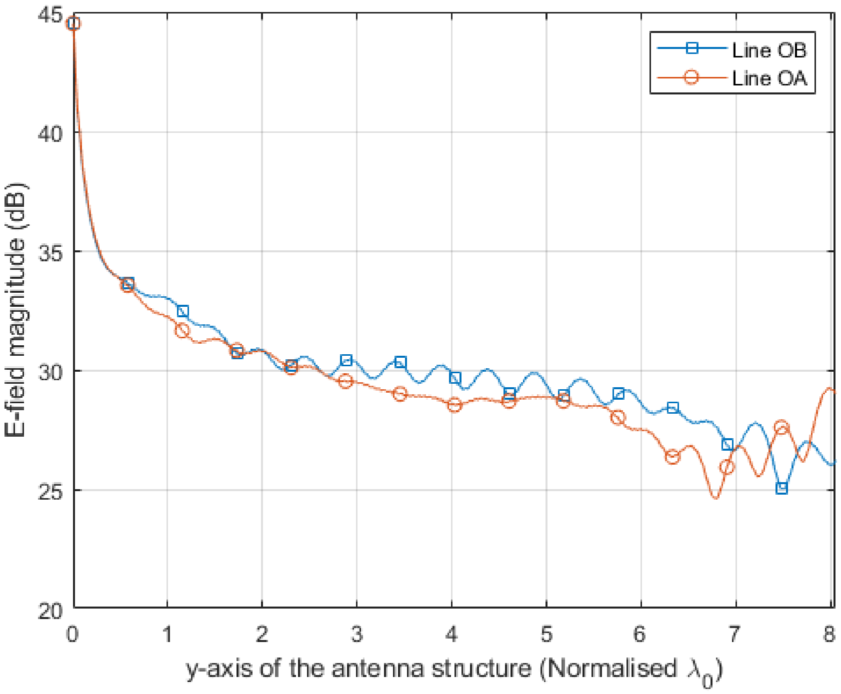

Figure 4.9. On-surface *E*-field along the line OA and OB.

4.1.3.2 Number of metallic cell rows

Before applying five radial rows of the metallic cells, one single row structure is used to design the surface wave antenna. Figure 4.10 (a) and (b) show the single and five rows structure. The magnitude of the *E*-field shows the peak value at the front edge of the SWL. The single row structure shows the sharp changing pattern in the on-surface *E*-field as shown in Figure 4.11 and thus the high variation level in the far-field radiation pattern in Figure 4.13. It can also be observed that the on-surface *E*-field shows very low values when the wave propagates through the metallic cell and increases to very high values in the gap. By adding four rows, the wave is no longer focused on propagating along the central metallic cell row. The five radial rows evenly scatter the wave instead of one row. Figure 4.12 shows a more gentle *E*-field change than the single row structure. The energy of the surface wave spreads out through more metallic cells in the five rows structure.

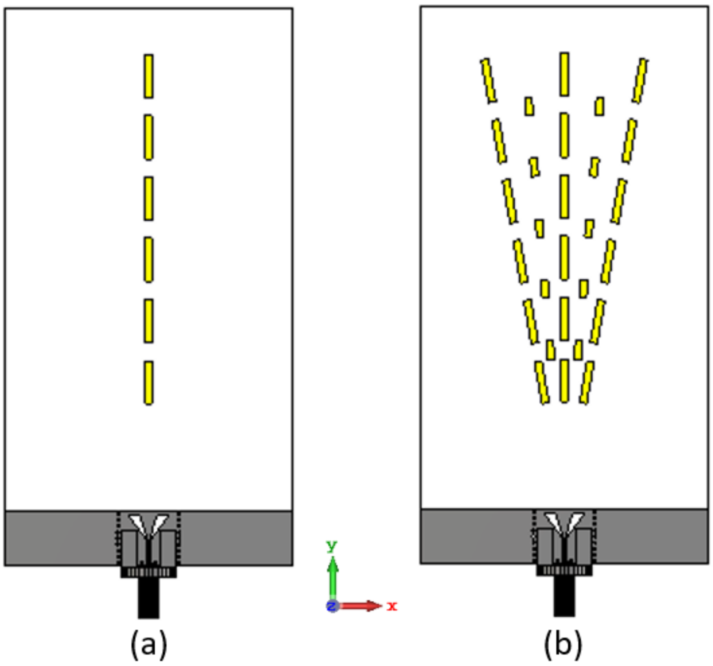

Figure 4.10. The surface wave antenna structure of (a) single row, and (b) multi rows.

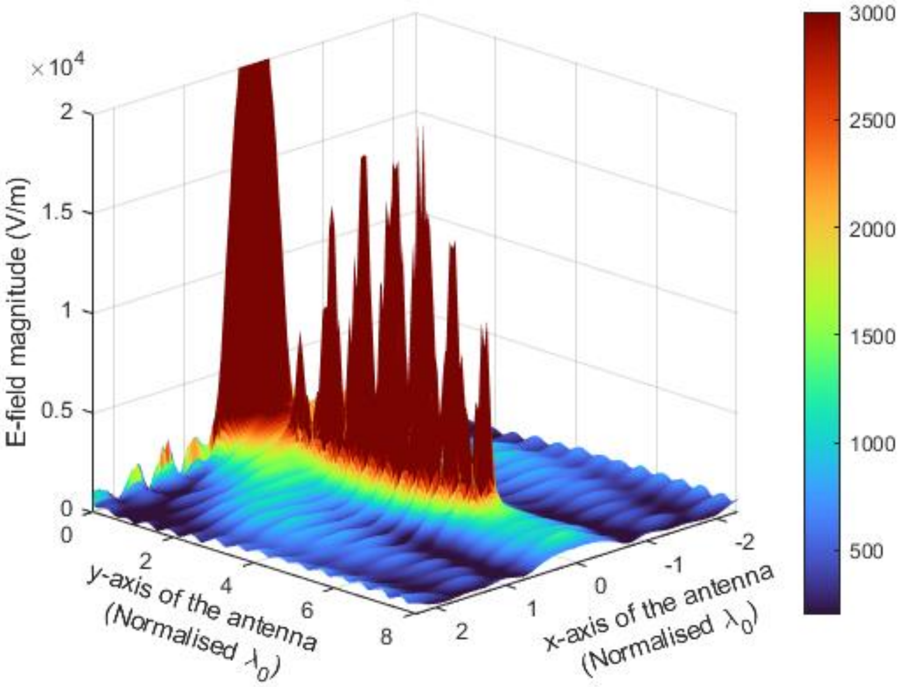

Figure 4.11. The on-surface *E*-field of one metallic cell row surface wave antenna.

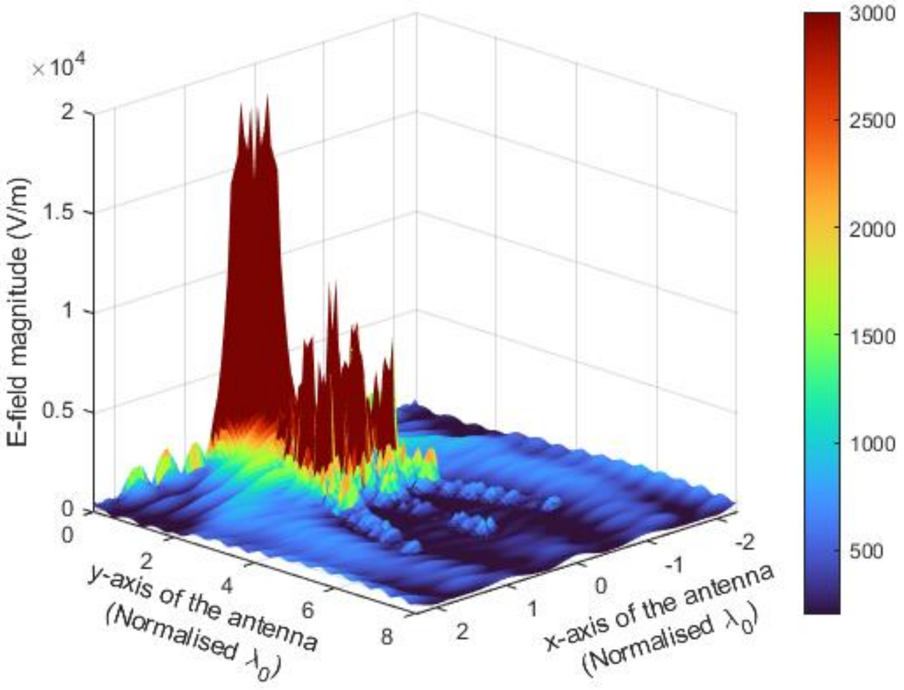

Figure 4.12. The on-surface *E*-field of five metallic cell rows surface wave antenna.

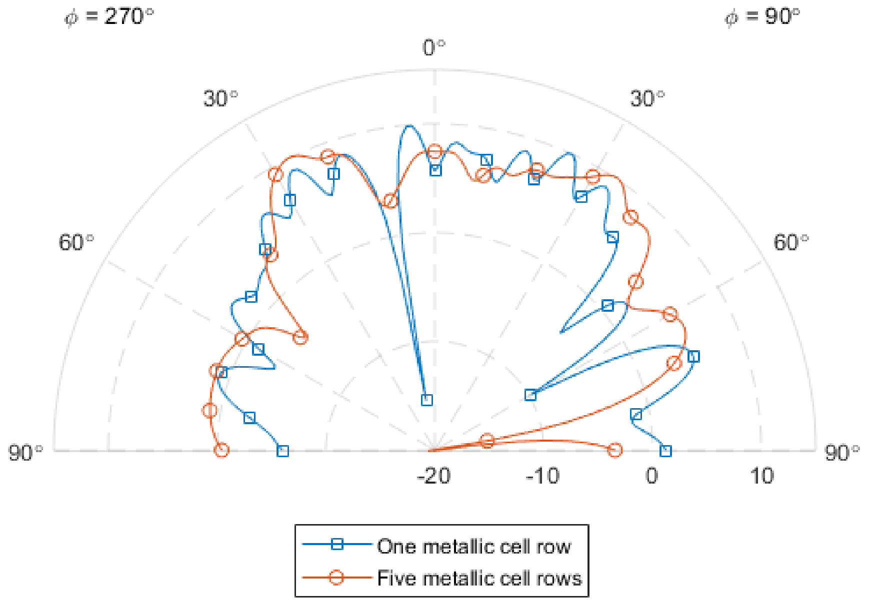

Figure 4.13. The radiation pattern of the surface wave antenna with the different number of rows of the metallic cells.

In Figure 4.13, the far-field radiation pattern of single and five rows structures has been compared. The five rows structure has a more stable radiation pattern in the far-field, and the nulls are largely improved especially in the direction of (ϕ, θ) = (270°, 10°) and (90°, 60°). Therefore, the five radial rows structure is used to design the proposed surface wave antenna.

4.1.4 Frequency and time domain solver

The time domain solver in CST Microwave Studio is based on the Finite Integration Technique (FIT), which uses the Finite Difference Time Domain (FDTD) method to solve Maxwell's equations on a time-grid space. It calculates the fields step by step through time at discrete locations and at discrete time samples by the Leap-frog updating scheme [124]. This updating scheme remains stable if the step width for the integration does not overcome a defined limit. The maximum usable time step is directly related to the minimum mesh step width used in the discretisation of the structure. Therefore, the smaller the mesh cells are, the longer the calculation time will be for the time domain solver. Time domain solver uses a hexahedral or a hexahedral transmission-line matrix meshing technique for the simulation.

On the other hand, the frequency domain solver uses the Finite Element Method (FEM) to solve Maxwell's equations. The frequency domain solver calculation carries out the simulation frequency by frequency, and each frequency sample requires a new equation system to be solved [125]. Therefore, the relationship between calculation time and frequency samples is linear. Thus, the frequency domain solver usually is the fastest when calculating only a small number of frequency samples. In CST, this solver uses either the hexahedral or tetrahedral meshing technique.

Both solvers are originally from the FIT, which works on the integral formulation of Maxwell’s equations. Therefore, it is pertinent that these two solvers give similar results if the mesh type and size and simulation parameters are properly defined for both solvers.

In this research, a solver with less simulation time is desirable as there are thousands of antenna models that need to be simulated to offer the near-zone *E*-field and far-field data samples to train the neural network models. The same surface wave antenna has been simulated by using both time and frequency domain solvers to evaluate which solver is time-efficient. In this solver comparison, the criterion is to choose the solver with a shorter simulation time based on similar simulation results. S_{11} and far-field radiation pattern have been plotted and compared to evaluate the difference in the performance of the solver.

As shown in Figure 4.14, both solvers show that the working frequency is from 34 GHz to 35 GHz and the bandwidth of frequency and time domain solver are 3.2% and 3.6% respectively. The S_{11} provided by the frequency and time domain solvers are -39.73 dB and -27.57 dB at 34.5 GHz respectively. Although there is a 12.16 dB difference, they can be considered as the similar performance as around -30 dB level is already a very low S_{11}. The radiation pattern provided by the two solvers are similar as shown in Figure 4.15, and the mean discrepancy between the two solvers is 0.33 dBi which is acceptable.

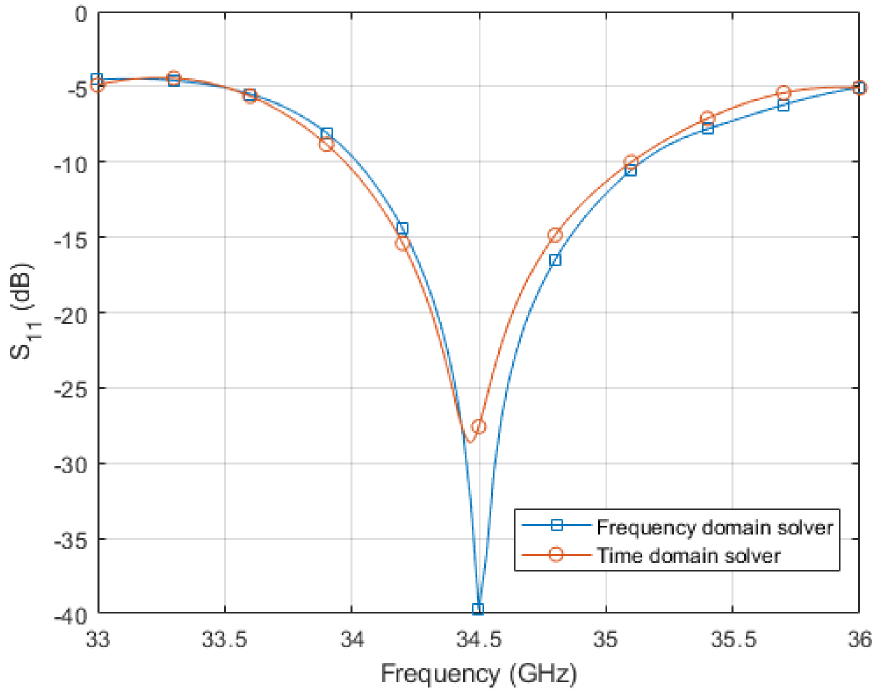

Figure 4.14. S_{11} comparison of frequency and time domain solver.

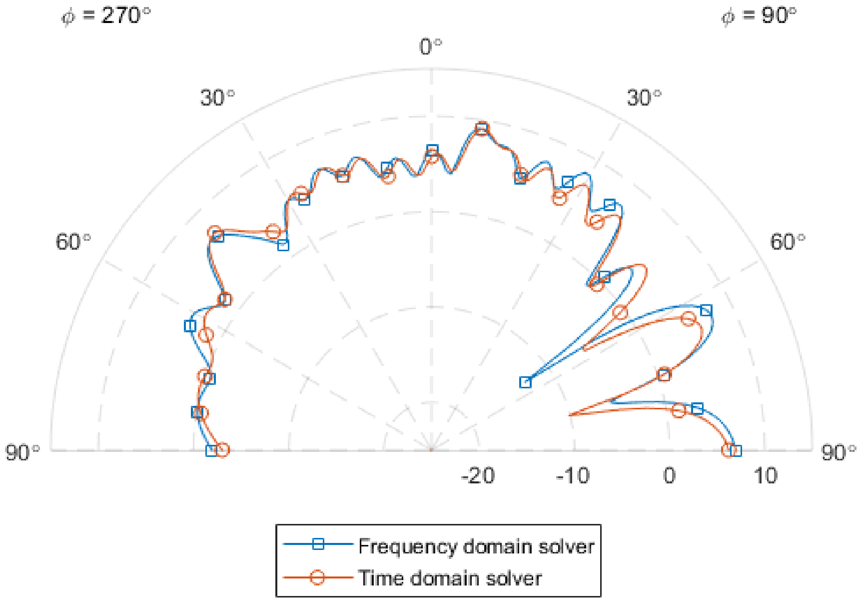

Figure 4.15. Radiation pattern comparison of frequency and time domain solver.

From the comparisons of S_{11} and far-field radiation pattern, the time and frequency domain solver show the same trend and similar results. However, the time domain solver costs 6 hours 26 minutes in simulations while the frequency domain solver only takes 1 hour, which is only 15% of the time domain solver in the same frequency range of simulation. Also as the operating bandwidth of the mmWave VLR is from 34 to 35 GHz, i.e. 2.9% bandwidth, therefore, the frequency domain solver is chosen to simulate the antenna models considering its time-efficient character in this surface wave antenna simulation.

4.2 Prediction results from far-field radiation pattern to near-zone *E*-field

As explained in Chapter 3, the WGAN and Bi-GRU neural network models are used to predict the near-zone *E*-field according to the input radiation pattern. In this section, the prediction results of the near-zone *E*-field will be presented. As discussed in Chapter 3.2, the performance of the Bi-GRU model is critical in this prediction. Therefore, the prediction accuracy of the Bi-GRU model will be assessed through the four evaluation methods defined in Chapter 3.2.5. The relationship between the prediction performance and the number of training datasets will be investigated. Also, the relationship between the prediction performance and the number of *E*-field monitor arrays will be discussed.

4.2.1 Prediction results of the near-zone *E*-field

The prediction of the near-zone *E*-field is presented in this section. The predicted near-zone E_x, E_y and E_z components of two field monitor arrays position 1 $(0, y, 0.12\lambda_0)$ and position 2 $(0.12\lambda_0, y, 0.5\lambda_0)$ from the combination of WGAN and Bi-GRU neural network models will be presented. And the predicted near-zone *E*-field will be compared with the CST simulated near-zone *E*-field, which is the observed standard value (test label), to calculate the prediction error for the evaluation of the near-zone *E*-field prediction performance.

In this near-zone *E*-field prediction, the proposed surface wave antenna with five radial rows is used to provide the near-zone *E*-field training data. Given a far-field radiation pattern, the combination of WGAN and Bi-GRU neural network models will output the predicted near-zone *E*-field with the size of 6×700, which corresponds to the E_x, E_y and E_z components of two field monitor arrays. From Figure 4.16 to Figure 4.21, the predicted near-zone *E*-field of a test case has been shown and each figure represents one row of the 6×700 matrix. The CST simulated near-zone *E*-field is shown in each figure and acts as the test label for calculating the prediction error. It can be observed that the predictions follow the changing pattern of the CST simulated near-zone *E*-field with acceptable prediction error, and the prediction error is shown in Table 4.1. The near-zone *E*-field magnitudes on the sampling line at $(0, y, 0.12\lambda_0)$ are larger than the one at $(0.12\lambda_0, y, 0.5\lambda_0)$. This is because the *E*-field decreases with the increasing distance from the antenna surface. In each *E*-field monitor array, the E_x component shows a relatively low value compared with the E_y and E_z components. This is mainly because the surface wave propagates radially from the SWL and the propagation direction of the surface wave align with the *y*-direction when $x = 0$.

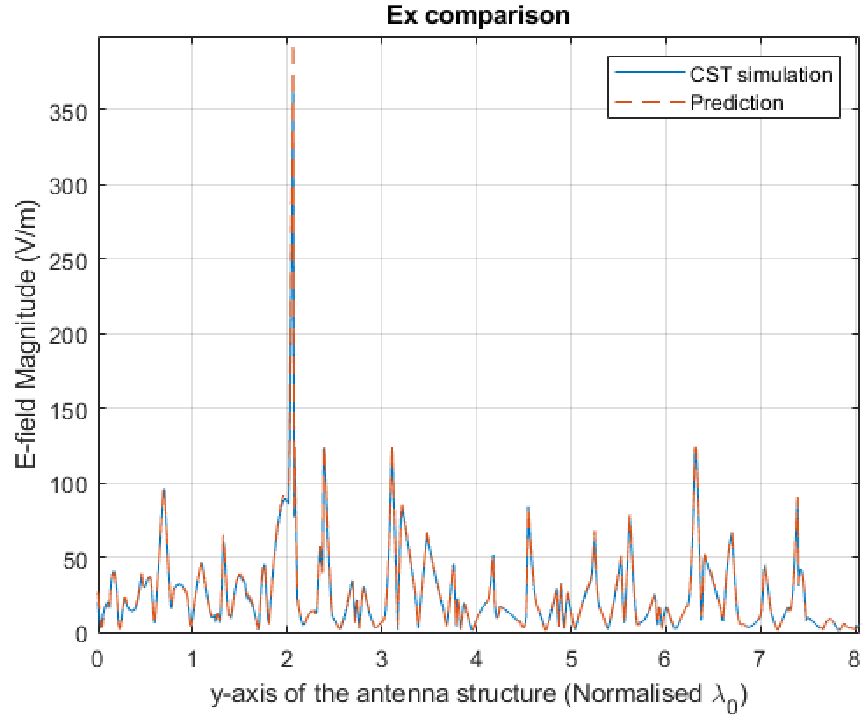

Figure 4.16. E_x comparison on the line at (0, y, $0.12\lambda_0$).

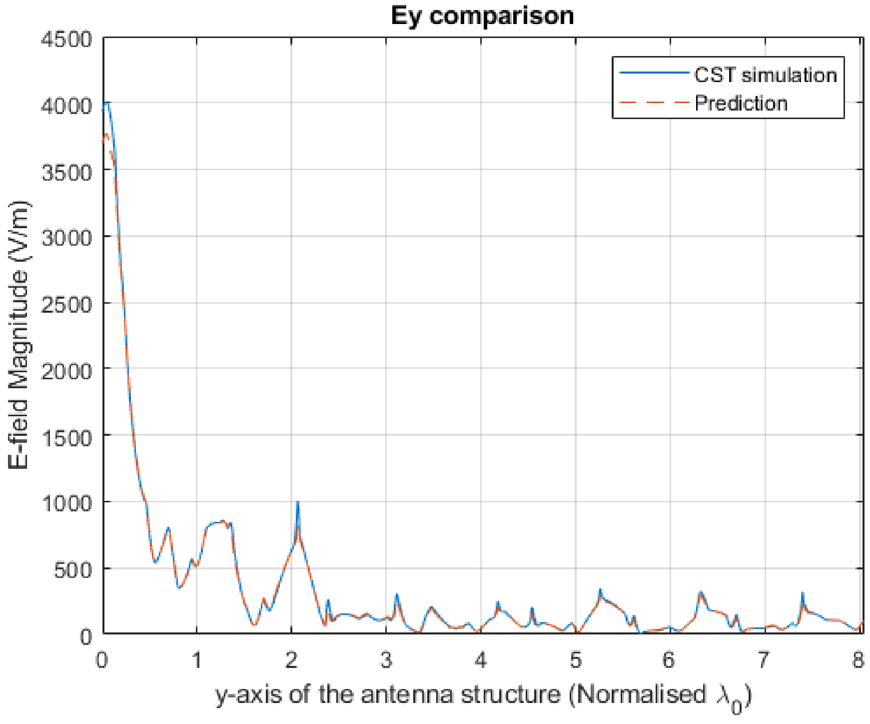

Figure 4.17. E_y comparison on the line at (0, y, $0.12\lambda_0$).

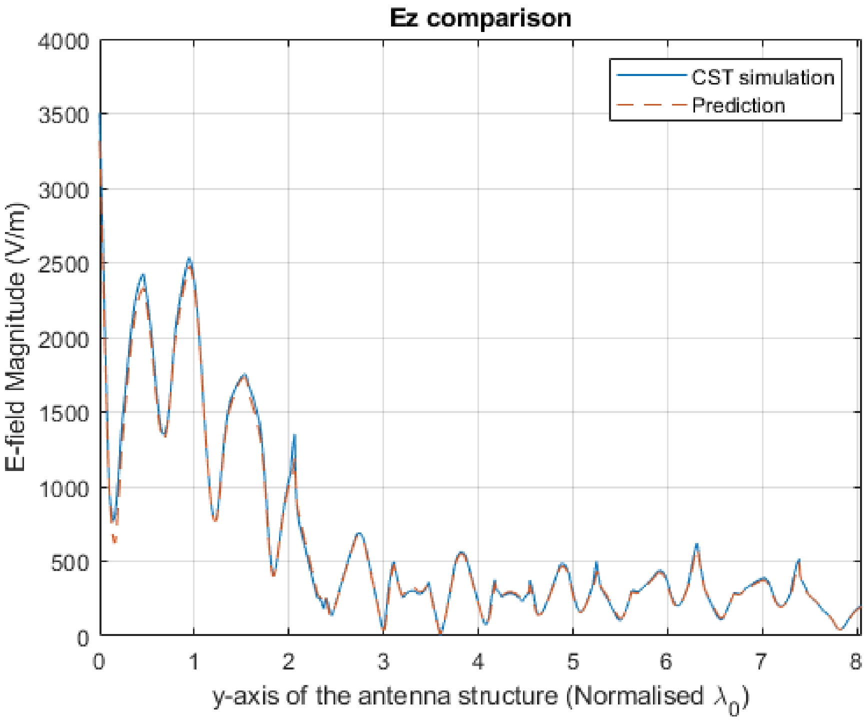

Figure 4.18. E_z comparison on the line at $(0, y, 0.12\lambda_0)$.

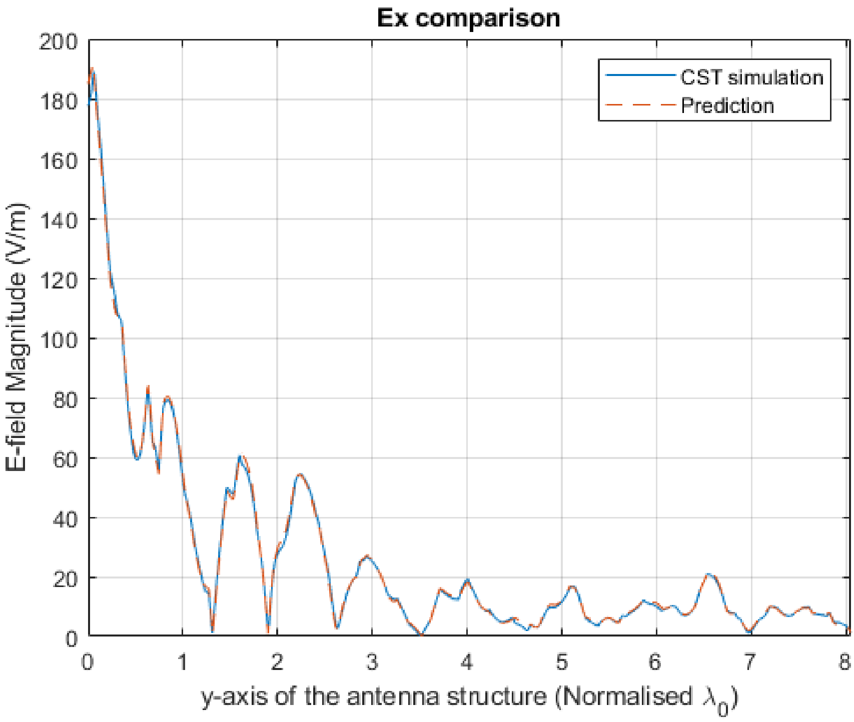

Figure 4.19. E_x comparison on the line at $(0.12\lambda_0, y, 0.5\lambda_0)$.

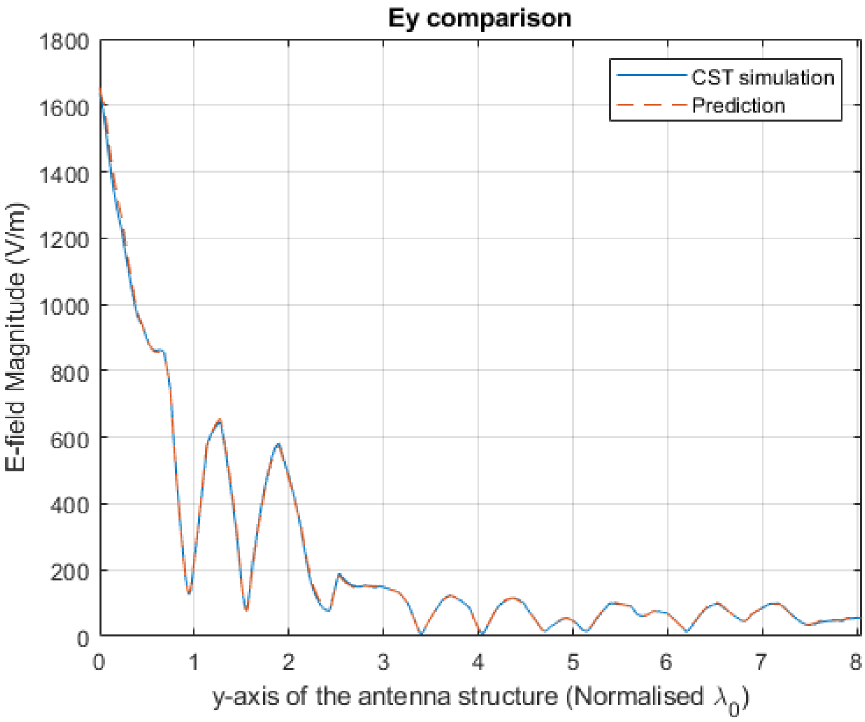

Figure 4.20. E_y comparison on the line at ($0.12\lambda_0$, y, $0.5\lambda_0$).

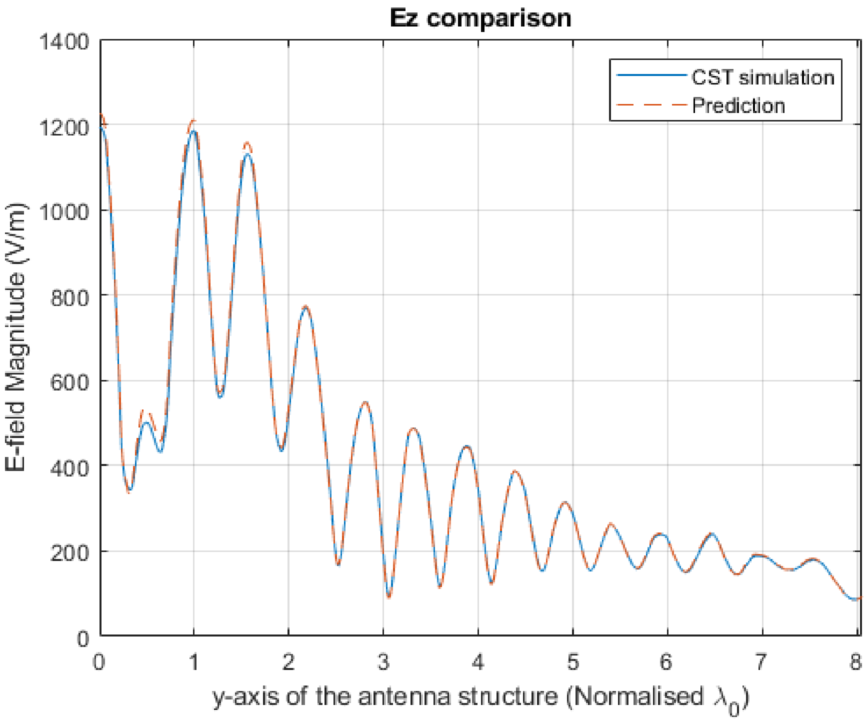

Figure 4.21. E_z comparison on the line at ($0.12\lambda_0$, y, $0.5\lambda_0$).

Table 4.1. Near-zone E-field prediction error of the test case.

	Position 1 (0, y, 0.12λ_0)			Position 2 (0.12λ_0, y, 0.5λ_0)		
E-field	E_x	E_y	E_z	E_x	E_y	E_z
Prediction Error	5.13%	6.28%	5.35%	5.12%	2.77%	1.52%

According to the percentage error defined in Chapter 3, Table 4.1 shows the prediction error of the E_x, E_y and E_z components of two field monitor arrays. It can be seen that the average prediction error of position 1 is larger than position 2. This is due to the abrupt changing pattern of the E-field at position 1. However, the average error of 5.58% among the three components of two field monitor arrays is an acceptable value.

Table 4.1 shows only one test case prediction result from the WGAN and Bi-GRU neural network models. Fifty random test cases are performed to evaluate the prediction performance of the WGAN and Bi-GRU neural network models in order to avoid bias and increase the reliability of the prediction. Fifty different radiation patterns are fed into the WGAN and Bi-GRU neural network models. These fifty radiation patterns are from the CST simulation of the proposed surface wave antenna with randomly distributed metallic cells of the central row. As mentioned in Chapter 3, the random distribution of the central metallic cell row means the period length and MSR are randomly chosen. The predicted near-zone E-field results of fifty cases have been compared with CST simulated near-zone E-field (test labels) to calculate the numerical results of the prediction error, which are shown in Table 4.2. The overall average error among the three components of two field monitor arrays is 4.3%.

Table 4.2. Averaged near-zone *E*-field prediction error of 50 test cases.

	Position 1 $(0, y, 0.12\lambda_0)$			Position 2 $(0.12\lambda_0, y, 0.5\lambda_0)$		
E-field	E_x	E_y	E_z	E_x	E_y	E_z
Prediction Error	6.47%	4.48%	3.78%	5.64%	2.77%	2.67%

4.2.2 Discussion

4.2.2.1 Relationship between near-zone *E*-field and far-field radiation pattern

As explained in Chapter 3, the Bi-GRU model is used to build the relationship between near-zone *E*-field and far-field and it is essential to the near-zone *E*-field prediction. The relationship is studied by the Bi-GRU neural network model by feeding the near-zone *E*-field data as input. The Bi-GRU output the far-field radiation pattern as the prediction result. The input size is 6×700 and the output size is 1×700. In this section, the prediction of the Bi-GRU model will be presented and the prediction results of the Bi-GRU will be assessed by four different evaluation methods defined in Chapter 3.

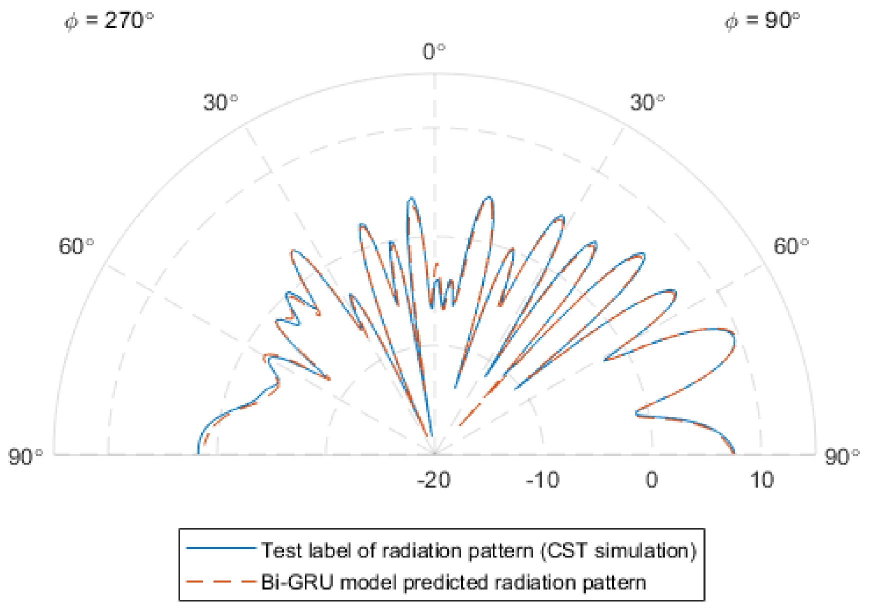

Figure 4.22. Far-field radiation pattern prediction results (predicted pattern 1).

A test case is used to evaluate the prediction performance of the Bi-GRU neural network model. The near-zone *E*-field of the test case is the input of the Bi-GRU model, and the predicted radiation pattern from Bi-GRU is shown in Figure 4.22. The CST simulated radiation pattern of the test case acts as the test label for comparison. From Figure 4.22, it can be seen that the predicted radiation pattern by Bi-GRU is very close to the CST simulated radiation pattern. This implies the feasibility and accuracy of this Bi-GRU model prediction. The Bi-GRU model shows a reliable prediction from the near-zone *E*-field to far-field radiation pattern. Four evaluation methods, mean squared error (MSE), correlation factor (CF), R-squared (R^2) and fidelity (cross-correlation, CR), are performed to do the numerical analysis and assess the prediction accuracy.

Table 4.3. The numerical results of the Bi-GRU prediction performance.

	MSE	CF	R^2	Fidelity
Value	0.7994	0.9842	0.9670	0.9838

To assist the readers to understand the meaning of the values provided by the four evaluation methods, the numerical results of the prediction shown in Figure 4.22 are presented in Table 4.3. The MSE is 0.7994 and this is not intuitive as it is an absolute value. However, with the visual aid of Figure 4.22, this can be more intuitive when compared with the results from other evaluation methods. The CF is close to 1 with the value of 0.9842, which means the prediction radiation pattern strongly correlates with the CST simulated radiation pattern. The value of R^2 shows that the prediction is very close to the test labels as it is very close to 1. The fidelity 0.9838 implies the similarity between the simulated and the predicted radiation pattern is high as 1 indicates the same.

The absolute value of the MSE shown in Table 4.3 is not intuitive when observing. Two other predicted radiation patterns of the same test case as Figure 4.22 are provided for comparison to have an intuitive and directional understanding of the values of the four evaluation methods. Figure 4.23 and Figure 4.24 show the predicted radiation patterns compared with those provided by the CST simulations.

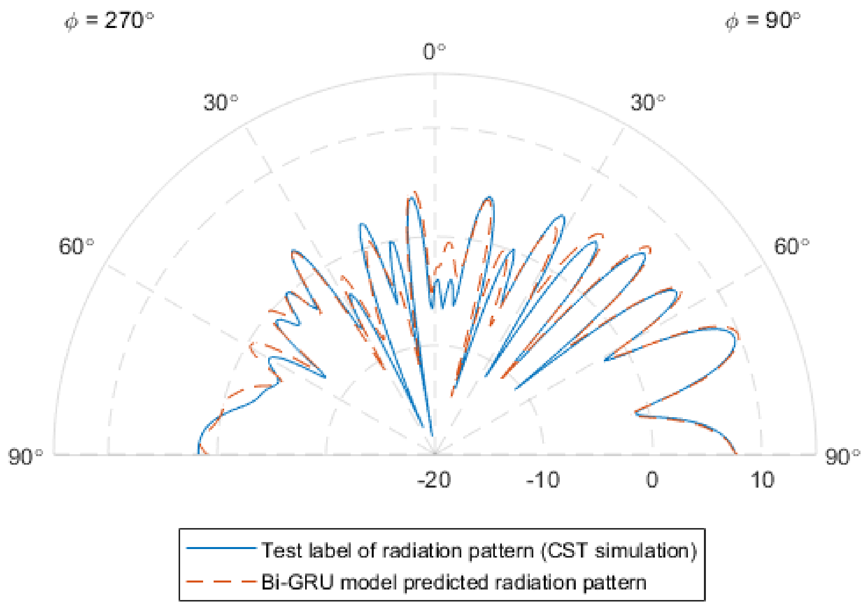

Figure 4.23. Far-field radiation pattern prediction results (predicted pattern 2).

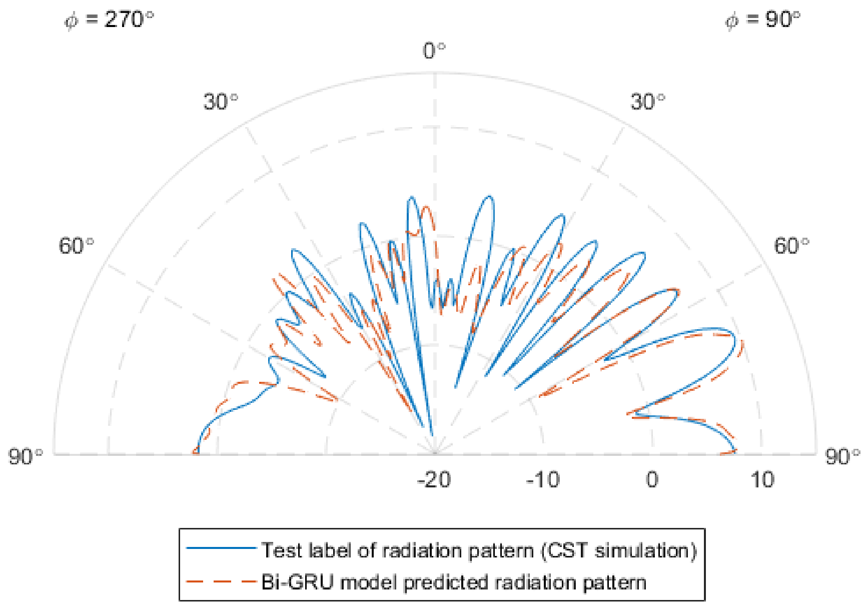

Figure 4.24. Far-field radiation pattern prediction results (predicted pattern 3).

Table 4.4. The numerical results of the Bi-GRU prediction performance of predicted patterns 1, 2 and 3.

	MSE	CF	R^2	Fidelity
Predicted pattern 1 (Figure 4.22)	0.7994	0.9842	0.9670	0.9838
Predicted pattern 2 (Figure 4.23)	6.2512	0.8702	0.7421	0.8776
Predicted pattern 3 (Figure 4.24)	14.0709	0.7074	0.4195	0.7170

From the comparison in Figure 4.22, Figure 4.23 and Figure 4.24, the prediction performance in Figure 4.22 is the best among three predicted radiation patterns. From Table 4.4, it can be seen that all of the four evaluation values of predicted pattern 1 are better than predicted pattern 2 and 3, which are consistent with the results shown in Figure 4.22, Figure 4.23 and Figure 4.24. The MSE of the three prediction cases increases, and the values are 0.7994, 6.2512 and 14.0709 respectively. With the visual aid of Figure 4.22, Figure 4.23 and Figure 4.24, the predicted pattern with an MSE value of 0.7994 can be considered as a good prediction. From predicted pattern 3 to 1, the CF, R^2 and fidelity are getting close to 1, which means the prediction performance is improved.

In these three predicted radiation patterns, they are predicted by using different Bi-GRU neural network models. The difference is the number of training datasets (1000, 2000 and 5000) used to train the Bi-GRU neural network model. Generally, the more the training datasets are used, the more accurate the prediction results. The relationship between the prediction performance and the training datasets will be discussed in the next section.

4.2.2.2 Relationship between the prediction performance and the training datasets

In this section, the relationship between the prediction performance of the Bi-GRU model and the training datasets will be investigated. During the investigation, two factors in the training datasets are discussed, which are the number of training datasets and the number of E-field monitor arrays applied in each dataset. Each training dataset consists of the near-zone E-field and far-field radiation patterns of surface wave antenna models simulated by CST. The number of training datasets indicates how many surface wave antenna models are used to provide the training data. And the number of E-field monitor arrays indicates how many field monitor arrays are applied in the near-zone for E-field data extraction. A test case will be performed to show the prediction performance of Bi-GRU models trained by different number of training datasets and field monitor arrays in near-zone E-field. Fifty test cases will be tested and the prediction performance will be assessed by the four evaluation methods. The average value of each evaluation method will be calculated to demonstrate the relationship between the prediction performance of the Bi-GRU model and the training datasets.

In this prediction model, the total number of surface wave antenna models are 5000. Different Bi-GRU models have been trained by the different number of the training datasets, which are 500, 1000, 2000, 3000, 4000 and 5000. Therefore, six Bi-GRU models are used to investigate the relationship between the number of training datasets and the prediction performance. In near-zone E-field monitor analysis, six field monitor arrays of E-field have been placed in the surface wave antenna models to collect observed standard values from CST simulation. Figure 4.25 shows four field monitor arrays with different x and z positions, and they are all along the y-axis of the surface wave antennas. In addition, Figure 4.26 shows the two field monitor arrays in the radial direction at different z positions. The positions of the arrays are shown in Table 4.5. All field monitor arrays have the same length, which is 70 mm starting from the front edge of the SWL. In each field monitor array, E_x, E_y and E_z components are extracted as the near-zone E-field training data.

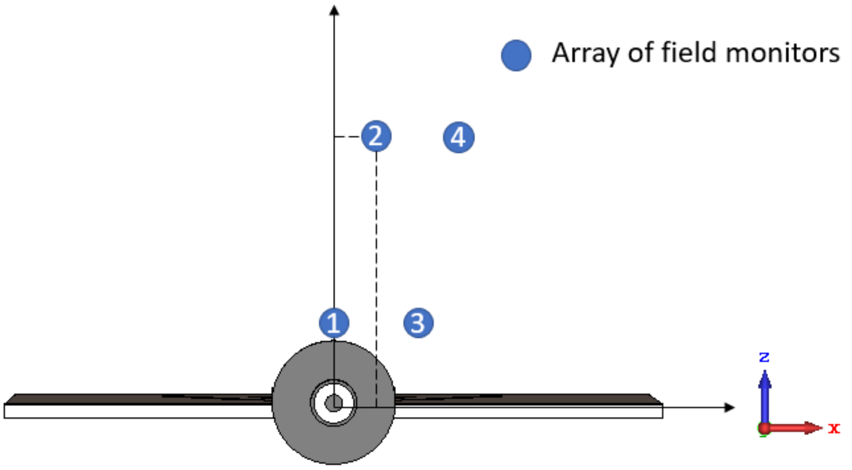

Figure 4.25. Diagram of the array of field monitors in near-zone *E*-field data extraction (Arrays 1 to 4).

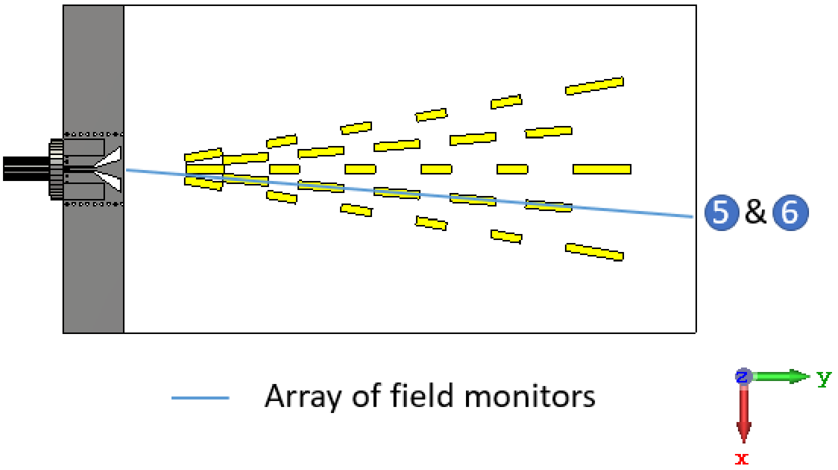

Figure 4.26. Diagram of the array of field monitors in near-zone *E*-field data extraction (Arrays 5 and 6).

Table 4.5. The positions of the field monitor arrays.

	z level	x / ϕ level	Direction
Position 1	$z = 0.12\lambda_0$	$x = 0$	y direction
Position 2	$z = 0.5\lambda_0$	$x = 0.12\lambda_0$	y direction
Position 3	$z = 0.12\lambda_0$	$x = 0.25\lambda_0$	y direction
Position 4	$z = 0.5\lambda_0$	$x = 0.5\lambda_0$	y direction
Position 5	$z = 0.12\lambda_0$	$\phi = 85^o$	Radial direction
Position 6	$z = 0.5\lambda_0$	$\phi = 85^o$	Radial direction

A test case is used to show the prediction performance by different near-zone *E*-field trained Bi-GRU models. Figure 4.27 shows the comparison of radiation patterns predicted by Bi-GRU models based on different field monitor arrays. Bi-GRU models are trained by the same number of training datasets (5000) but different number of *E*-field monitor arrays. It can be seen that all of the predictions are reasonably fitted with the test label, but it is difficult to visually verify which case is better. The numerical results shown in Table 4.6 can help to quantify the assessment. Although the numerical results indicate the prediction performances of the three cases are similar, the case with 2-array *E*-field monitors shows the best performance among all three cases. The performance of the 6-array case is slightly better than the 4-array case. It is worth mentioning that this comparison result can only be applied to this specific surface wave antenna model. More models are necessary to conclude the performance of different field monitor arrays.

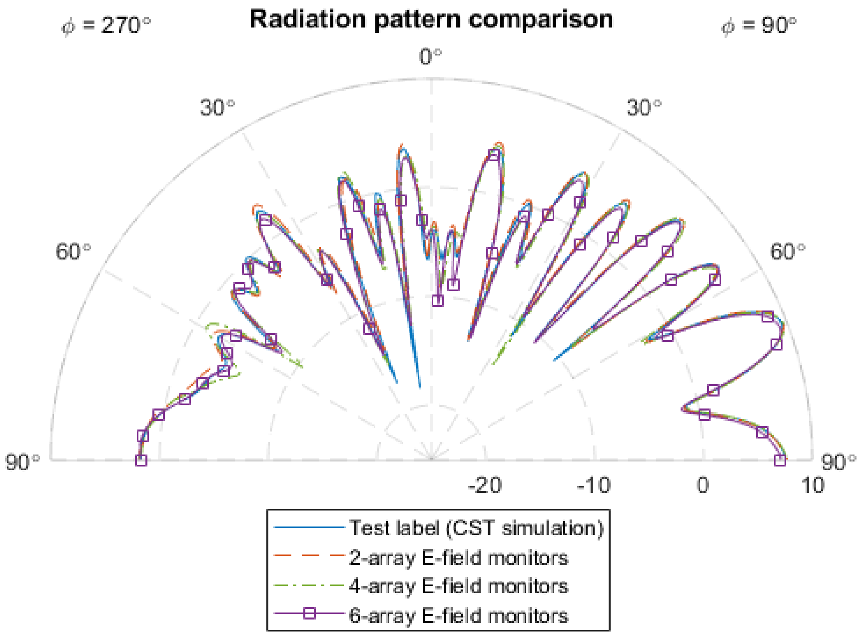

Figure 4.27. Prediction performance of Bi-GRU models trained by the different number of arrays of *E*-field monitors.

Table 4.6. Prediction performance of Bi-GRU models trained by the different number of *E*-field monitor arrays.

Number of arrays	MSE	CF	R^2	Fidelity
2-array	0.9074	0.9838	0.9626	0.9819
4-array	1.5947	0.9672	0.9342	0.9703
6-array	1.1478	0.9774	0.9526	0.9764

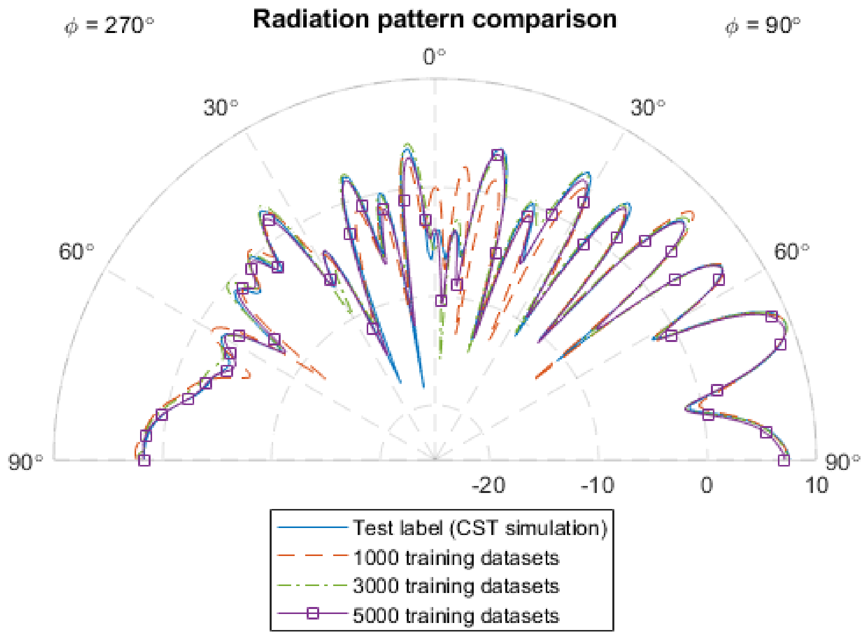

Figure 4.28. Prediction performance of Bi-GRU models trained by the different number of training datasets.

Table 4.7. Prediction performance of Bi-GRU models trained by the different number of training datasets.

Training datasets	MSE	CF	R^2	Fidelity
1000	9.9376	0.8522	0.6427	0.7522
3000	2.1550	0.9561	0.9111	0.9553
5000	0.9074	0.9838	0.9626	0.9819

Figure 4.28 shows the prediction performance of Bi-GRU models trained by the different number of training datasets. The model trained by 1000 training datasets has the largest discrepancy among the three cases. From Table 4.7, it can be seen that the Bi-GRU model trained by 5000 datasets has the best performance.

As mentioned earlier, only focusing on a specific test case (surface wave antenna model) would introduce bias. Therefore, in order to get a reliable relationship regarding the prediction performance and training dataset, fifty test cases are tested and the averaged results of the four evaluation methods are shown in Figure 4.29 to Figure 4.36.

Figure 4.29 depicts the decreasing trend of the average MSE value with the number of training datasets increasing. This implies that the more the training datasets are used, the better the prediction performance. Each point in the figure represents the average value among fifty test cases. In training datasets 500 and 1000, the 2-array *E*-field monitor case has the largest MSE while the 6-array case has the smallest MSE. However, the MSE value tends to be the same with the number of training datasets increasing. This observation can be explained by the 6-array case is equivalent to having more data when the training datasets is less. The contribution of the 4 extra arrays of *E*-field data becomes insignificant when the training datasets are over 2000. Figure 4.30 shows the percentage of MSE improvement of different training datasets. The MSE of 1000 training datasets has significantly improved from 500 training datasets. The average improvement is over 50% when the training datasets changes from 500 to 1000. The improvement percentage of MSE is around 39% when the training datasets change from 4000 to 5000.

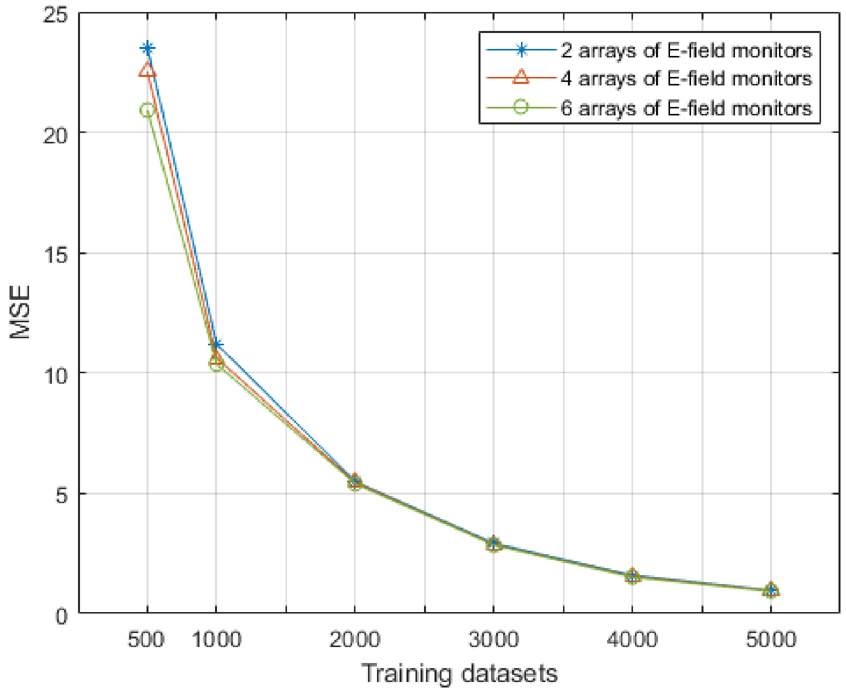

Figure 4.29. The relationship between MSE and the number of training datasets.

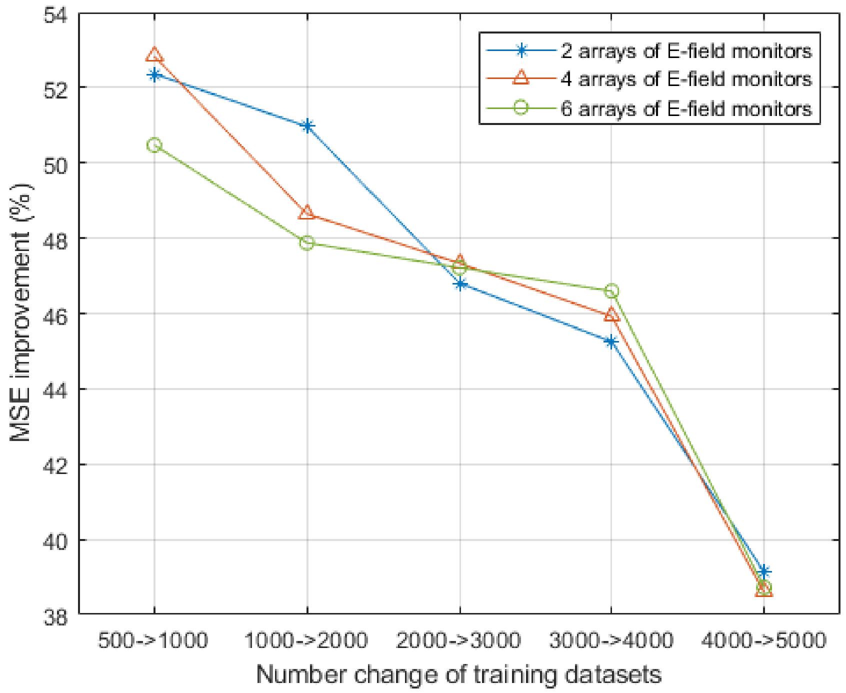

Figure 4.30 The percentage value of MSE improvement.

Figure 4.31 shows the improvement of the CF with the increasing number of training datasets. The CF value changes from 0.61 to 0.97 when training datasets change from 500 to 5000. When training datasets are 500, the CF values of different field monitor arrays of *E*-field cases are similar. At training datasets 5000, the CF of the 6-array *E*-field monitor is 0.976, which is 0.003 larger than the rest cases. In Figure 4.32, it can be seen that the improvement rate decreases with the number of training datasets increasing. The improvement percentage of CF is only 0.13% when the training datasets change from 4000 to 5000.

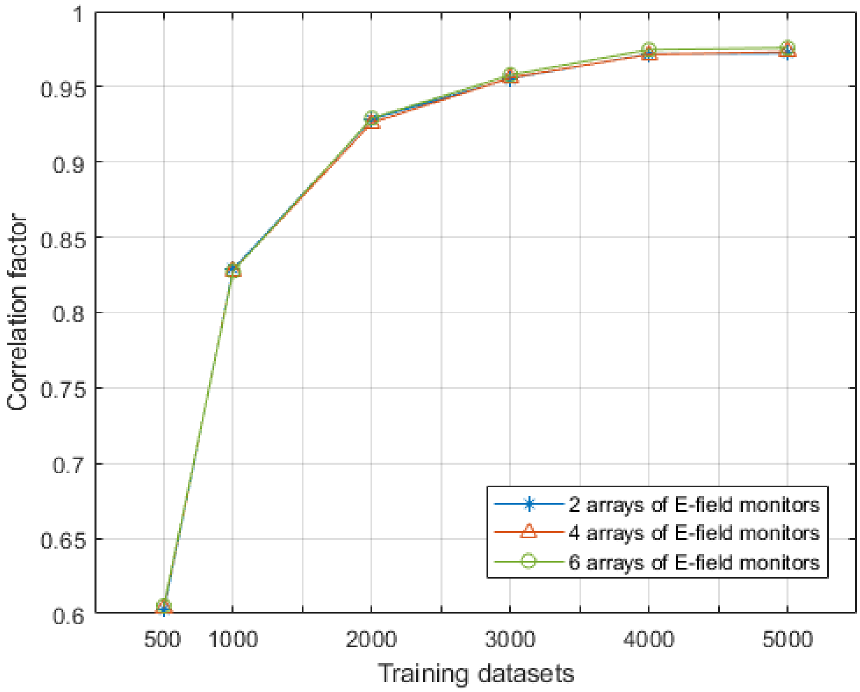

Figure 4.31. The relationship between CF and the number of training datasets.

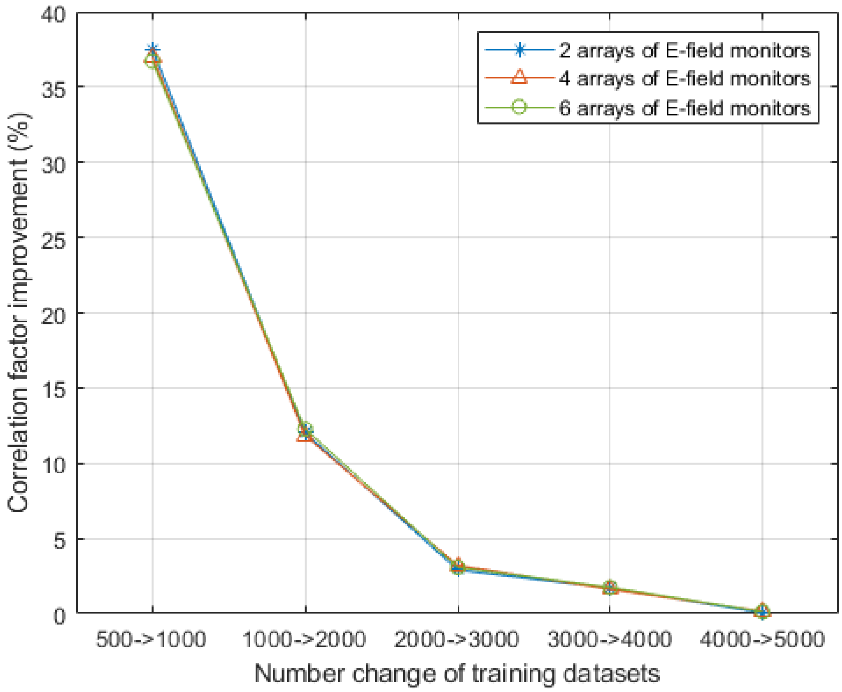

Figure 4.32. The percentage value of CF improvement.

Figure 4.33 and Figure 4.34 shows the R^2 values of the prediction performance of the Bi-GRU models that are trained by the different number of datasets. From 500 to 1000 datasets, the R^2 value has improved around 89%, which is from 0.31 to 0.6. The most significant improvement occurs when datasets are from 500 to 1000. R^2 shows the 0.45% improvement percentage when the training datasets change from 4000 to 5000.

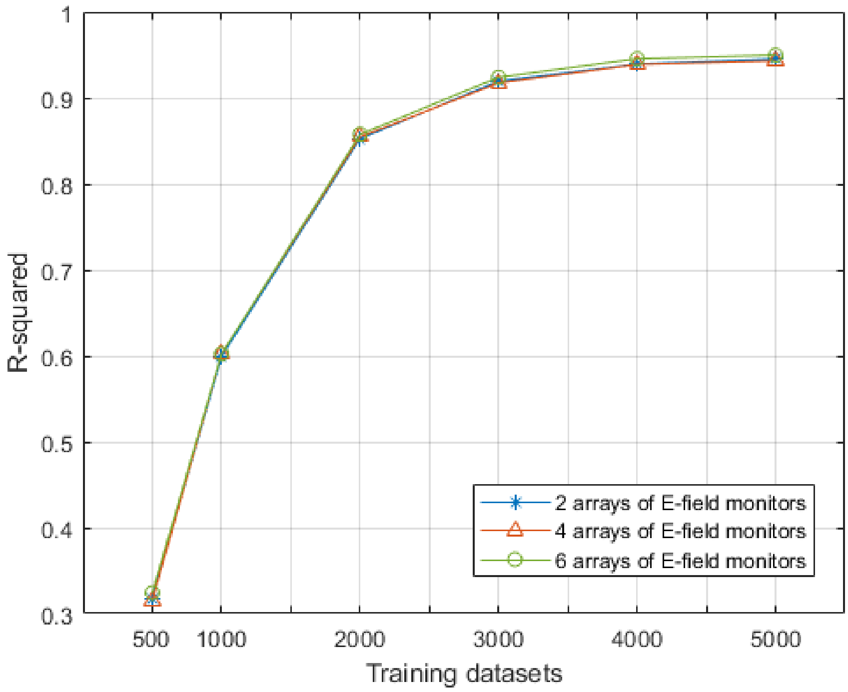

Figure 4.33. The relationship between R^2 and the number of training datasets.

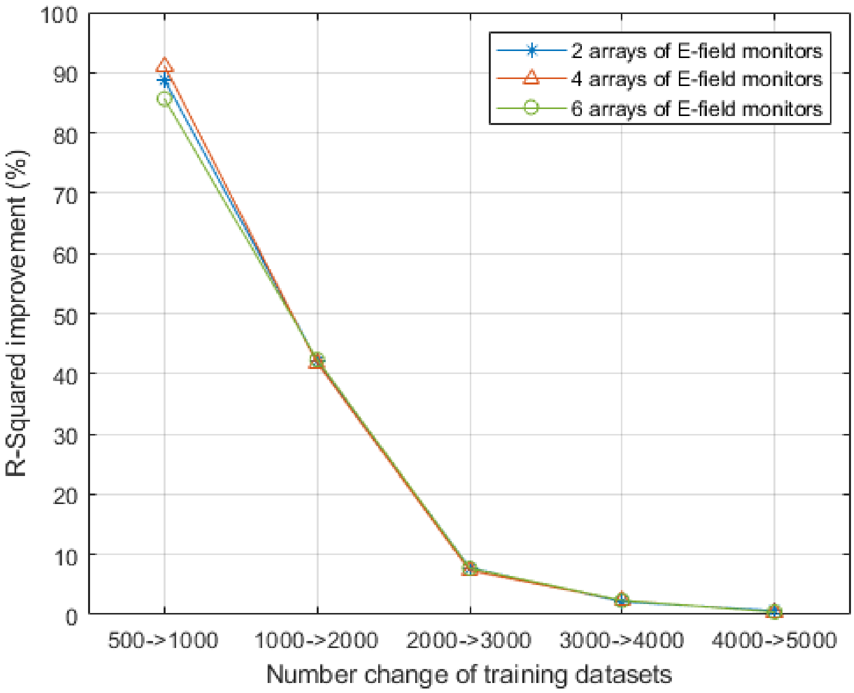

Figure 4.34. The percentage value of R^2 improvement.

The numerical analysis of the fidelity evaluation is shown in Figure 4.35 and Figure 4.36. The changing trend is similar to the CF evaluation method. The fidelity is improved from 0.535 to 0.976 with the number of training datasets increasing.

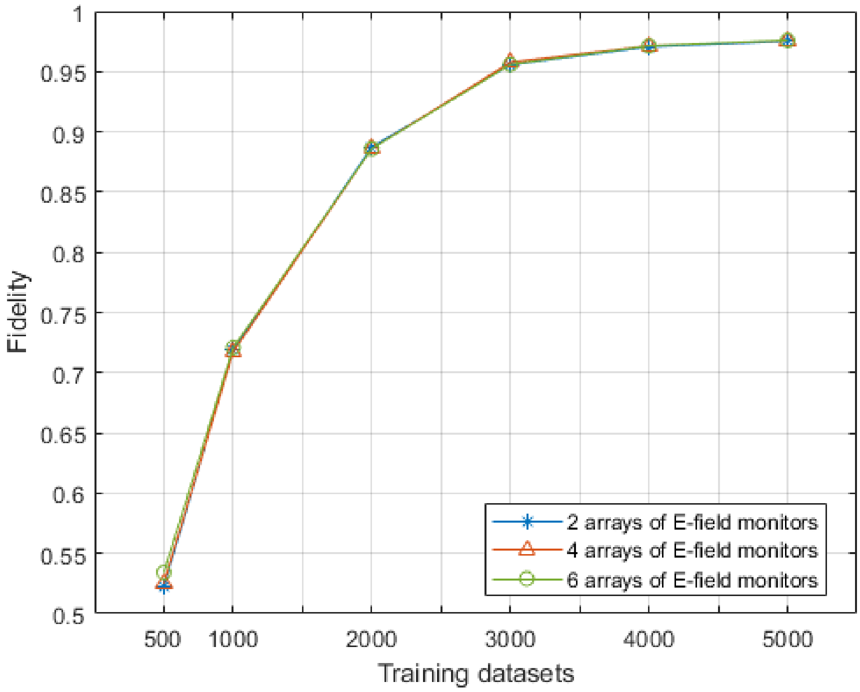

Figure 4.35. The relationship between fidelity and the number of training datasets.

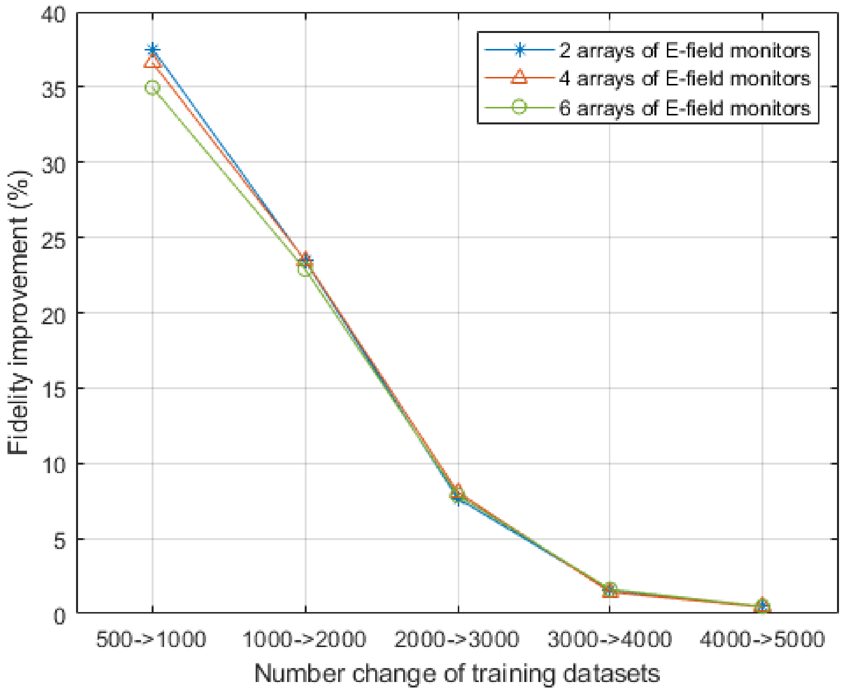

Figure 4.36. The percentage value of fidelity improvement.

From the four evaluation methods analysis, increasing the number of training datasets improves the prediction performance of the Bi-GRU model. The more training datasets are used, the more accurate and reliable the prediction results. However, when the training datasets reach 4000, the improvement of the prediction performance enters a saturation region which means the improvement percentage is smaller than 2% in CF, R^2 and fidelity. Therefore, the total training datasets are 5000 in this neural network training considering the computational cost and the training time of the neural network. As for the *E*-field monitor arrays, it can be observed that the prediction performance is similar to different arrays of *E*-field monitor when the training datasets are the same. Therefore, 2-array *E*-field monitors are chosen to extract the near-zone *E*-field data in consideration of the fact that the training time becomes longer with more *E*-field data input.

Once the near-zone *E*-field is predicted, it can be used to put into another Bi-GRU neural network model to generate the metallic cell pattern on the antenna surface. This Bi-GRU neural network model takes E_x and E_y components of the near-zone *E*-field on the line at $(0, y, 0.12\lambda_0)$ as the input.

And the output is the metallic cell pattern, which is represented by the binary numbers. The prediction results from the near-zone *E*-field to metallic cell pattern will be presented in the next section.

4.3 Prediction results from near-zone *E*-field to metallic cell pattern

In this section, the prediction results of metallic cell pattern will be given by comparing them with the test labels. The prediction accuracy will be defined as an indicator to assess the prediction performance. In the discussion section, the metallic cell pattern prediction accuracy under different period lengths of the metallic cell pattern and different mark-to-space ratios (MSRs) will be investigated. As explained in Chapter 3, the MSR is defined as the length ratio of metallic cells and the gap between the cells within a period. The relationship between the prediction accuracy and the number of training datasets will be given at the end of this section.

4.3.1 Simulation results

In the metallic cell pattern prediction, the near-zone *E*-field used is the magnitude of the E_x and E_y component on the line at (0, y, 0.12λ_0). The prediction of the metallic cell pattern focuses on the line along the y-direction. The prediction line is divided into 700 data points and the space between adjacent points is 0.1 mm, which is around 0.012λ_0. This space is considered as the resolution of the prediction. It is simple to design the metallic cells without considering their width once the metallic cell pattern prediction results are obtained since the width is fixed as 1 mm (rectangular shape metallic cell). The length of the metallic cell can be designed according to the distance from the SWL to the predicted data point. Once the positions of the metallic cells in the central radial row are obtained, the rest of the rows can be defined according to the position relationship between the radial rows.

In Figure 4.37, the predicted metallic cell pattern of the surface wave antenna model with period length λ_0 MSR = 1:4 is labelled in orange asterisks. The blue circle markers are the test labels, which are the standard metallic cell pattern of this surface wave antenna extracted from CST. The *y*-axis metal on/off is the binary label of the metallic cell pattern where on (1) indicates metal and off (0) is no metal.

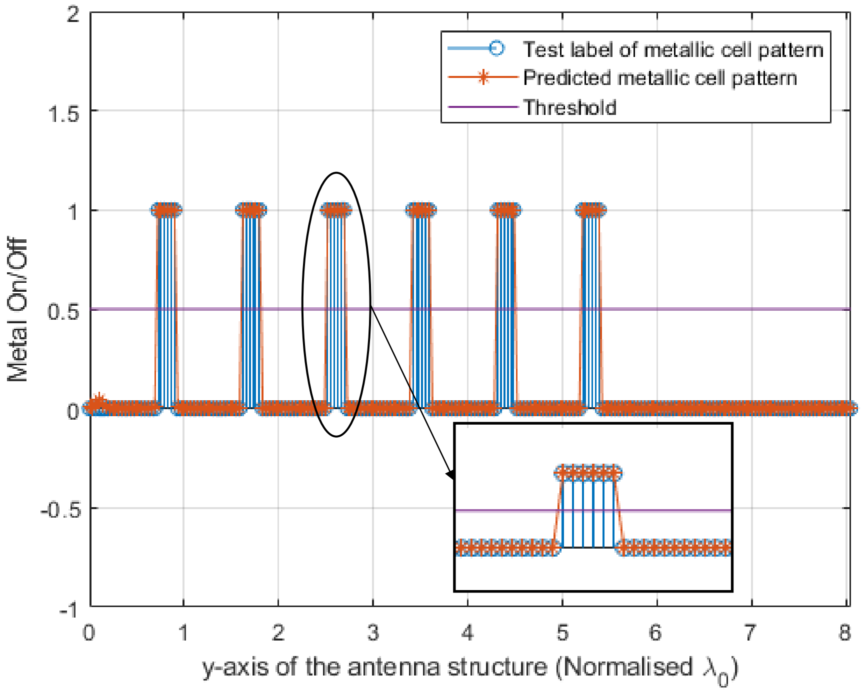

Figure 4.37. Metallic cell pattern prediction result of the surface wave antenna with constant period length λ_0 MSR = 1:4.

In this metallic cell pattern prediction Bi-GRU model, the logistic function is used as an activation function and thus the output range is [0, 1]. The threshold will then be set to 0.5 to distinguish whether the predicted point is metal or not. When the output of the Bi-GRU is less than the threshold value, it means there is no metal at such prediction point. If the output value is located in the range [0.5, 1], it indicates there is metal at the given prediction point. The predicted results are not necessarily the same as 0 or 1 since the predicted value has to be rounded. In this case, the prediction of the last metallic cell can be considered as all correct. The prediction accuracy is defined as the correct predicted data points divided by the total data points. For example, the metallic cell pattern prediction accuracy is 100 % for the case shown in Figure 4.37. To avoid bias and increase the reliability of the prediction, fifty test cases with different constant period lengths and MSRs are used to evaluate the accuracy of the metallic cell pattern prediction. The average prediction accuracy among fifty cases is 99.75%.

4.3.2 Discussion

To demonstrate the feasibility and accuracy of the Bi-GRU neural network model, the predictions of different period lengths, including randomly distributed metallic cell patterns, have to be performed. Furthermore, different MSR of metallic cell patterns also need to be predicted to investigate the relationship between the prediction accuracy and MSR. On the other hand, the relationship between the training datasets and the prediction performance will be investigated.

4.3.2.1 Prediction of different period lengths

In this section, different period lengths, including gradually increasing, gradually decreasing and random, have been studied in order to include more possibilities and prove the feasibility of the Bi-GRU neural network model. In the proposed surface wave antenna, the central metallic cell row has six rectangular metallic cells. Therefore, there are six periods of the metallic cell along the central metallic cell row. In the case of the gradually increasing period length, the length of the first period and the increasing step are chosen randomly. The lengths of the subsequent periods are defined by the length of the former period plus the increasing step. And the length of the metallic cell can be calculated by using the period length and the MSR. The MSR value is the same among six periods. In the specific case of Figure 4.38, the lengths of the first period and the increasing step are both $0.4\lambda_0$, and the MSR = 1:3. In terms of the gradually decreasing period length, the length of the first period and the decreasing step are chosen randomly as well. The lengths of the subsequent periods are defined by the length of the former period minus the decreasing step. In Figure 4.39, the length of the first period and the decreasing step are $2\lambda_0$ and $0.35\lambda_0$ respectively. And the MSR is equal to 1:3. For the random period length, the six lengths of the periods are chosen randomly and each of them is unrelated. And the value of the MSR is random as well.

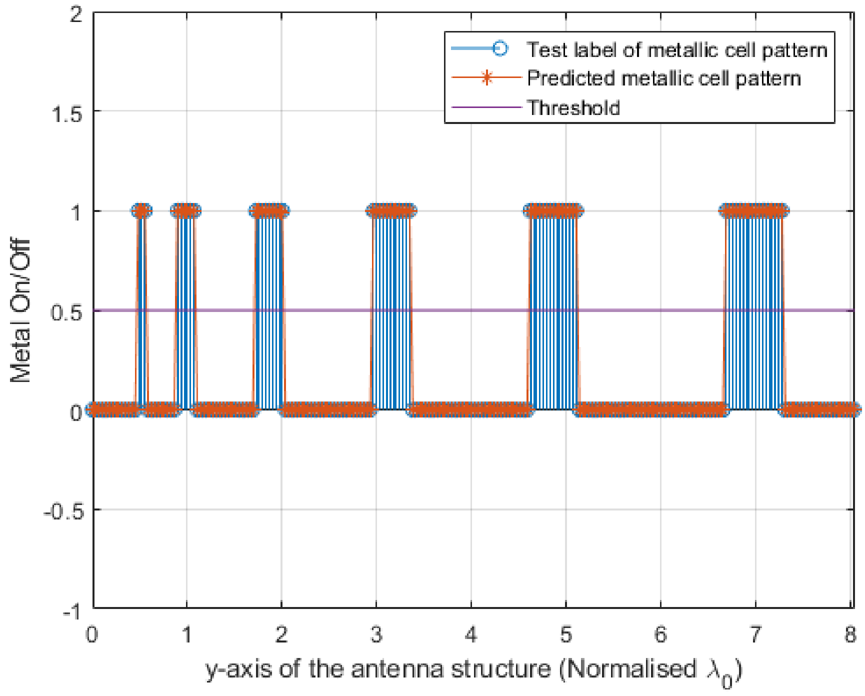

Figure 4.38. Metallic cell pattern prediction results (gradually increasing period length).

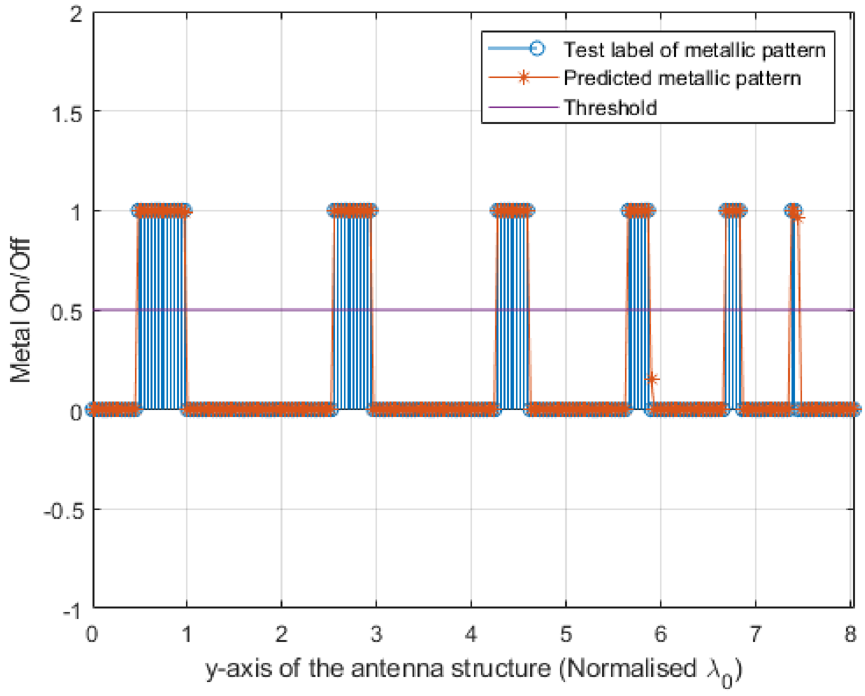

Figure 4.39. Metallic cell pattern prediction results (gradually decreasing period length).

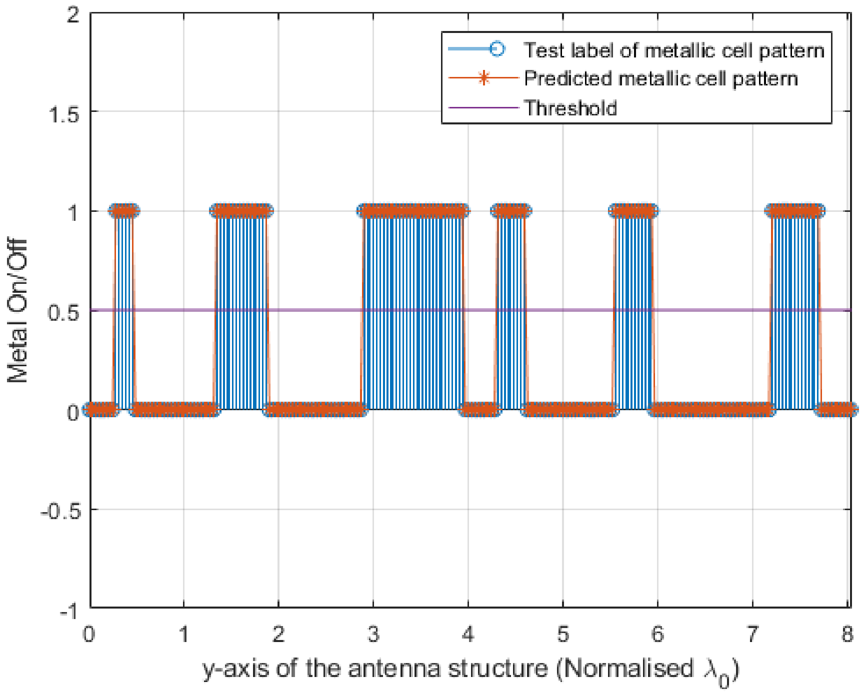

Figure 4.40. Metallic cell pattern prediction results (random period length).

In Figure 4.38, the comparison between the test label and the predicted metallic cell pattern of the gradual increasing period length has been shown. The orange asterisks are perfectly overlapped with the blue circles, which indicates the prediction accuracy is 100% in this particular case. In Figure 4.39, the prediction result misses one data point at the last metallic cell, which gives the 99.86% of prediction accuracy in the gradual decreasing period length case. As for the random period length case, the prediction accuracy reaches 100%, as shown in Figure 4.40.

As mentioned earlier, only focusing on a specific test case would introduce bias. Therefore, fifty test cases of each kind of different period length are predicted. The average prediction accuracies of gradually increasing, gradually decreasing and random period length are 99.51%, 99.46% and 99.42% respectively. Along with the prediction accuracy of the constant period (99.75%), the overall average prediction accuracy is 99.54%. These prediction results prove the feasibility of the proposed Bi-GRU neural network model under different period lengths. Therefore, the trained Bi-GRU neural network model can be considered as a reliable prediction model to predict the metallic cell pattern from the near-zone *E*-field.

4.3.2.2 Prediction of different mark-to-space ratio

In this section, different MSR under constant, gradually increasing, gradually decreasing and random period length have been studied to investigate the relationship between MSR and prediction accuracy. The length of the period is λ_0 in the constant period length case. In the gradually increasing case, the length of the first period and the increasing step are $0.5\lambda_0$ and $0.3\lambda_0$ respectively. In the gradually decreasing case, the length of the first period and the decreasing step are $1.5\lambda_0$ and $0.2\lambda_0$ respectively.

In the surface wave antenna model with constant period length case, seven different MSR subcases have been predicted by Bi-GRU neural network model. The metallic cell pattern prediction results are shown in Figure 4.41. Four cases out of seven are in 100% prediction accuracy, while the lowest prediction accuracy is 99.43%. Even in the lowest accuracy case, the prediction fails 0.57%, which corresponds to 4 data points. And this prediction error is acceptable in the antenna design.

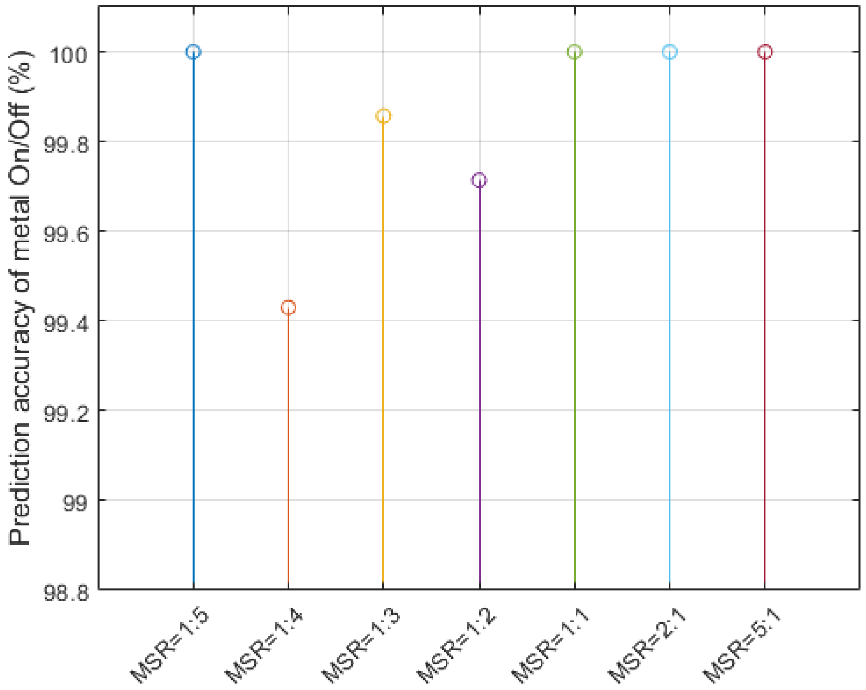

Figure 4.41. Metallic cell pattern prediction results of different MSR with constant period length case.

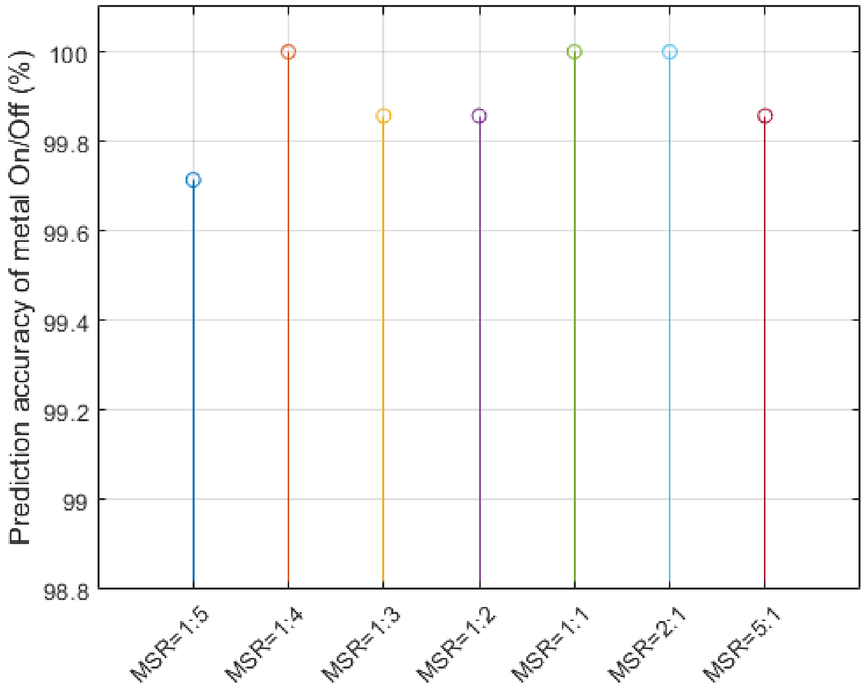

Figure 4.42. Metallic cell pattern prediction results of different MSR with gradually increasing period length.

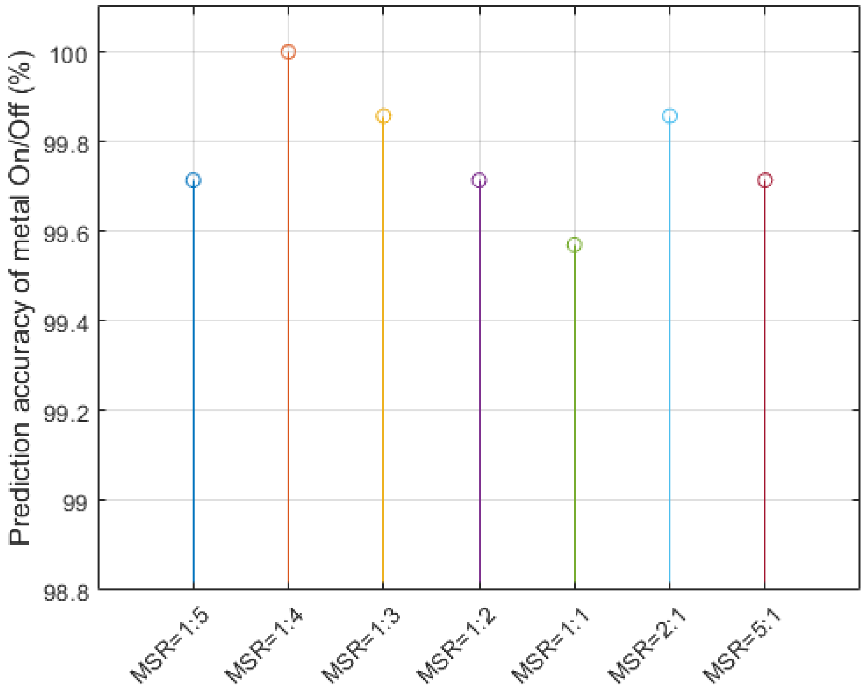

Figure 4.43. Metallic cell pattern prediction results of different MSR with gradually decreasing period length.

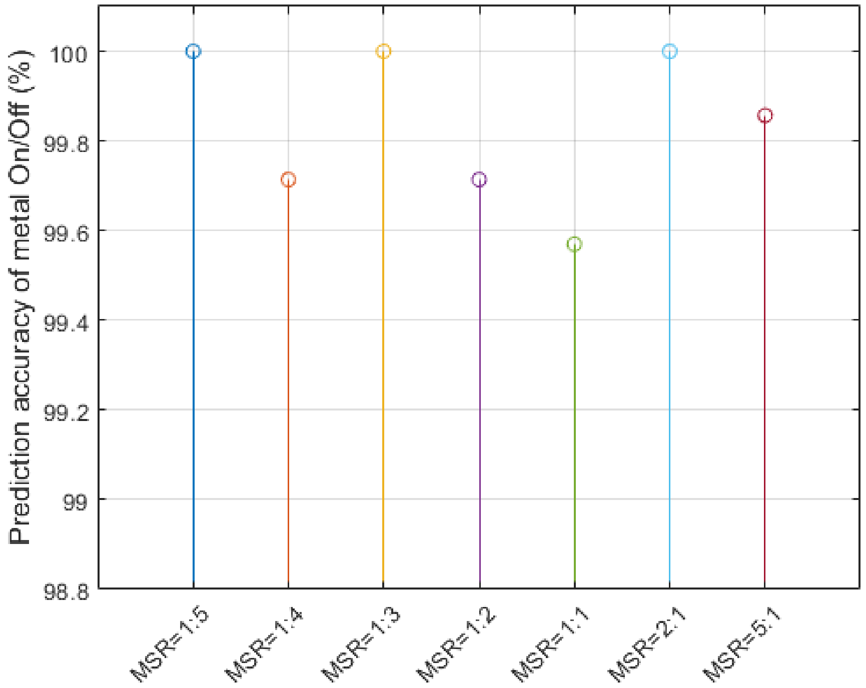

Figure 4.44. Metallic cell pattern prediction results of different MSR with random period length.

The surface wave antenna models with gradually increasing and decreasing period length cases have also been predicted to verify the feasibility of the Bi-GRU neural network model. Different MSR subcases are studied, and the prediction accuracies are shown in Figure 4.42 and Figure 4.43. In the cases of gradually increasing period length, the lowest prediction accuracy is the subcase MSR = 1:5 with the prediction accuracy of 99.7%. In the cases of gradually decreasing period length, the lowest prediction accuracy 99.57% is the subcase MSR = 1:1. In Figure 4.44, different MSR cases under random period length have been predicted, and the lowest prediction accuracy is the case MSR 1:1 with the prediction accuracy of 99.57%.

The covariance has been introduced in order to investigate the relationship between the metallic prediction accuracy and the MSR. The correlation coefficient of constant, gradually increasing, gradually decreasing and random period length is 0.125, 0.051, 0.084 and 0.143 respectively. Four values are positive which indicates the prediction accuracy and MSR is in positive tendency in the linear relationship. However, the magnitude of the correlation coefficient is insignificant and can be ignored. Therefore, a conclusion that the MSR does not affect the metallic cell pattern prediction accuracy can be made.

4.3.2.3 Relation between the prediction accuracy and the number of training datasets

In general, the more datasets used to train the Bi-GRU model, the more reliable and accurate the Bi-GRU model. The performance of different Bi-GRU models trained by the different number of datasets has been studied.

Different Bi-GRU models have been trained by the different number of the training datasets, which are 500, 1000, 2000, 3000, 4000 and 5000 training datasets. Therefore, six Bi-GRU models are used to investigate the relationship between the number of training datasets and the prediction accuracy. Each training dataset comprises the magnitude of E_x and E_y components on the line at $(0, y, 0.12\lambda_0)$ and the metallic cell pattern data (0 or 1) of one surface wave antenna model. The metallic cell pattern has been tested by the six different Bi-GRU models and the prediction results are shown in Figure 4.45. Each point in the figure represents the average prediction accuracy among fifty test cases. It can be observed that the prediction accuracy is improved with more datasets trained. The prediction accuracy is largely improved from the training datasets 500 to 1000, which is from 86.5% to 96.2%. The Bi-GRU model trained by 2000 datasets shows a good prediction accuracy, which is 98.52%. After 3000 training datasets, the improvement is less than 2%, as can be observed in Figure 4.46. And from training datasets 3000 upwards, the improvement percentage is 0.02%, which is very close to 0. Therefore, the total training datasets are 5000 in the metallic cell pattern prediction considering the computational cost and the training time of the neural network.

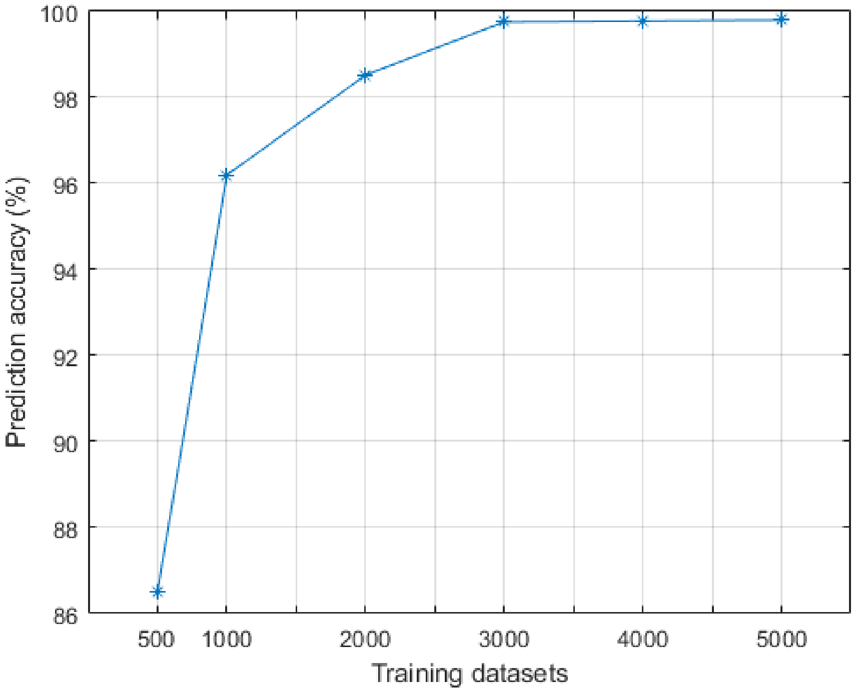

Figure 4.45. The relationship between prediction accuracy and the number of training datasets.

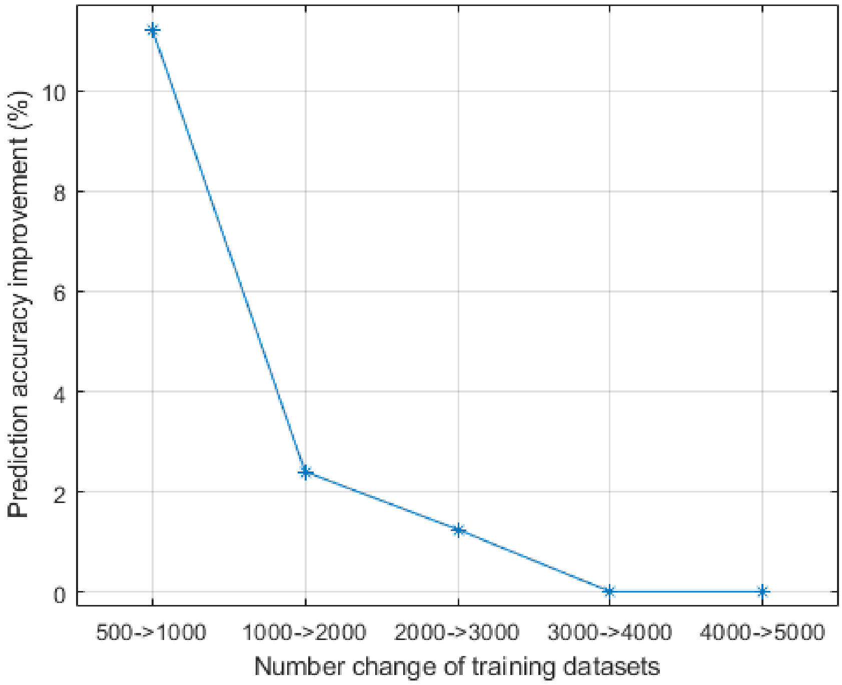

Figure 4.46. The percentage value of prediction accuracy improvement.

4.4 Summary

In this chapter, the EM simulation results of the coplanar SWL have been presented. The coplanar SWL is working at 34.5 GHz with a bandwidth of 2.9%. The total efficiency and the radiation efficiency at 34.5 GHz are 94.2% and 94.4% respectively. The 10 dB angular range of the surface wave is 51°. All of the five radial rows of the metallic cells are located within the angular range area.

In the near-zone *E*-field prediction, the overall prediction error among fifty test cases is 4.3%. The performance of the Bi-GRU model used in near-zone *E*-field prediction has been discussed. Four evaluation methods, MSE, CF, R^2 and fidelity, have been used to comprehensively assess the prediction performance of the Bi-GRU model in near-zone *E*-field prediction. The number of the training datasets is an important factor that affects the performance of the prediction model. In this prediction, the training datasets are 5000 since the percentage of the improvement is less than 2%.

In the metallic cell pattern prediction, the prediction accuracy reaches 100% in the constant period length cases. The overall average prediction accuracy among constant, gradually increasing, gradually decreasing and random period length cases is 99.54%. The MSR is proved not to affect the metallic cell pattern prediction accuracy. In terms of the relationship between prediction accuracy and the size of training datasets, the more data feed into the Bi-GRU model, the more reliable and accurate the Bi-GRU model. It takes about 30 hours of training time to train the neural network models with 1000 datasets. Therefore, a trade-off exists between prediction accuracy and the training time of the neural network model.

5 Cosecant-squared radiation pattern surface wave antenna

In this chapter, the proposed neural network-based method will be used to design a surface wave antenna with cosecant-squared radiation pattern. A dual-sided 30º cosecant-squared radiation pattern will be served as the target of the neural network prediction models for generating the metallic cell patterns on the surface wave antenna. Such antenna can offer a wider observation range than that of the existing antenna in the mmWave VLR system. On the other hand, the radar system can receive an almost constant power value due to the character of the cosecant-squared radiation pattern. The cosecant-squared radiation pattern antenna design procedures will be introduced step by step. The near-zone *E*-field will be predicted and utilised for generating the metallic cells pattern, which will be 3D-modelled into the surface wave antenna structure in CST. And the near-zone *E*-field and far-field radiation pattern generated by the electromagnetic (EM) wave simulation results from CST will be used to verify the neural network prediction. The performance, S_{11} and radiation pattern, of the fabricated antenna prototype will be validated in the anechoic chamber.

In order to demonstrate the angular coverage range of the dual-sided cosecant-squared radiation pattern that the proposed neural network prediction models can predict, dual-sided 10º, 20º and 40º cosecant-squared radiation pattern will be applied to the neural network prediction model to design the antennas. In the neural network prediction models, only the positions and lengths of the metallic cells of the proposed antenna are considered as the adjustable parameters. The angular separation between radial rows of the metallic cells and the shape of the metallic cells can also be tuned to have different far-field radiation patterns. Therefore, only considering the positions and lengths of metallic cells of the antenna limits the diversity of the radiation pattern that the antenna can generate. These limitations regarding the angular separation of the radial rows and the shape of metallic cells will be analysed and discussed.

5.1 Cosecant-squared radiation pattern antenna

As described in Chapter 1, the antenna used in the mmWave VLR system is a scalar feed horn antenna with the gain enhancement of a Gaussian lens. By adjusting the feed horn, the main beam of the antenna is offset from the vertical axis by 0.18°. With the help of the turntable underneath, this 0.18° offset can form a conical beam, as shown in Figure 5.1 (a). However, it can only offer a very narrow circular observation area, which is 1.2 m in diameter. Due to its high gain and narrow 3 dB beamwidth, the received power fluctuates when insects fly through the beam area. Therefore, a dual-sided cosecant-squared radiation pattern surface wave antenna is proposed to obtain a large observation area and constant receiving power. Such dual-sided cosecant-squared radiation pattern antenna does not have any antenna tilting, and the reliability and repeatability are higher.

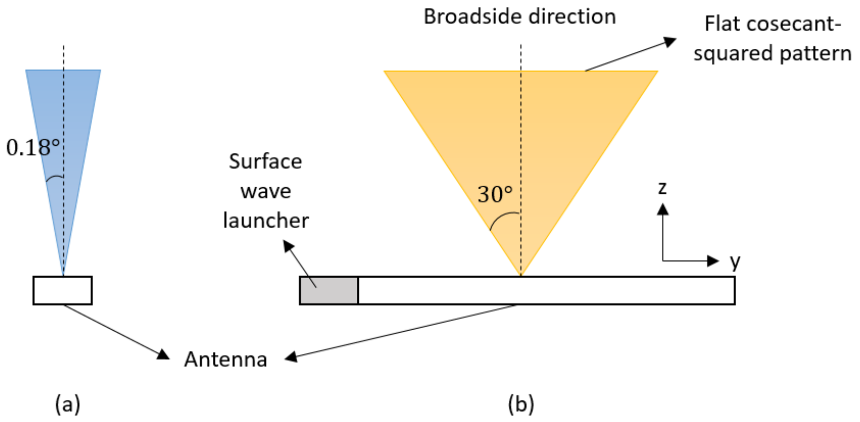

Figure 5.1. The beam diagram of (a) existing antenna in the mmWave VLR and (b) proposed surface wave antenna.

Figure 5.1 (b) shows the beam area of the proposed flat cosecant-squared radiation pattern surface wave antenna. In this design, a dual-sided 30° cosecant-squared radiation pattern in *yz*-plane is used to offer the flat pattern in the far-field. The dual-sided cosecant-squared radiation pattern is formed by symmetrically aligning two single 30° range cosecant-squared radiation patterns around the broadside direction of the radiation pattern. The single 30° cosecant-squared radiation pattern is selected to offer the flat beam without tilting the antenna, and the symmetrical arrangement can provide the flat pattern across the broadside direction. This flat radiation pattern can offer a more constant signal strength as a target moves at a constant height within the beam. And this will benefit the data processing of the mmWave VLR system.

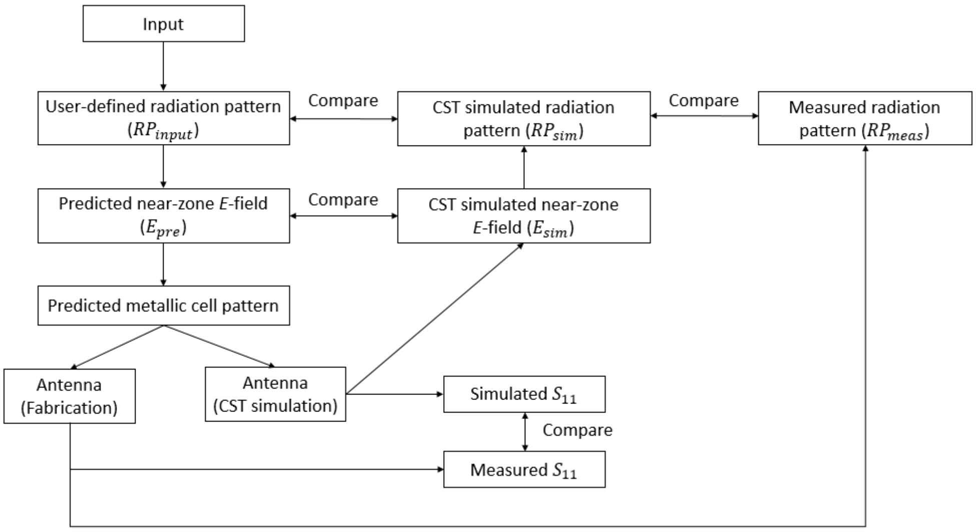

Figure 5.2. Diagram of surface wave antenna design and verification.

This section is organised by the diagram shown in Figure 5.2. The dual-sided cosecant-squared radiation pattern acts as the user-defined radiation pattern (RP_{input}), which is used as the input of the near-zone E-field prediction models to generate the corresponding near-zone E-field (E_{pre}). This E_{pre} will be the input of the metallic cell pattern prediction model. Once the metallic cell pattern of the dual-sided cosecant-squared radiation pattern is generated, it will be modelled in CST simulation software. The simulated near-zone E-field E_{sim} and radiation pattern RP_{sim} results extracted from CST will then be compared with E_{pre} and RP_{input} respectively to verify the accuracy of the proposed neural network prediction models. The antenna prototype will be fabricated for measurement. The measured results of the surface wave antenna prototype will be evaluated and the measured results will be compared with the EM simulation results.

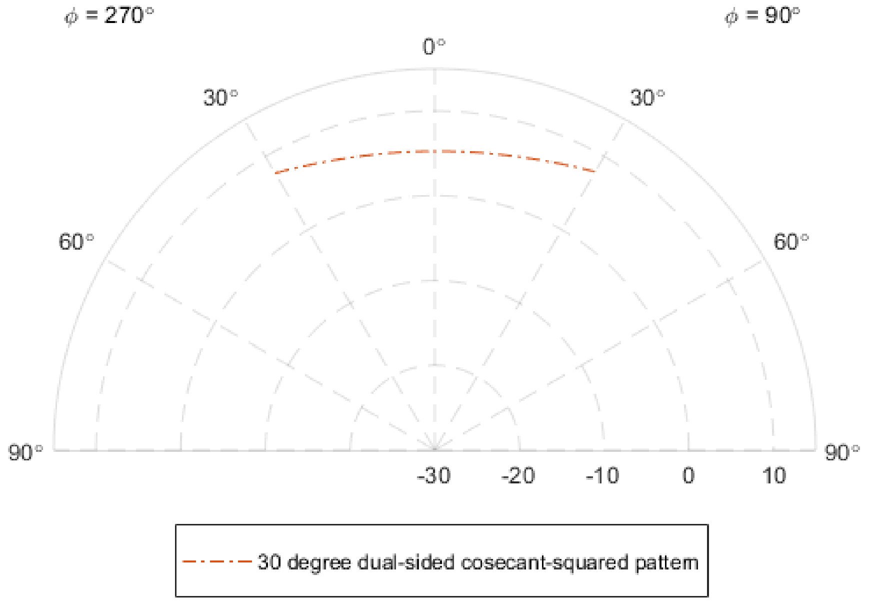

Figure 5.3. The input dual-sided 30º cosecant-squared radiation pattern.

Figure 5.3 shows the user-defined dual-sided 30º cosecant-squared radiation pattern (RP_{input}). The input radiation pattern only regulates the dual-sided 30º range, whereas the range beyond the dual-sided 30º does not have any regulation. At the present stage, this research mainly focuses on the radiation pattern in the *yz*-plane. The 30º dual-sided cosecant-squared radiation pattern is served as the input to the neural network prediction models without considering the radiation pattern outside the range. The outside range is defined as the range of θ that are not included within the dual-sided cosecant-squared radiation pattern angular range in the *yz*-plane. The corresponding near-zone *E*-field and the metallic cell pattern can then be predicted after feeding the dual-sided 30º cosecant-squared radiation pattern into the prediction models. The neural network prediction results and the EM simulation results will be shown in the following sections.

5.1.1 Results of the neural network prediction models

The results of the neural network prediction models are divided into two parts, which are the predicted near-zone *E*-field and the predicted metallic cell pattern. By feeding the ideal cosecant-squared radiation pattern into the near-zone *E*-field neural network prediction models, the neural network models predict all three components of the near-zone *E*-field (E_x, E_y and E_z) on the lines at (0, *y*, 0.12λ_0) and (0.12λ_0, *y*, 0.5λ_0). The predicted near-zone *E*-field components of two positions are shown in Figure 5.4 and Figure 5.5 respectively. From the figures, it can be observed that the E_x component is relatively small compared with the other two components. Due to the unknown near-zone *E*-field corresponding to the input cosecant-squared radiation pattern, the accuracy of the prediction cannot be evaluated and verified until the metallic cell pattern is predicted and 3D-modelled in CST for generating the EM simulation results. Therefore, the prediction accuracy of the near-zone *E*-field will be evaluated later in this section.

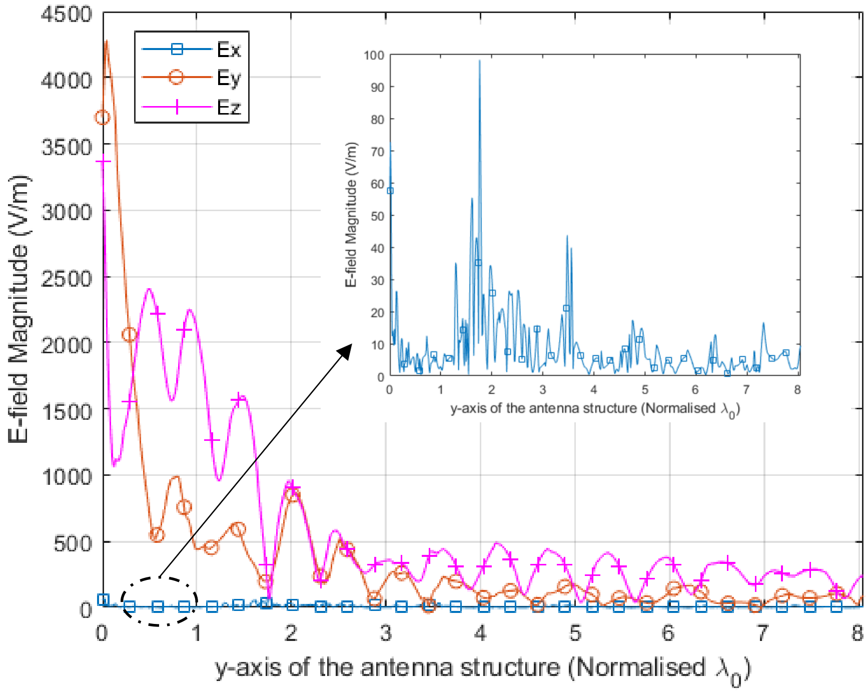

Figure 5.4. The predicted near-zone *E*-field on the line at (0, *y*, 0.12λ_0).

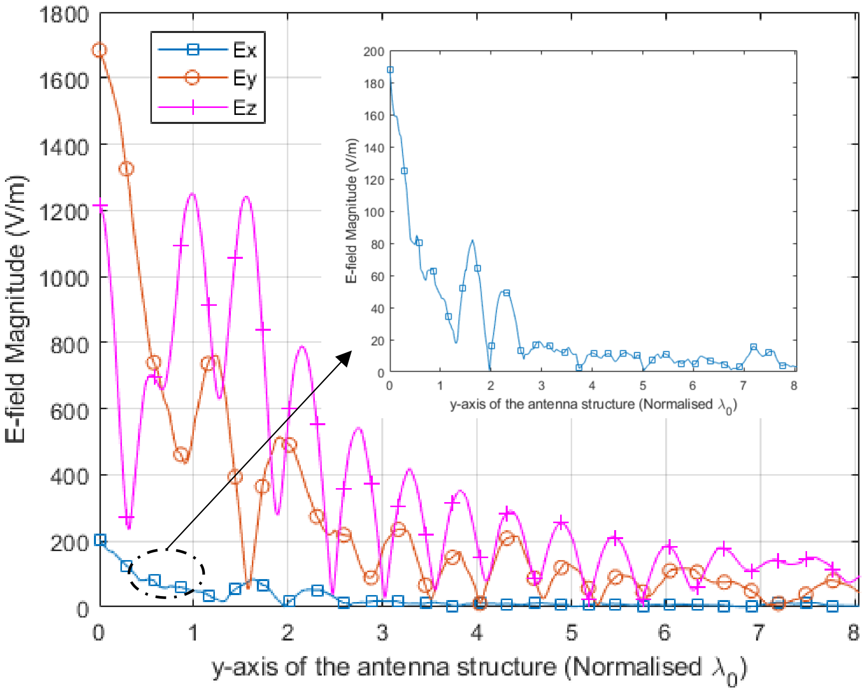

Figure 5.5. The predicted near-zone *E*-field on the line at ($0.12\lambda_0$, *y*, $0.5\lambda_0$).

After obtaining the predicted near-zone *E*-field, the metallic cell pattern neural network prediction model is utilised to generate the corresponding metallic cell pattern on the antenna surface. And the metallic cell pattern of the central radial row is shown in Figure 5.6. The metal on or off denotes the value 1 or 0 in the figure, where 1 means there is metal and 0 indicates no metal at that point. Therefore, the distribution of the metallic cell of the surface wave antenna can be designed according to the value on the *y*-axis.

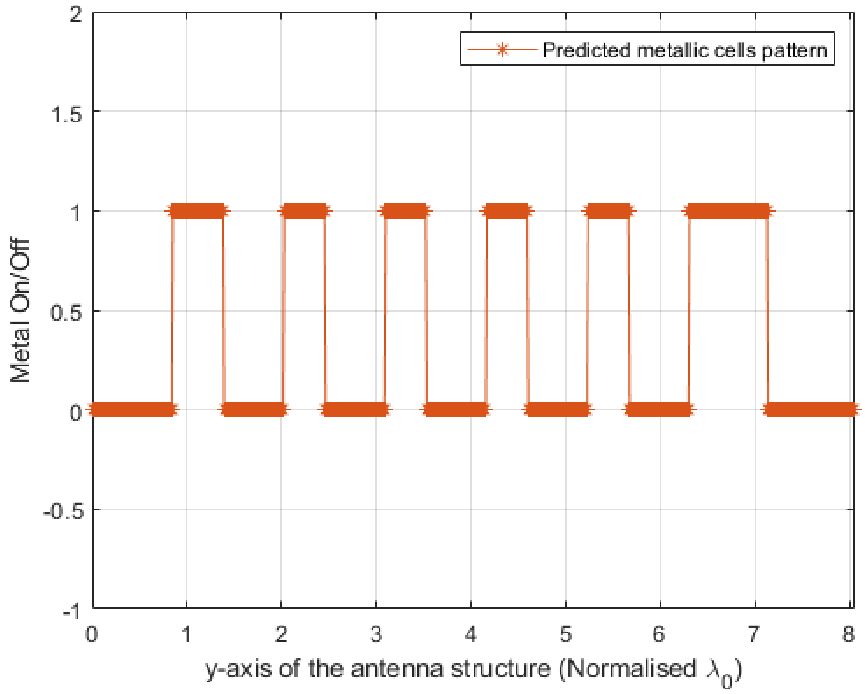

Figure 5.6. The predicted metallic cell pattern of the central radial row.

5.1.2 EM simulation results

Once the positions of the metallic cells in the central radial row are obtained, the rest of the rows can be defined according to the position relationship between the radial rows. The first and fifth radial rows have the same metallic cell patterns as the central radial row but with a 10º angular separation from the central row. The radial positions of the metallic cells of the rows next to the central row are determined by the positions of gaps in the central row and are 5º angularly separated from the central row. With the predicted metallic cell pattern, the cosecant-squared radiation pattern surface wave antenna can be designed. The proposed 30º dual-sided cosecant-squared radiation pattern surface wave antenna is shown in Figure 5.7.

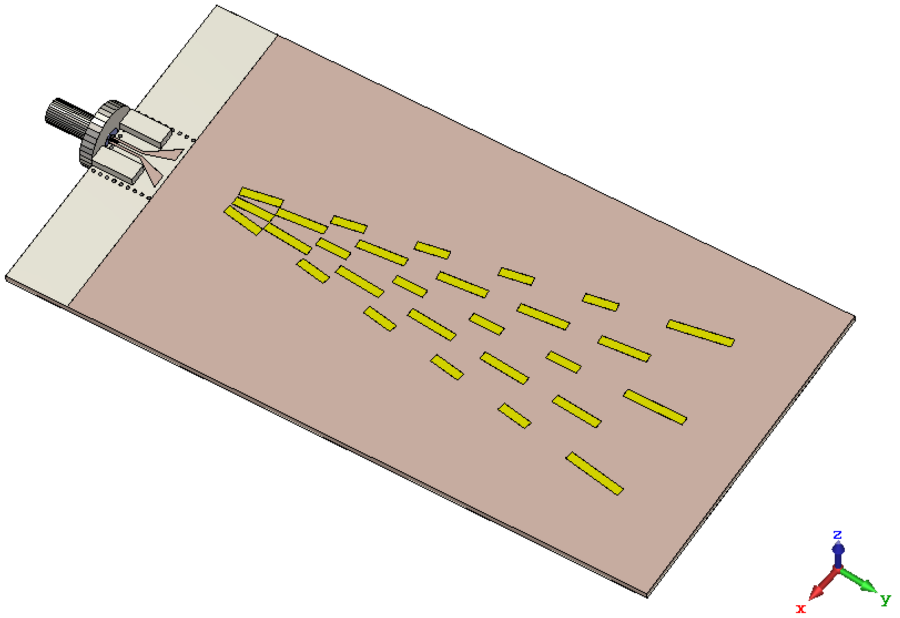

Figure 5.7. The 30° dual-sided cosecant-squared radiation pattern surface wave antenna.

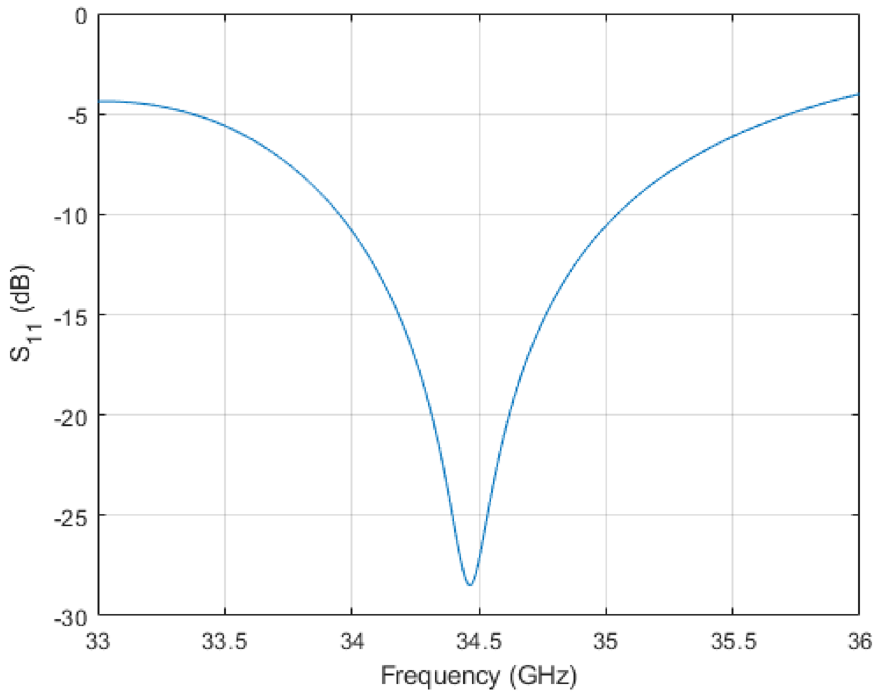

Figure 5.8. Simulated S_{11} of the surface wave antenna.

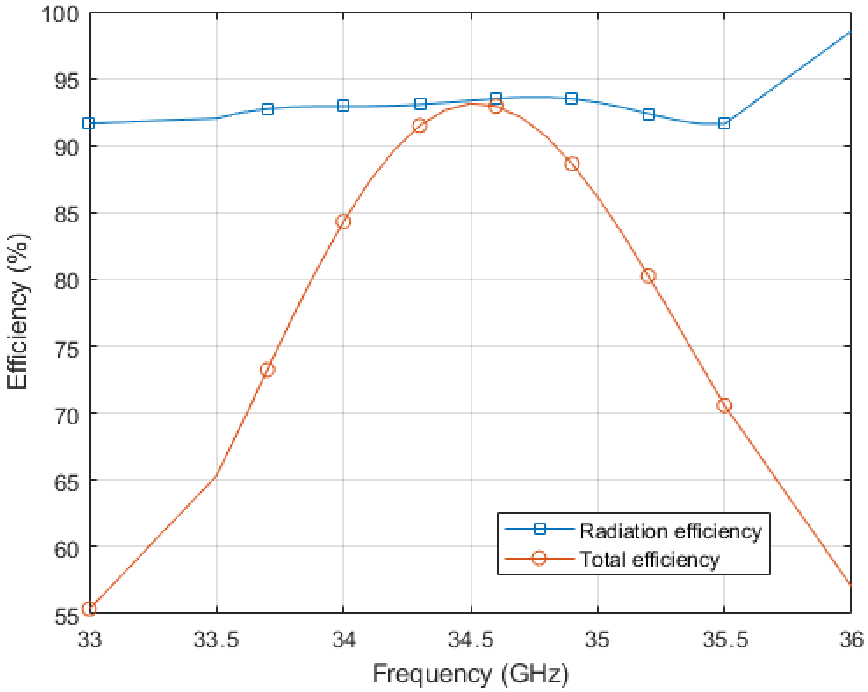

Figure 5.9. The radiation and total efficiency of the surface wave antenna.

The simulated S_{11} is shown in Figure 5.8, and it shows the operating bandwidth of 3.2% from 33.95 GHz to 35.05 GHz (centred at 34.5 GHz), which covers the operating frequency band of the mmW VLR system. The S_{11} at 34.5 GHz is -27.26 dB. Figure 5.9 shows the radiation and total efficiency of the surface wave antenna. The simulated total efficiency and the radiation efficiency at 34.5 GHz are 93.34% and 93.14% respectively. Within the frequency band from 34 to 35 GHz, the total efficiency of the surface wave antenna is over 84.31%.

The CST simulated near-zone *E*-field results of the two positions of the field monitor array are compared with the predicted version and the comparison results are shown from Figure 5.10 to Figure 5.15. The predicted and simulated near-zone *E*-field shows a reasonable degree of consistency and the discrepancies in percentage between them are shown in Table 5.1. Ideally, the predicted and the simulated near-zone *E*-field should be the same because the CST uses the metallic cell pattern produced by the predicted near-zone *E*-field in the simulation. The discrepancies mainly come from the decision-making mechanism in the metallic cell pattern prediction neural network model. The metallic cell pattern prediction is considered as a classification problem. The neural network model produces a number between 0 and 1 as the output and this number is compared with the threshold (0.5) to produce the final decision, which is the metal on or off. Any value that is larger than the threshold will be considered as metal on. For example, the output value of 0.5 and 0.6 shows the same result, even they are calculated from different near-zone *E*-field values. Similar near-zone *E*-field values could generate the same metallic cell pattern. In this comparison, the averaged discrepancy value among E_x, E_y and E_z components of two positions is 6.22%, which is acceptable. The discrepancy is defined as the averaged value of the ratio of the difference between simulation and prediction to simulated values.

Table 5.1. The discrepancies between the predicted and simulated near-zone *E*-field.

	Position 1 (0, y, 0.12λ_0)			Position 2 (0.12λ_0, y, 0.5λ_0)		
E-field	E_x	E_y	E_z	E_x	E_y	E_z
Discrepancies	8.87%	4.21%	3.85%	8.7%	5.38%	6.29%

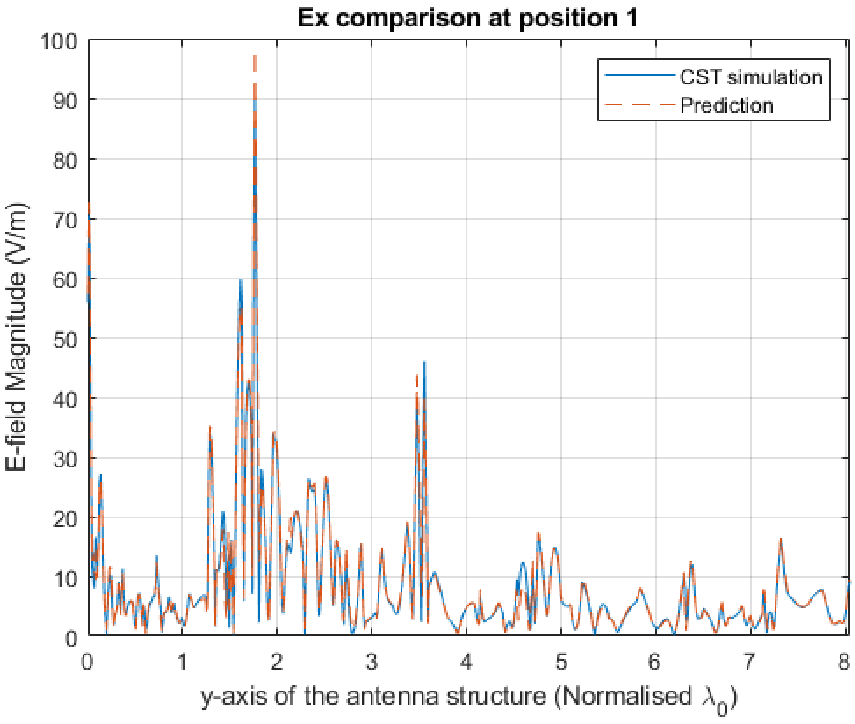

Figure 5.10. E_x comparison on the line at (0, y, 0.12λ_0).

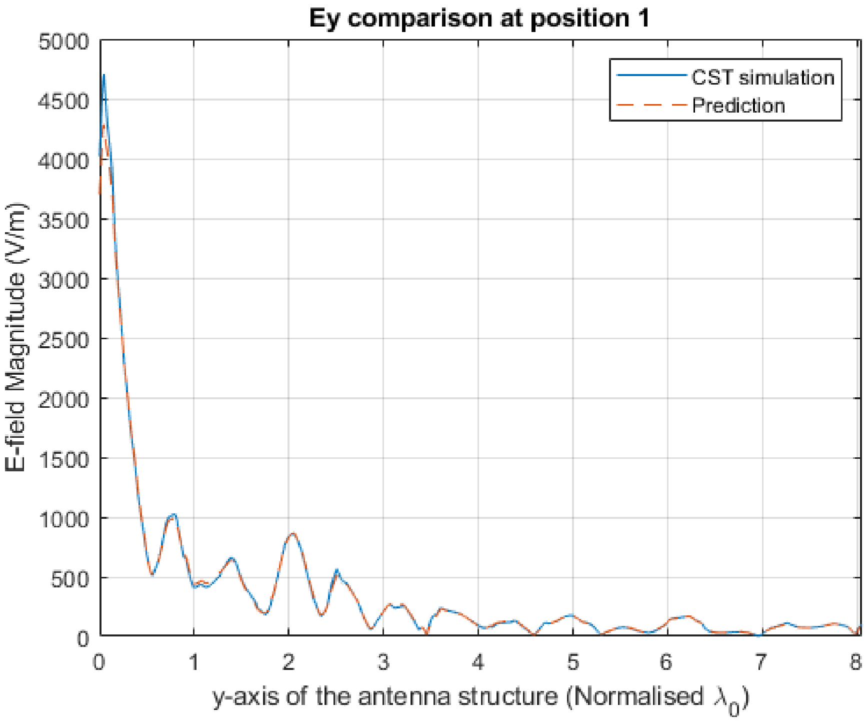

Figure 5.11. E_y comparison on the line at $(0, y, 0.12\lambda_0)$.

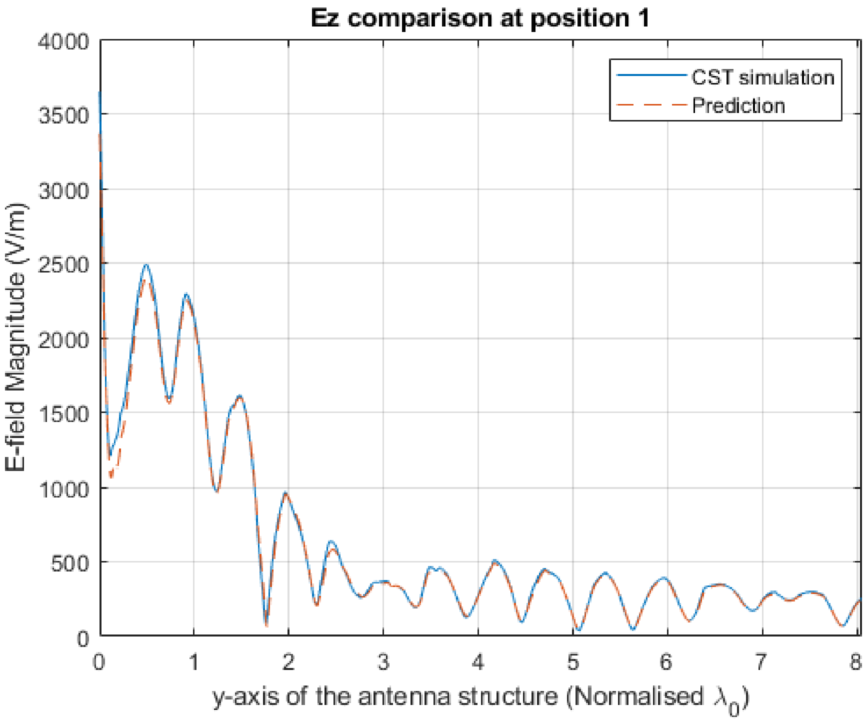

Figure 5.12. E_z comparison on the line at $(0, y, 0.12\lambda_0)$.

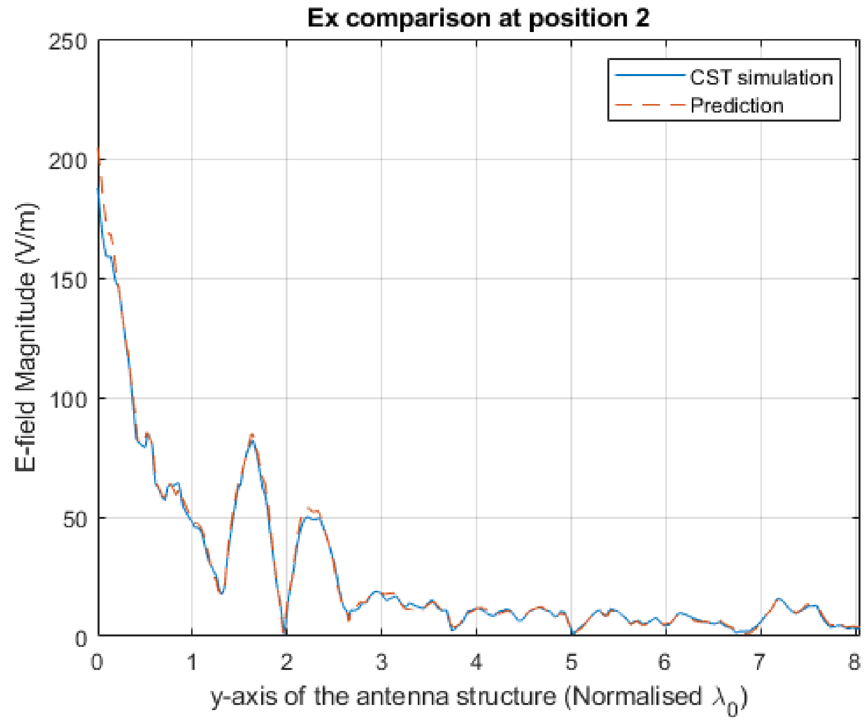

Figure 5.13. E_x comparison on the line at ($0.12\lambda_0$, y, $0.5\lambda_0$).

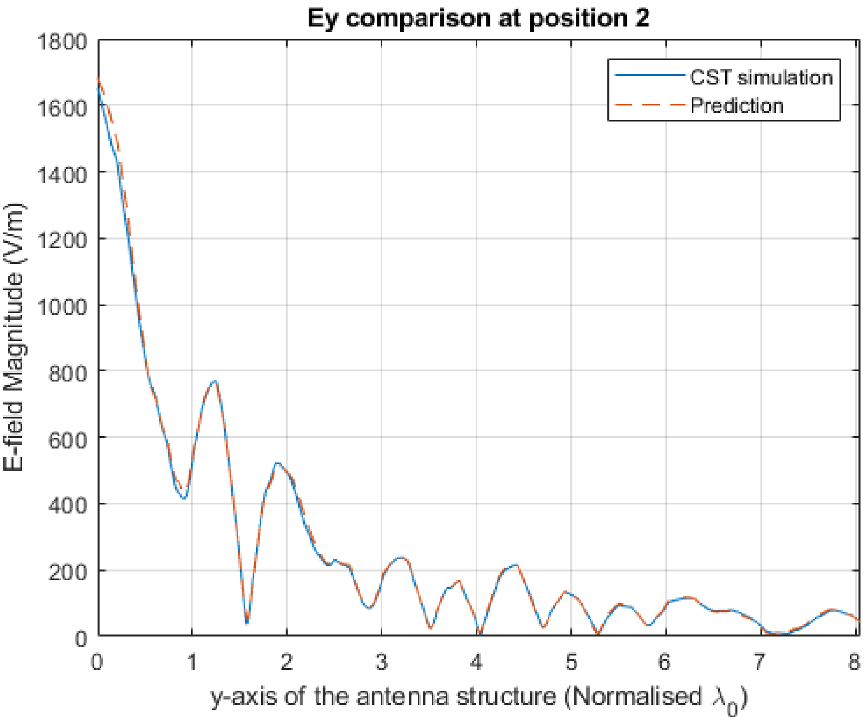

Figure 5.14. E_y comparison on the line at ($0.12\lambda_0$, y, $0.5\lambda_0$).

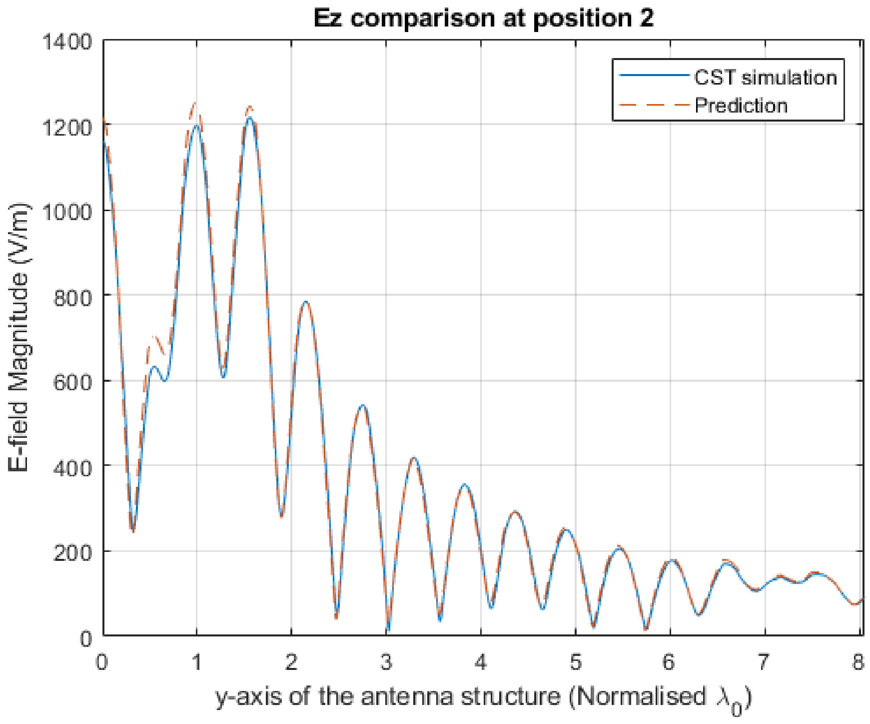

Figure 5.15. E_z comparison on the line at $(0.12\lambda_0, y, 0.5\lambda_0)$.

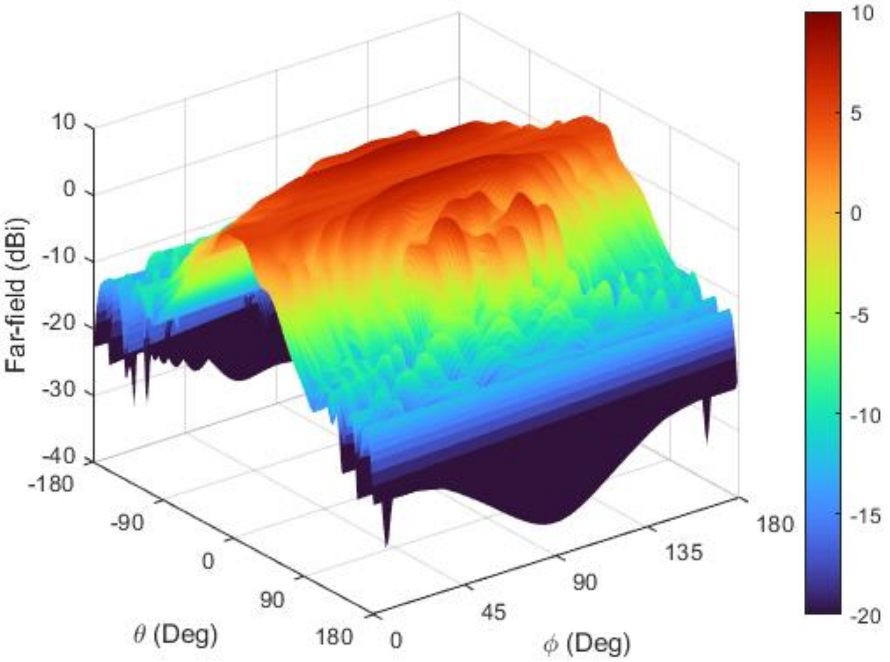

Figure 5.16. The 3D far-field radiation pattern of the surface wave antenna at 34.5 GHz.

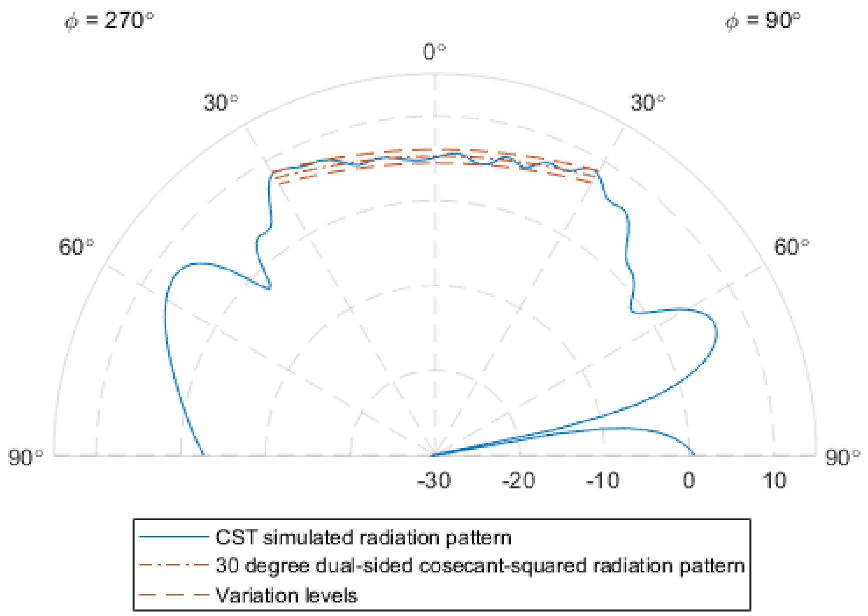

Figure 5.17. The far-field radiation pattern (*yz*-plane) of the surface wave antenna at 34.5 GHz.

Figure 5.16 shows the 3D far-field radiation pattern of the 30° dual-sided cosecant-squared radiation pattern surface wave antenna. For θ less than 0, the minus sign represents the plane of $\phi = 360^\circ - \phi_i$, where ϕ_i, is the value on the ϕ-axis. If $\phi = 90^\circ$ is selected, $\theta = (0, -180^\circ)$ means $(\phi, \theta) = (270^\circ, 0^\circ)$ to $(270^\circ, 180^\circ)$. Figure 5.17 shows the corresponding plane (from $(\phi, \theta) = (270^\circ, 90^\circ)$ to $(90^\circ, 90^\circ)$) radiation pattern of the predicted surface wave antenna at 34.5 GHz. At the present stage, only the 30° dual-sided cosecant-squared radiation pattern is used to regulate the far-field radiation pattern in the neural network prediction models. The radiation pattern outside the cosecant-squared radiation pattern range is not considered due to the fact that only metallic cells distribution of surface wave antenna is utilised as the studying parameter to the prediction models. The shape of the metallic cell and the angular separation between radial rows would be additional studying parameters to the prediction models. With more studying parameters, the neural network prediction models will gain more flexibility and become more robust to regulate the outside range radiation pattern. And this will be discussed in section 5.3.

The ideal 30º dual-sided cosecant-squared radiation pattern is set as the goal to the neural network models. From Figure 5.17, it can be observed that the CST simulated radiation pattern is within ± 1dBi variation from the ideal cosecant-squared radiation pattern in the range from (ϕ, θ) = (270º, 30º) to (90º, 30º). The maximum gain is 8.49 dBi at (ϕ, θ) = (90º, 29º). This radiation pattern improves the diameter of the circular observation range from 1.2 m of the original scalar feed horn antenna to 9.8 m.

5.1.3 Experimental results

After EM simulation verification, the surface wave antenna is fabricated and evaluated. As the operating frequency of the antenna is 34.5 GHz (λ_0 = 8.69 mm), therefore, the laser-cutting technology is used to fabricate the antenna to guarantee the fabrication precision. The main dimensions of the antenna are recapped for the readers. The total length of the surface wave antenna is 77.56 mm and the length from the front edge of the surface wave launcher to the far end is 70 mm. The width of the antenna is 40 mm. In the surface wave launcher area, the diameter and the separation of the via holes are 0.4 mm and 0.45 mm respectively. The central pin of the feed line has a width of 0.3 mm and the gaps next to it is 0.2 mm. This has been confirmed under the microscope to ensure the dimension of the fabricated antenna is the same as the simulation.

From Figure 5.18, it can be seen that the fabricated antenna is 70.5 mm in length from the front edge of the surface wave launcher and the length in the launcher area is around 7.5 mm. Figure 5.19 shows the dimensions of the surface wave launcher. The central pin width is 0.3 mm and the gap next to it is 0.2 mm, which are the same as the simulation. The diameter and gap of the via holes agree with the simulation as well. The prototype is then fixed into the anechoic chamber to test the far-field characteristics. The experiment setup is shown in Figure 5.20. A 90º aluminium arm is utilised to hang the high-frequency (5 – 50 GHz) dual-ridge horn antenna. The motor inside the white pillar drives the aluminium arm to rotate for measuring the surface wave antenna. In this research, the surface wave antenna is designed to monitor high-flying insects. Therefore, only the upper half of the radiation pattern is supposed to be measured.

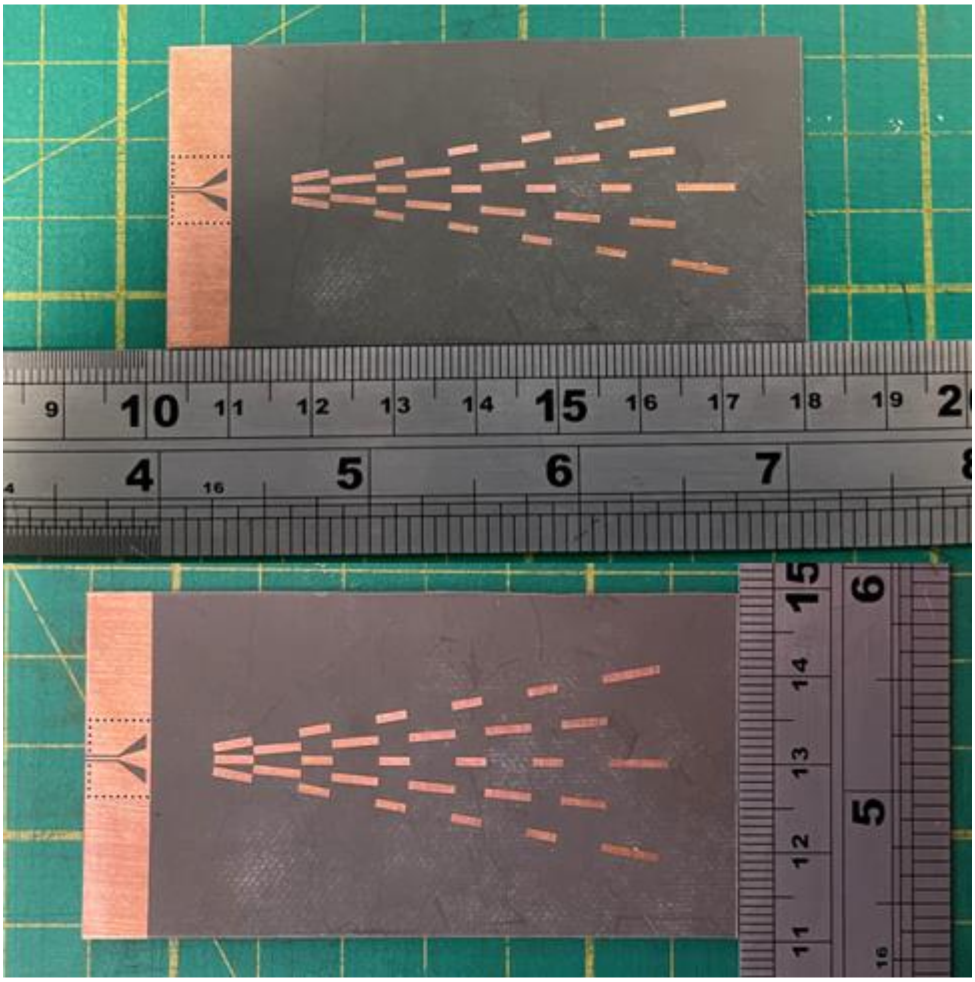

Figure 5.18. Dimensions of the fabricated prototype of the surface wave antenna.

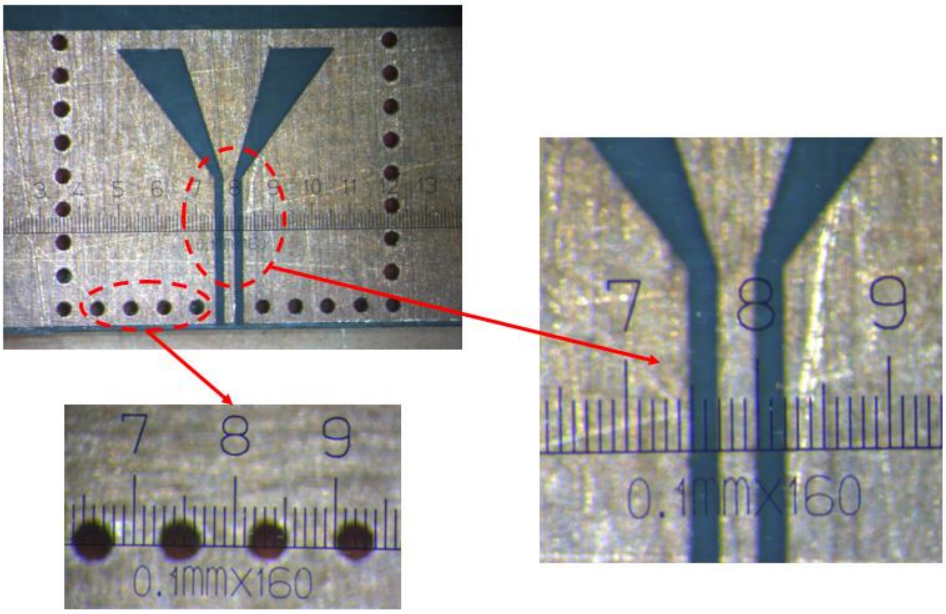

Figure 5.19. Dimensions of the surface wave launcher.

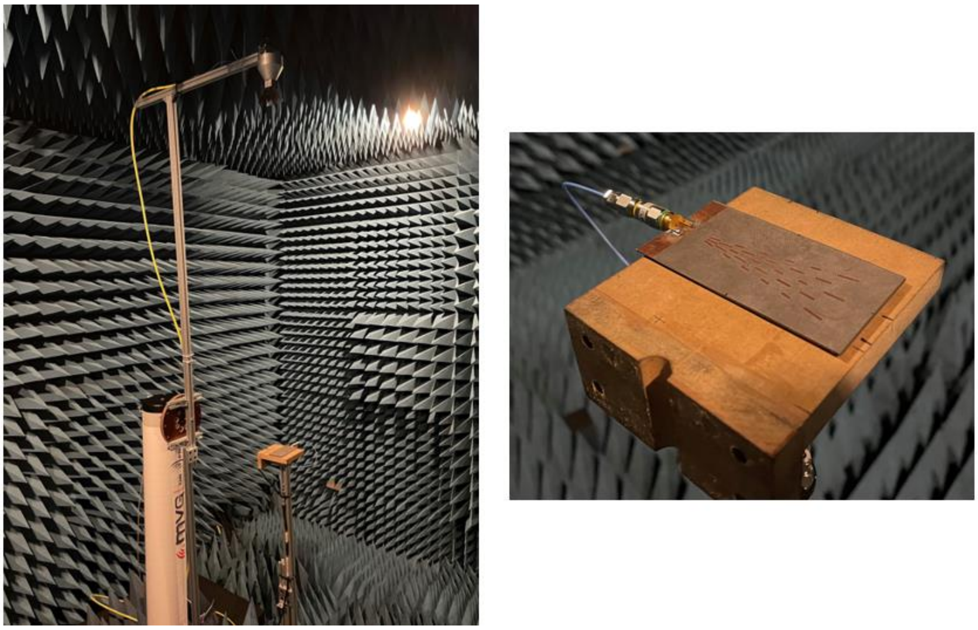

Figure 5.20. Experiment setup in the anechoic chamber.

Figure 5.21 shows the reasonable agreement of the S_{11} between the simulation and measurement. The operating bandwidth of the measurement is 3.74%, which is similar to the simulation bandwidth (3.2%). The measured S_{11} is -22.63 dB at 34.5 GHz, which is 4.63 dB difference from the simulation. However, considering the -20 dB level, 4.63 dB difference, which may be caused by the insertion loss of the connectors, does not show significant difference regarding the performance. In Figure 5.22, the simulated and measured gain at (ϕ, θ) = (90º, 30º) of the surface wave antenna has been compared. It shows a similar trend from 34 GHz to 35 GHz. The difference at 34.5 GHz is around 0.5 dBi and the average gain difference is 0.36 dBi within the operating frequency band. This measurement error is acceptable when considering the fact that the operating frequency of the antenna is 34.5 GHz.

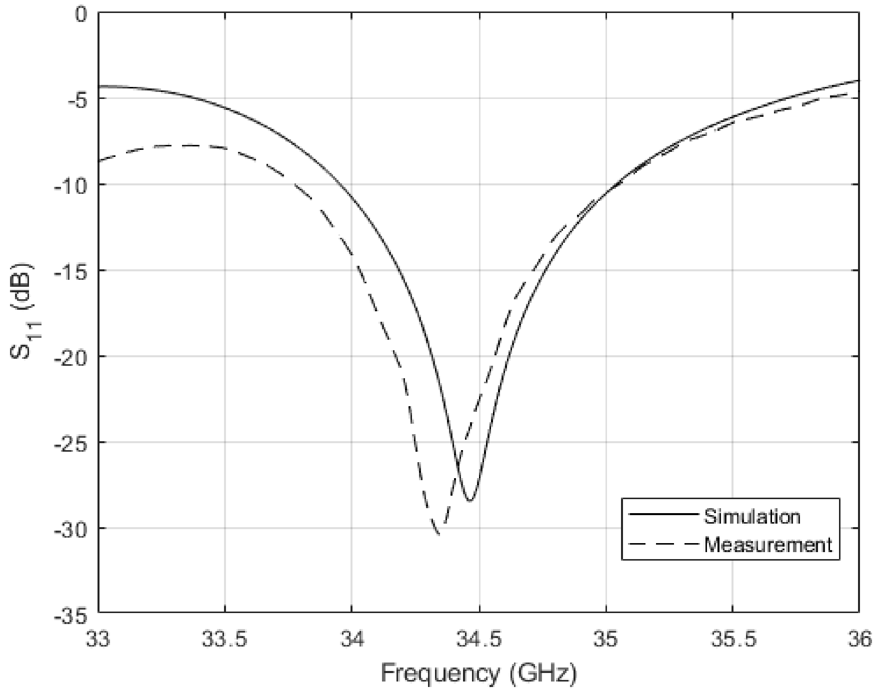

Figure 5.21. Simulated and measured S_{11} of the surface wave antenna.

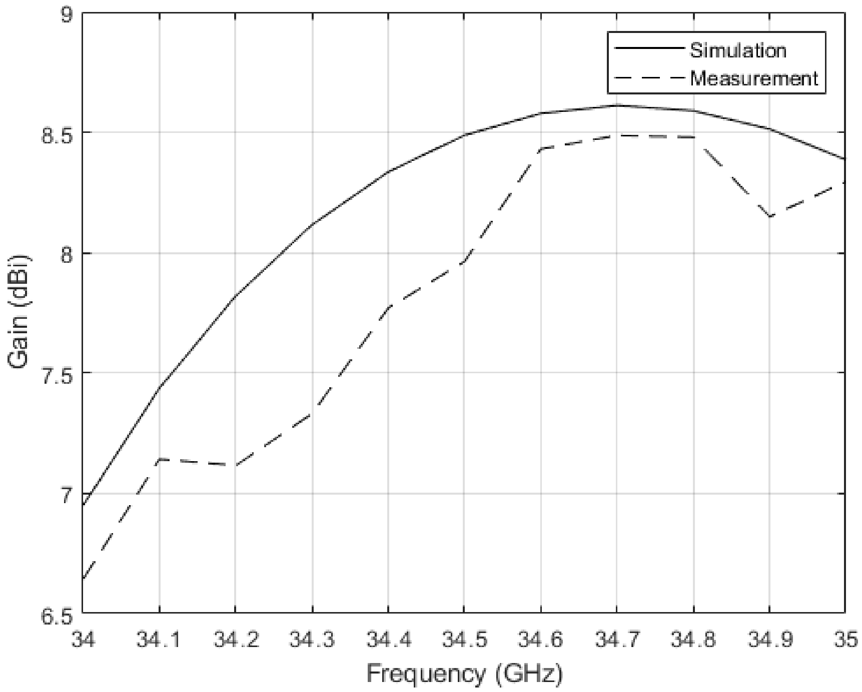

Figure 5.22. Simulated and measured gain at (ϕ, θ) = (90º, 30º) of the surface wave antenna.

The normalised simulated and measured *E*-plane (*yz*-plane) and *H*-plane (*xz*-plane) radiation pattern at 34 GHz, 34.5 GHz and 35 GHz are presented from Figure 5.23 to Figure 5.28. Both *E*-plane and *H*-plane co-polarisation show a good degree of consistency between the measurement and simulation. In the *E*-plane comparison, it can be observed that the measured cross-polarisation is less than -20 dB, which means the antenna is linearly polarised. It should be mentioned that the simulation results of *E*-plane cross-polarisation are shown as a square at -40 dB since they are less than -70 dB. This is because the CST simulation is ideal without considering the small deviation in symmetry in the practical fabrication and the loss in the experiment. In the *H*-plane comparison, the measured results co-polarisation is similar to the simulation, while the cross-polarisation shows larger discrepancies. The reason is that there are different types of losses, such as connection loss and cable loss, during the experimental operation. And the minor asymmetry introduced to the prototype in the fabrication also contributes to the discrepancy.

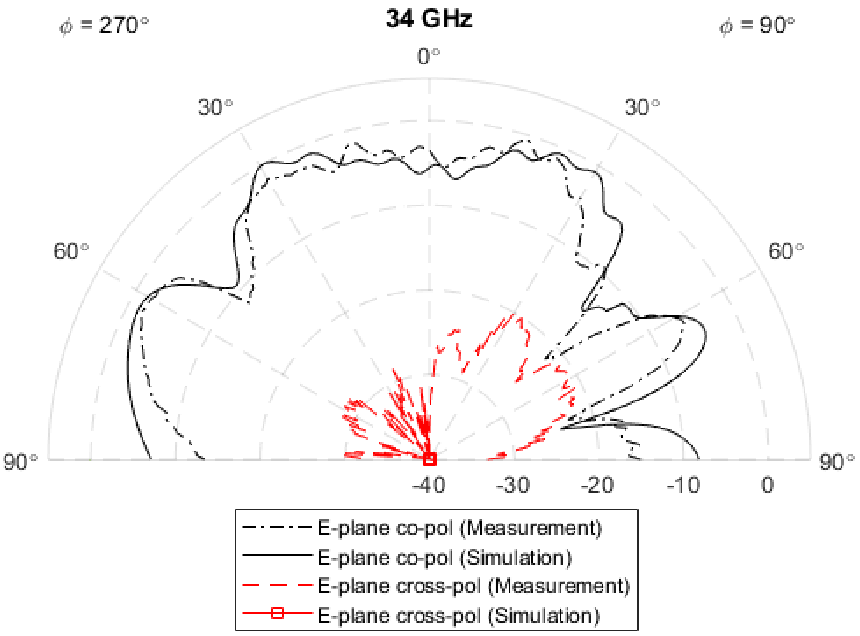

Figure 5.23. Simulated and measured *E*-plane at 34 GHz.

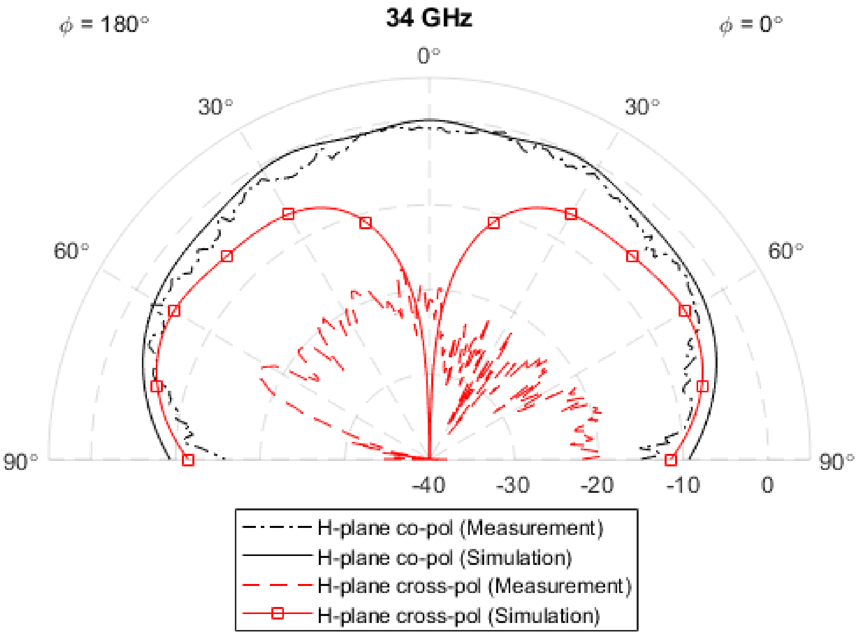

Figure 5.24. Simulated and measured *H*-plane at 34 GHz.

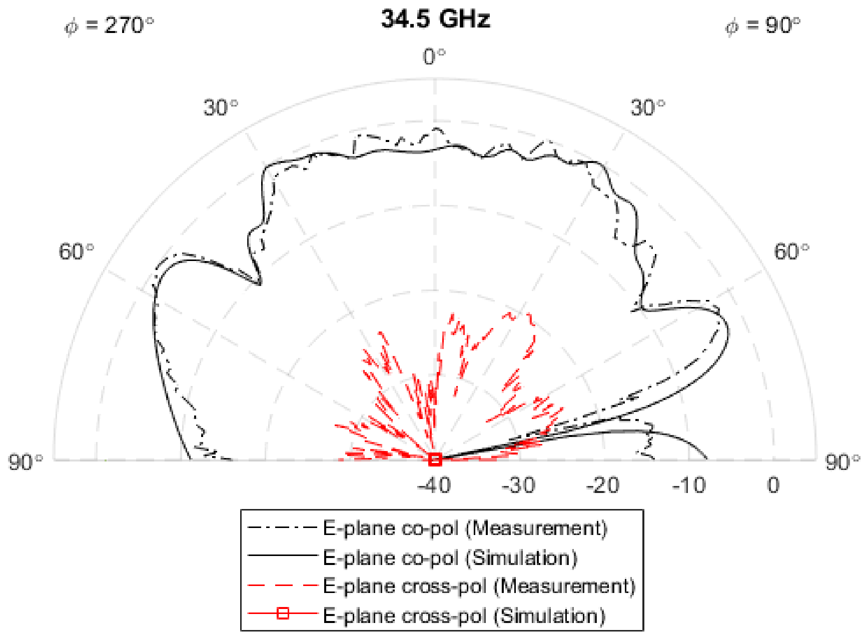

Figure 5.25. Simulated and measured *E*-plane at 34.5 GHz.

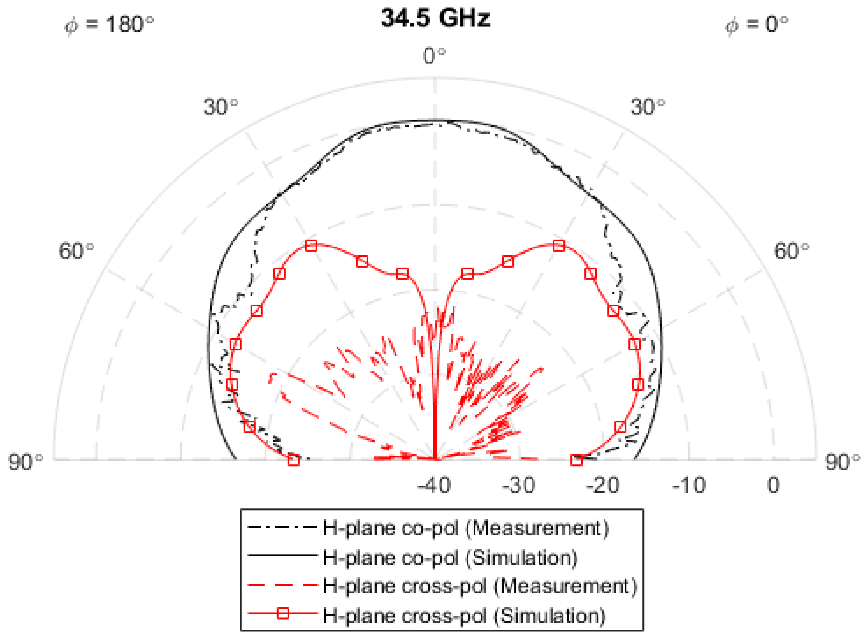

Figure 5.26. Simulated and measured *H*-plane at 34.5 GHz.

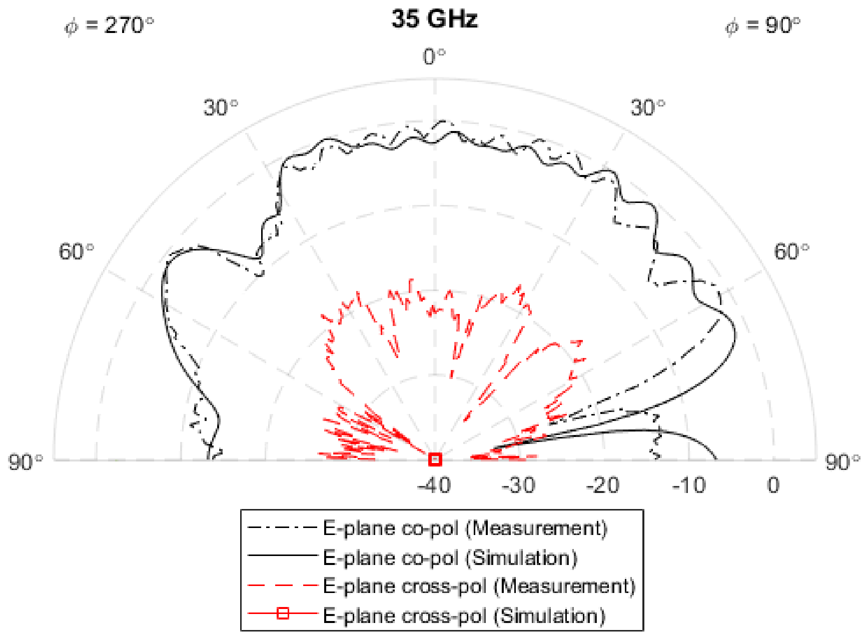

Figure 5.27. Simulated and measured *E*-plane at 35 GHz.

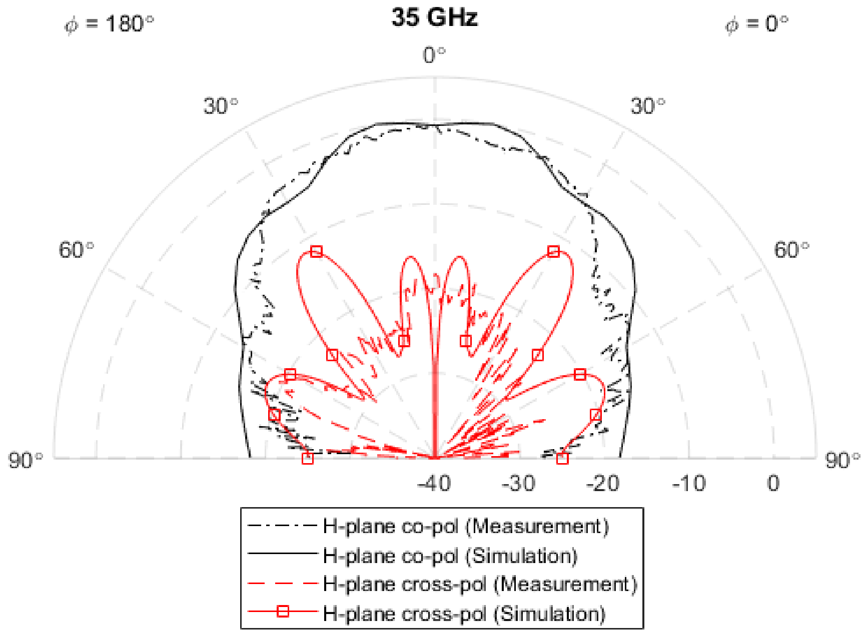

Figure 5.28. Simulated and measured *H*-plane at 35 GHz.

The neural network prediction focuses on 34.5 GHz, and the *E*-plane and *H*-plane comparison at 34.5 GHz verifies the feasibility of the proposed neural network prediction method. In Figure 5.25, the *E*-plane co-polarisation comparison between simulation and measurement shows good consistency. The main discrepancies come from the range (ϕ, θ) = (270°, 15°) to (90°, 3°) and (90°, 30°) to (90°, 45°). This may be caused by the measurement surroundings in the anechoic chamber. The aluminium arm in Figure 5.20 may introduce reflection to the antenna-under-test. Due to the limited torque of the motor in the pillar, the weight of the aluminium arm should be as light as possible. Therefore, it is challenging to attach absorbers to the aluminium arm to reduce the reflection. Although discrepancies exist between measurement and simulation in the *E*-plane co-polarisation, the measured results show the feasibility of the proposed neural network method. In the next section, the angular coverage range that the proposed neural network method can predict will be shown.

5.2 The angular coverage range of the dual-sided cosecant-squared radiation pattern

The dual-sided 30° cosecant-squared radiation pattern is utilised as the user-defined radiation pattern input to the proposed neural network prediction models. The predicted near-zone *E*-field and metallic cell pattern on the antenna surface are verified by the CST simulation. The simulated far-field radiation pattern shows less than 1 dBi variation from the input cosecant-squared radiation pattern. The neural network prediction method is feasible to predict the metallic cell pattern and design the surface wave antenna according to the desired radiation pattern. In this section, 10° and 20° dual-sided cosecant-squared radiation patterns will be the input pattern to investigate the angular coverage range that the neural network prediction models can predict.

By using the 10° and 20° dual-sided cosecant-squared radiation pattern as the input pattern, the neural network prediction model gives the corresponding near-zone *E*-field and metallic cell pattern on the surface. The predicted near-zone *E*-field of the 10º dual-sided case results are shown in Figure 5.29 and Figure 5.30. The prediction is similar to the simulation with acceptable discrepancies and the discrepancies are shown in Table 5.2. The average value of the discrepancies is 6.42%. For the 20º dual-sided case, the predicted near-zone *E*-field results are shown in Figure 5.31 and Figure 5.32. The numerical results of the comparison are shown in Table 5.3 and the average difference between the CST simulation and the neural network prediction is 5.65%. The metallic cell pattern is predicted after obtaining the near-zone *E*-field data. And the predicted central row +metallic cell pattern of 10º and 20º dual-sided cases are shown in Figure 5.33 and Figure 5.34. The predicted metallic cell pattern is used to design the surface wave antenna in CST. After simulation, the far-field radiation pattern at 34.5 GHz is used to compare with the input dual-sided cosecant-squared radiation pattern to verify the angular coverage range that the proposed neural network model can predict.

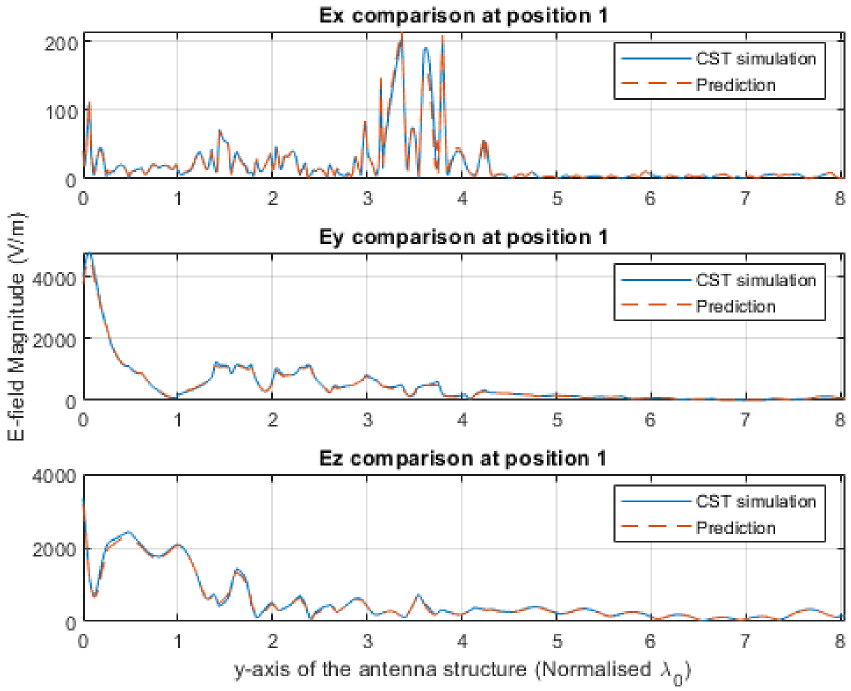

Figure 5.29. E_x, E_y, and E_z comparison on the line at (0, *y*, 0.12λ_0) of 10º dual-sided case.

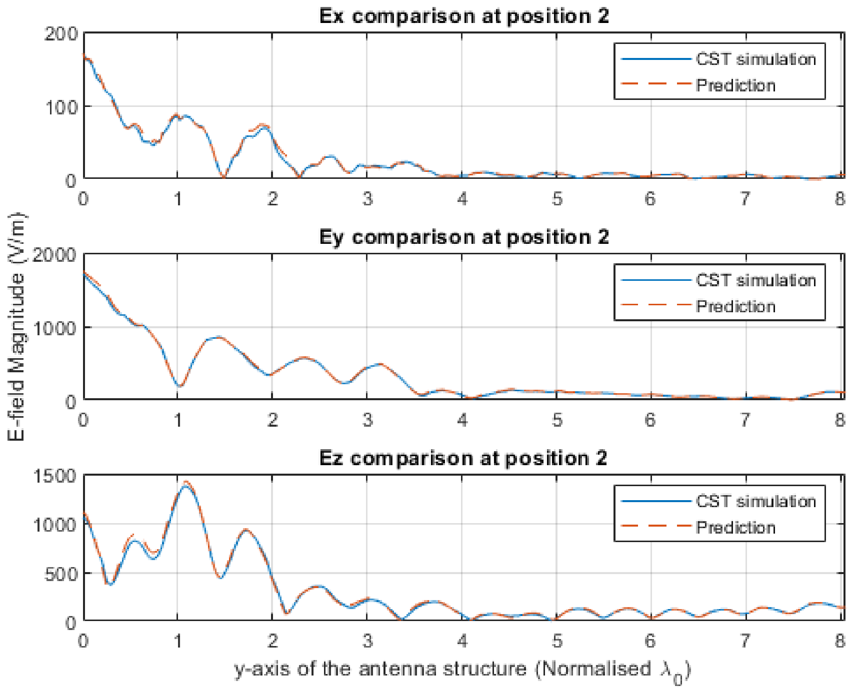

Figure 5.30. E_x, E_y, and E_z comparison on the line at $(0.12\lambda_0, y, 0.5\lambda_0)$ of 10° dual-sided case.

Table 5.2. The discrepancies between the predicted and simulated near-zone *E*-field (10° dual-sided case).

	Position 1 $(0, y, 0.12\lambda_0)$			Position 2 $(0.12\lambda_0, y, 0.5\lambda_0)$		
E-field	E_x	E_y	E_z	E_x	E_y	E_z
Discrepancies	8.36%	4.58%	4.54%	8.19%	4.31%	8.52%

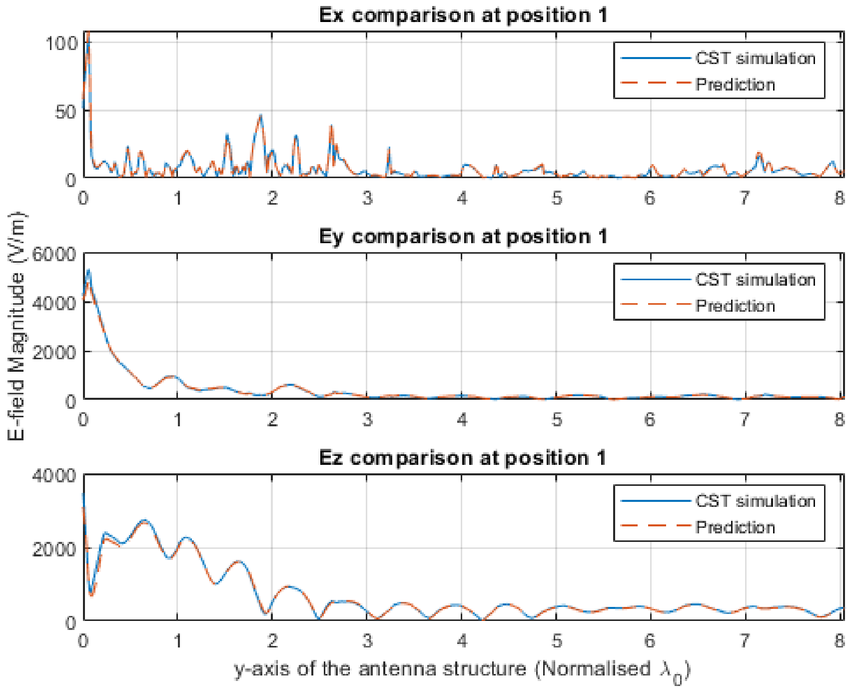

Figure 5.31. E_x, E_y, and E_z comparison on the line at (0, y, $0.12\lambda_0$) of 20° dual-sided case.

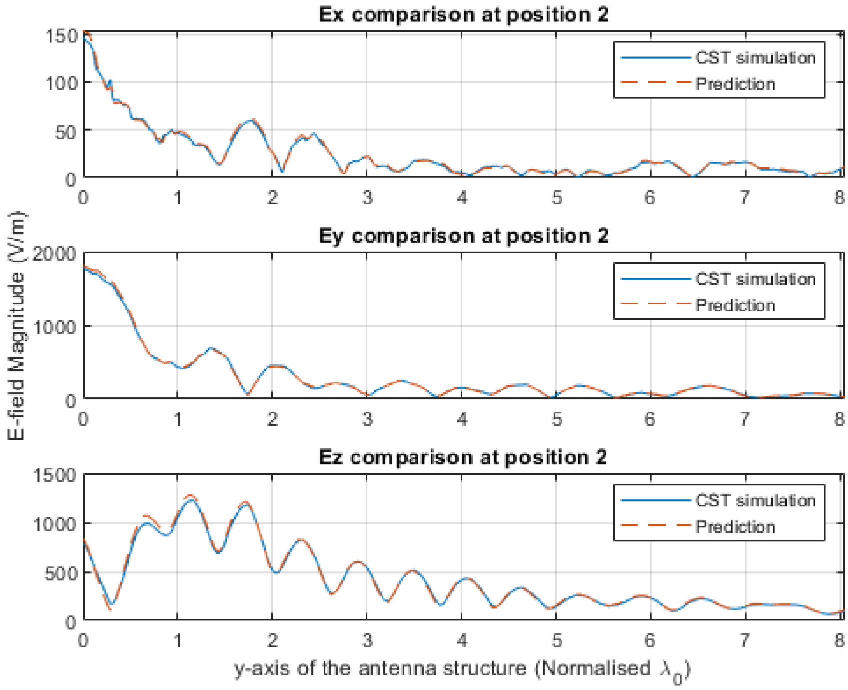

Figure 5.32. E_x, E_y, and E_z comparison on the line at ($0.12\lambda_0$, y, $0.5\lambda_0$) of 20° dual-sided case.

Table 5.3. The discrepancies between the predicted and simulated near-zone *E*-field (20° dual-sided case).

	Position 1 (0, y, $0.12\lambda_0$)			Position 2 ($0.12\lambda_0$, y, $0.5\lambda_0$)		
E-field	E_x	E_y	E_z	E_x	E_y	E_z
Discrepancies	8.79%	4.46%	3.55%	8.47%	4.2%	4.45%

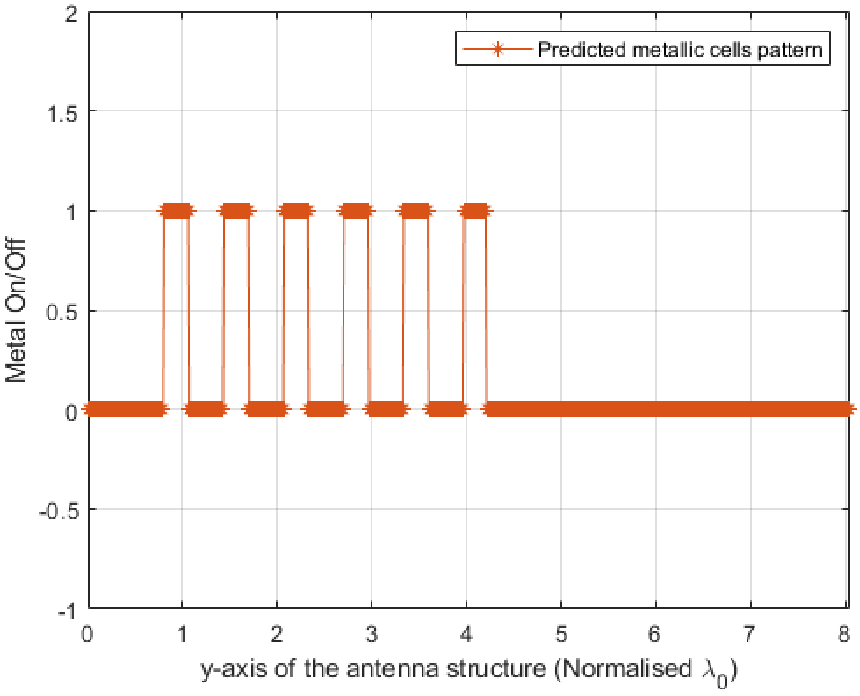

Figure 5.33. The predicted metallic cell pattern of the central radial row (10° dual-sided case).

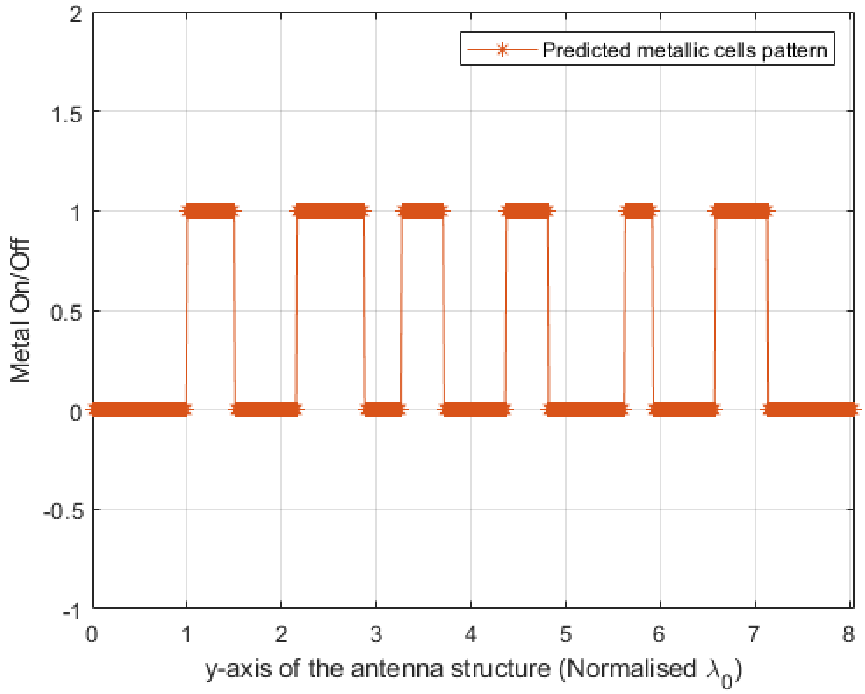

Figure 5.34. The predicted metallic cell pattern of the central radial row (20° dual-sided case).

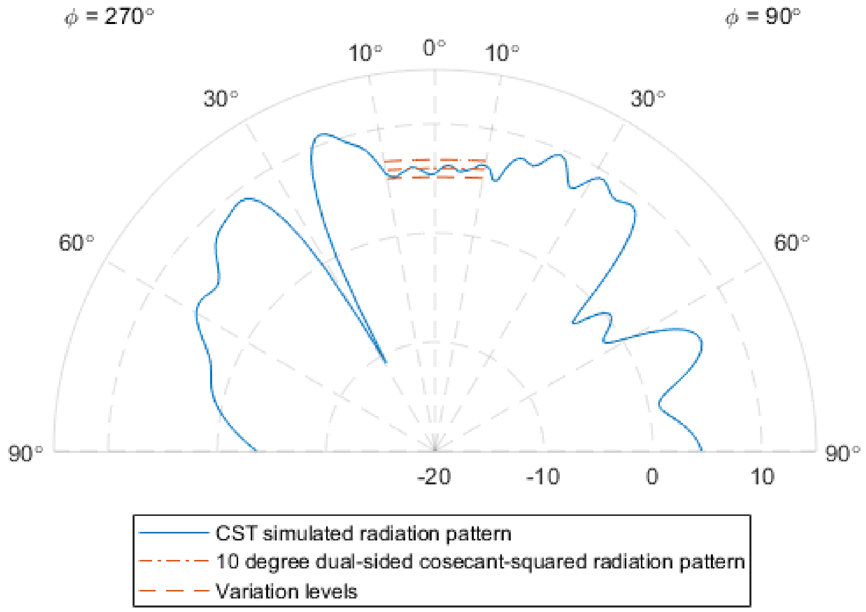

Figure 5.35. The far-field radiation pattern (*yz*-plane) of the 10° dual-sided case.

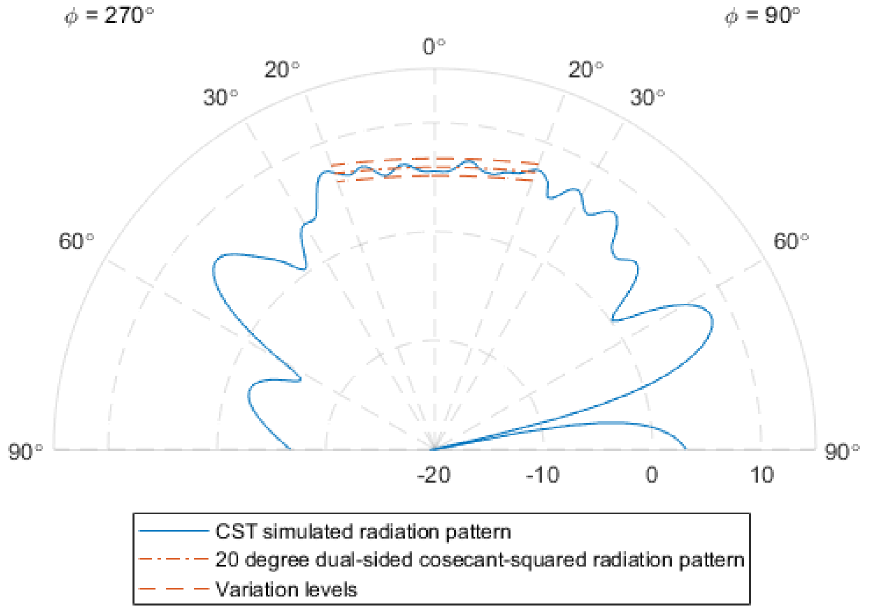

Figure 5.36. The far-field radiation pattern (*yz*-plane) of the 20º dual-sided case.

The CST simulated radiation pattern (*yz*-plane) of two cases at 34.5 GHz are shown in Figure 5.35 and Figure 5.36. It can be observed that the simulated radiation pattern follows the input radiation patterns (10º and 20º dual-sided cosecant-squared radiation pattern). In the cosecant-squared radiation pattern range, the variation level of the simulated radiation pattern is less than 1 dBi in both cases. This indicates that the neural network prediction models effectively generate the near-zone *E*-field and metallic cell pattern that fulfils the requirement.

Different range cosecant-squared radiation patterns have been served as the input radiation pattern to the proposed neural network prediction models. And the simulated radiation pattern follows the input radiation pattern and shows a good degree of consistency. This implies that the proposed neural network prediction models have the flexibility to predict the metallic cell pattern according to different input cosecant-squared radiation patterns. However, it can be seen that the maximum gain is not inside the cosecant-squared radiation pattern range in Figure 5.35 and Figure 5.36, which means the maximum gain is sacrificed when designing the surface wave antenna. This is because the input radiation pattern does not regulate the outside range radiation pattern. At this stage, it is difficult to regulate the whole range radiation pattern from (ϕ, θ) = (270º, 90º) to (90º, 90º) since the shape of the metallic cell is fixed and only the metallic cell position and length are considered in the prediction of the neural network models. Only varying the positions and lengths of the metallic cells limits the diversity of radiation patterns. And this limitation of the proposed neural network prediction method will be discussed in the next section.

5.3 Limitations and discussion

The feasibility and flexibility of the proposed neural network prediction models have been proved by the 10º, 20º and 30º dual-sided cosecant-squared radiation patterns cases. Although the predicted radiation pattern shows consistency with the ideal cosecant-squared radiation pattern, the outside range radiation pattern cannot be controlled by the prediction models. On the other hand, one of the primary purposes of replacing the original scalar horn antenna of the VLR system is to obtain a wide observation range. The larger angle of the cosecant-squared radiation pattern, the wider the observation range. At this stage, the maximum angle of the dual-sided cosecant-squared radiation pattern achieved is 30º. The limitations mentioned above is because of the limited metallic cell parameters (only metallic cell positions and lengths) considered. In this section, the limitation of the proposed neural network prediction method will be discussed through the analysis of the 40º dual-sided cosecant-squared radiation pattern case and the outside range radiation pattern suppression case. Due to the limited time in this research project, the possible solutions to the limitations are proposed at the end of this section and the verification will be investigated in future work.

5.3.1 Limitations

When using the 40º dual-sided cosecant-squared radiation pattern as the input radiation pattern to the neural network prediction models, the corresponding near-zone *E*-field can be predicted and the results are shown in Figure 5.37

and Figure 5.38. The predicted near-zone *E*-field results are then used to predict the metallic cell pattern on the surface, and the result is shown in Figure 5.39. By using this metallic cell pattern (each asterisk is 0.1 mm) to design the antenna, the simulated radiation pattern is shown in Figure 5.40.

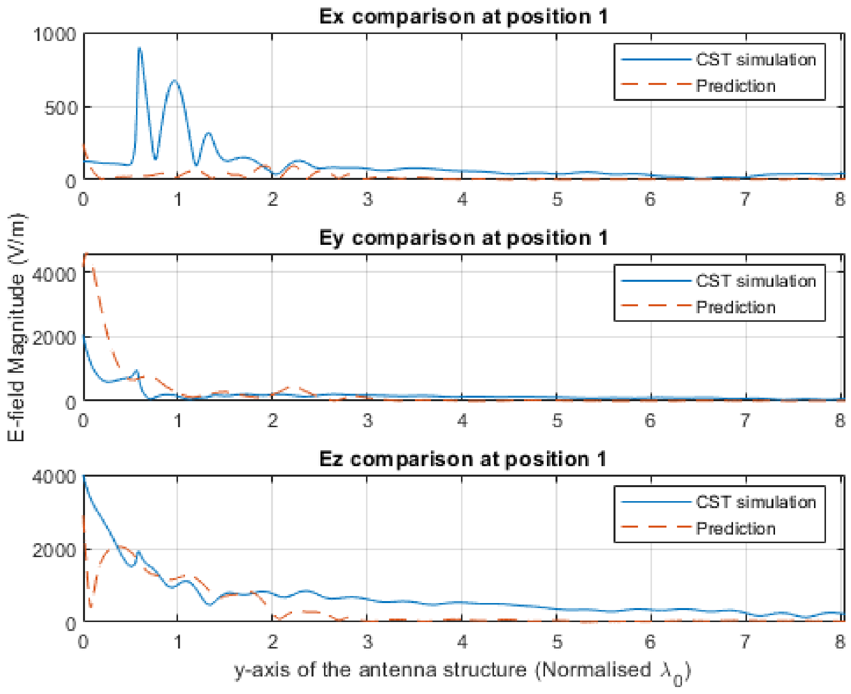

Figure 5.37. E_x, E_y, and E_z comparison on the line at (0, y, $0.12\lambda_0$) of 40° dual-sided case.

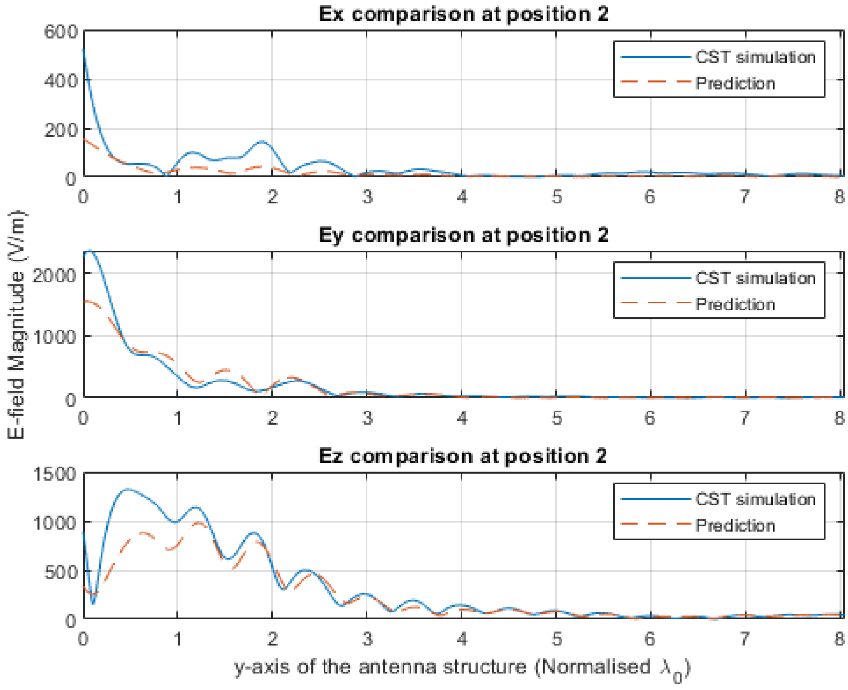

Figure 5.38. E_x, E_y, and E_z comparison on the line at ($0.12\lambda_0$, y, $0.5\lambda_0$) of 40º dual-sided case.

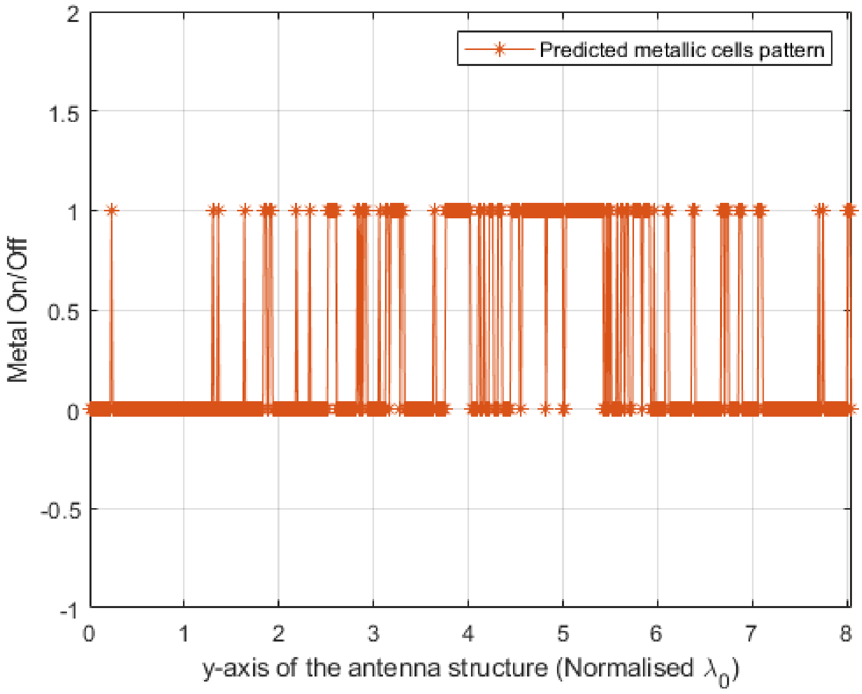

Figure 5.39. The predicted metallic cell pattern of the central radial row.

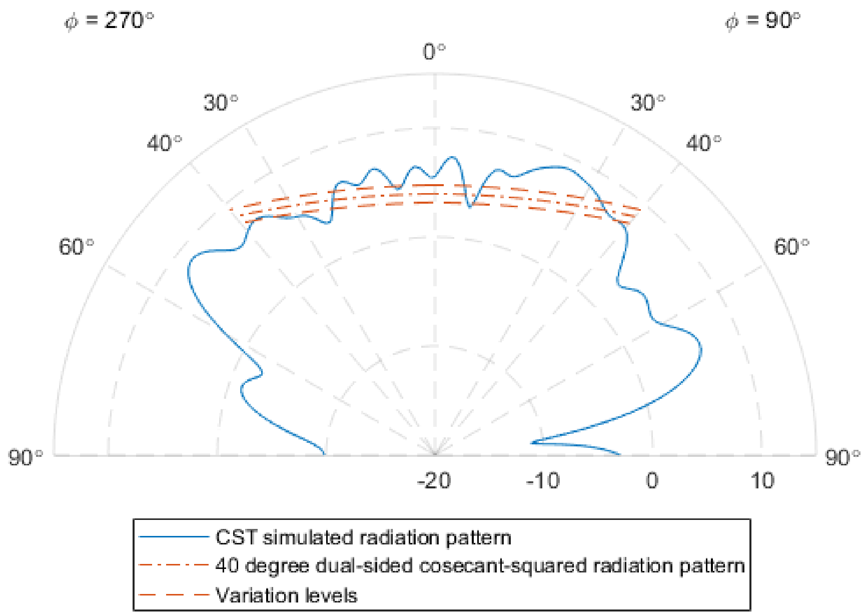

Figure 5.40. The far-field radiation pattern (*yz*-plane) of the 40° dual-sided case.

As shown in Figure 5.40, the simulated radiation pattern does not follow the input pattern. And the variation of the simulated radiation pattern is beyond ±1 dBi level and is not acceptable. This may be caused by the massive spikes in the metallic cell pattern prediction. As can be seen from Figure 5.39, the predicted metallic cell pattern shows many spikes (single orange asterisk) instead of connected asterisks like the cases in Figure 5.33 and Figure 5.34. It is difficult to transfer these impractical dimensions and design the metallic cell pattern of the antenna properly. Every asterisk is predicted from the near-zone *E*-field and should not be ignored. However, the input radiation pattern cannot be achieved by the surface wave antenna, which is designed according to these spikes.

Both parts of the neural network prediction models, near-zone *E*-field prediction and metallic cell pattern prediction, are proved to have accurate predictions from the results shown in Chapter 4. This means the predicted near-zone *E*-field is highly likely to be correct and the metallic cell pattern prediction model is reliable. If the 40° dual-sided case is achievable by the proposed antenna structure, the predicted metallic cell pattern should be the connected asterisks instead of massive spikes like Figure 5.39. Therefore, more metallic cell parameters, such as different cell shapes and angular separation, can be explored to achieve the 40º dual-sided cosecant-squared radiation pattern.

When trying to suppress the gain in the outside range of the input radiation pattern, the simulated radiation pattern of the antenna shows significant discrepancies in the outside range. The variation level of the simulated radiation pattern within the cosecant-squared area is large than 1 dBi. However, from Figure 5.41, the simulated radiation pattern drops from (ϕ, θ) = (90º, 30º) to (90º, 54º) and from (ϕ, θ) = (270º, 30º) to (270º, 90º), which indicates the outside range of the simulated pattern is trying to follow the input radiation pattern. Although the simulated radiation pattern shows unsatisfactory results, it shows that the changing trend follows the input radiation pattern. The reason is similar to the 40º dual-sided case. The 5º angular separation radial rows of rectangular shape metallic cells antenna structure may limit the possibility of the radiation pattern generation. Therefore, the possible solution would be increasing the variety of the metallic cell pattern distribution. In addition to the limited metallic cell pattern parameters considered, another possible reason could be the sharp transition changing pattern at (ϕ, θ) = (270º, 30º) and (90º, 30º) of the input dual-sided cosecant-squared radiation pattern. In real antenna design, this kind of sharp transition changing pattern in radiation pattern is difficult to achieve. Therefore, the transition changing pattern between inside and outside range of the cosecant-squared radiation pattern could be gentle, such as linearly and exponentially decreasing to the suppressed value (10 dBi in this case). And this will be addressed in the discussion part to investigate the effects of different transition changing patterns.

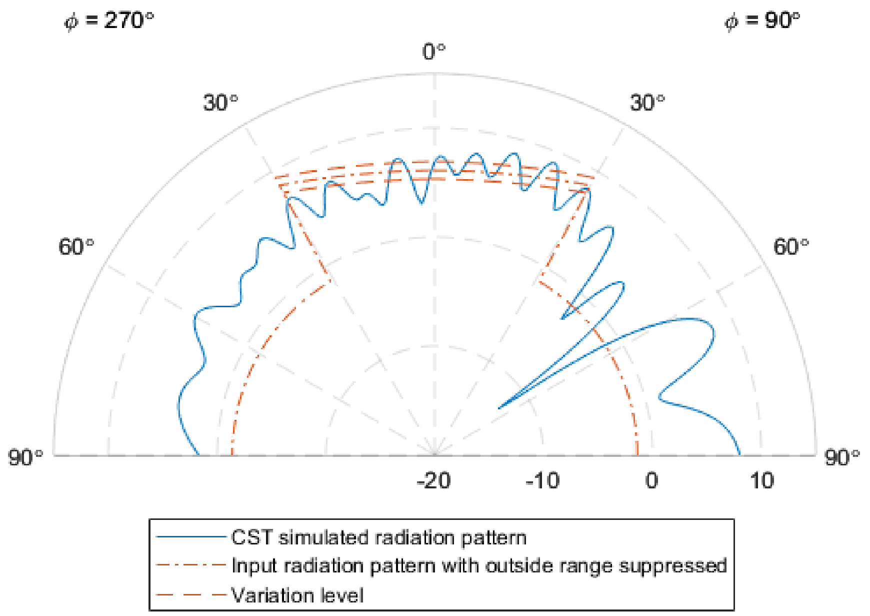

Figure 5.41. Dual-sided cosecant-squared radiation pattern with outside range suppression.

5.3.2 Discussion

In the 40° dual-sided case, the limitation is highly likely due to the limited metallic cell parameters considered. As for the case of outside range radiation pattern suppression, the limitation may be from both the limited metallic cell parameters considered and the sharp changing pattern in the transition. In this section, the possible solutions to the limited metallic cell parameters will be discussed. Different transition changing pattern between the inside and outside range of the cosecant-squared radiation pattern will be defined. Due to the limited time in this research, only preliminary ideas are verified and shown in this section. Detailed investigation will be carried out in future work.

5.3.2.1 Metallic cell parameters

In the neural network prediction model, the shape of the metallic cell focuses on rectangular, and the angular separation is fixed as 5°. In order to make the metallic cell distribution flexible, different shapes of the metallic cell and different separation angles between radial rows are introduced.

To investigate whether different cell shapes and the angular separations between radial rows have an effect on the near-zone *E*-field and radiation pattern, three antenna structures are studied and shown in Figure 5.42. The positions of the metallic cells are the same, (a) uses rectangular metallic cells and the angular separation between the radial rows is 5º; (b) utilises trapezium metallic cells and the angular separation is 5º; (c) applies rectangular metallic cells and the angular separation is 10º. The trapezium shape cell is defined by using d_2 and the ratio of d_1 to d_2, in Figure 5.42 (b) case, d_1 = 2 mm and d_2 = 0.5 mm.

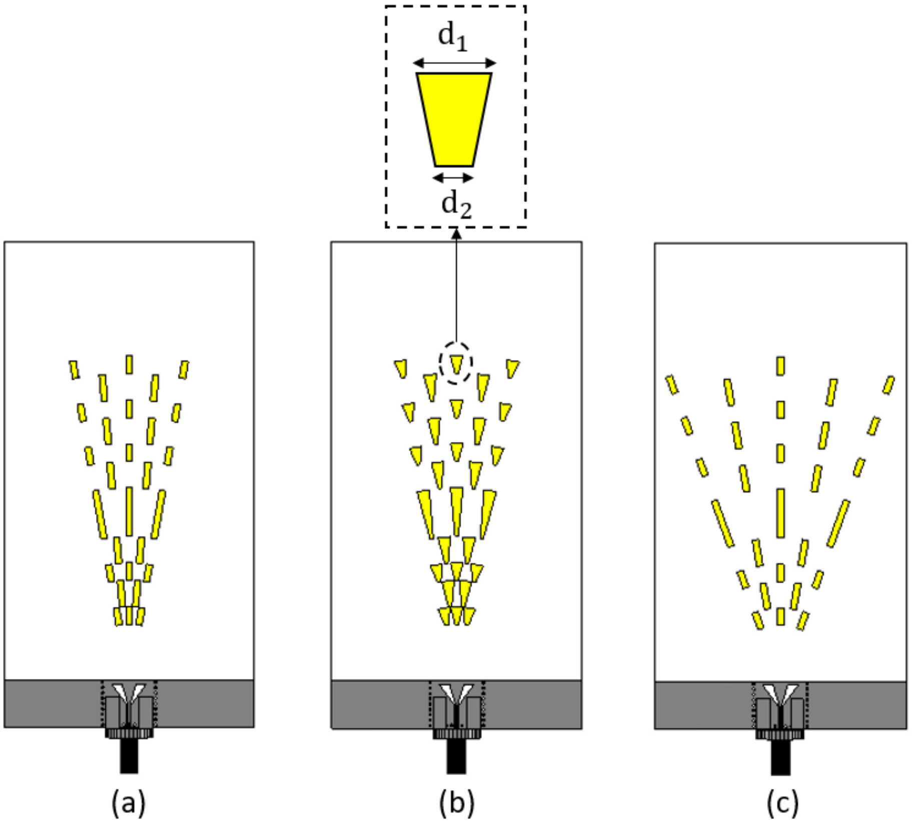

Figure 5.42. Surface wave antenna with (a) rectangular shape and 5º angular separation, (b) trapezium shape and 5º angular separation, (c) rectangular shape and 10º angular separation.

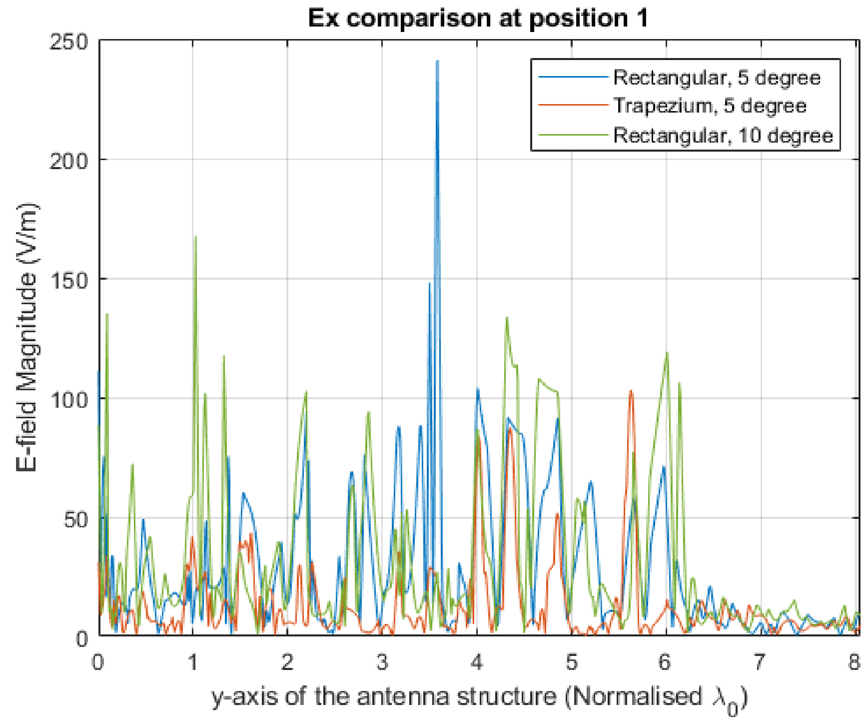

Figure 5.43. E_x comparison on the line at (0, y, 0.12λ_0) of three antennas.

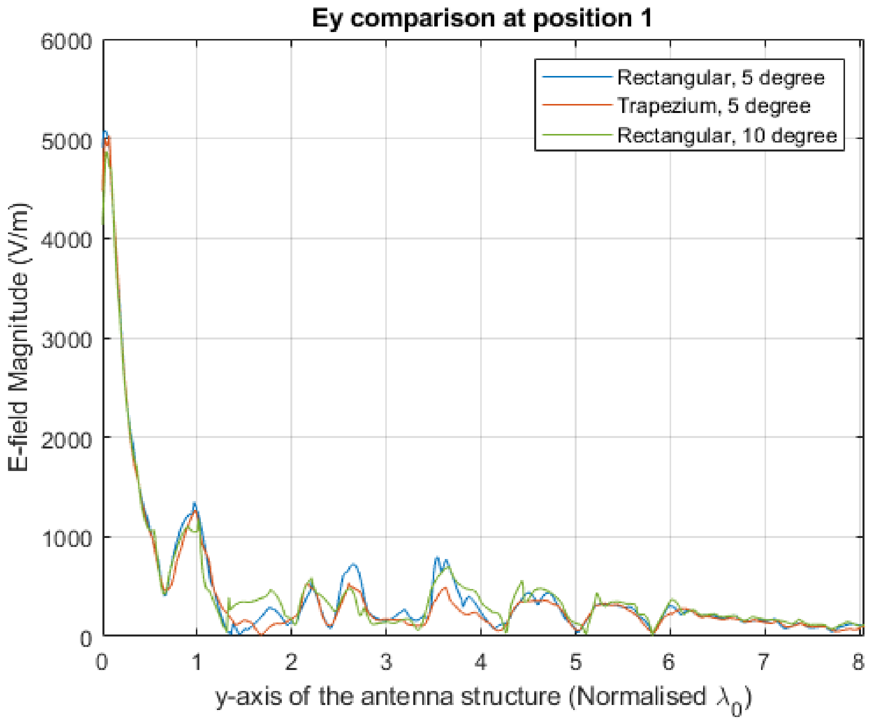

Figure 5.44. E_y comparison on the line at (0, y, 0.12λ_0) of three antennas.

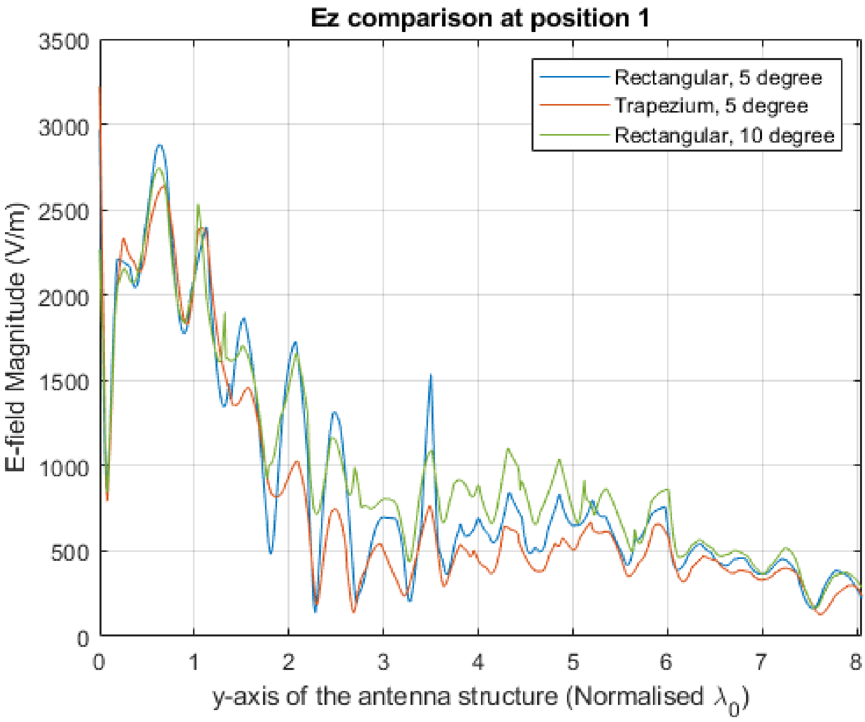

Figure 5.45. E_z comparison on the line at (0, y, $0.12\lambda_0$) of three antennas.

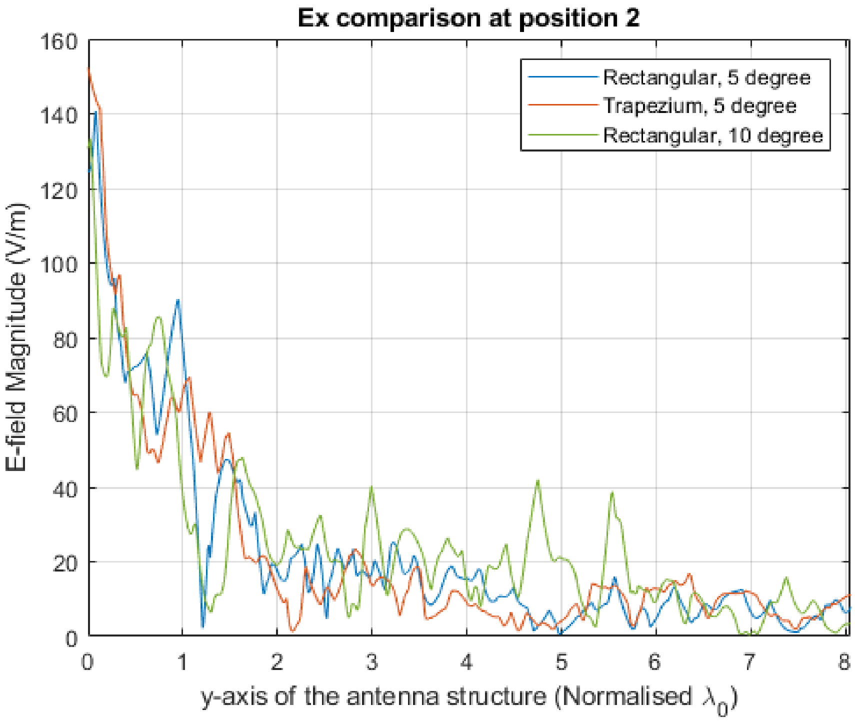

Figure 5.46. E_x comparison on the line at ($0.12\lambda_0$, y, $0.5\lambda_0$) of three antennas.

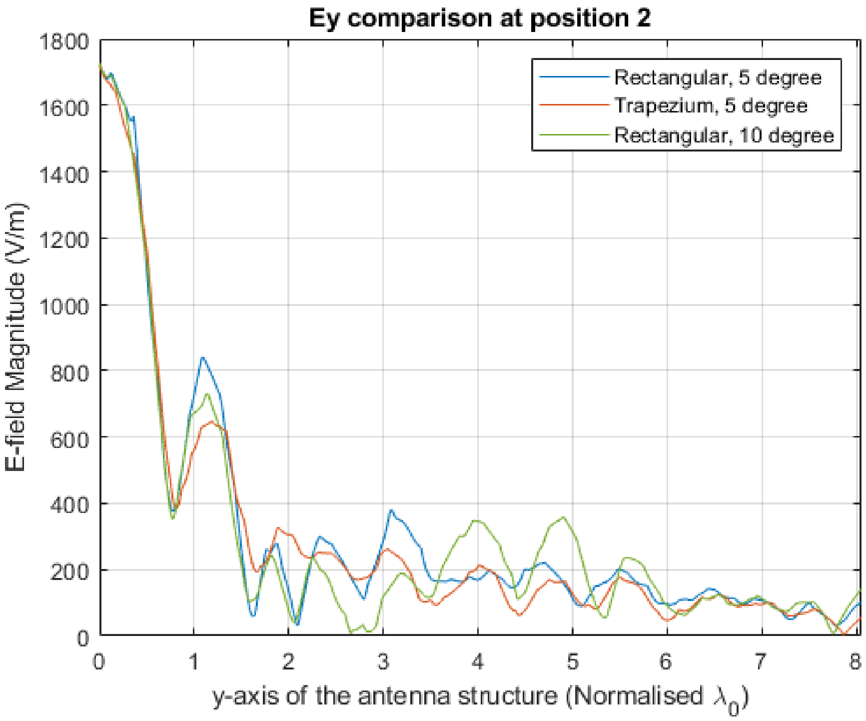

Figure 5.47. E_y comparison on the line at ($0.12\lambda_0$, y, $0.5\lambda_0$) of three antennas.

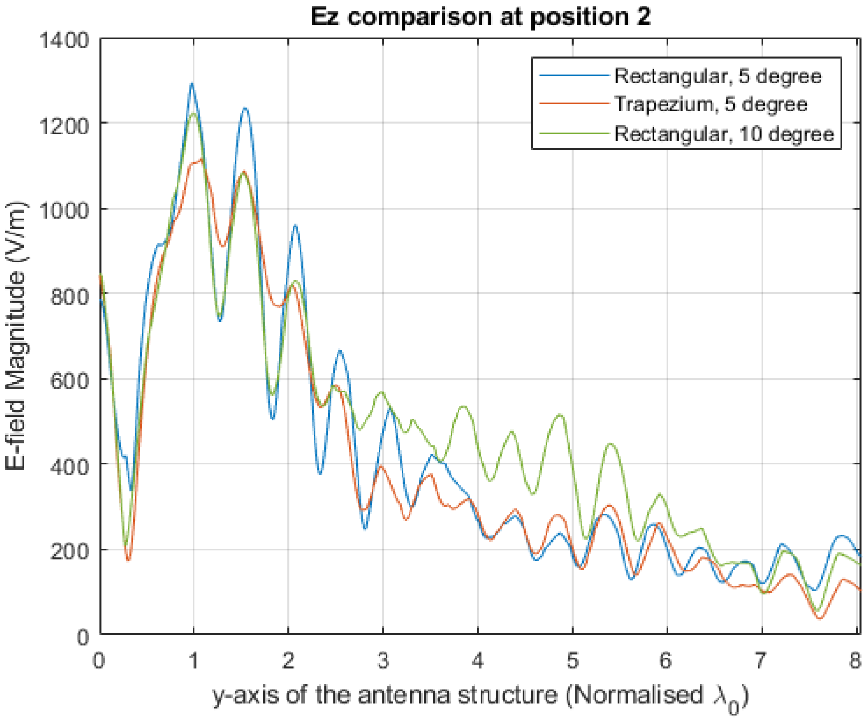

Figure 5.48. E_z comparison on the line at ($0.12\lambda_0$, y, $0.5\lambda_0$) of three antennas.

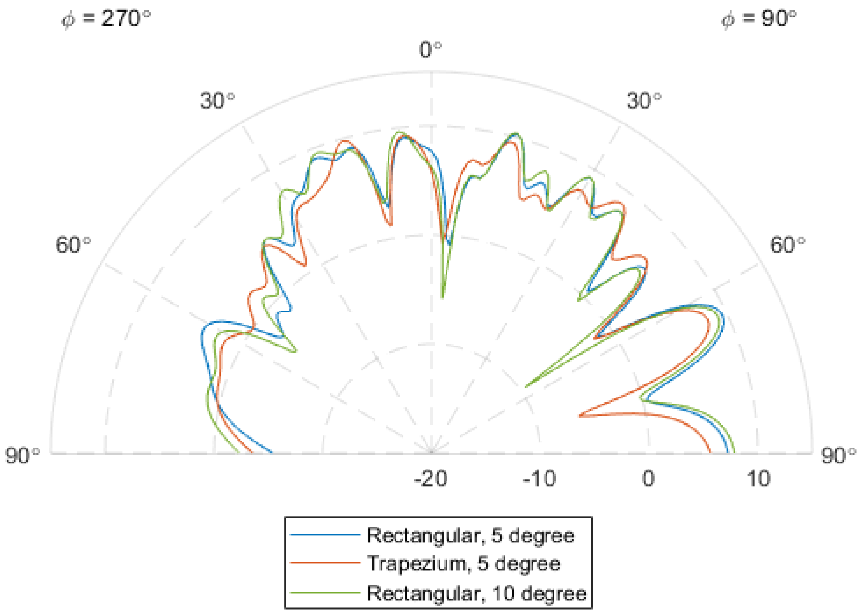

Figure 5.49. Radiation pattern comparison of three antennas.

The comparisons of the near-zone *E*-field of three antennas are shown from Figure 5.43 to Figure 5.48. And the radiation patterns of the three antennas are shown in Figure 5.49. It can be confirmed that the near-zone *E*-field and far-field radiation pattern would be different with different angular separation and cell shapes since the propagation of the surface wave is affected by the different distributions of the metallic cells. In Figure 5.43 and Figure 5.46, the E_x component shows the most difference, which means it is more sensitive to the cell shape and angular separation change among the three *E*-field components. Although the E_x component shows smaller values than E_y and E_z, the E_x component would be an appropriate indicator when predicting the metallic cell pattern in future improvement to the proposed neural network prediction model. In the E_y comparison, all three cases show similar values at position 1 but relatively large differences in ($2\lambda_0$, $6\lambda_0$) of the *x*-axis at position 2. In the E_z comparison, the rectangular shape metallic cell with 10° angular separation shows relatively large values.

Different shapes of the metallic cell and different separation angles between radial rows have been shown to affect the near-zone *E*-field and the far-field radiation pattern. The lengths d_1 and d_2 are introduced to define the trapezium shape of the metallic cells. By varying the ratios d_1/d_2, more shapes of the metallic cell can be achieved. Different shapes can be considered as different labels to the neural network prediction models. The neural network prediction models can output a shape label along with the metallic cell pattern as the final prediction results when multiple shapes are considered. In terms of angular separation, the angular separation between adjacent rows is the same in the comparison in Figure 5.42. This comparison is to prove whether the angular separation has an effect on the near-zone *E*-field and far-field radiation pattern. However, the angular separation between radial rows could be different in order to increase the diversity of the antennas.

The angular separation, the value of d_2 and the ratio d_1/d_2 can be the additional metallic cell parameters to the neural network models. By varying the values of angular separation, d_2 and the ratio d_1/d_2, the neural network model obtains more near-zone *E*-field and far-field radiation pattern data to train and increases the diversity of the predicted metallic cell pattern. More parameters introduced to the neural network will increase the complexity of the neural network. Therefore, more training datasets are essential to such a deep and complex neural network during the training stage. More *E*-field monitor arrays are required to extract more near-zone *E*-field data and then to train the neural network prediction models. The neural network model requires more near-zone *E*-field data to extract the features, and thus it can output more metallic cell parameters to guide the antenna design.

5.3.2.2 Different transition changing pattern

When trying to suppress the gain in the outside range of the input cosecant-squared radiation pattern, the simulated radiation pattern did not agree well with the input radiation pattern. The reason could be the limited metallic cell parameters considered. Moreover, the sharp transition changing pattern may also affect the prediction of the neural network models. In this section, in order to investigate the effect of transition changing pattern, the linearly and exponentially decreasing transition changing patterns are used as the input radiation pattern to the neural network prediction models. Suppressed values, 10 and 20 dBi, are introduced to investigate the effect of the different suppressed values.

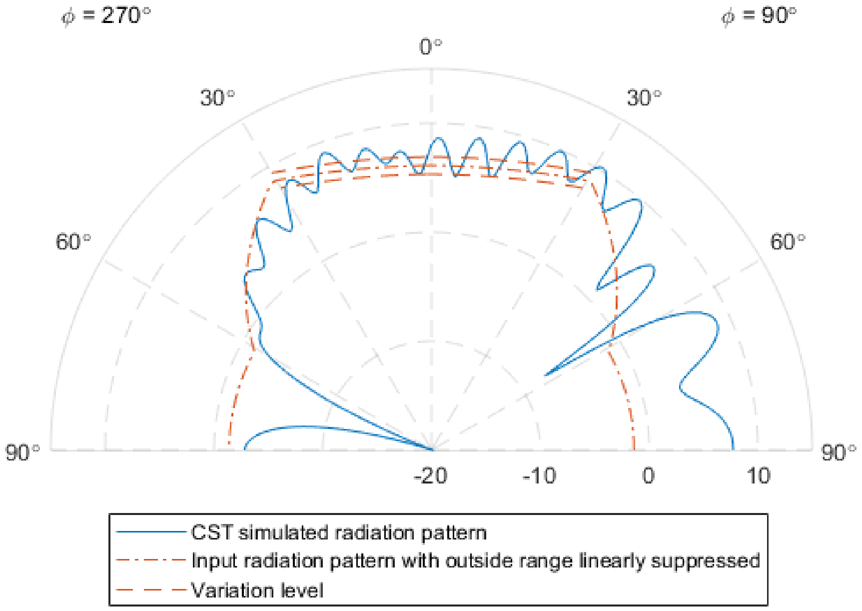

Figure 5.50. 30º dual-sided cosecant-squared radiation pattern with outside range linearly suppressed.

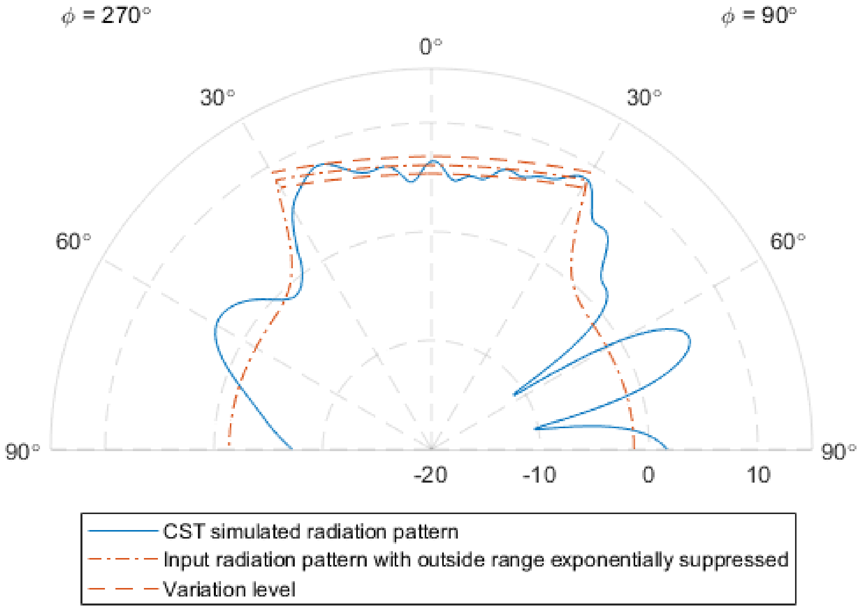

Figure 5.51. 30º dual-sided cosecant-squared radiation pattern with outside range exponentially suppressed.

Figure 5.50 and Figure 5.51 shows the dual-sided cosecant-squared radiation pattern with outside range linearly and exponentially suppressed, respectively. The difference between the two input radiation patterns is from (ϕ, θ) = (270°, 60°) to (270°, 30°) and (ϕ, θ) = (90°, 30°) to (90°, 60°). In the linearly decreasing transition changing pattern case, the radiation pattern linearly drops 10 dBi from the maximum gain at 30° to 60° both in ϕ = 90° and 270° direction. Whereas in the exponentially decreasing case, the 10 dBi drop is done by exponentially decreasing in the same angular range. Compared with Figure 5.41, the linearly and exponentially transition changing pattern shows the better suppression effect. In Figure 5.50, it can be observed that the simulated outside range radiation pattern follows the input pattern from (ϕ, θ) = (270°, 60°) to (270°, 30°). In the range from (ϕ, θ) = (90°, 60°) to (90°, 30°), although the simulated radiation pattern does not show ideal agreement, the trend of the simulated and input radiation pattern is similar. The simulated radiation pattern in the 30° dual-sided cosecant-squared range shows better performance than Figure 5.41. When the input radiation pattern has a sudden change at (ϕ, θ) = (270°, 60°) and (90°, 60°), and the simulated radiation pattern shows significant drops at (ϕ, θ) = (270°, 63°) and (90°, 58°). In Figure 5.51, the simulated radiation pattern shows better agreement in the 30° dual-sided cosecant-squared range than the linearly decreasing case. The simulated radiation pattern follows the input pattern in the range from (ϕ, θ) = (270°, 30°) and (270°, 43°), while it shows a similar trend with the input pattern in the range from (ϕ, θ) = (90°, 30°) and (90°, 52°).

From the comparison of sharp (Figure 5.41), linear and exponential transition pattern, it can be concluded that the transition changing pattern affect the prediction of the neural network models. In Figure 5.50 and Figure 5.51, the input radiation pattern has the regulation effect to some extent. This brings a direction of thought, which is based on defining an appropriate transition changing pattern to tackle the suppression problem. When defining the transition changing pattern, the suppressed value should be considered. The suppressed value is 10 dBi in the linearly and exponentially suppressed cases. Different suppressed values of the outside range pattern need to be investigated to confirm if it affects the prediction of the neural network models.

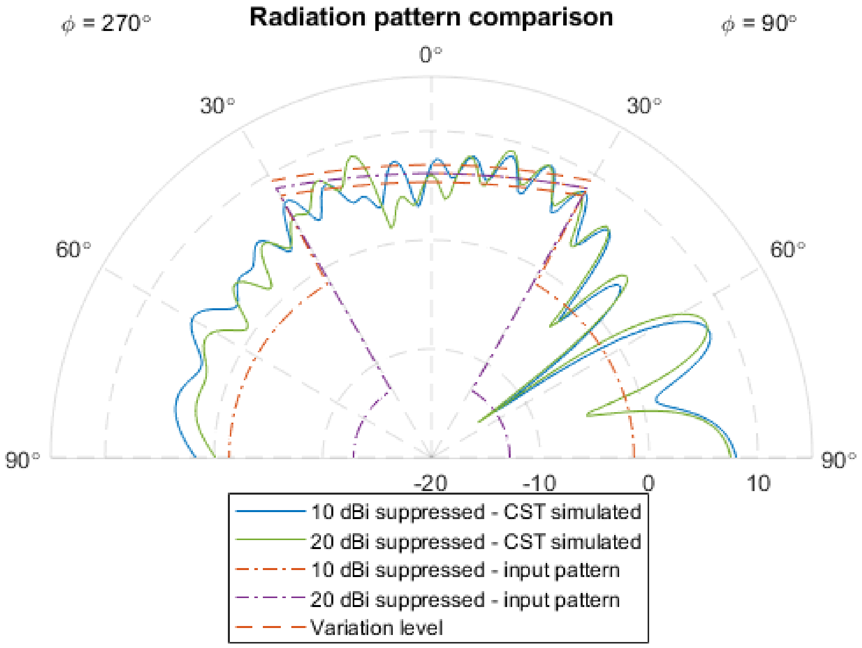

Figure 5.52. 30º dual-sided cosecant-squared radiation pattern with different suppressed values.

Figure 5.52 shows the input and simulated radiation patterns with different suppressed values. The 30º dual-sided cosecant-squared range of the two input radiation patterns is the same, while the suppressed value of the outside range is 10 dBi and 20 dBi respectively. It can be seen that the simulated radiation patterns of the two cases are similar. The simulated radiation pattern of 20 dBi suppressed case shows lower gain than the 10 dBi suppressed case in the range from (ϕ, θ) = (270º, 90º) and (270º, 30º), which indicates that the suppressed value affects the prediction of the neural network models. Therefore, the suppressed value of the outside range pattern needs to be considered when defining the appropriate transition changing pattern.

Different transition changing patterns have different effects on neural network prediction. Therefore, the transition changing pattern is required to be defined properly to solve the suppression problem in future work.

5.4 Summary

In this chapter, the proposed neural network-based method has been used to design the dual-sided 30º cosecant-squared radiation pattern surface wave antenna, and such antenna offers a wider circular observation range (9.8 m in diameter) than the existing scalar horn antenna (1.2 m in diameter). The achieved radiation pattern is within ± 1 dBi variation from the ideal input cosecant-squared radiation pattern. The prototype of the proposed antenna has been tested and the comparisons between the CST simulation and measurement results in terms of S_{11}, gain and radiation pattern show a good degree of consistency. The angular coverage range that the proposed neural network-based method can predict has been proved through dual-sided 10º and 20º cosecant-squared radiation pattern cases. The limitations of the proposed neural network prediction models have been discussed and the proposed solutions have been presented.

6 Conclusions and future work

In this thesis, the main aim is to design a surface wave antenna with the cosecant-squared radiation pattern in the far-field by utilising a neural network-based method. During the project, the neural network prediction models are proposed and its prediction performance has been evaluated. By using the neural network models, a surface wave antenna with a 30º dual-sided cosecant-squared radiation pattern is designed and the prototype has been fabricated and evaluated. The conclusion of this research work will be divided into two parts; they are the proposed neural network models and the proposed surface wave antenna. The limitations of this research in its present form will be discussed and further research that can improve the current results will be introduced in future work.

6.1 Conclusions

6.1.1 Proposed neural network prediction models

The proposed neural network prediction method consists of two parts; they are i) the prediction of the near-zone *E*-field from the defined far-field radiation pattern and ii) from the near-zone *E*-field to the on-surface metallic cell pattern. In the first prediction part, a combination of the WGAN and Bi-GRU neural network models has been used. In the second part, another Bi-GRU neural network model with different configurations is used to predict the metallic cell pattern. The detailed mechanism of the prediction models has been introduced and discussed in Chapter 3. The prediction performance has been explicitly assessed by using different evaluation methods. In the prediction of near-zone *E*-field, the average prediction error among E_x, E_y and E_z components of 50 test cases is 4.3%. In the prediction of metallic cell pattern, the average prediction accuracy achieved is 99.54%.

6.1.2 Proposed surface wave antenna

The cosecant-squared radiation pattern surface wave antenna proposed has a simple geometry and is low cost. It comprises a coplanar surface wave launcher, five radial rows of metallic cells in rectangular shape and a piece of conductor-backed microwave dielectric substrate. The surface wave launcher is designed according to the grounded coplanar waveguide and substrate integrated waveguide. Such launcher offers 2.9% impedance bandwidth and 94.2% total efficiency at centre frequency 34.5 GHz. The distribution of the metallic cell is predicted by the proposed neural network prediction model. The predicted antenna shows less than 1 dBi variation in radiation pattern from the input dual-sided 30º cosecant-squared radiation pattern. The fabricated prototype of the dual-sided 30º cosecant-squared radiation pattern antenna operates in the frequency band 33.77 to 35.05 GHz, which covers the frequency band of the mmWave FMCW VLR system. The gain of the antenna is 8.49 dBi at $(\phi, \theta) = (90^\circ, 29^\circ)$, which gives a circular observation area with a diameter of 9.8 m with the help of the turntable underneath the antenna.

6.2 Future work

During this research, a few limitations have been identified. Suggestions for solving the limitations are provided in this section as the direction of future research. The limitations have two categories, which are on the gain of the proposed antenna and on the neural network prediction models. In the proposed antenna, the main limitation is that the maximum gain is relatively low compared with the existing antennas used in the mmWave FMCW VLR system. In the neural network prediction models, the maximum range of the cosecant-squared radiation pattern achieved at this stage is 30º dual-sided. Moreover, another limitation is the outside range radiation pattern cannot be regulated at this stage. Therefore, the future work will be stated separately in two sub-sections.

6.2.1 Future work in antenna

It is worth noting that the dual-sided 30º cosecant-squared radiation pattern antenna has a gain of 8.49 dBi. Compared with the existing antennas, the combination of scalar horn and Gaussian lens, the proposed antenna has a low gain due to the low-profile antenna structure. Therefore, the proposed surface wave antenna has a limited detection range in height. The printed dielectric lens could be a feasible solution to increase the gain. As suggested in [126], a printed dielectric slab can be loaded on the top of the proposed antenna, acting as a partially reflecting surface. By optimising the height and distance of the slab, the gain can be enhanced to an ideal value. On the other hand, as discussed in [127] and [128], metasurface could be another feasible solution to increase the gain of the proposed hologram-based surface wave antenna. Therefore, either printed dielectric slab and metasurface could be investigated in future to improve the gain of the proposed antenna.

6.2.2 Future work in neural network prediction models

In terms of the limited angular range of the cosecant-squared radiation pattern, the reason could be that only the metallic cell positions and lengths have been considered as the parameters to the neural network prediction models. Therefore, the metallic cell distribution may limit the diversity of the radiation pattern that the antenna can generate. If the neural network models can learn more possibilities of the antenna structure, such as different shapes and angular separation, the neural network prediction models can produce more radiation patterns in the far-field.

In future work, the number of radial rows may not be limited to five and could be more, and the distribution of the metallic cells in each radial row can be independent. Thus, the neural network models can predict the distribution of each row separately. At the same time, as discussed in Chapter 5, the shape of the metallic cell could be changed to different shapes, which will introduce more variables. Furthermore, the angular separation between radial rows could be regarded as another parameter to the neural network prediction models. All of these proposed solutions are intended to produce more possibilities for the antenna structure.

In addition to increasing the metallic cell parameters, defining an appropriate transition changing pattern is another possible solution to tackle the regulation of the outside range radiation pattern problem. As discussed in Chapter 5, different transition changing patterns and suppressed values of the outside range radiation pattern have different effects on the neural network prediction models. Therefore, more suppressed values and transition changing patterns can be studied to suppress the outside range radiation pattern effectively.

At the same time, more parameters introduced to the neural network will increase the complexity of the neural network. Therefore, more training datasets are essential to such a deep neural network. At the present stage, the training datasets are generated by multi computers to accelerate the data extraction time. It is advised to use CST servers to run the surface wave antenna models as the servers compute fast. In terms of the training of the neural network, compared to the CPU, the GPU server has better performance in terms of computation time. Therefore, using GPU servers to train the neural network models is recommended.

On the other hand, the complexity of the neural network model may be increased when introducing more parameters since the original neural network setting may not be enough for studying many parameters. The hyperparameters such as the number of layers and the number of neurons in the hidden layers could be revised accordingly. In the training of deep neural network models, the learning rate needs to be tuned to avoid gradient explosion or vanishing problems.

7 Reference

[1] Food and Agriculture Organization of the United Nations, “Scientific review of the impact of climate change on plant pests: A global challenge to prevent and mitigate plant-pest risks in agriculture, forestry and ecosystems,” 2021.

[2] M. N. Sallam, “Insect Damage: Post-harvest Operations,” *ICIPE-Post-harvest Compendium.*, p. 56, 2001.

[3] ICIPE, “Vision and Strategic framework towards 2020,” in *ICIPE Science Press*, 1997, pp. 1–28.

[4] A. D. Smith, J. R. Riley, and R. D. Gregory, “A method for routine monitoring of the Aerial Migration of Insects by Using a Vertical-Looking Radar,” *Philos. Trans. Biol. Sci.*, vol. 340, pp. 393–404, 1993.

[5] J. W. Chapman and D. Reynolds, “Vertical-Looking Radar: A New Tool for Monitoring High-Altitude Insect Migration,” *Bioscience*, vol. 53, no. 4, pp. 4–10, 2009.

[6] J. Yang, K. F. Tong, K. S. Lim, A. Reynolds, and C. Rawlings, “Development of Millimeter-wave FMCW Vertical-looking Entomological Radar System,” *2019 IEEE Int. Work. Electromagn. Appl. Student Innov. Compet. iWEM 2019*, pp. 1–2, 2019.

[7] H. Chu, P. Li, and Y. X. Guo, “A Beam-Shaping Feeding Network in Series Configuration for Antenna Array with Cosecant-Square Pattern and Low Sidelobes,” *IEEE Antennas Wirel. Propag. Lett.*, vol. 18, no. 4, pp. 742–746, 2019.

[8] A. Brunner, “Possibilities of Dimensioning Doubly Curved Reflectors for Azimuth-Search Radar Antennas,” *IEEE Trans. Antennas Propag.*, vol. 19, no. 1, pp. 52–57, 1971.

[9] C. Wolff, “Radartutorial: Antennae Techniques.”

[10] R. S. Elliott and G. J. Stern, “A new technique for shaped beam synthesis of equispaced arrays,” *IEEE Trans. Antennas Propag.*, vol. 32, no. 10, pp. 1129–1133, 1984.

[11] Z. Shafiq, M. Kuznetcov, V. G. G. Buendia, D. E. Anagnostou, and S. K. Podilchak, “A Planar Horn Antenna for TM Surface Wave Launching using Substrate Integrated Waveguide Technology,” *13th Eur. Conf. Antennas Propagation, EuCAP 2019*, pp. 2019–2021, 2019.

[12] J. E. Turner, M. S. Jessup, and K. F. Tong, “A novel technique enabling the realisation of 60 GHz body area networks,” *9th Int. Work. Wearable Implant. Body Sens. Networks*, no. 1, pp. 58–62, 2012.

[13] J. Yang and K. F. Tong, “Cosecant-Squared Radiation Pattern Surface Wave Antenna for Millimeter-wave FMCW Vertical-Looking Radar System,” *IEEE Asia-Pacific Microw. Conf.*, pp. 801–803, 2020.

[14] S. K. Podilchak, A. P. Freundorfer, and Y. M. M. Antar, “Surface-wave launchers for beam steering and application to planar leaky-wave antennas,” *IEEE Trans. Antennas Propag.*, vol. 57, no. 2, pp. 355–363, 2009.

[15] H. M. Barlow and A. L. Cullen, “Surface waves,” *Proc. IEEE - Part III Radio Commun. Eng.*, vol. 100, no. 68, pp. 329–341, 1953.

[16] M. Z. Yaqoob, A. Ghaffar, M. A. S. Alkanhal, M. Y. Naz, A. H. Alqahtani, and Y. Khan, “Electromagnetic surface waves supported by a resistive metasurface-covered metamaterial structure,” *Sci. Rep.*, vol. 10, no. 1, pp. 1–17, 2020.

[17] S. A. Schelkunoff, “Anatomy of ‘Surface waves,’” *IRE Trans. Antennas Propag.*, vol. 7, no. 5, 1959.

[18] J. Wan, K. F. Tong, and C. H. Chan, “Simulation and experimental verification for a 52 GHz wideband trapped surface wave propagation system,” *IEEE Trans. Antennas Propag.*, vol. 67, no. 4, pp. 2158–2166, 2019.

[19] K. K. Wong, K. F. Tong, Z. Chu, and Y. Zhang, “A Vision to Smart Radio Environment: Surface Wave Communication Superhighways,” *IEEE Wirel. Commun.*, vol. 28, no. 1, pp. 112–119, 2021.

[20] L. Felson, “Radiation from a Tapered Surface Wave Antenna,” *IRE Trans. Antennas Propag.*, vol. 8, no. 6, pp. 577–586, 1960.

[21] J. L. Volakis, *Antenna Engineering Handbook*, 4th ed. McGraw-Hill Education, 2007.

[22] D. Deslandes and K. Wu, “Analysis and design of current probe transition from grounded coplanar to substrate integrated rectangular waveguides,” *IEEE Trans. Microw. Theory Tech.*, vol. 53, no. 8, pp. 2487–2494, 2005.

[23] P. Baniya and K. L. Melde, “360° Switched Beam SIW Horn Arrays at 60 GHz, Phase Centers, and Friis Equation,” *United States Natl. Comm. URSI Natl. Radio Sci. Meet. Usn. NRSM*, pp. 113–114, 2021.

[24] C. M. Angulo and W. S. C. Chang, “The Launching of Surface Waves by a Parallel Plate Waveguide,” *IRE Trans. Antennas Propag.*, vol. 7, no. 4, pp. 359–368, 1959.

[25] J. L. G. Tornero, A. M. Ros, M. A. Martinez, A. M. Sala, G. Goussetis, and S. K. Podilchak, “A simple parallel-plate wave launcher in substrate integrated waveguide technology,” *IEEE Int. Symp. Antennas Propag. Usn. Natl. Radio Sci. Meet.*, pp. 480–481, 2015.

[26] V. G. G. Buendia, S. K. Podilchak, G. Goussetis, and J. L. Gomez-Tornero, “A TM0 surface wave launcher by microstrip and substrate integrated waveguide technology,” *11th Eur. Conf. Antennas Propag.*, pp. 3859–3862, 2017.

[27] S. K. Podilchak, L. Matekovits, A. P. Freundorfer, K. Esselle, and Y. M. M. Antar, “Modulated strip-line leaky-wave antenna using a printed grating lens and a surface-wave source,” *14th Int. Symp. Antenna Technol. Appl. Electromagn. Am. Electromagn. Conf.*, pp. 26–28, 2010.

[28] S. K. Podilchak, A. P. Freundorfer, and Y. M. M. Antar, “Broadside radiation from a planar 2-D leaky-wave antenna by practical surface-wave launching,” *IEEE Antennas Wirel. Propag. Lett.*, vol. 7, pp. 517–520, 2008.

[29] S. K. Podilchak, A. P. Freundorfer, and Y. M. M. Antar, “A study of planar leaky-wave antenna designs fed by practical surface-wave launchers,” *6th Eur. Conf. Antennas Propagation, EuCAP*, pp. 265–266, 2012.

[30] P. Baniya and K. L. Melde, “Switched beam SIW horn arrays at 60 GHz for 360° reconfigurable chip-to-chip communications with interference considerations,” *IEEE Access*, vol. 9, pp. 100460–100471, 2021.

[31] L. Wang, M. Garcia-Vigueras, M. Alvarez-Folgueiras, and J. R. Mosig, “Wideband H-plane dielectric horn antenna,” *IET Microwaves, Antennas Propag.*, vol. 11, no. 12, pp. 1695–1701, 2017.

[32] P. Baniya and K. L. Melde, “Switched beam SIW horn arrays at 60 GHz for 360° reconfigurable chip-to-chip communications,” *IEEE Radio Wirel. Symp.*, vol. 9, 2021.

[33] B. D. R. Jackson, C. Caloz, and T. Itoh, “Leaky-Wave Antennas,” *Proc. IEEE*, vol. 100, no. 7, 2012.

[34] J. Yang and K. Tong, “Metallic Pattern Prediction For Surface Wave Antennas Using Bidirectional Gated Recurrent Unit Neural Network,” *IEEE-APS Top. Conf. Antennas Propag. Wirel. Commun.*, pp. 82–86, 2021.

[35] S. F. Mahmoud and Y. M. M. Antar, “Leaky wave antennas: Theory and design,” *Natl. Radio Sci. Conf.*, pp. 1–8, 2013.

[36] S. F. Mahmoud and Y. M. M. Antar, “Chapter 13 Printed Leaky Wave Antennas,” in *Microstrip and Printed Antennas*, John Wiley & Sons, Ltd., 2011, pp. 435–462.

[37] F. Xu and K. Wu, “Understanding leaky-wave structures: A special form of guided-wave structure,” *IEEE Microw. Mag.*, vol. 14, no. 5, pp. 87–96, 2013.

[38] P. Debnath and S. Chatterjee, “Substrate integrated waveguide antennas and arrays,” *Int. Conf. Electron. Mater. Eng. Nano-Technology*, 2017.

[39] J. Liu, D. R. Jackson, and Y. Long, “Substrate integrated waveguide (SIW) leaky-wave antenna with transverse slots,” *IEEE Trans. Antennas Propag.*, vol. 60, no. 1, pp. 20–29, 2012.

[40] T. Yoneyama and S. Nishida, “Nonradiative Dielectric Waveguide for Millimeter-Wave Integrated Circuits,” *IEEE Trans. Microw. Theory Tech.*, vol. 29, no. 11, pp. 1188–1192, 1981.

[41] J. L. Gómez-Tornero, J. Pascual-García, and A. Álvarez-Melcon, “A novel leaky-wave antenna combining an image NRD guide and a strip circuit,” *IEEE Antennas Wirel. Propag. Lett.*, vol. 4, no. 1, pp. 289–292, 2005.

[42] T. Zhao, D. R. Jackson, J. T. Williams, and A. A. Oliner, “Simple CAD model for a dielectric leaky-wave antenna,” *IEEE Antennas Wirel. Propag. Lett.*, vol. 3, no. 1, pp. 243–245, 2004.

[43] F. Scattone *et al.*, “Truncated Leaky-Wave Antenna With Cosecant-Squared Radiation Pattern,” *IEEE Antennas Wirel. Propag. Lett.*, vol. 17, no. 5, pp. 841–844, 2018.

[44] T. Zhao, D. R. Jackson, J. T. Williams, H. Y. D. Yang, and A. A. Oliner, “2-D periodic leaky-wave antennas - Part I: Metal patch design,” *IEEE Trans. Antennas Propag.*, vol. 53, no. 11, pp. 3505–3514, 2005.

[45] S. K. Podilchak, S. F. Mahmoud, A. P. Freundorfer, and Y. M. M. Antar, “Perturbation analysis of planar periodic leaky-wave antennas fed by cylindrical surface-waves,” *30th URSI Gen. Assem. Sci. Symp.*, vol. 10, pp. 174–178, 2011.

[46] P. Checcacci, V. Russo, and A. Scheggi, “Holographic antennas,” *IEEE Trans. Antennas Propag.*, vol. 18, no. 6, pp. 811–813, 1970.

[47] M. Nannetti, F. Caminita, and S. Maci, “Leaky-wave based interpretation of the radiation from holographic surfaces,” *IEEE Antennas Propag. Soc. AP-S Int. Symp.*, pp. 5813–5816, 2007.

[48] K. Iizuka, M. Mizusawa, S. Urasaki, and H. Ushigome, “Volume-Type Holographic Antenna,” *IEEE Trans. Antennas Propag.*, vol. AP-23, pp. 807–810, 1975.

[49] M. ElSherbiny, A. E. Fathy, A. Rosen, G. Ayers, and S. M. Perlow, “Holographic antenna concept, analysis, and parameters,” *IEEE Trans. Antennas Propag.*, vol. 52, no. 3, pp. 830–839, 2004.

[50] E. Almajali, D. McNamara, S. S. Alja’afreh, M. S. Sharawi, and I. Mabrouk, “A low-profile holographic antenna with dual-metasurface and printed Yagi feed,” *AEU - Int. J. Electron. Commun.*, vol. 111, p. 152921, 2019.

[51] A. Sutinjo and M. Okoniewski, “A surface wave holographic antenna for broadside radiation excited by a traveling wave patch array,” *IEEE Trans. Antennas Propag.*, vol. 59, no. 1, pp. 297–300, 2011.

[52] R. Wang *et al.*, “Migratory Insect Multifrequency Radar Cross Sections for Morphological Parameter Estimation,” *IEEE Trans. Geosci. Remote Sens.*, vol. 57, no. 6, pp. 3450–3461, 2019.

[53] S. Karimkashi, A. R. Mallahzadeh, and J. Rashed-Mohassel, “A new shaped reflector antenna for wide beam radiation patterns,” *Int. Symp. Microwave, Antenna, Propag. EMC Technol. Wirel. Commun.*, vol. 6, pp. 535–538, 2007.

[54] A. K. Behera, A. Ahmad, S. K. Mandal, G. K. Mahanti, and R. Ghatak, “Synthesis of cosecant squared pattern in linear antenna arrays using differential evolution,” *IEEE Conf. Inf. Commun. Technol.*, pp. 1025–1028, 2013.

[55] A. Foudazi, A. R. Mallahzadeh, and M. M. S. Taheri, “Pattern synthesis for multi-feed reflector antenna using IWO algorithm,” *6th Eur. Conf. Antennas Propag.*, pp. 1–5, 2012.

[56] R. Sauleau and B. Barès, “A complete procedure for the design and optimization of arbitrarily shaped integrated lens antennas,” *IEEE Trans. Antennas Propag.*, vol. 54, no. 4, pp. 1122–1133, 2006.

[57] K. Tekkouk, J. Hirokawa, R. Sauleau, M. Ettorre, M. Sano, and M. Ando, “Dual-Layer Ridged Waveguide Slot Array Fed by a Butler Matrix with Sidelobe Control in the 60-GHz Band,” *IEEE Trans. Antennas Propag.*, vol. 63, no. 9, pp. 3857–3867, 2015.

[58] M. Y. Rafiq, G. Bugmann, and D. J. Easterbrook, “Neural network design for engineering applications,” *Comput. Struct.*, vol. 79, no. 17, pp. 1541–1552, 2001.

[59] J. H. Garrett, “Where and why artificial neural networks are applicable in civil engineering,” *Journal of Computing in Civil Engineering,* vol. 8, no. 2. pp. 129–130, 1994.

[60] M. Nwadiugwu, “Neural Network, Artificial Intelligence and the Computational Brain,” pp. 1–36, 2015.

[61] J. Jordan, “Neural Network: Representation,” 2017.

[62] M. Sundermeyer, R. Schlüter, and H. Ney, “LSTM neural networks for language processing,” *Annu. Conf. Int. speech Commun. Assoc.*, pp. 194–197, 2012.

[63] A. Creswell, W. Tom, D. Vincent, K. Arulkumaran, B. Sengupta, and A. Bharath, “Generative adversarial network: An overview,” *IEEE Signal Process. Mag.*, vol. 35, no. 1, 2018.

[64] R. Dey and F. M. Salem, “Gate-variants of Gated Recurrent Unit (GRU) neural networks,” *IEEE 60th Int. Midwest Symp. Circuits Syst.*, no. 2, pp. 1597–1600, 2017.

[65] G. E. Dahl, T. N. Sainath, and G. E. Hinton, “On the importance of initialization and momentum in deep learning,” *ICASSP, IEEE Int. Conf. Acoust. Speech Signal Process. - Proc.*, no. 2010, pp. 8609–8613, 2013.

[66] T. Dietterich, “Overfitting and Undercomputing in Machine Learning,” *ACM Comput. Surv.*, vol. 27, no. 3, pp. 326–327, 1995.

[67] S. Agatonovic-Kustrin and R. Beresford, “Basic concepts of artificial neural network (ANN) modeling and its application in pharmaceutical research,” *J. Pharm. Biomed. Anal.*, vol. 22, no. 5, pp. 717–727, 2000.

[68] X. Glorot, A. Bordes, and Y. Bengio, “Deep sparse rectifier neural networks,” in *Journal of Machine Learning Research*, 2011, vol. 15, no. May 2014, pp. 315–323.

[69] A. L. Maas, A. Y. Hannun, and A. Y. Ng, “Rectifier nonlinearities improve neural network acoustic models,” *ICML Work. Deep Learn. Audio, Speech Lang. Process.*, vol. 28, 2013.

[70] L. Yang and A. Shami, “On hyperparameter optimization of machine learning algorithms: Theory and practice,” *Neurocomputing*, vol. 415, pp. 295–316, 2020.

[71] L. Hertel, J. Collado, P. Sadowski, J. Ott, and P. Baldi, “Sherpa: Robust hyperparameter optimization for machine learning,” *SoftwareX*, vol. 12, p. 100591, 2020.

[72] F. Hutter, J. Lücke, and L. Schmidt-Thieme, “Beyond Manual Tuning of Hyperparameters,” *KI - Kunstl. Intelligenz*, vol. 29, no. 4, pp. 329–337, 2015.

[73] H. B. Curry, “The method of steepest descent for non-linear minimization problems,” in *Quarterly of Applied Mathematics*, 1944, vol. 2, no. 3, pp. 258–261.

[74] S. S. Du, J. D. Lee, H. Li, L. Wang, and X. Zhai, “Gradient descent

finds global minima of deep neural networks," in *36th International Conference on Machine Learning*, 2019, pp. 3003–3048.

[75] L. N. Smith, "A disciplined approach to neural network hyper-parameters: Part 1 -- learning rate, batch size, momentum, and weight decay," 2018.

[76] I. J. Goodfellow, Y. Bengio, and A. Courville, *Deep learning*. Cambridge, MA, USA: MIT Press, 2016.

[77] S. Amari, "Backpropagation and stochastic gradient descent method," *Neurocomputing*, vol. 5, no. 4–5, pp. 185–196, 1993.

[78] S. Bonnabel, "Stochastic gradient descent on riemannian manifolds," *IEEE Trans. Automat. Contr.*, vol. 58, no. 9, pp. 2217–2229, 2013.

[79] S. Ruder, "An overview of gradient descent optimization algorithms," pp. 1–14, 2016, [Online]. Available: https://arxiv.org/pdf/1609.04747.

[80] D. Masters and C. Luschi, "Revisiting Small Batch Training for Deep Neural Networks," pp. 1–18, 2018, [Online]. Available: http://arxiv.org/abs/1804.07612.

[81] Y. Bengio, "Practical recommendations for gradient-based training of deep architectures," in *Neural networks: Tricks of the trade*, Springer, 2012, pp. 437–478.

[82] S. Ioffe and Christian Szegedy, "Batch Normalization: Accelerating Deep Network Training by Reducing," *J. Mol. Struct.*, vol. 1134, pp. 63–66, 2015.

[83] S. Ioffe, "Batch Renormalization: Towards Reducing Minibatch Dependence in Batch-Normalized Models," *Adv. Neural Inf. Process. Syst.*, vol. 34, no. 5, pp. 1945–1953, 2017.

[84] Y. Wu and J. Johnson, "Rethinking 'Batch' in BatchNorm," 2021, [Online]. Available: http://arxiv.org/abs/2105.07576.

[85] N. Srivastava, G. Hinton, A. Krizhevsky, I. Sutskever, and R. Salakhutdinov, “Dropout: A Simple Way to Prevent Neural Networks from Overfitting,” *J. Mach. Learn. Res.*, pp. 1929–1958, 2014.

[86] D. M. Hawkins, “The Problem of Overfitting,” *J. Chem. Inf. Comput. Sci.*, vol. 44, no. 1, pp. 1–12, 2004.

[87] X. Ying, “An Overview of Overfitting and its Solutions,” *J. Phys. Conf. Ser.*, vol. 1168, no. 2, 2019.

[88] P. Baldi and P. Sadowski, “Understanding dropout,” *Adv. Neural Inf. Process. Syst.*, 2013.

[89] M. K. Alsmadi, K. Bin Omar, S. A. Noah, and I. Almarashdah, “Performance comparison of multi-layer perceptron (Back Propagation, Delta Rule and Perceptron) algorithms in neural networks,” *IEEE Int. Adv. Comput. Conf. IACC*, vol. 7, pp. 296–299, 2009.

[90] A. Sharif Ahmadian, “Chapter 7: Numerical Modeling and Simulation,” in *Numerical Models for Submerged Breakwaters*, 2016, pp. 109–126.

[91] H. Takase, K. Gouhara, and Y. Uchikawa, “Time sequential pattern transformation and attractors of recurrent neural networks,” *Proc. Int. Jt. Conf. Neural Networks*, vol. 3, pp. 2319–2322, 1993.

[92] K. Cho *et al.*, “Learning phrase representations using RNN encoder-decoder for statistical machine translation,” *Conf. Empir. Methods Nat. Lang. Process.*, pp. 1724–1734, 2014.

[93] Y. Su and C. C. J. Kuo, “On extended long short-term memory and dependent bidirectional recurrent neural network,” *Neurocomputing*, vol. 356, pp. 151–161, 2019.

[94] M. Ravanelli, P. Brakel, M. Omologo, and Y. Bengio, “Light Gated Recurrent Units for Speech Recognition,” *IEEE Trans. Emerg. Top. Comput. Intell.*, vol. 2, no. 2, pp. 92–102, 2018.

[95] Q. Lu, Z. Zhu, F. Xu, D. Zhang, W. Wu, and Q. Guo, “Bi-GRU sentiment classification for chinese based on grammar rules and bert,” *Int. J. Comput. Intell. Syst.*, vol. 13, no. 1, pp. 538–548, 2020.

[96] S. C. B. Lo, H. P. Chan, J. S. Lin, H. Li, M. T. Freedman, and S. K. Mun, “Artificial convolution neural network for medical image pattern recognition,” *Neural Networks*, vol. 8, no. 7–8, pp. 1201–1214, 1995.

[97] A. A. M. Al-Saffar, H. Tao, and M. A. Talab, “Review of deep convolution neural network in image classification,” *Int. Conf. Radar, Antenna, Microwave, Electron. Telecommun. ICRAMET*, pp. 26–31, 2017.

[98] B. B. Traore, B. Kamsu-Foguem, and F. Tangara, “Deep convolution neural network for image recognition,” *Ecol. Inform.*, vol. 48, no. September, pp. 257–268, 2018.

[99] J. Yang and J. Li, “Application of Deep Convolution Neural Network,” *14th Int. Comput. Conf. Wavelet Act. Media Technol. Inf. Process.*, 2017.

[100] Y. Pang, M. Sun, X. Jiang, and X. Li, “Convolution in convolution for network in network,” *IEEE Trans. Neural Networks Learn. Syst.*, vol. 29, no. 5, pp. 1587–1597, 2018.

[101] D. D. Pukale, S. G. Bhirud, and V. D. Katkar, “Content-based Image Retrieval using Deep Convolution Neural Network,” *Int. Conf. Comput. Commun. Control Autom.*, pp. 1–5, 2018.

[102] Q. J. Zhang, K. C. Gupta, and V. K. Devabhaktuni, “Artificial neural networks for RF and microwave design - From theory to practice,” *IEEE Trans. Microw. Theory Tech.*, vol. 51, no. 4, pp. 1339–1350, 2003.

[103] F. Wang, “Knowledge-based neural models for microwave design,” *IEEE Trans. Microw. Theory Tech.*, vol. 45, no. 12, pp. 2333–2343, 1997.

[104] M. Vai and S. Prasad, “Microwave Circuit Analysis and Design by a Massively Distributed Computing Network,” *IEEE Trans. Microw. Theory Tech.*, vol. 43, no. 5, pp. 1087–1094, 1995.

[105] J. Xu, M. C. E. Yagoub, R. Ding, and Q. J. Zhang, “Neural-based dynamic modeling of nonlinear microwave circuits,” *IEEE Trans. Microw. Theory Tech.*, vol. 50, no. 12, pp. 2769–2780, 2002.

[106] C. Gianfagna, H. Yu, M. Swaminathan, R. Pulugurtha, R. Tummala, and G. Antonini, “Machine-Learning Approach for Design of Nanomagnetic-Based Antennas,” *J. Electron. Mater.*, vol. 46, no. 8, pp. 4963–4975, 2017.

[107] S. K. Jain, “Bandwidth enhancement of patch antennas using neural network dependent modified optimizer,” *Int. J. Microw. Wirel. Technol.*, vol. 8, no. 7, pp. 1111–1119, 2016.

[108] J. Tak, A. Kantemur, Y. Sharma, and H. Xin, “A 3-D-printed W-band slotted waveguide array antenna optimized using machine learning,” *IEEE Antennas Wirel. Propag. Lett.*, vol. 17, no. 11, pp. 2008–2012, 2018.

[109] L. Weng, “From GAN to WGAN,” 2019, [Online]. Available: http://arxiv.org/abs/1904.08994.

[110] S. Meng, X. Q. Jiang, Y. Gao, H. Hai, and J. Hou, “Performance Evaluation of Channel Decoder based on Recurrent Neural Network,” *J. Phys. Conf. Ser.*, vol. 1438, no. 1, 2020.

[111] S. K. Sahoo, M. Adhikary, A. Biswas, and M. J. Akhtar, “GCPW to SIW transition for planar excitation of ku-band substrate integrated end-fire antennas,” *IEEE Indian Conf. Antennas Propag.*, pp. 15–18, 2019.

[112] F. Xu and K. Wu, “Guided-wave and leakage characteristics of substrate integrated waveguide,” *IEEE Trans. Microw. Theory Tech.*, vol. 53, no. 1, pp. 66–72, 2005.

[113] R. Kazemi, A. E. Fathy, S. Yang, and R. A. Sadeghzadeh, “Development of an ultra wide band GCPW to SIW transition,” *IEEE Radio Wirel. Symp.*, pp. 171–174, 2012.

[114] T. Djerafi, A. Doghri, and K. Wu, *Handbook of Antenna Technologies*. 2015.

[115] E. B. Joy, W. M. Leach, G. P. RODRIGUE, and D. T. Paris, “Applications of Probe-Compensated Near-Field Measuremen,” *IEEE Trans. Antennas Propag.*, vol. 26, no. 3, 1978.

[116] D. T. Paris, W. M. Leach, and E. B. Joy, “Basic theory of probe-compensated near-field measurements,” *IEEE Trans. Antennas Propag.*, no. 3, pp. 373–379, 1978.

[117] J. S. Hollis and H. A. Ecker, “Determination of Far-Field Antenna Patterns from Near-Field Measurements,” *Proc. IEEE*, vol. 61, no. 12, pp. 1668–1694, 1973.

[118] Constantine A. Balanis, *Antenna Theory Analysis and Design*. John Wiley & Sons, Ltd., 1982.

[119] C. Villani, “The Wasserstein distances,” in *Grundlehren der mathematischen Wissenschaften*, 2009, pp. 93–111.

[120] Q. Liu, G. Ma, and C. Cheng, “Data Fusion Generative Adversarial Network for Multi-Class Imbalanced Fault Diagnosis of Rotating Machinery,” *IEEE Access*, vol. 8, pp. 70111–70124, 2020.

[121] J. Xu, Z. Li, B. Du, M. Zhang, and J. Liu, “Reluplex made more practical: Leaky ReLU,” *IEEE Symp. Comput. Commun.*, 2020.

[122] F. Pedregosa *et al.*, “Scikit-learn: Machine Learning in Python (MLP classifier),” *J. Mach. Learn. Res.*, vol. 12, pp. 2825–2830, 2011.

[123] W. Hilberg, “From Approximations to Exact Relations for Characteristic Impedances,” *IEEE Trans. Microw. Theory Tech.*, vol. 17, no. 5, pp. 259–265, 1969.

[124] CST Studio Suite 2020, “Time Domain Solver Overview.” .

[125] CST Studio Suite 2020, “Frequency Domain Solver Overview.” .

[126] Z. Hamzavi-Zarghani, L. Matekovits, and A. Yahaghi, “Improved Gain Graphene Based Leaky Wave Antenna Loaded by Dielectric Slab in THz Regime,” *13th Eur. Conf. Antennas Propag.*, pp. 13–15, 2019.

[127] F. Khajeh-Khalili and Y. Dohni-Zadeh, “High-Gain Multi-Layer Antenna Using Metasurface for Application in Terahertz Communication Systems,” *Int. J. Electron. Device Phys.*, 2019.

[128] M. Faenzi *et al.*, “Metasurface leaky-wave antennas: A comparison between slot and patch implementation,” *8th Eur. Conf. Antennas Propag.*, pp. 1234–1237, 2014.

A. Appendix: Near-field to far-field transformation

The detailed computation process of the NF2FF will be given here. Following the Chapter 3 section 3.2.1, the relationship between the near-field and the far-field for planar systems is given by

$$E(x, y, z) = \frac{1}{4\pi^2} \iint_{-\infty}^{\infty} f(k_x, k_y) e^{-jkr} dk_x dk_y \tag{A.1}$$

Where

$$f\left(k_x, k_y\right) = \overrightarrow{a_x} f_x\left(k_x, k_y\right) + \overrightarrow{a_y} f_y\left(k_x, k_y\right) + \overrightarrow{a_z} f_x\left(k_x, k_y\right) \tag{A.2}$$

$$k = \overrightarrow{a_x} k_x + \overrightarrow{a_y} k_y + \overrightarrow{a_z} k_z \tag{A.3}$$

$$r = \overrightarrow{a_x} x + \overrightarrow{a_y} y + \overrightarrow{a_z} z \tag{A.4}$$

Where $f\left(k_x, k_y\right)$ is the plane wave spectrum of the field.

The E_x and E_y components of the E-field over a plane surface ($z = 0$) from (A.1 are

$$E_{xa}(x, y, z = 0) = \frac{1}{4\pi^2} \iint_{-\infty}^{\infty} f_x(k_x, k_y) e^{-j(k_x x + k_y y)} dk_x dk_y \tag{A.5}$$

$$E_{ya}(x,y,z=0) = \frac{1}{4\pi^2}\iint_{-\infty}^{\infty} f_y(k_x,k_y)e^{-j(k_x x+k_y y)}dk_x dk_y$$

(A.6)

The E_x and E_y components of the plane wave spectrum, $f_x\left(k_x,k_y\right)$ and $f_y\left(k_x,k_y\right)$, are defined as

$$f_x\left(k_x,k_y\right) = \int_{-b/2}^{b/2}\int_{-a/2}^{a/2} E_{xa}(x,y,z=0)e^{+j\left(k_x x+k_y y\right)}dxdy$$

(A.7)

$$f_y(k_x,k_y) = \int_{-b/2}^{b/2}\int_{-a/2}^{a/2} E_{ya}(x,y,z=0)e^{+j\left(k_x x+k_y y\right)}dxdy$$

(A.8)

The far-field radiation pattern of the antenna can then be calculated as

$$E_\theta(r,\theta,\phi) \approx j\frac{ke^{-jkr}}{2\pi r}(f_x cos\phi + f_y sin\phi)$$

(A.9)

$$E_\phi(r,\theta,\phi) \approx j\frac{ke^{-jkr}}{2\pi r}cos\theta(-f_x sin\phi + f_y cos\phi)$$

(A.10)

$$E(r,\theta,\phi) = E_\theta(r,\theta,\phi) + E_\phi(r,\theta,\phi) \approx j\frac{ke^{-jkr}}{2\pi r}[cos\theta\, f(k_x,k_y)]$$

(A.11)

During implementation, the *E*-field data from CST simulation is employed as the input to the NF2FF algorithm. The simulation requires a plane surface, which is z_0 in height from the antenna. The plane is divided into a rectangular grid of M×N points spaced by Δx and Δy, as shown in Figure A.1. Each point is defined by the coordinates $(m\Delta x, n\Delta y)$ where $-\frac{M}{2} \leq m \leq \frac{M}{2} - 1$ and $-\frac{N}{2} \leq n \leq \frac{N}{2} - 1$. The value of M and N are determined by the linear dimensions of the sampling plane divided by the sampling space. Defining the width (*a*) and length (*b*) of the rectangular grids, M and N can be calculated by using (A.12 and (A.13. The sampling points on the rectangular plane are chosen to be less than 0.5λ_0 to meet the requirement of Nyquist sampling criterion.

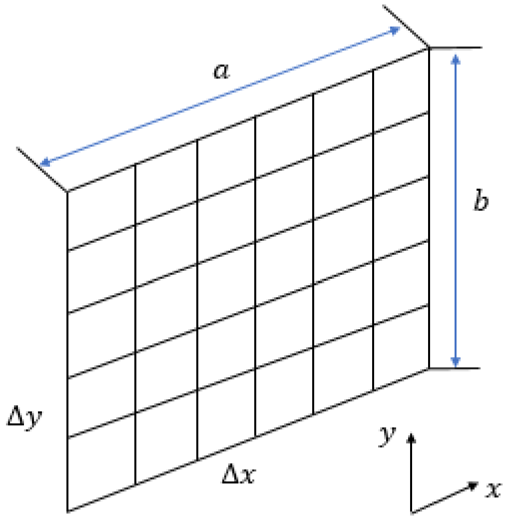

Figure A.1. Sampling rectangular plane.

$$M = \frac{a}{\Delta x} + 1 \tag{A.12}$$

$$N = \frac{b}{\Delta y} + 1 \tag{A.13}$$

The E_x and E_y components of the rectangular sampling plane at the grid points can be expressed by (A.14 and (A.15. By applying the E_x and E_y components equations, f_x and f_y in (A.7 and (A.8 can be calculated using the fast Fourier transform algorithm. And the k_x and k_y is given by (A.16 and (A.17. The wavenumber spectrum points are the same as the number of points in the near-field distribution.

$$E_{xa}(x,y,z=0) = \sum_{n=-\frac{N}{2}}^{\frac{N}{2}-1} \sum_{m=-\frac{M}{2}}^{\frac{M}{2}-1} E_x(m\Delta x, n\Delta y, 0) \times \frac{\sin(\frac{\pi}{\Delta x}x - m\pi)}{\frac{\pi}{\Delta x}x - m\pi} \frac{\sin(\frac{\pi}{\Delta y}y - n\pi)}{\frac{\pi}{\Delta y}y - n\pi} \tag{A.14}$$

$$E_{ya}(x,y,z=0) = \sum_{n=-\frac{N}{2}}^{\frac{N}{2}-1} \sum_{m=-\frac{M}{2}}^{\frac{M}{2}-1} E_y(m\Delta x, n\Delta y, 0) \times \frac{\sin(\frac{\pi}{\Delta x}x - m\pi)}{\frac{\pi}{\Delta x}x - m\pi} \frac{\sin(\frac{\pi}{\Delta y}y - n\pi)}{\frac{\pi}{\Delta y}y - n\pi} \tag{A.15}$$

$$k_x = \frac{2\pi m}{M\Delta x} \tag{A.16}$$

$$k_y = \frac{2\pi n}{N\Delta x} \tag{A.17}$$

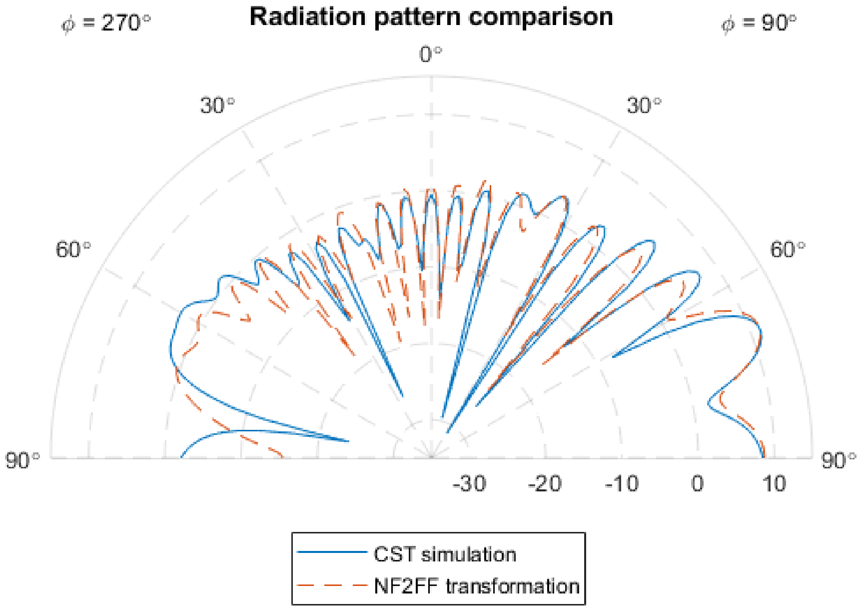

Figure A.2. Radiation pattern of NF2FF transformation.

By selecting the *E*-field data of the $z_0 = 0.5\lambda_0$ surface, the far-field radiation pattern is calculated through the NF2FF transformation algorithm, as shown in Figure A.2. In Figure A.2, the NF2FF transformation pattern shows some discrepancies with the CST simulation. The reason is that the sampling spacing in the algorithm is $0.125\lambda_0$, thus, the rectangular grids are 3600 in the NF2FF transformation. While the CST simulation has one million mesh grids. Therefore, the computation accuracy of the NF2FF transformation is not enough compared with the CST simulation. Although there are some discrepancies, the envelope of the NF2FF transformed radiation pattern is similar to the CST simulated, which implies the NF2FF transformation algorithm is feasible.

B. Appendix: Mathematical prediction model

Following the Chapter 3 section 3.3.1.1, the first order of the Fourier, Gaussian and exponential mathematical prediction model are given by

$$f(x) = a_1 + a_2\cos(wx) + a_3\sin(wx) \tag{B.1}$$

$$g(x) = b_1 e^{-(\frac{x-b_2}{b_3})^2} \tag{B.2}$$

$$h(x) = c_1 e^{c_2 x} \tag{B.3}$$

Where a_1, a_2, a_3, w, b_1, b_2, b_3, c_1 and c_2 are the mathematical prediction model parameters.

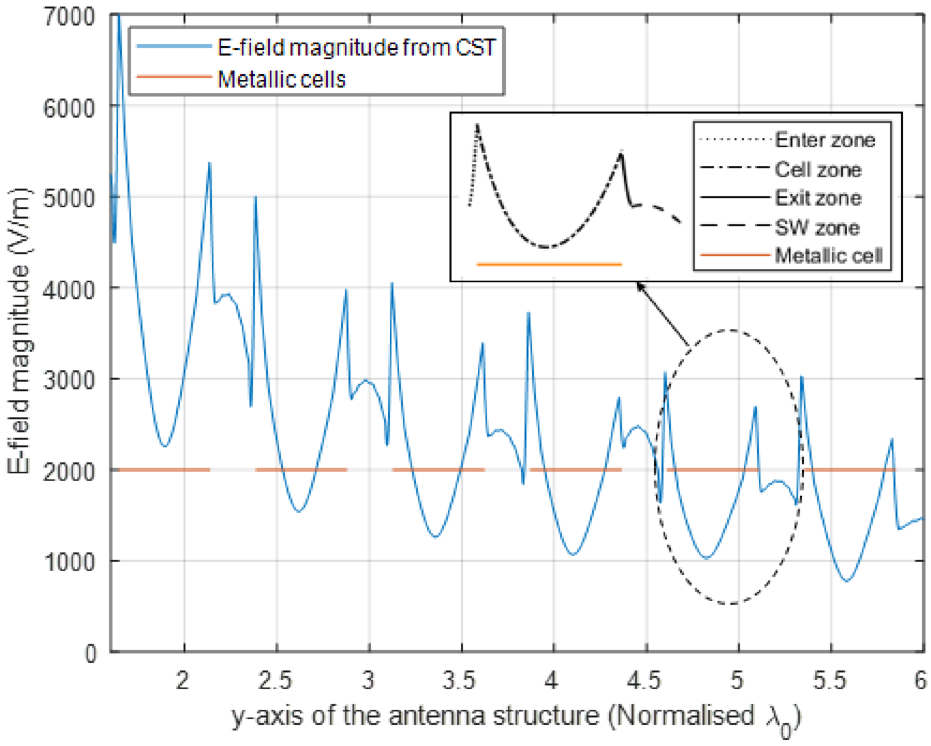

Figure B.1. Changing patterns of the on-surface *E*-field magnitude at 34.5 GHz.

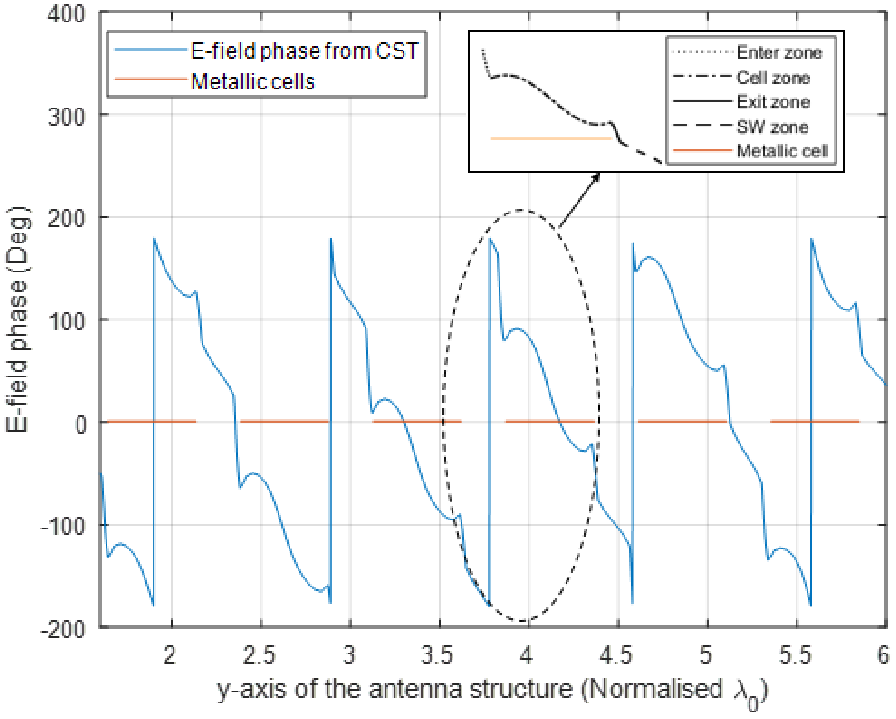

Figure B.2. Changing patterns of the on-surface *E*-field phase at 34.5 GHz.

When the wave propagates through the surface, the magnitude and phase of the *E*-field have different changing patterns at different positions relative to the cell, as shown in Figure B.1 and Figure B.2. This variation pattern through each cell can be divided into four zones, which are enter zone, cell zone, exit zone and surface wave (SW) zone. The magnitude and phase of the *E*-field show the regular and periodic changing patterns when the wave propagates through the metallic cell. In the magnitude mathematical prediction model, the enter and exit zone are fitted with the 1st order Fourier model provided by Matlab Fitting Toolbox. The cell zone and surface wave zone are fitted with 2nd order exponential and 1st order Gaussian model respectively. In the phase mathematical prediction model, the enter zone, cell zone and exit zone are fitted with 1st order Fourier model, and the surface wave zone uses 1st order Gaussian model. The lowest order fitting models are applied to reduce the complexity as much as possible under the premise of ensuring low fitting error.

1) Mathematical prediction model – *E*-field magnitude

From Figure B.1, the magnitude changes from a lower value to maxima when the wave closes to the front edge of the metallic cell. The magnitude decreases with the wave going through the cell and increases before the wave leaves. The magnitude then drops after the wave leaves the cell. The magnitude of each metallic cell shows a similar changing pattern except the absolute value. Therefore, the changing patterns can be normalised before applying the mathematical prediction model. The maximum magnitude value of each metallic cell can be predicted by a mathematical model either.

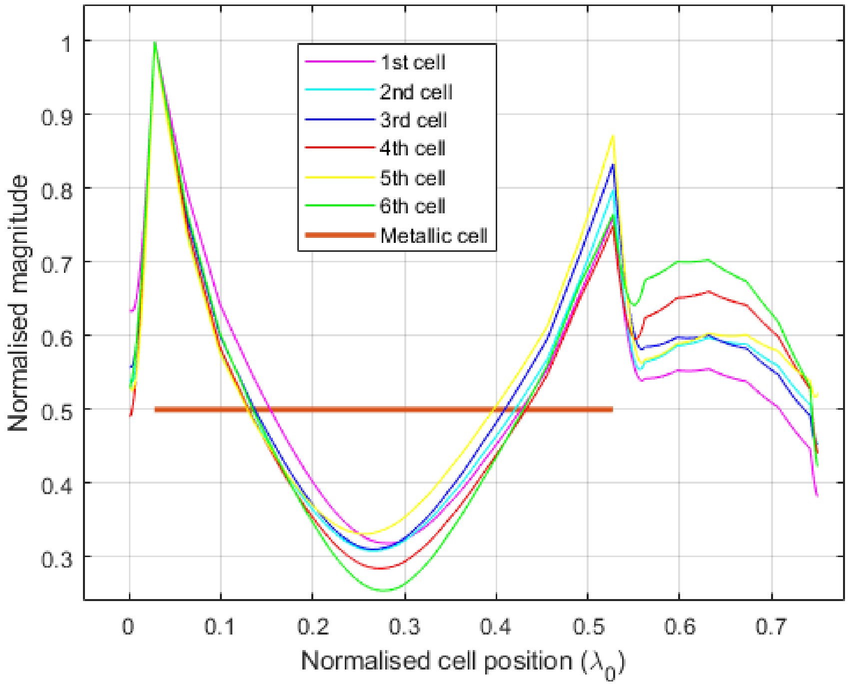

Figure B.3. Normalised magnitude changing pattern of each metallic cell at 34.5 GHz.

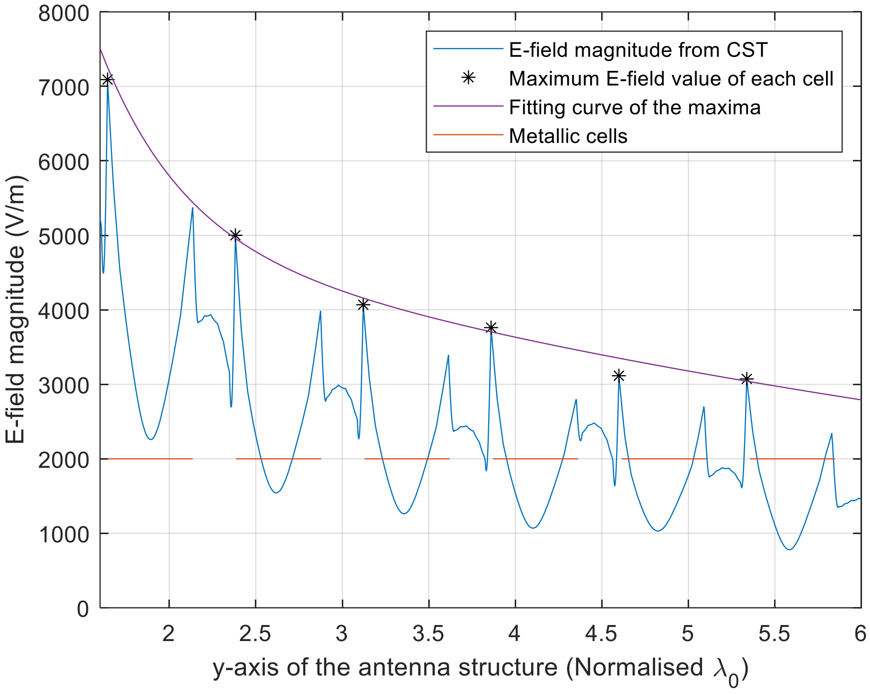

Figure B.4. The fitting curve of the maxima of each metallic cell at 34.5 GHz.

Figure B.3 shows the normalised changing pattern of each cell. It can be seen that all of the metallic cells show a similar changing pattern. Therefore, the mathematical prediction model can be obtained by averaging those patterns. (B.4, (B.5, (B.6 and (B.7 show the mathematical model of the enter zone, cell zone, exit zone and surface wave zone. Figure B.4 show the fitting curve of the maxima of each metallic cell and the equation is expressed as (B.8. The exact value of the magnitude can be calculated by multiplying the normalised mathematical models with the corresponding maxima. The magnitude of the on-surface *E*-field can be obtained by using the normalised mathematical model and the maxima equation.

$$Mag(x_1) = 0.9681 - 0.4171\cos(57.21x_1) - 0.08144\sin(57.21x_1) \tag{B.4}$$

$$Mag(x_2) = 1.218\, e^{-7.805x_2} + 0.04476\, e^{5.514x_2} \tag{B.5}$$

$$Mag(x_3) = 0.8332 + 0.2314\cos(47.24x_3) - 0.091\sin(47.24x_3) \tag{B.6}$$

$$Mag(x_4) = 0.6198 \times e^{-(\frac{x_4 - 0.6679}{0.2755})^2} \tag{B.7}$$

$$E_{MaxMag} = 7.365 \times 10^4 e^{-1.981x} + 6070e^{-0.1224x} \tag{B.8}$$

Where x_1, x_2, x_3, x_4 and x denote the position of the data point.

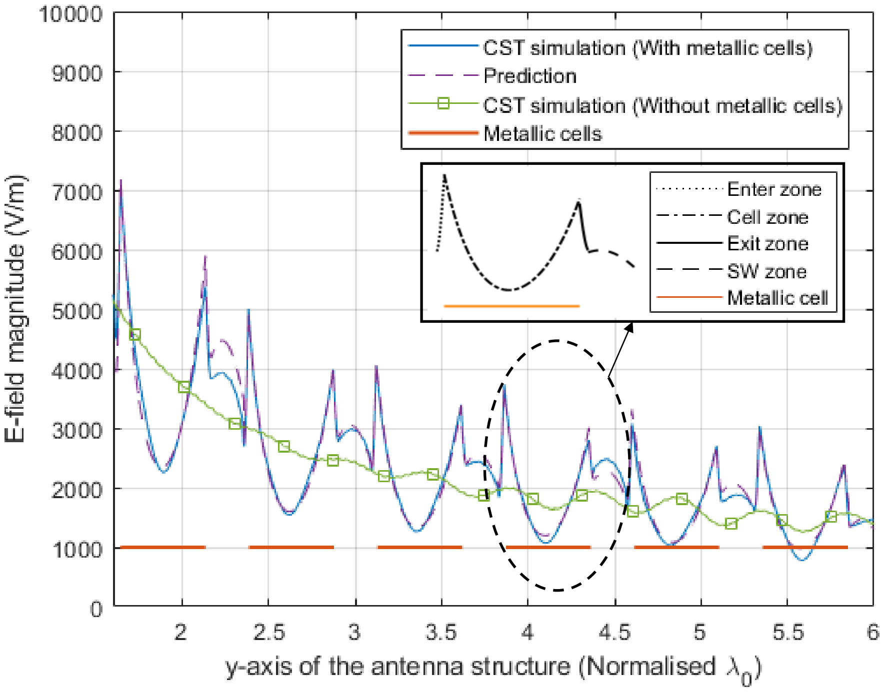

Figure B.5. Magnitude comparison between prediction and CST simulation at 34.5 GHz.

The comparisons of the predicted and simulated magnitude of the *E*-field at 34.5 GHz is shown in Figure B.5. The magnitude of the surface wave antenna without the cells are also presented in the figure for comparison; the variation of magnitude in the four zones can then be easily observed. In Figure B.5, the magnitude has a sudden rise in the enter zone and has a drop in the exit zone. In the surface wave zone, the magnitude tends to follow the changing trend of the magnitude of the surface wave launcher structure. The prediction error of magnitude is 4.62% at 34.5 GHz.

To demonstrate the feasibility of the mathematical model across the frequency, the mathematical model has been investigated under different frequency. A 2 GHz bandwidth from 33.5 GHz to 35.5 GHz has been considered as a frequency span. In the mathematical model of each zone, the a_1, a_2, a_3, w, b_1, b_2, b_3, c_1 and c_2 are frequency dependent parameters. Therefore, curve fitting tools are applied to those parameters to investigate the relationship between parameters and frequency. In the four zones of magnitude mathematical prediction model, 1st order Fourier model has been used in the enter and exit zone while 2nd order exponential model and 1st order Gaussian model has been applied to cell zone and SW zone respectively. Therefore, in the enter zone and exit zone model, there are four parameters, which are a_1, a_2, a_3 and w. In the cell zone and maxima prediction model, c_1, c_2, c_3 and c_4 are the frequency dependent parameters. There are three parameters b_1, b_2 and b_3 in the SW zone model. From the Figure B.6 to Figure B.9, the relationship between parameters and frequency of each zone have been defined. Figure B.10 shows the relationship between fitting parameters and the maxima prediction. The magnitude of each zone at the frequency band from 33.5 GHz to 35.5 GHz can be predicted.

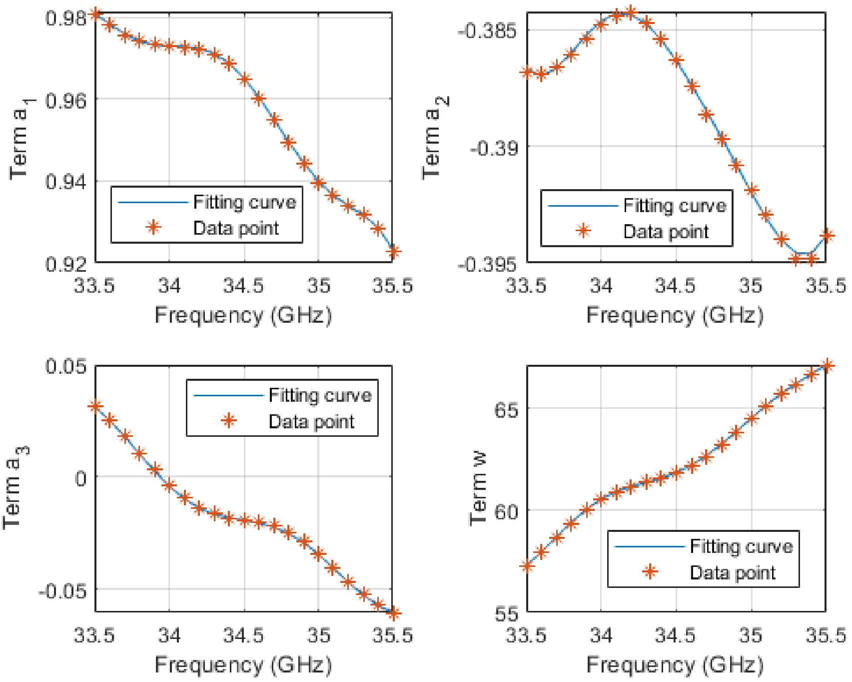

Figure B.6. The relationship between parameters and frequency in the enter zone magnitude mathematical model.

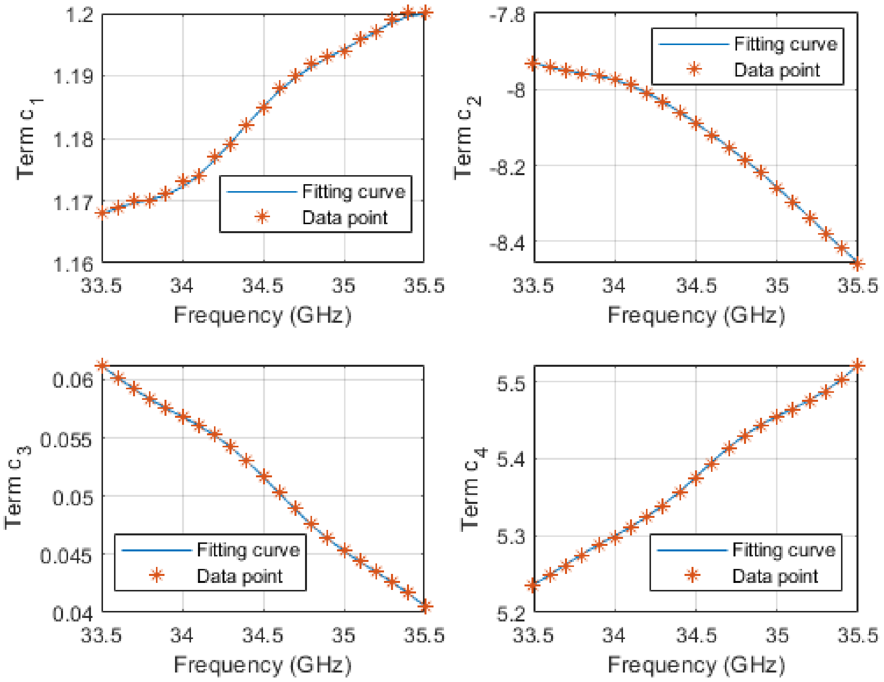

Figure B.7. The relationship between parameters and frequency in the cell zone magnitude mathematical model.

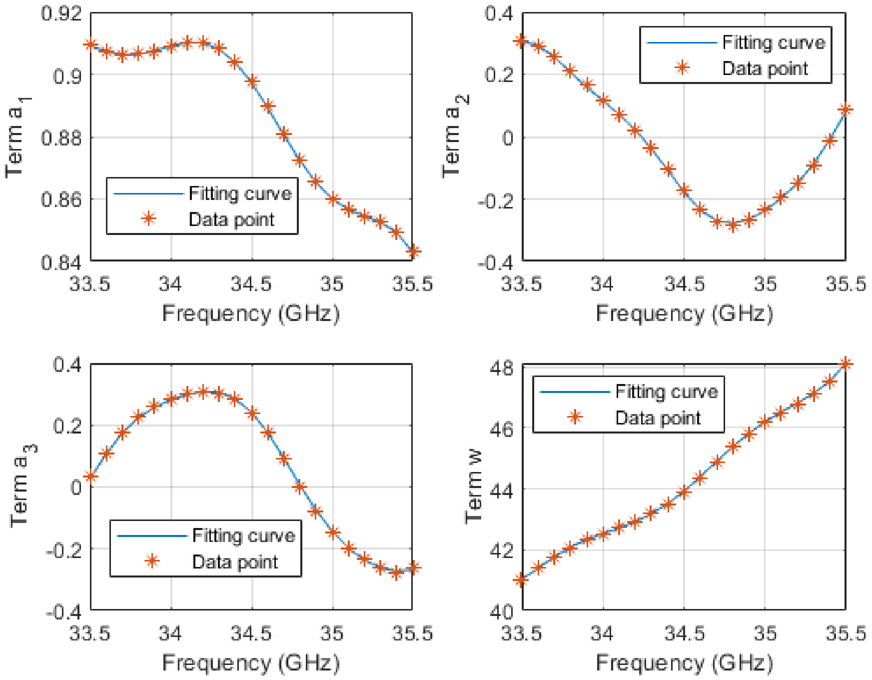

Figure B.8. The relationship between parameters and frequency in the exit zone magnitude mathematical model.

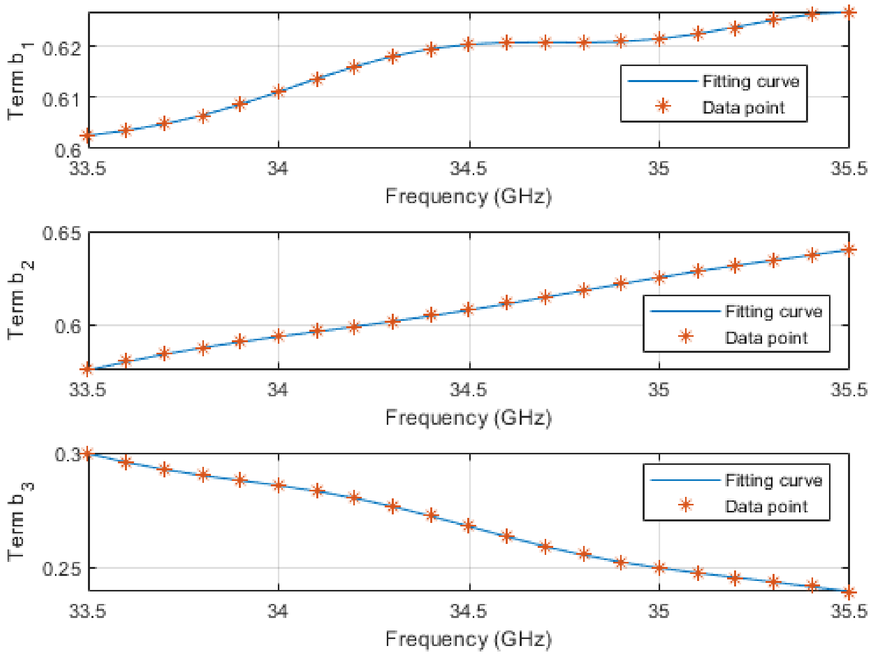

Figure B.9. The relationship between parameters and frequency in the SW zone magnitude mathematical model.

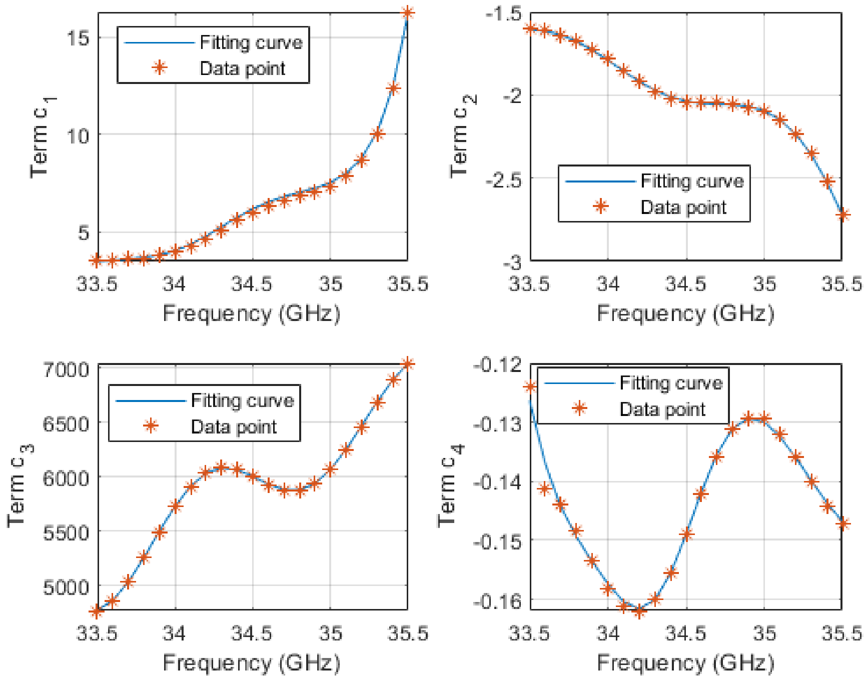

Figure B.10. The relationship between parameters and frequency in the magnitude maxima prediction mathematical model.

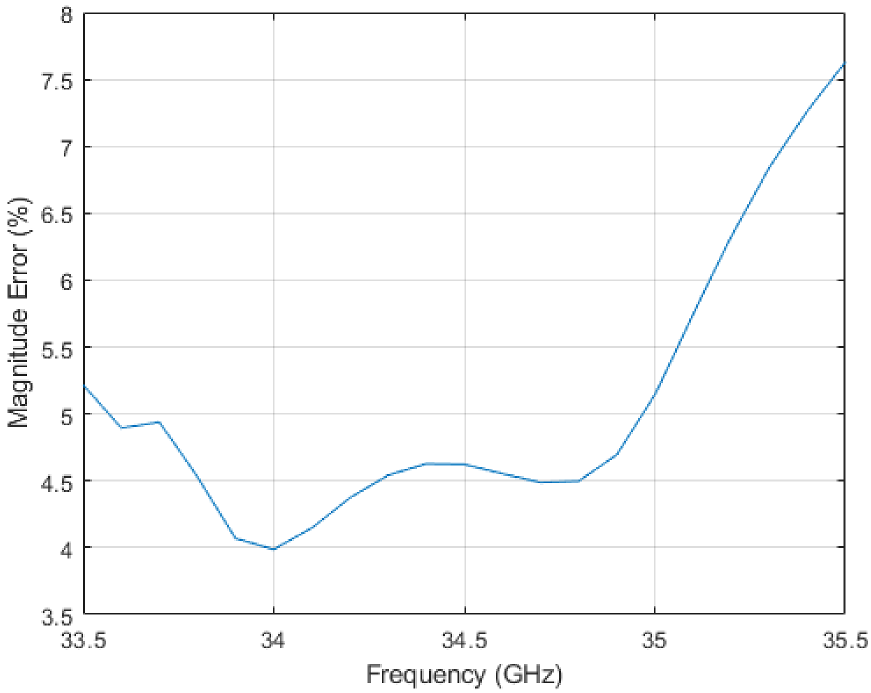

Figure B.11. Magnitude prediction error.

Figure B.11 depicts the magnitude prediction error across the 2 GHz frequency span from 33.5 GHz to 35.5 GHz. The maximum error is 7.63% at 35.5 GHz while the minimum error is 3.98% at 34 GHz. The average error is 4.45% from 34 GHz to 35 GHz, which corresponds to the operation frequency band of the VLR.

2) Mathematical prediction model – *E*-field phase

In the phase case, the four zones changing pattern can still be observed. The similar method as magnitude mathematical prediction model is implemented to derive the average of changing pattern. The average phase changing pattern is shown in Figure B.12. In the phase changing pattern, the 1st order Fourier model is applied to enter zone, cell zone and exit zone, while the 1st order Gaussian model is used to define the change of SW zone. The mathematical models are expressed as (B.9, (B.10, (B.11 and (B.12 for enter zone, cell zone, exit zone and SW zone respectively.

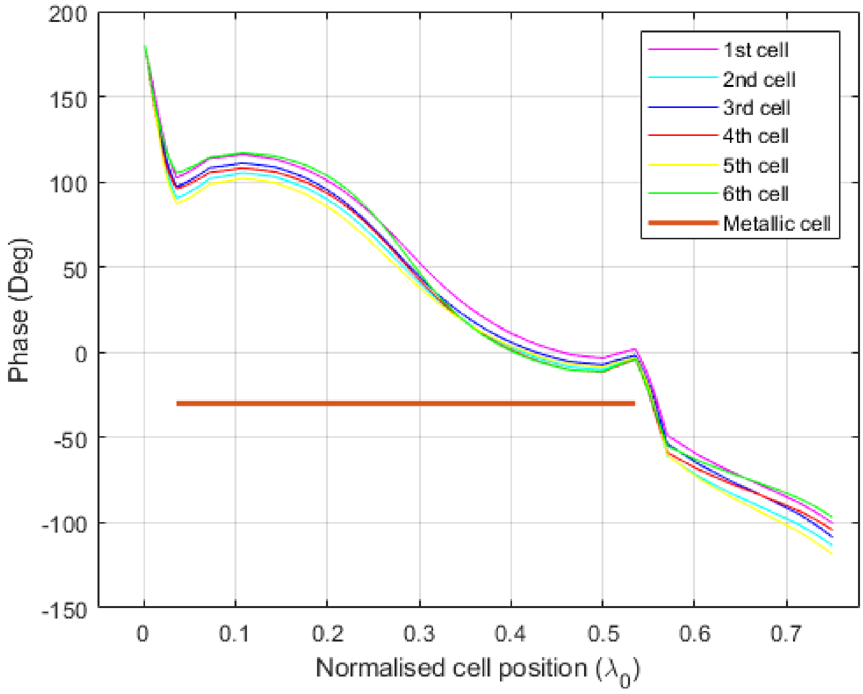

Figure B.12. Phase changing pattern of each metallic cell at 34.5 GHz.

$$Phase(x_1) = 169.4 + 15.07\cos(44.92x_1) - 66.93\sin(44.92x_1) \tag{B.9}$$

$$Phase(x_2) = 54.23 + 35.78\cos(8.67x_2) + 46.75\sin(8.67x_2) \tag{B.10}$$

$$Phase(x_3) = -56.01 - 46.76\cos(29.28x_3) + 42.07\sin(29.28x_3) \tag{B.11}$$

$$Phase(x_4) = -135.1 \times e^{-(\frac{x_4 - 0.9647}{0.4121})^2} \tag{B.12}$$

Where x_1, x_2, x_3 and x_4 denote the position of the data point.

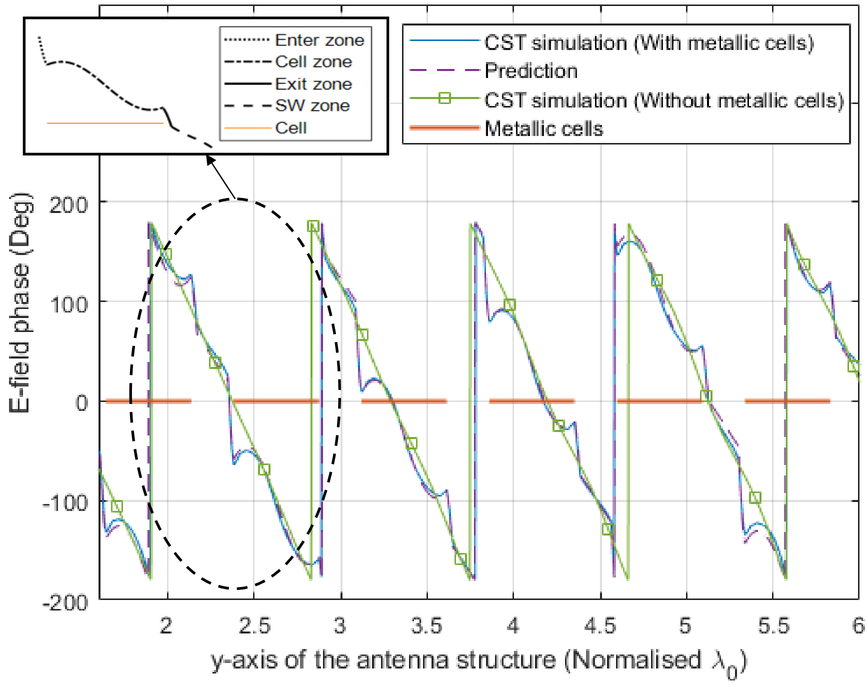

Figure B.13. Phase comparison between prediction and CST simulation at 34.5 GHz.

The comparisons of simulated and predicted phase of the *E*-field at 34.5 GHz is shown in Figure B.13. The phase of the surface wave antenna without the metallic cells are also shown in the figure for comparison. In Figure B.13, the phase changes rapidly in the enter and exit zone. While in the surface wave zone, the phase change is getting slower and follows the phase change of standard surface wave. The prediction error of magnitude is 4.6° at 34.5 GHz.

The curve fitting tools are applied to those parameters to investigate the relationship between parameters and frequency. In the four zones of phase mathematical prediction model, the 1st order Fourier model has been used in the enter, cell and exit zone respectively while the 1st order Gaussian model has been applied to SW zone. Therefore, four parameters, which are a_1, a_2, a_3 and w, need to be investigated in the enter, cell and exit zone. In the SW zone model, parameters b_1, b_2 and b_3 are the main factors. The phase of each zone at the frequency band from 33.5 GHz to 35.5 GHz can then be predicted.

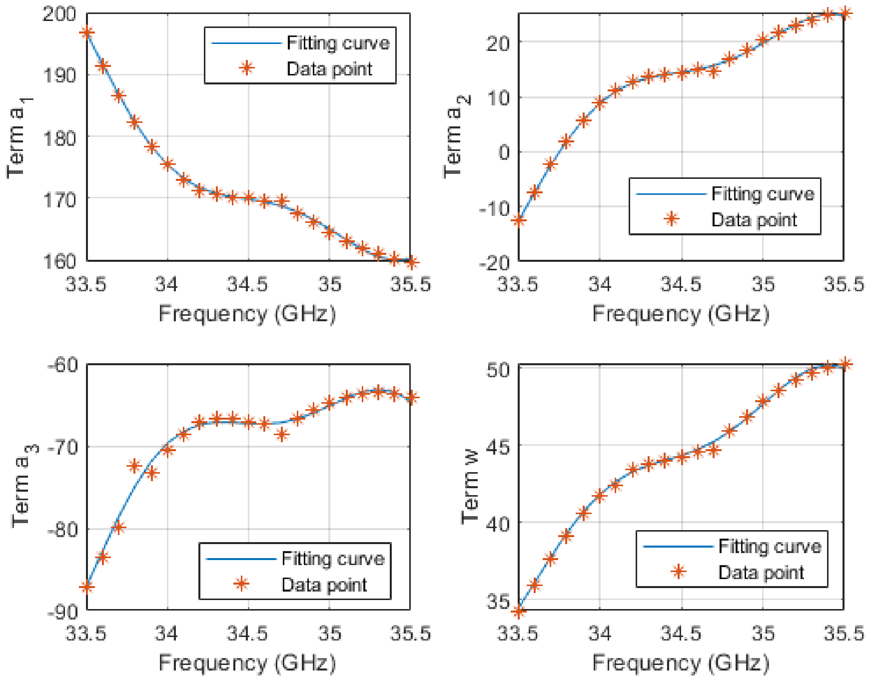

Figure B.14. The relationship between parameters and frequency in the enter zone phase mathematical model.

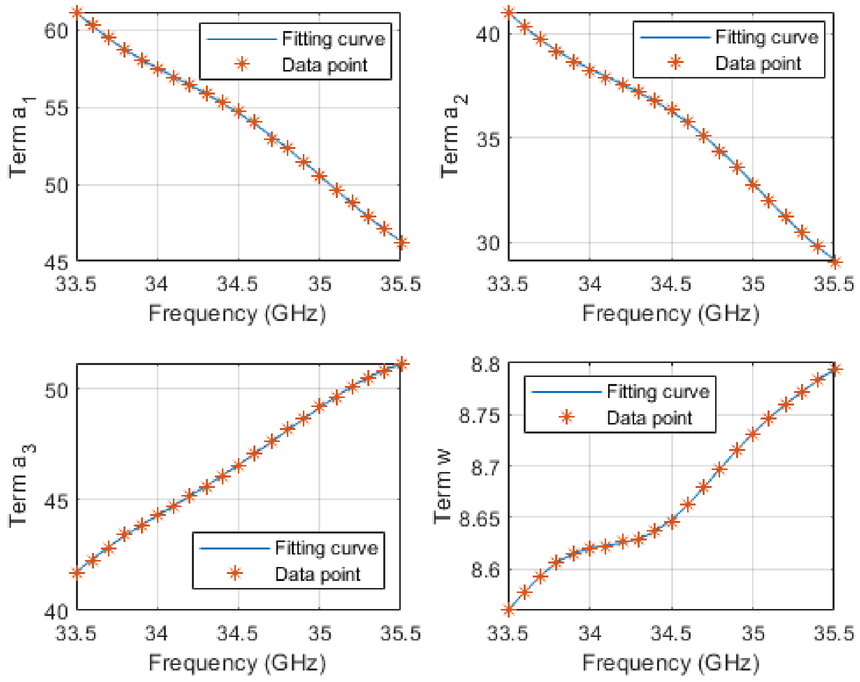

Figure B.15. The relationship between parameters and frequency in the cell zone magnitude phase model.

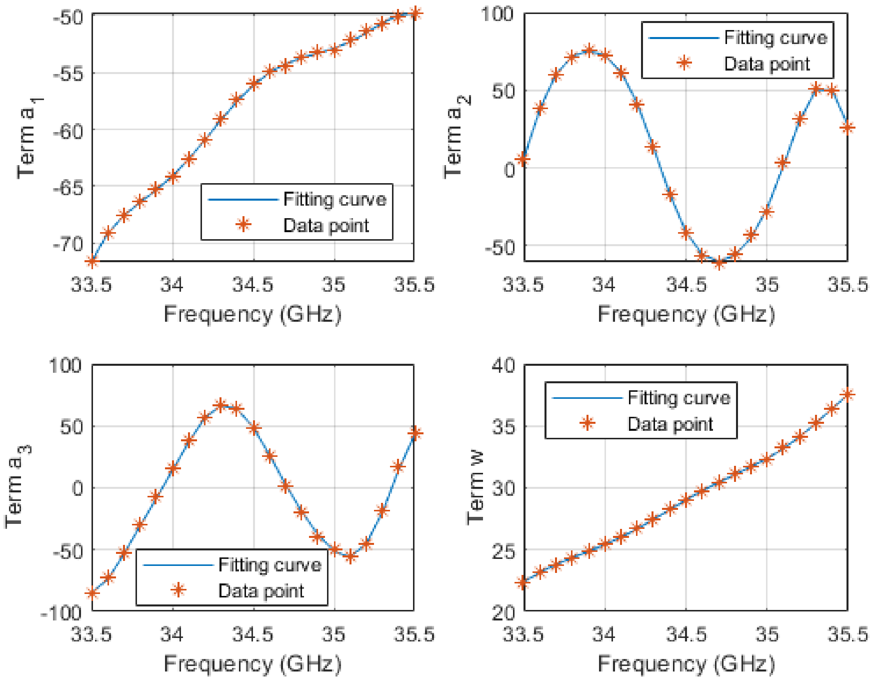

Figure B.16. The relationship between parameters and frequency in the exit zone magnitude phase model.

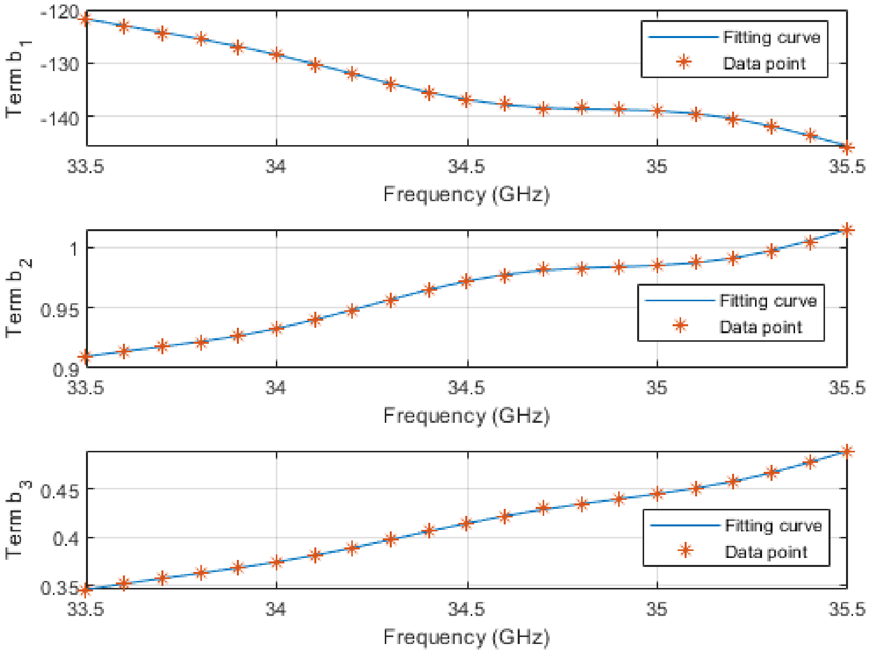

Figure B.17. The relationship between parameters and frequency in the SW zone magnitude phase model.

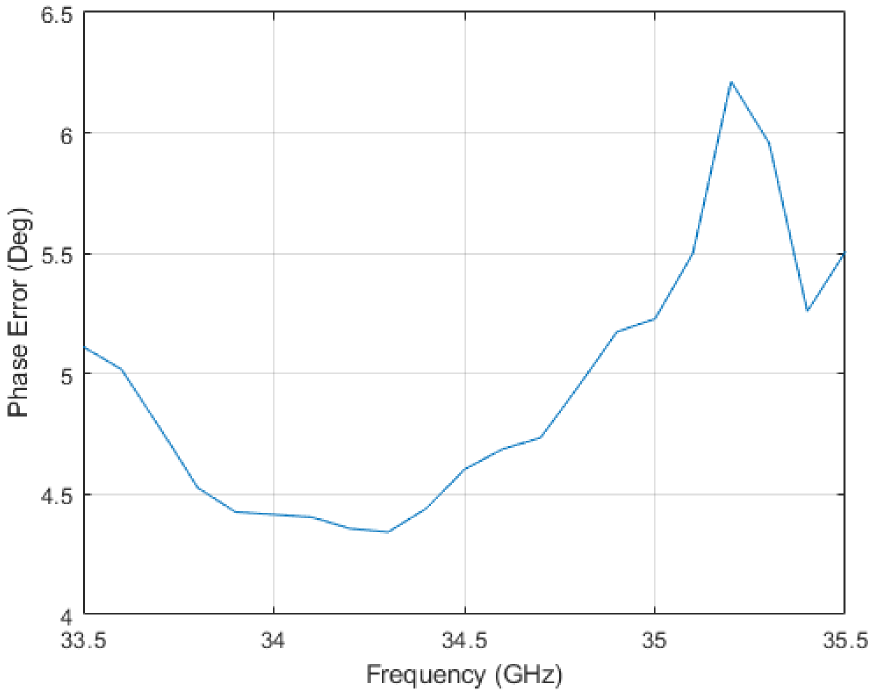

Figure B.18. Phase prediction error.

The prediction error of frequency from 33.5 GHz to 35.5 GHz is shown in Figure B.18. The maximum error is 6.21º at 35.2 GHz, while the minimum error is 4.3º at 34.3 GHz. In the operating frequency band of the VLR, the average phase prediction error is 4.61º.